

“Solidification Modeling of Austenitic Cast Iron: A Holistic Approach“

Von der Fakultät für Georessourcen und Materialtechnik
der Rheinisch-Westfälischen Technischen Hochschule Aachen

zur Erlangung des akademischen Grades eines
Doktors der Ingenieurwissenschaften

genehmigte Dissertation

vorgelegt von **Dipl.-Ing.**

Björn Pustal

aus Heidelberg

Berichter: Univ.-Prof. Dr.-Ing. Andreas Bührig-Polaczek
Univ.-Prof. Dr.rer.nat. Dr.h.c. Günter Gottstein

Tag der mündlichen Prüfung: 11. Mai 2010

Diese Dissertation ist auf den Internetseiten der Hochschulbibliothek online verfügbar

Titel: Solidification Modeling of Austenitic Cast Iron: A Holistic Approach

Autor: Björn Pustal

Gießerei-Institut der RWTH Aachen

Intzestr. 5

52072 Aachen

Reihe: Ergebnisse aus Forschung und Entwicklung, Band 1

ISBN: 978-3-9813872-0-9 (eBook)

© 2010 Gießerei-Institut der RWTH Aachen und der Autor

Diese Dissertation ist auf den Internetseiten der Hochschulbibliothek der RWTH Aachen online verfügbar.

Bibliografische Information der Deutschen Nationalbibliothek

Die Deutsche Nationalbibliothek verzeichnet diese Publikation in der Deutschen Nationalbibliografie; detaillierte bibliografische Daten sind im Internet über <http://dnb.d-nb.de> abrufbar.

Verlag: Gießerei-Institut der RWTH Aachen

Intzestr. 5

D-52072 Aachen

Tel.: +49 (0)241 8095880

Fax.: +49 (0)241 8092276

E-Mail: sekretariat@gi.rwth-aachen.de

Internet: www.gi.rwth-aachen.de

Danksagung / Acknowledgement

Nach über acht Jahren am Gießerei-Institut, in denen ich mit vielen Menschen zusammengearbeitet habe, möchte ich mich bedanken bei ...

... Prof. Dr.-Ing. A. Bührig-Polaczek für die Betreuung und die Freiheit, die Ausrichtung meiner Forschungen selbstständig gestalten zu können. Für seine kritischen Anregungen und das mir entgegengebrachte Vertrauen bedanke ich mich.

... Prof. Dr.rer.nat. Dr.h.c. G. Gottstein für die Übernahme des Koreferats und die gute langjährige Zusammenarbeit.

... der Deutschen Forschungsgemeinschaft (DFG) für die kontinuierliche finanzielle Förderung der entstandenen Arbeit im Rahmen des Sonderforschungsbereiches 370 *Integrative Werkstoffmodellierung* und später im Rahmen des Transferbereichs 63 *Praxisrelevante Modellierungswerkzeuge*.

... allen Kollegen am Gießerei-Institut und bei ACCESS, die mich stets tatkräftig unterstützt haben. Mein besonderer Dank gilt Dr. Uwe Vroomen für die herzliche und gute Zusammenarbeit sowie auch Emir Subasic für die Übernahme der Rechnergruppe und die Durchführung der Abgüsse in Nortorf. Dr. Benkt Hallstedt möchte ich danken für die fruchtbaren Diskussionen sowie die Durchführung der DTA und der Vergleichsrechnungen zur Softwarevalidierung. Ganz besonders hervorheben möchte ich meine Dankbarkeit für das sorgfältige Korrekturlesen dieser Arbeit durch Hannah Siebert und Dr. Stefan Benke sowie Dr. Georg Schmitz für die hilfreichen Tipps zum Prüfungsvortrag. Darüber hinaus sein Dr. Ralf Berger und Dr. Bernd Böttger für ihre Hilfe gedankt. Für das freundliche und kollegiale Miteinander sowie zahlreiche unvergessene Mittagessen danke ich Annemarie Bulla, Dr. Gottfried Laschet, Dr. Georg Ehlen, Dr. Mahmoud Ahmadein, Mohamed Yamine Jouani, Dr. Menghuai Wu und Prof. Dr. Andreas Ludwig.

... Tobias Müller, Martin Feller, Ulrich Althaus und Peter Otten für die stets freundliche technische Unterstützung und tatkräftige Mitwirkung bei verschiedenen Projekten wie der GI-Homepage. Phillip Jörres sei gedankt für die Umsetzung des graphischen Frontends und Felix Münchhaffen für das Erstellen eines einfachen Lizenzmanagers für das hier vorgestellte Programm.

... den guten Geistern im Sekretariat: Brigitte Vanweersch, Ingeborg Thouet und Sabine Wolters, die mir mit Rat und Tat bei administrativen Fragen aller Art zur Seite standen sowie den Kolleginnen und Kollegen der Metallographie, dem Fotolabor, der Analytik,

der mechanischen Werkstatt und der Gießhalle für ihre Unterstützung bei den experimentellen Arbeiten.

... den Mitarbeitern von CLAAS GUSS: Dr. Christine Bartels, Uwe Schmidt, Ferdinand Gaßner und Dr. Andreas Huppertz sowie bei den Mitarbeitern von MAGMA: Erik Hepp, Dr. Marc Schneider, Dr. Jörg C. Sturm und Dr. Erwin Flender für die gute Kooperation und die Bereitschaft bei diesem Projekt mitzuwirken. In besonderer Hinsicht gilt mein Dank Dr. Wilfried Schäfer, der mit mir die Schnittstellen zur Prozesssimulation ausgearbeitet hat.

... Bernd Hoffmann, Dr. Rainer Koch und Tibor Schweikert für die Ermutigung zur Fortbildung, bei meinen Eltern für die finanzielle Hilfe während meines Studiums, die stets offene Tür und ihr Verständnis über die Jahre. Ganz besonders danke ich meiner geliebten Frau ♡ Sabine Kühlich ♡ für ihre Güte, Geduld und die moralische Unterstützung während der Endphase meiner Promotion und seit 04.07.2010 natürlich auch dem guten Bruno ♡, der uns mit großer Freude erfüllt!

Table of Contents

0	Executive Summary	I
0.1	Introduction and Motivation	I
0.2	State-of-the-Art	III
0.3	Model Description	IV
0.3.1	Model Characteristics	IV
0.3.2	Representative Volume Element	VI
0.3.3	Species Conservation Equation	VII
0.3.4	Species Flux Balance	VII
0.3.5	Morphology and Averaged Quantities	VIII
0.3.6	Dendrite Arm Coarsening	VIII
0.3.7	Thermodynamic Calculations	IX
0.3.8	Time-Temperature Correlation	IX
0.3.9	Solution Algorithm	X
0.3.10	Coupling to Process Simulation	XI
0.4	Experiments and Evaluation	XII
0.4.1	Production of Castings	XII
0.4.2	Chemical Analysis	XIII
0.4.3	Microstructure Characterization	XIII
0.4.4	Electron Probe Micro Analysis	XIII
0.4.5	X-Ray Analysis	XIV
0.5	Model Sensitivity and Model Validation	XV
0.5.1	Introduction	XV
0.5.2	Comparison of Submodels	XVI
0.5.3	Variation of the Chemical Composition	XIX
0.5.4	Comparison with Solidification Kinetics from DTA	XIX
0.5.5	Simulation Setup	XX
0.5.6	Distributions of Microstructural Quantities	XXI
0.5.7	Comparison of Cooling Curves	XXI
0.5.8	Validation of Porosity Predictions	XXIII
0.6	Summary and Conclusions	XXIV
1	Introduction and Motivation	1

2	Fundamentals	5
2.1	Objectives	5
2.2	Microsegregations	5
2.3	Thermodynamics	6
2.3.1	Fundamental Laws and Equations	6
2.3.2	Equilibrium Conditions	8
2.3.3	Gibbs-Thomson Relation	9
2.4	Transport Equations and Constitutive Laws	10
2.5	Finite Volume Method	12
2.6	Cast Iron and Graphite Shape	12
3	State-of-the-Art	19
3.1	Objectives	19
3.2	Material Models for Solidification	19
3.3	Austenitic Ductile Iron	23
3.4	Formation of Chunky Graphite	24
4	Model Description	27
4.1	Objectives	27
4.2	Model Characteristics	28
4.3	Microsegregation Model	30
4.3.1	Representative Volume Element	30
4.3.2	Species Conservation Equation	32
4.3.3	Species Flux Balance	33
4.3.4	Morphology and Averaged Quantities	35
4.3.5	Front-Tracking	38
4.3.6	Implementation of Cross-Diffusion	39
4.3.7	Dendrite Arm Coarsening	39
4.4	Specific Quantities	41
4.5	Thermodynamic Calculations	43
4.5.1	TQ-Interface	43
4.5.2	Precipitation Simulation	43
4.5.3	Phase Activation	45
4.5.4	Thermodynamic Properties	45
4.6	Time-Temperature Correlation	46
4.7	Graphical Frontend	47
4.8	Solution Algorithm	48
4.9	Coupling to Process Simulation	50
4.10	Postprocessing	52
5	Experiments and Evaluation	53

5.1	Objectives	53
5.2	Production of Castings	53
5.3	Chemical Analysis	55
5.4	Microstructure Characterization	55
5.5	Differential Thermal Analysis	56
5.6	Electron Dispersive X-Ray Analysis	57
5.7	Electron Probe Micro Analysis	58
5.8	X-Ray Analysis	59
6	Model Sensitivity and Model Validation	63
6.1	Objectives	63
6.2	Introduction	64
6.3	Model Sensitivity	65
6.3.1	Comparison of Submodels	65
6.3.2	Comparison of Databases	69
6.3.3	Variation of Chemical Composition	70
6.3.4	Impact of Mold Filling	73
6.4	Model Validation	76
6.4.1	Cross-Diffusion and Solidification Model	76
6.4.2	Comparison with Microsegregations from EPMA	77
6.4.3	Diffusion Solver	78
6.4.4	Comparison with Solidification Kinetics from DTA	79
6.5	Coupled Simulations: Model Application and Validation	80
6.5.1	Simulation Setup	80
6.5.2	Cooling Characteristics of Reference Elements	81
6.5.3	Distributions of Microstructural Quantities	82
6.5.4	Comparison of Cooling Curves	82
6.5.5	Validation of Porosity Prediction	84
7	Summary and Conclusions	87
8	Bibliography	93
A	Nomenclature and Abbreviations	101
B	Deduction of Averaged Quantities	107
C	Discretization of Governing Equations	111
C.1	Species Conservation Equation	111
C.2	Species Flux Balance	115
D	Analytical Diffusion Solution	119

E	Structure Charts	121
F	Table of Figures	129
G	Table of Tables	133
H	Abstract	135
I	Curriculum Vitae	137
J	Zusammenfassung	139
K	Lebenslauf	141

0. Executive Summary

0.1 Introduction and Motivation

Environmental and cost demands placed on technical products, such as castings, are constantly on the increase, and this has been particularly apparent over the last two decades. These demands are met by lightweight designs and improvements in efficiency. This involves the development of new materials and processing concepts alongside gradual improvements to existing concepts. Austenitic cast iron, for instance, is a corrosion-resistant material suitable for higher temperatures. The reduction of defects in castings through alloy or process development achieves more homogeneously distributed properties and enables lightweight designs or applications demanding higher loads and temperatures. It is widely accepted that process simulations enable a deep understanding of complex phenomena and have contributed largely to the enormous technical progress of recent times. More and more companies are also discovering the benefits of material and thermodynamic simulations in material development.

The solidification behavior of alloys is impacted by the quantitative contribution of various kinetic effects, such as constitutional, curvature, or kinetic undercooling. These effects are all associated with species diffusion, either in a bulk mixture phase, ahead of a curved solid-liquid interface, or across a curved interface. The conclusion is simple: solidification would be impossible without diffusion, even in pure alloys, since the rearrangement of atoms into an ordered crystal structure could not proceed. It is therefore desirable to find a general approach describing these kinetic effects, or at least the dominant ones, quantitatively. Some alloys tend to be very sensitive to diffusive effects, especially when fast and slow diffusing species are present, as in the case of austenitic cast iron, which is the focus of the present work. According to Stefanescu (Ste02), "Cast iron is one of the most complex, if not the most complex, alloys used in industry, mostly because it can solidify with formation of either a stable (austenite-graphite) or a metastable (austenite-cementite) eutectic. Furthermore, depending on composition and cooling rate, several graphite shapes can be obtained at the end of solidification".

This work is aimed at modeling the solidification kinetics of austenitic cast iron on a thermodynamic physical basis, while keeping the approach simple enough to obtain time-

efficient predictions enabling a direct coupling to process simulation. When a casting solidifies, heat is usually extracted through its surfaces. This leads to differences in local cooling conditions, microstructures, defects, and hence, properties. On the other hand, microstructure evolution and the associated latent heat released by crystallization is a time-dependent process. This is especially characteristic for cast iron. It is therefore meaningful to couple heat transport simulation on the process scale and material simulation on the microscale to take account of local interaction effects between both scales.

An undesirable, but common casting defect is shrinkage porosity. This is due to volume reduction on crystallization. However, some phases, such as graphite in cast iron, increase in volume on precipitation and therefore help prevent shrinkage porosity. The accuracy of shrinkage prediction in the solid-liquid phase mixture is therefore a direct function of the accuracy of phase fraction and phase volume prediction.

Microsegregation models predict phase fractions and concentration profiles (microsegregations) in a representative part of the microstructure. Microsegregations build up in solid phases through redistribution of alloying elements ahead of the moving solid-liquid interface and are reduced by diffusion of species. Furthermore, averaged thermodynamic properties for the resulting phase mixture, such as heat capacity, density, or latent heat, can be obtained. These are necessary in order to determine the heat transport on the process scale when a coupling of both scales is desired. Other, more sophisticated approaches for simulating microstructures, such as the phase field method or the cellular automaton technique, are too time-consuming for a direct coupling. The author is aware of only one commercial microsegregation model that neither provides a programming interface for a direct coupling nor seems to be stable and fast enough for such an undertaking. For these reasons, the author was motivated to develop a model based on the work of predecessors, such as Greven (Gre00) and Fackeldey (FLS96).

Section 0.2 of this summary provides a review of recent microsegregation modelings and couplings. Section 0.3 starts by comparing the features of the model presented to those of the most comprehensive, state-of-the-art models. Furthermore, the concept of the model and its realization are outlined. In order to validate the microsegregation model itself, coupling to the temperature solver and coupling to the porosity prediction, extensive experimental work has been carried out casting and analyzing GJSA-XNiCr 20-2 clamp-rings, as explained in Section 0.4. Section 0.5 provides an answer to the question as to how sensitive the particular submodels are to variations in cooling characteristics and chemical composition. First, the stand-alone version of the code is validated and then the coupled version with reference to the clamp-ring casting. Section 0.6 summarizes the main results and conclusions of this work.

0.2 State-of-the-Art

As distinct from empirical models, solidification modeling on the microscale involves space-resolved physics-based calculations which model the time-dependent microstructure evolution. Andersson et al. (AHJA90) and, later, Crusius et al. (CIK⁺92) started to develop a tool for diffusion-controlled transformation (DICTRA¹) which was commercialized in 1995. It is the most commonly used product today because it offers a wide range of applications and is the only commercially available microsegregation software the present author is aware of. Kraft and Chang (KC97) reviewed a large number of microsegregation models. These models encompass a range of different morphologies, solid state diffusion, dendrite arm coarsening, and undercooling effects. The authors concluded that microsegregation models, in relation to all of the effects discussed, are capable of predicting microsegregation very accurately. Kattner et al. (KBC96) coupled a microsegregation model to thermodynamic calculations in order to predict the solidification path of an eight-component superalloy. Xie et al. (XYD⁺03) studied the solidification of an AA7050 alloy. They have compared various geometrical assumptions, that is plate-like, cylindrical, and spherical geometry, with an experimental test case and concluded that the cylindrical geometry shows the closest correlation.

Two and three dimensional material simulation methods not only reveal solidification kinetics, but also information about microstructure, even for complex multicomponent and multiphase systems. However, this information is expensive in terms of computation time when morphological information is not required as a result, but can be provided as an input quantity. For purely predicting solidification kinetics, one-dimensional approaches generate similar results, while needing considerably less computation time. In contrast to empirical material models, such as the Avrami (Avr40) model, microsegregation models reproduce the kinetics on a physical and thermochemical basis. Thus, microsegregation models in combination with thermodynamic and kinetic databases constitute a general approach. Empirical models are in principle restricted to the particular alloy under consideration. Dioszegi and Svensson (DS05) proposed an inverse kinetic analysis in order to determine the parameters for such a model.

It would thus seem to be the case that coupling a microsegregation model with a process simulation tool is desirable in order to take advantage of local precipitation kinetics. This was proposed by Sasikumar and Exner (SE92). Kraft (Kra95) used a simplified approximation for this coupling. A first, but indirect, coupling was presented by Fekeldey et al. (FLS96) in which the microsegregation simulations are performed after temperature simulation. Directly coupled results for a two-dimensional casting were first presented by Banerjee et al. (BSKB97). They had been using a simplified model to treat diffusion in the solid phase according to Wang and Beckermann (WB96). Greven (Gre00) coupled

¹DICTRA is a trademark of Thermo-Calc AB, Stockholm, Sweden

a microsegregation model to a finite element temperature solver. He introduced directly coupled simulations for three-component aluminum alloys and a simple step casting discretized with an FEM mesh consisting of 400 nodes. This model was further developed by Pustal et al. (PBL⁺03) and applied to a more complex case where an AA2024 ingot casting including gating system was simulated with a mesh consisting of 3000 nodes, although the model was still restricted to three-component systems. Both Greven and Pustal applied a direct coupling procedure where microsegregation simulations were performed for every particular finite element. This means, redundant and time-consuming microsegregation simulations are performed, for example, at symmetrically placed nodes.

Lacaze (Lac99) utilized a microsegregation model to study the solidification behavior of a spheroidal graphite iron consisting of the three fundamental components: iron, carbon, and silicon. Lacaze found that on solidification pronounced microsegregations build up, which are expected to impact the subsequent solid state transformations, as suggested by Dorazil (Dor91). Svensson and Dugic (SD99) demonstrated that it is possible to calculate an average density of the phase mixture (liquid and solid phases) by using molar volumes of each phase and molar masses of the elements in order to predict the shrinkage behavior of cast iron. Celentano et al. (CDGB08) coupled a macroscopic FEM temperature solver with a microsegregation model for ductile iron by taking into account nucleation and diffusion-controlled growth, which is determined by the carbon and silicon profile. This model is using a quasi-stationary analytical solution that was proposed by Su et al. (SOYF84) with a polynomial description of liquidus and solidus line, but only on eutectic solidification.

0.3 Model Description

0.3.1 Model Characteristics

Tab. 1 compares the characteristics of the approach presented to the most comprehensive coupled and uncoupled state-of-the-art models. Besides the coupled version of the present code, also a stand-alone version was programmed to enhance its applicability and testability.

Apart from the present work, the commercial software DICTRA is the only listed model that accounts for cross-diffusion and allows for the precipitation of multiple solid phases, as described by Andersson et al. (AHH⁺02). However, DICTRA's multiphase concept is based on additional volumes called cells and are not generated automatically when an additional phase becomes active. Cells and cell size need to be predefined by the user. At the same time, DICTRA provides additional features which are not focused on in the present work. The model of Xie et al. (XYD⁺03) accounts for dendrite arm coarsening by an approach of Beaverstock (Bea97) which was extended by Rappaz and Boettinger

Tab. 1: Comparing the features of the present approach to the most comprehensive state-of-the-art microsegregation models.

Model Reference	Pustal Present Work	Greven (Gre00)	Celentano (CDGB08)	DICTRA (AHH ⁺ 02)	Kattner (KBC96)	Xie (XYD ⁺ 03)
Porosity-Coupling	3D	—	—	—	—	—
Macro-Coupling	3D	3D	2D	—	—	—
Components	n	3	3	n	n	n
Solid Phases	m	2	2	2 ⁺	2	2
Cross-Diffusion	yes	—	—	yes	—	—
Geometry	mixed	1	3	1, 2, 3	1	1, 2, 3
DAS coarsening	(RB99)	(RHE86)	—	—	—	(Bea97)
Thermodynamics	TC	CA	—	TC	OA	PE
Diffusion Solver	num.	num.	anal.	num.	num.	num.

TC: Thermo-Calc

CA: ChemApp

OA: Own Approach

PE: PANENGINE

(RB99). The model of Xie et al. is coupled to the commercial thermodynamic software module PANENGINE². Both, DICTRA and the model of Xie et al. account for multiple geometries of the representative volume element, that is plate-like geometry, cylindrical geometry, and spherical geometry. This geometry concept was generalized in the present work in order to map mixed geometries on the representative volume element, as described in Section 0.3.5. Celentano et al. (CDGB08) present a coupled approach for cast iron which is somewhat limited compared to the uncoupled models mentioned. The most comprehensive coupled model is based on the work of Greven (Gre00), which is a precursor version to the present work. Greven’s model is restricted to a number of distinct three-component aluminum alloys and coupled to the thermodynamic software interface ChemApp³. Diffusion and dendrite arm coarsening were simulated only on primary solidification of a step casting with a mesh consisting of 400 nodes. Subsequently to Greven, Hofmeister (Hof02) reports a similar version. The additional features of this version, the coupling to Thermo-Calc and diffusion during the complete solidification process, were added and described by Pustal et al. (PBL⁺03). Since Greven and Hofmeister published their work, comprehensive changes, improvements, and enhancements were made to the code. Unique features of the model presented with reference to Tab. 1 are: (1) direct coupling to the porosity prediction according to Section 0.3.10, (2) innovative concept of coupling to the process simulation according to Section 0.3.10, (3) multiphase concept by generalizing the local phase fraction approach, as described in Section 0.3.2, and (4) mixed geometry concept through the introduction of a geometry factor, which is explained in Section 0.3.5.

²PANENGINE is a trademark of CompuTherm LLC, Madison, USA

³ChemApp is a trademark of GTT GmbH, Herzogenrath, Germany

0.3.2 Representative Volume Element

One example of a typical, representative volume element (RVE) is shown in Fig. 1. The characteristic length of the RVE corresponds, for instance, to an average grain radius or half of an average dendrite arm spacing $\lambda/2$ as shown. In the RVE shown, two solid phases α and β are growing from the left side into the liquid phase L on the right. The concentration profiles x^α and x^L are plotted on the left ordinate as function of the spatial variable s . The concentration profile in the β -phase is omitted in the diagram for the sake of clarity.

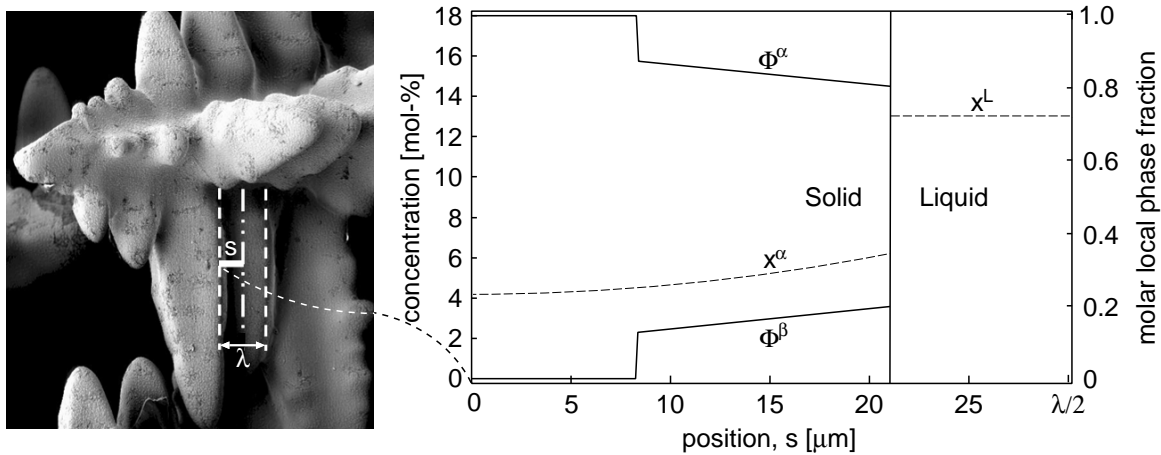


Fig. 1: Multiphase concept in the RVE of the microsegregation model (right). The characteristic length corresponds to half of an average dendrite arm spacing (left) or to an average grain radius for example.

A diffusion type needs to be selected for each phase, that is complete mixing, final diffusion, or no diffusion. The solid phases and the liquid phase are strictly separated from each other by the solid-liquid interface, and diffusion is modeled in each contemplated phase. Exchange of species between phases is realized by boundary conditions which depend on the diffusion type selected for each phase. If, for example, no diffusion is assumed for the α -phase, the concentration profiles are impacted by redistribution only. In this case, the imposed interface concentration *x , originating from a thermodynamic equilibrium calculation, is simply interpolated between *x and the interface concentration of the previous time step. The index “ $*$ ” is used for quantities at the solid-liquid interface. When final diffusion is selected for the α -phase, a diffusion simulation is performed based on this interpolated concentration profile. Following an approach of Chen and Chang (CC92) for eutectic growth of two solid diffusion phases, a local phase fraction ${}^*\phi^j$ of each solid phase j is introduced. This local quantity depends on the change in phase fraction Δf^j of the solid phase j and the changes in phase fractions Δf^b of all m currently precipitated solid phases:

$${}^*\phi^j = \Delta f^j / \sum_{b=1}^m \Delta f^b . \quad (0.1)$$

This definition implies that ϕ^j is a complementary function at each location of the RVE.

0.3.3 Species Conservation Equation

To calculate the microsegregation patterns of each species i within each diffusion phase j , the species conservation equation is adapted to the microsegregation model by multiplication of the local phase fraction ϕ^j :

$$\frac{\partial(\phi^j x_i^j)}{\partial t} + \text{div}(\phi^j \mathbf{j}_i^j) = \phi^j \dot{X}_i^j . \quad (0.2)$$

The first term of the species conservation equation takes account of a time-dependent change in concentration x^j . The diffusive fluxes \mathbf{j}_i^j may be either chemically or thermodynamically constituted. Alternatively, as in the present work, Eq. (0.3) may be used involving both approaches. The specific diffusive flux is modeled as a function of the gradients of all n alloying elements by introduction of the chemical diffusion matrix \mathbf{D} :

$$\mathbf{j}_i^j = - \sum_{b=1}^n \mathbf{D}_{ib}^j \mathbf{grad}(x_b^j) . \quad (0.3)$$

The diffusion matrix can be deduced from the mobility matrix which is extended for thermodynamic influences, as demonstrated by Campbell et al. (CBK02). The interdependence of the diffusing alloying elements is often referred to as *cross-diffusion*. The species source term \dot{X} is introduced for an intended modeling of solid state transformation.

0.3.4 Species Flux Balance

For the microsegregation model, flux balance equations are used to determine the new phase fractions adding the contributions due to back-diffusion. An integral version of an enhanced flux balance is given by Eq. (0.4). It is similar to the well-known lever rule, while taking account of the average concentrations $\langle x_i \rangle^L$ in the liquid phase L and in m solid phases j . These concentrations are weighted according to their phase fraction f . The sum of these products equals the average initial concentration $\langle x_i \rangle^0$, as represented by:

$$\langle x_i \rangle^L f^L + \sum_{j=1}^m \langle x_i \rangle^j f^j = \langle x_i \rangle^0 . \quad (0.4)$$

This integral flux balance is quite useful since it is self-conserving. However, when applying this balance equation to obtain phase fractions, potential programming or modeling errors may go unrecognized due to this conservative property. Moreover, numerical integration over the whole RVE is required to obtain average concentrations in each phase. Therefore, Eq. (0.4) is used as check sum defining a relative failure in concentration. In

order to determine the phase fractions, local flux balance equations at the solid-liquid interfaces are used instead of Eq. (0.4), which is reformulated in rate form and rearranged as follows:

$$\sum_{j=1}^m \left(\star x_i^L - \star x_i^j \right) \partial f^j = \sum_{j=1}^m \partial \langle x_i \rangle^j f^j + \partial \langle x_i \rangle^L f^L . \quad (0.5)$$

Here, the condition $\sum \partial f^j = -\partial f^L$ was applied and quantities at the interface are denoted by “ \star ”. The chemical fluxes $\partial \langle x_i \rangle^j f^j$ into the solid phases j are deduced from local concentration gradients $\mathbf{grad}(\star x_i^j)$ at the interface according to Eq. (0.3).

0.3.5 Morphology and Averaged Quantities

The solidification morphology of cast iron can be partially dendritic and partially globular. The predominance of the particular morphology depends on the nucleation and growth conditions of austenite and graphite. A one-dimensional RVE enables the reproduction of simple geometries only. In order to map mixed morphologies on the RVE, a geometry factor for diffusion g within the range $[1, 3]_{\mathbb{R}}$ is introduced, where 1 corresponds to plate-like, 2 to cylindrical, and 3 to globular geometry. For dendritic solidification morphologies, a value between a plate-like and a cylindrical geometry of 1.5 may be selected, or for dendritic-globular solidification morphologies, as for ductile iron, a value of 2.7 may, for instance, be appropriate.

0.3.6 Dendrite Arm Coarsening

For alloys with a dendritic solidification morphology, the dendrite arm spacing defines the length of the RVE and hence the diffusion distances inside the RVE. Additional kinetic effects are introduced by application of a dendrite arm coarsening model since diffusion distances evolve with time, and therefore, these are a function of cooling conditions. The coarsening model implemented is limited to the effect of dendrite arm ripening on solidification. Kattamis et al. (KCF67) formulated the undercooling associated with a curved interface as concentration shift by using the slope of the liquidus line m_i^L for a linearized two-component system. Beaverstock (Bea97) and Rappaz and Boettinger (RB99) applied this method to linearized multicomponent systems. This approach is adapted for use with the microsegregation model, but the phase diagram is linearized locally at each time step. Furthermore, the curvature $C = (\tilde{g} - 1)/r$, which depends on the geometry coefficient for coarsening \tilde{g} and the correlation $R = (f^S)^{1/g} \lambda$ between the radius R of the larger dendrite arm, the fraction solid f^S , and the dendrite arm spacing λ are introduced in the present work. The current dendrite arm spacing $\nu \lambda$ is then given in rate form as:

$$\begin{aligned} \nu\lambda &= \left(\omega\lambda^3 + \dot{\lambda}\partial t \right)^{\frac{1}{3}}, \text{ with} \\ \dot{\lambda} &= \frac{\gamma(\tilde{g} - 1)}{(f^S)^{2/g} \Delta S^{L,S} \left[\ln\left(1 - \frac{r_0}{R}\right) + \frac{r_0}{R} \right]} \sum_{i=1}^n \frac{D_i^L}{m_i^L (x_i^L - x_i^S)}. \end{aligned} \quad (0.6)$$

Due to dendrite arm coarsening, the liquid phase region grows together with the RVE by $\Delta l = \dot{\lambda}/2 \Delta t$. This is implemented in an explicit manner and also changes phase fractions, thermodynamic properties, and composition of the liquid phase. Because of the integration over the dissolution time of the smaller dendrite arm, Eq. (0.6) consists only of quantities that are related to a physical meaning.

0.3.7 Thermodynamic Calculations

To perform thermodynamic calculations by using Thermo-Calc during the runtime of the microsegregation software, the thermodynamic query interface (tq-interface), as described by Sundman and Chen (SC), is linked to the code as a shared library. For the species flux balance equation (0.5), equilibrium concentrations at the solid-liquid interface are required. These are obtained by precipitation simulations using Thermo-Calc. For this step, a set of thermodynamic constraints is defined to reduce the number of degrees of freedom to zero. These equilibrium conditions are namely: (1) a constant pressure $P = 1013.15$ hPa, (2) a total number of moles of the system $N^0 = 1$ mol, (3) a temperature T according to Section 0.3.8, and (4) an input composition \tilde{x}_i^L of the liquid phase according to Eq. (0.7). This input concentration equals the liquid concentration of the preceding time step ${}_{\omega}x_i^L$, but it is further modified by the absolute diffusive fluxes $\mathbf{J}_{i,e}^j$ into the solid phases:

$$\tilde{x}_i^L = {}_{\omega}x_i^L + \sum_{j=1}^m \left[\mathbf{J}_{i,e}^j \theta \right]_{-\omega\theta}^{\nu\theta} \Delta t / {}_{\omega}f^L. \quad (0.7)$$

θ is an underrelaxation factor weighting the diffusive flux of the previous ω and the current ν time step.

0.3.8 Time-Temperature Correlation

To facilitate solidification from the liquid state, temperature needs to be reduced over time. This has been implemented using three different methods: (1) reading a data file where time and temperature are correlated in an arbitrary manner, (2) assuming a constant cooling rate, and (3) assuming a constant specific heat extraction rate. The first and second method are simple, whereas in the third method temperature is deduced

from the heat conservation equation. Heat diffusion and advection are not considered in this simple heat transport problem, and their corresponding terms are therefore omitted:

$$C_p \frac{\partial T}{\partial t} + L_f \frac{\partial f^S}{\partial t} = \dot{h} . \quad (0.8)$$

0.3.9 Solution Algorithm

During main processing the various models and equations are processed in a certain sequence and under certain conditions so as to solve the so-called Stefan problem (Ste99). The solution of this problem requires solving the transient species transport problem in an expanding solid phase region which is itself part of the solution.

The actual main processing starts after preprocessing by reading in a data file for simulation and initialization of global variables. In a loop over time in discrete steps, time is correlated to temperature according to Section 0.3.8 or, alternatively, the temperature of each reference element is forwarded to the microsegregation software from the process simulation, as described in Section 0.3.10. The solidification state is classified as liquid, mushy, or solid and is preselected by the current temperature and fraction liquid. Below the liquidus temperature and above the a priori unknown solidification temperature, the solidification module is invoked, as described in the following paragraph. Later, the enthalpy change versus temperature is determined for solving the heat conservation equation. At the end of the time-loop, results are written to screen, files, diagrams, or forwarded to process simulation to calculate the temperature field of the subsequent time step.

On solidification the concentrations in the liquid phase not only change due to thermodynamics, but also due to diffusion, taken account of by manipulation of the input concentrations according to Eq. (0.7) for subsequent thermodynamic calculations (cf. Section 0.3.7). For an iteration, the corresponding variables are initialized and diffusion coefficients are deduced from thermodynamic databases. At each time step, an iteration is invoked, aimed at identifying the new phase fractions, which depend on the amount of solute diffusion into the mixture phases. For the given ambient pressure, current temperature, and manipulated liquid concentrations, multiphase equilibrium calculations are performed in order to determine the solid-liquid interface concentrations for each phase. With these equilibrium concentrations and the current concentration gradients, which are evaluated at the solid-liquid interfaces, flux balance equations (0.5) are assigned and solved. This overdetermined system of flux balance equations is solved by application of a Householder algorithm (Hou58). In the newly solidified volume, the concentrations are interpolated by using the equilibrium interface concentrations, which also serve later as Dirichlet boundary conditions to compute the species transport. The iteration is exited when the liquid concentration of the depending species and the change in liquid fraction

converge. The dendrite arm coarsening is determined by Eq. (0.6), while phase fractions and liquid concentrations are modified accordingly.

0.3.10 Coupling to Process Simulation

The microsegregation model was directly coupled to the temperature solver of the commercial process simulation tool MAGMASOFT⁴ (Stu04). Direct coupling means that both codes interact on runtime by exchanging results. Moreover, these results are interdependent. For the given problem, local properties of the solid-liquid phase mixture, the temperature field, as well as the time step width are exchanged. Local properties are density, heat capacity, latent heat of fusion, and fraction solid, which are derived from the mixture of individual phases with an average composition. The coupling to the temperature solver requires density, heat capacity, and latent heat of fusion, while this solver provides in return the temperature at each finite volume element. The local cooling characteristic defines the development of phase fractions and therefore also the properties of the phase mixture forwarded at each time step. Coupling to the algorithm for porosity prediction requires local density and fraction solid as determined by the microsegregation model and provided via the same interface.

MAGMASOFT applies an FVM discretization which results in a large number of volume elements. It is almost impossible to simulate the precipitation kinetics of phases at each such volume element for industrial castings within a reasonable time. Therefore, a scheme was developed consisting of *reference elements*, for which microsegregation simulations are actually carried out, while for the remaining elements, called *interpolation elements*, an interpolation of all required thermodynamic data over temperature or time is executed. The required steps of this concept are: (1) Definition of reference elements above liquidus temperature by a preferably homogeneous distribution in terms of temperature differences between the reference elements. Below liquidus temperature the reference elements are fixed. (2) Saving the thermodynamic properties (f^j , H , C_p , ρ) of the phase mixture with temperature and solidification time at each reference element. *Solidification time* refers to the time elapsed once the liquidus temperature has been reached. (3) The incremental change in properties at interpolation elements is determined by interpolation between the nearest neighboring reference elements. When the slope of change over temperature becomes too steep, the properties of each reference element are assumed to change over time instead. The nearest neighbors are selected by similarity criteria relating to temperature, solidification time, and liquid fraction since the assignment of thermophysical data is not necessarily unique. Furthermore, a variable is defined reflecting the number of phases currently precipitated from the liquid phase by a prime factor. This is required for the interpolation over temperature since properties may change discontinuously when a phase is activated

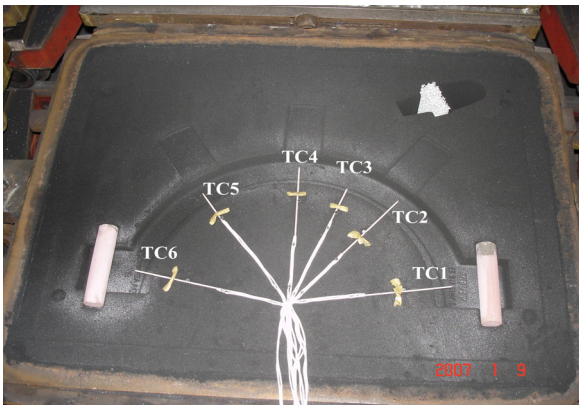
⁴MAGMASOFT is a registered trademark of Magma Gießereitechnologie GmbH, Aachen, Germany

or deactivated. (4) An internal time-loop is implemented to pass over reference elements or to add additional time steps if necessary.

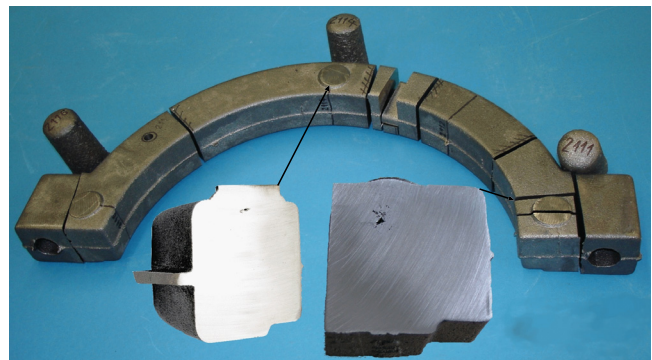
0.4 Experiments and Evaluation

0.4.1 Production of Castings

A series of eight clamp-rings made of GJSA-XNiCr20-2 was cast in a foundry under production conditions with variation of the inoculation state and the number of feeders, i.e. the central feeder was omitted for four castings. Fig. 2 (a) shows the drag of a green sand mold. Thermocouples of type S were used to record cooling curves at positions 1 through 6. The initial casting temperature in the case of the first, good inoculation treatment (castings c_a - c_d) was 1403°C , and, in the case of the second, poor inoculation treatment (castings c_e - c_h) was 1425°C . The castings c_a , c_b , c_e , and c_f were produced using all three feeders, whereas c_c , c_d , c_g , and c_h using only two feeders. In Fig. 2 (b) clamp-ring c_b is photographed together with a magnified cross-section at the right flange where porosity was detected. Porosity was also found at its counterpart to the left and, less pronounced, directly below the neck of the central feeder.



(a)



(b)

Fig. 2: (a) Drag of a green sand mold with thermocouples of type S numbered from 1-6 and (b) GJSA-XNiCr20-2 casting c_b with cut-off feeders and two magnified porous cross-sections, one below the central feeder and one below the feeder at the right flange.

The cooling curves below the left and right feeder at the flange show symmetry. Furthermore, it is notable that none of the exothermic feeders ignited to provide external heat. To evaluate the eutectic temperature, the castings c_a through c_f were considered. The eutectic temperatures were averaged over the cooling curves included, and the average was approx. 1190°C . This value was confirmed by differential thermal analysis which yields a eutectic temperature in the range 1185°C to 1195°C . Furthermore, a fraction

solid curve could be deduced from DTA, which is compared to the simulation results in Section 0.5.4.

0.4.2 Chemical Analysis

Composition analyses were carried out using a number of different methods summarized in Tab. 2. Coin samples were chilled for optical emission spectrometry (OES), while for inductively coupled plasma (ICP), infrared (IR), and gravimetric analysis samples or drilling chips from casting c_b were retained. In the case of the second method, as enumerated in Tab. 2, carbon and sulfur were measured using IR; manganese, phosphorus, chromium, nickel, and magnesium using ICP; and silicon gravimetrically. However, the analyses showed inconsistency, leading to an uncertainty about alloy composition, which is quantified by the root mean square deviation (RMSD).

Tab. 2: Comparison of various analyses of the same cast alloy. The values are given in wt.-%.

method	Ni	C	Si	Mn	Cr	P	S	Mg
1. OES	20.90	2.66	2.46	1.28	1.22	0.01	0.00	0.04
2. ICP, IR, grav.	20.10	2.80	2.76	1.20	1.00	0.01	0.01	0.05
3. grav.	20.60	2.90	2.53	1.14	1.08	<0.05	0.02	0.05
average value	20.53	2.78	2.58	1.21	1.10	0.01	0.01	0.05
RMSD	0.40	0.13	0.16	0.07	0.11	0.00	0.01	0.01

0.4.3 Microstructure Characterization

In Fig. 3 (a) a polished and etched sample is presented, cut from below the feeder at the left flange of clamp-ring c_b . The microstructure in this casting was analyzed along a horizontal and a vertical line by taking the pictures 1 through 16 and 18 through 35, respectively. Three distinct zones A, B, and C were identifiable. In chill zone A, at the rim of the sample, a clearly globular eutectic morphology in an austenite matrix formed containing well-distributed small carbides and some chunky graphite, as shown in Fig. 3 (b). Zone B and C consist mainly of austenitic dendrites surrounded by chunky graphite and a small number of large areas of carbides. Sometimes, islands of eutectic grains appear in zone B and C, as can be seen in Fig. 3 (c). Zone C also includes shrinkage porosity.

0.4.4 Electron Probe Micro Analysis

For quantitative carbon analysis by using electron probe micro analysis (EPMA), a sample was retained from clamp-ring c_a in the proximity of the right flange. The element distribution within the microstructure of a eutectic region was measured, as shown in

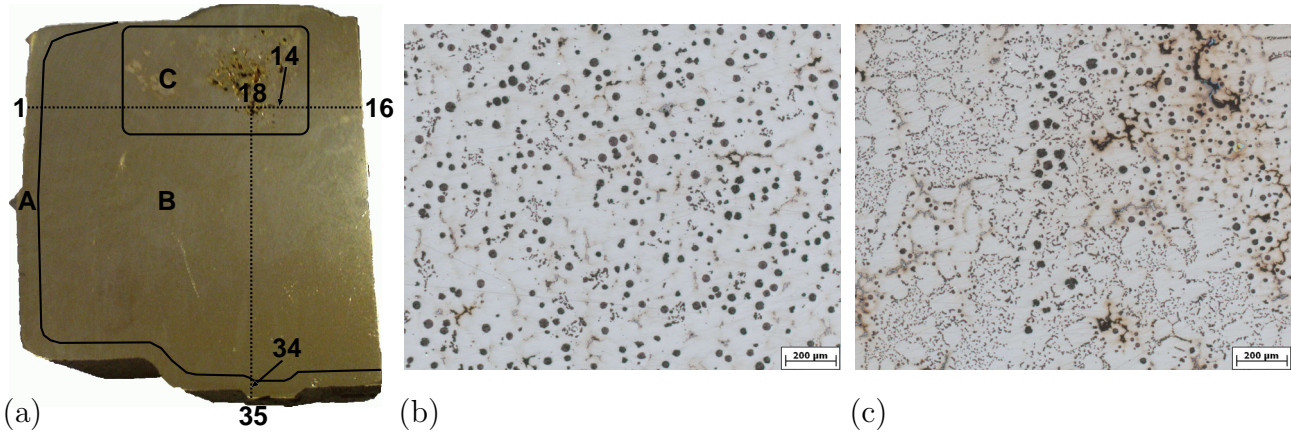


Fig. 3: (a) A polished and etched sample retained from clamp-ring c_b below the feeder at the left flange. (b) Microstructure in zone A (picture 34) and (c) in zone C (picture 14).

Fig. 4 (a). This finely structured eutectic area is a mixture of eutectic austenite, chunky graphite, a silicide and M7C3 where M can be iron, chromium, or manganese. The eutectic region is surrounded by an austenite matrix. The backscattering electron picture displays two line scans A and B. Line scan B in Fig. 4 (b) passes through austenite, the finely structured eutectic region, M7C3, again a mixed region, and ends in silicide.

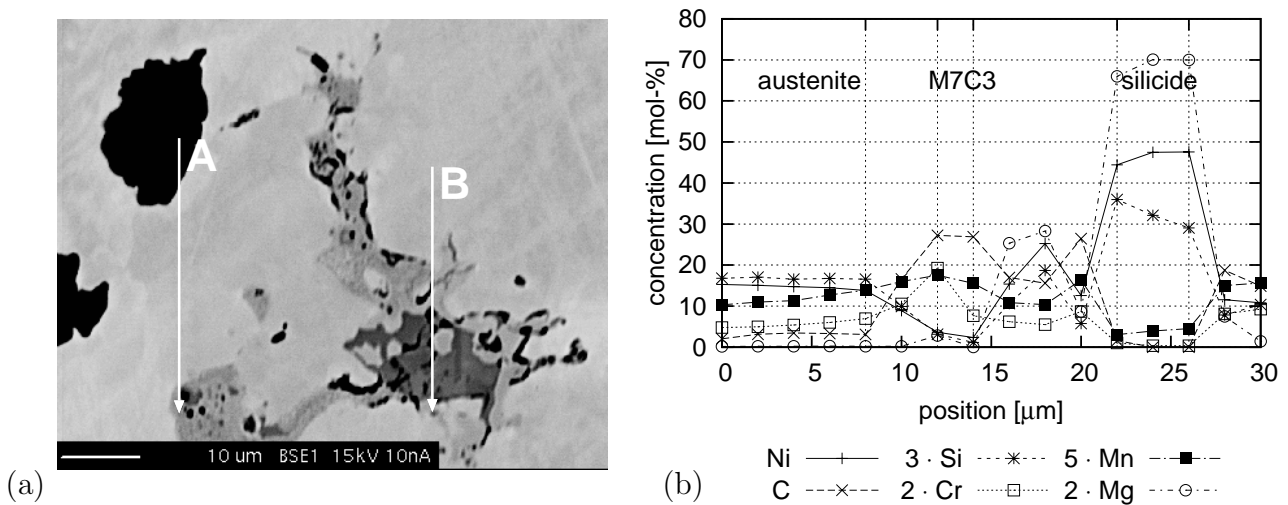


Fig. 4: (a) SEM backscatter electron picture of a eutectic region indicating (b) line scan B.

0.4.5 X-Ray Analysis

The castings c_a , c_c , c_d , c_f , c_g , and c_h were cut consecutively into slices using a water-jet cutter. Here and in the following sections of this summary, only the castings c_c , c_d , c_g , and c_h without central feeder are discussed. Casting c_c is shown in Fig. 5 (a). It shows a shrinkage cavity at location A, whereas the porous locations B and C shift towards the flange and D towards the ring. In the case of clamp-ring c_d in Fig. 5 (b), a massive

shrinkage cavity formed at location D, while compared to casting c_c , porosity A, B, and C are less pronounced and distributed along the center line. The overall porosity within the regions A, B, C, and D of clamp-ring c_g extends in a similar way as in the case of casting c_c , but the location of porosity is shifted. Casting c_g is falsified due to molding material break-off at the left flange. The level of occurrence of porosity in casting c_h is between that of casting c_c and c_d . Resuming this experiment, it may be conclude

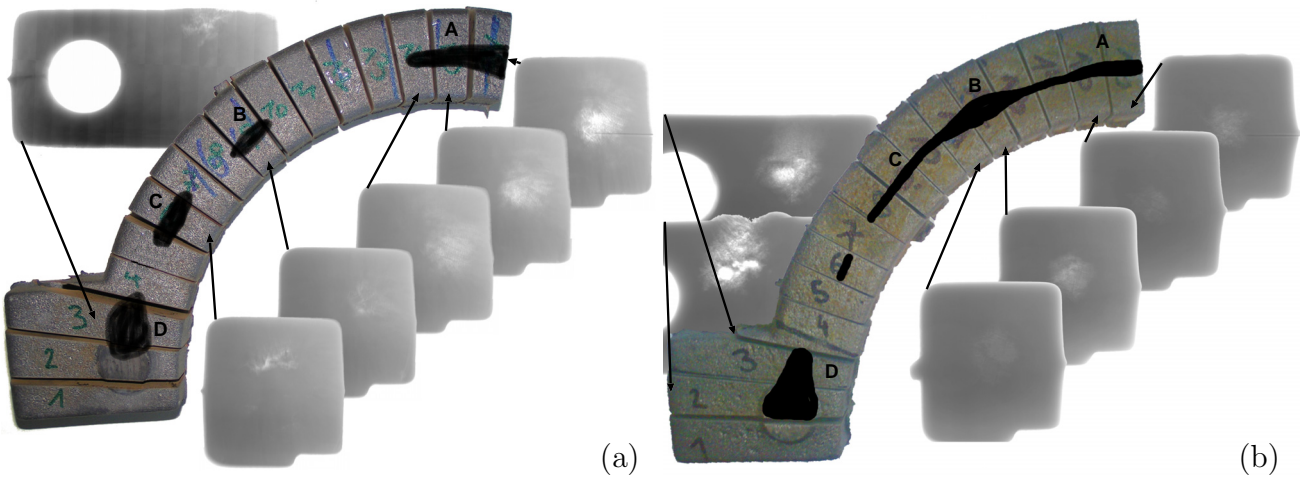


Fig. 5: (a) One half of casting c_c and (b) casting c_d . Both were cut into 16 slices and have no central feeder. The slices have been x-rayed to locate porosity as shown. For better comparison with simulated results, locations containing porosity are marked black on the castings.

firstly that porosity at location D was detected in all cases. In the case of the castings c_g and c_h , it is of a medium extend, while casting c_d shows a massive shrinkage cavity. Secondly, porosity along the center line of the ring was detected in every case. Thirdly, inoculation treatment does not appear to impact the formation of porosity. The variation of the location of porosity is due to statistical effects, since porosity forms on entrained particles. To take account of this effect, the porosity of the castings c_c , c_d , c_g , and c_h were superimposed in Fig. 13.

0.5 Model Sensitivity and Model Validation

0.5.1 Introduction

For the material simulations carried out in this section, the following initial, boundary, and runtime conditions applied: (1) the first composition given in Tab. 2; (2) the phases liquid, austenite, graphite, M7C3, and cementite; (3) the temperature is usually determined by using the three parameters $T_{\text{ini}} = 1405^\circ\text{C}$, $T_{\text{end}} = 1000^\circ\text{C}$, and $\dot{h} = -1000\text{ W/kg}$; and (4) for the dendrite arm coarsening model $\lambda_{\text{ini}} = 20\ \mu\text{m}$, $\gamma = 0.2\text{ J/m}^2$, and $r/R = 0.5$ were applied. As shown in Fig. 3, the predominant microstructure of GJSA-XNiCr20-2 is dendritic with chunky graphite. Fig. 1 shows the

shape of a dendrite arm, which corresponds most closely to an ellipsoid. This shape was approximated by applying a geometry coefficient $\tilde{g} = 1.7$ for dendrite arm coarsening. In contrast, a geometry coefficient $g = 2.3$ for diffusion was selected since this corresponds to a mixed geometry of imperfect spheres with a geometry coefficient of 2.9 and dendrite arms with a geometry coefficient of 1.7. Within the scope of a sensitivity analysis a number of these conditions are successively varied, as specified in the context.

0.5.2 Comparison of Submodels

In Fig. 6 (a), the development of fraction liquid over temperature is plotted for equilibrium and a Gulliver-Scheil solution, that is no diffusion in austenite and complete mixing in liquid. These two approximations are compared to microsegregation simulations at a heat extraction rate of 1000 W/kg. For this extraction rate, the chemical diffusion model results in a solidification time of 4.6 min, with cross-diffusion 5.6 min, and with cross-diffusion in combination with dendrite arm coarsening 5.5 min. It is notable that for this kind of alloy, solidification behavior in the case of chemical diffusion is very different from the model which takes account of the cross-diffusion effect. Without this effect, solidification ends in a eutectic-like manner at approx. 1154 °C. This appears to be unnatural when compared, for example, to the DTA measurements in Fig. 10. As the heat extraction rate reduces to 100 and 10 W/kg, solidification time increases and at 1 W/kg the solutions of all approaches reflect the equilibrium solution.

The abrupt end of solidification in the case of chemical diffusion can be explained by looking at the development of the liquid concentrations on solidification in Fig. 6 (b). In contrast to the situation with cross-diffusion, there is depletion of nickel and silicon in the liquid phase while the concentrations of chromium and manganese increase in the same manner as the fraction liquid decreases over temperature. Conversely, the slope of the carbon concentration appears to be constant. In this way, a critical concentration is reached at which the two solid phases, austenite and graphite, can grow without chemical restrictions. The formation of this critical composition is given for a wide range of heat extraction rates. An investigation was able to show that this range is given for solidification times between 6 s and 8.1 h.

In Fig. 7, the impact of cross-diffusion is highlighted by comparing carbon profiles resulting from simulations with and without cross-diffusion. The carbon profile at the end of solidification in a simulation with chemical diffusion is nearly homogeneously distributed in austenite at a level of approx. 7.0 mol-%. To highlight the impact of cross-diffusion, the gradient of nickel in austenite is plotted on the right ordinate. This impacts the diffusion of carbon as quantified by the chemical diffusion matrix. Nickel promotes significantly the up-hill diffusion of carbon in combination with other alloying elements. The simulation results indicate that the gradients of nickel and silicon are negative, while

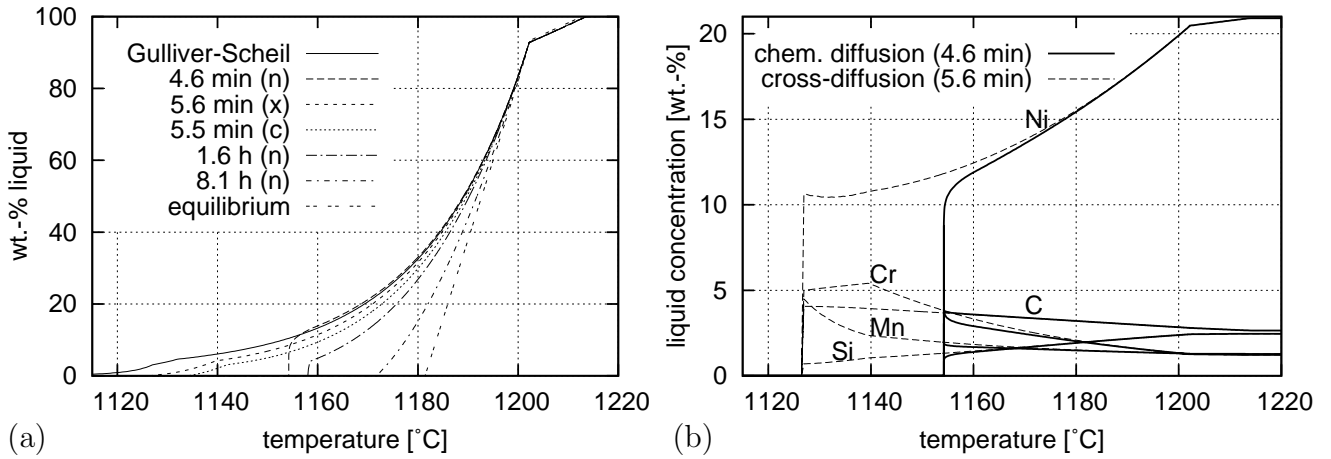


Fig. 6: (a) Impact of submodels on the liquid fraction where (n) labels chemical diffusion, (x) cross-diffusion, and (c) cross-diffusion combined with dendrite arm coarsening. On application of the chemical diffusion model, the heat extraction rate was varied: $50 \text{ W/kg} \hat{=} 1.6 \text{ h}$ and $10 \text{ W/kg} \hat{=} 8.1 \text{ h}$. (b) The liquid concentrations during solidification give an indication of the abrupt decrease in liquid fraction on application of the chemical diffusion model.

the diffusion interaction coefficients are positive. Conversely, the gradients of chromium and manganese are positive, while the diffusion interaction coefficients are negative. Summation of the individual diffusive fluxes of carbon according to Eq. (0.3) leads to strong up-hill diffusion, resulting in a pronounced microsegregation profile of carbon. This effect explains the promotion of graphite formation with increasing nickel content.

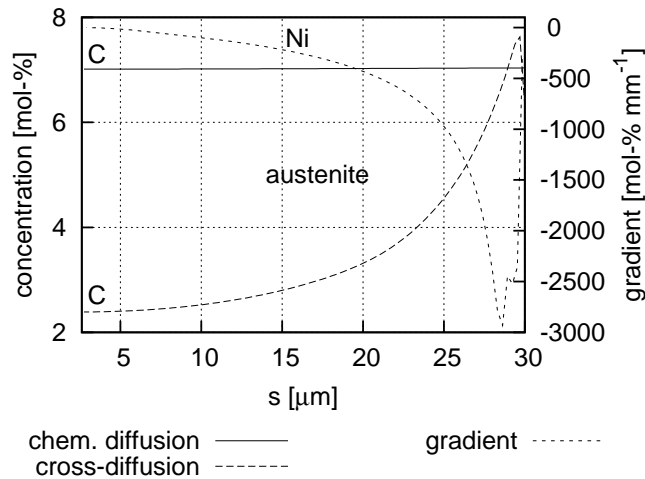


Fig. 7: Comparison of the microsegregation patterns of carbon at the end of solidification taking / not taking account of cross-diffusion effects in austenite. As an example for the diffusive interaction of species in the case of the cross-diffusion model, the gradient of nickel is plotted on the right ordinate, which shows a positive cross-diffusion coefficient and explains the strong up-hill diffusion of carbon.

The phase fractions and solidification temperatures are not only sensitive to heat extraction rate, but also to cooling characteristics. This is demonstrated by comparing

phase fractions over temperature in Fig. 8 (a) at a constant cooling rate, a constant heat extraction rate, and a cooling curve resulting from a coupled simulation at a position of the clamp-ring which exhibits fast cooling. All three time-temperature correlations are selected so as to obtain a solidification time of approx. 135 s. The resulting phase fractions and the solidification temperatures are very similar for the constant cooling rate and constant heat extraction rate model, where approx. 0.4 and 0.43 wt.-% M7C3 is formed, respectively. When, in contrast, the displayed cooling curve is applied, significantly less graphite is formed and no M7C3. The reason for this behavior is that the early stage of solidification, where usually most of the dendrite arm coarsening takes place, is passed very fast. This leads to a dendrite arm spacing of only 22.51 μm , which is very close to the initial value of 20.00 μm . Due to this small DAS, the solidification behavior is closer to equilibrium compared to the case at a constant heat extraction rate resulting in a DAS of 31.10 μm . Applying a constant cooling rate leads to slower cooling during primary formation of austenite, and, consequently, a DAS of 36.25 μm results. This is because the coarsening rate is high at the beginning of solidification when the dendrite arm radius is small, as shown in Fig. 8 (b). Thus, dendrite arm coarsening is behind the sensitivity of the model to cooling characteristics, but slightly reduces sensitivity when only the heat extraction rate is varied.

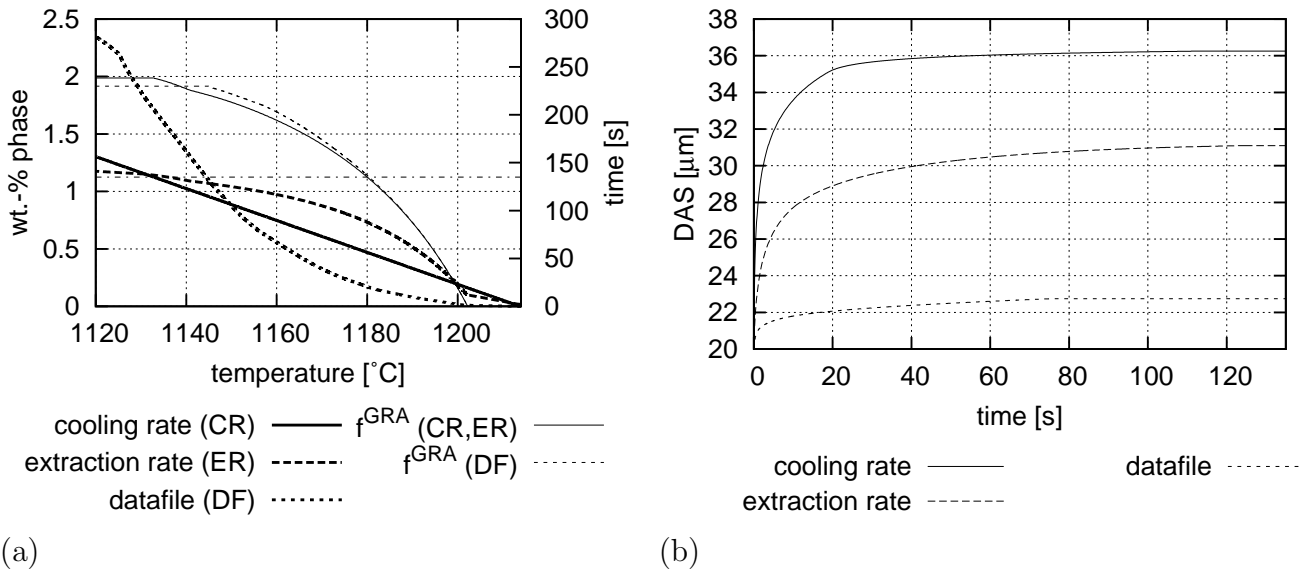


Fig. 8: (a) Three different cooling characteristics (CR: cooling rate, ER: heat extraction rate, DF: cooling curve from a data file) and its impact on the resulting graphite fraction, when solidification time is kept constant at approx. 135 s (dash-dot line); (b) the corresponding dendrite arm coarsening.

0.5.3 Variation of the Chemical Composition

Spear (Spe93) states that the promotion of graphite formation with nickel content is because nickel reduces the solubility of carbon in austenite. However, this appears to be only half the truth, as clarified in Fig. 9 (a), graphite correlates linearly over the nickel content and no carbides are formed as long as cross-diffusion effects are neglected. Conversely, when cross-diffusion effects are taken into account, up to 10 wt.-% nickel a considerable amount of cementite and above this value, M7C3 is precipitated in addition to graphite. Furthermore, significantly more graphite is formed than in the case without cross-diffusion since the slope of increase is steeper. Thus, it is concluded that the graphite promoting effect of nickel is mostly due to cross-diffusion since this leads to strong up-hill diffusion of carbon in austenite, which enriches the carbon concentration in the liquid phase, as discussed in Section 0.5.2. Fig. 9 (b) reveals a minimum of the liquidus temperature at about 20 wt.-% nickel, and with further additions of nickel the liquidus temperature rises again up to 1396 °C at 35 wt.-%. The eutectic temperature shows a linear increase over the nickel concentration. It should be noted that the solidification range spreads more steeply when cross-diffusion is taken into account.

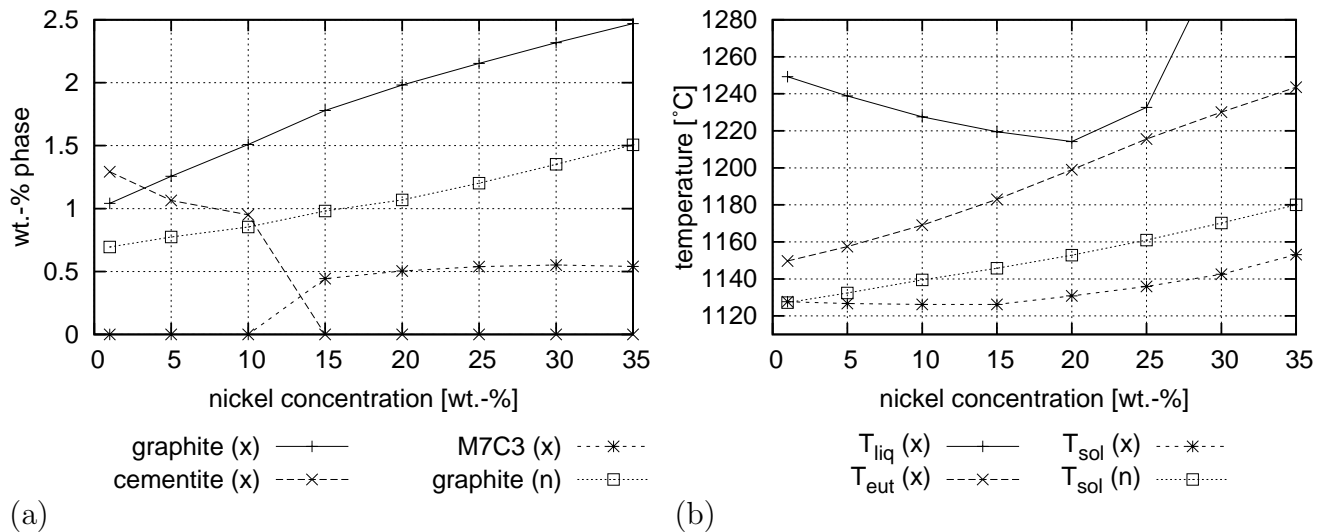


Fig. 9: (a) Impact of nickel on phase fractions and (b) transformation temperatures applying the models without (n) and with (x) cross-diffusion.

0.5.4 Comparison with Solidification Kinetics from DTA

A fraction solid curve, deduced as an average curve from three DTA cycles, is compared to microsegregation simulations in Fig. 10. The microsegregation simulations include cross-diffusion and dendrite arm coarsening, where all three databases are applied in combination with the first compositions listed in Tab. 2. With reference to the DTA processing conditions, a constant cooling rate of 10°C/min was applied for the simula-

tions. Compared to the experimental non-equilibrium eutectic temperatures, in the range from 1185 °C to 1195 °C deduced from DTA, or to the cooling curves in Fig. 12, which reveal approx. 1190 °C, all equilibrium eutectic temperatures are predicted to be too high by about 21 to 43 °C. It should be noted that the non-equilibrium eutectic temperature on solidification of the clamp-ring is about 15 °C lower than the averaged value shown. Thus, the solidification range is even smaller which changes the solidification kinetics accordingly. However, when TCFE4 (TCF06) and TCFE5 (TCF07) are applied, there is good correlation of solidification temperatures. Regarding IRON-01c (IRO09), the solidification range is predicted to be too large. The slope of the experimental fraction solid curve indicates a hypoeutectic composition since it further increases as graphite starts precipitating. The best approximation of this slope yields the microsegregation code in combination with TCFE4. However, at the end of solidification, the experimental slope is steeper than the predictions with TCFE4 or TCFE5 show. Moreover, the other concentrations listed in Tab. 2 were tested, as well as the cross-diffusion model without dendrite arm coarsening by assuming a constant DAS of approx. 50 μm . Summarizing these findings, the database TCFE4 in combination with the cross-diffusion and dendrite arm coarsening model most closely reflects the experimental solidification kinetics.

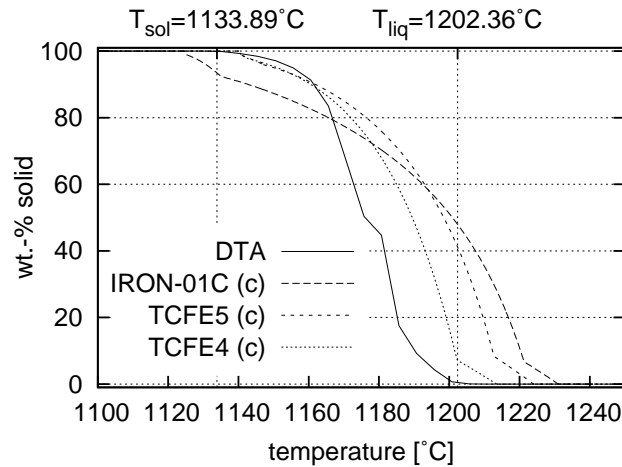


Fig. 10: Comparing the fraction solid deduced from DTA with various databases, including cross-diffusion and dendrite arm coarsening, which is denoted by (c).

0.5.5 Simulation Setup

Fully coupled material and process simulations were performed for a casting with and without a central feeder. Since the experiments and the simulated temperature field at the beginning of solidification indicate a symmetrical solidification behavior in the casting, the simulations were performed for one half of a clamp-ring at an initial temperature of 1405 °C in a green sand mold at initially 20 °C. The experiments also indicate that none of the exothermic feeders ignited, as can be seen from Fig. 12. Therefore, the

feeders were modeled as isolating feeders. In the microsegregation simulations initial and boundary conditions were applied, as explained in Section 0.5. A grid consisting of 959616 volume elements was generated with 47985 metal cells, and during simulation 306 reference elements were selected. Simulations ran for approx. 60 h on a current standard PC using an open source operating system. The same problem has also been solved using only 50 reference elements in approx. 10 h with similar results, using 28 reference elements in approx. 9 h with slight differences regarding the phase distribution, and using 10 reference elements in 5.5 h, which generated an inverse distribution of phases. This study reveals that in order to generate consistent results, a number of 50 reference elements is sufficient for the clamp-ring casting.

0.5.6 Distributions of Microstructural Quantities

During the solidification simulation, austenite, graphite, and the metal carbide M7C3 were precipitated from the liquid phase. The patchy impression of the results is due to the interpolation procedure, introduced in Section 0.3.10. This procedure is not based on geometric data, but on similarity criteria in relation to the cooling conditions. In this spirit, two reference elements meeting the similarity criteria for the particular interpolation element are generally selected. Obviously, these reference elements are not necessarily in the immediate neighborhood of the corresponding interpolation element. Slight differences in cooling characteristics lead to variation in phase fraction. For this reason, the fluctuations in the results are not significant. However, the trend of the results is significant.

Fig. 11 (a,b) indicates the formation of more graphite and metal carbides in areas of low cooling rate. It would appear to make sense that in regions of low cooling more austenite is formed, since solidification is closer to equilibrium than in regions exposed to fast cooling. In these regions, however, also the DAS increases accompanied by increasing diffusion distances and thus resulting in a departure from equilibrium. The dendrite arm coarsening at the hot spot below and inside the feeder is shown in Fig. 11 (c). Moreover, this effect is significantly supported by cross-diffusion since the carbon flux progresses in opposite direction of the carbon gradient, that is towards the liquid phase, as can be seen in Fig. 7. Thus, this excessive carbon promotes graphite and metal carbide formation. These effects are accompanied by a decreasing solidification temperature, departing from equilibrium, as shown in Fig. 11 (d). This material behavior increases the hot spot effect in the area below the feeder.

0.5.7 Comparison of Cooling Curves

In Fig. 12 the experimental cooling curves of casting c_c and c_d are compared to the virtual cooling curves resulting from a coupled simulation. The virtual cooling curves

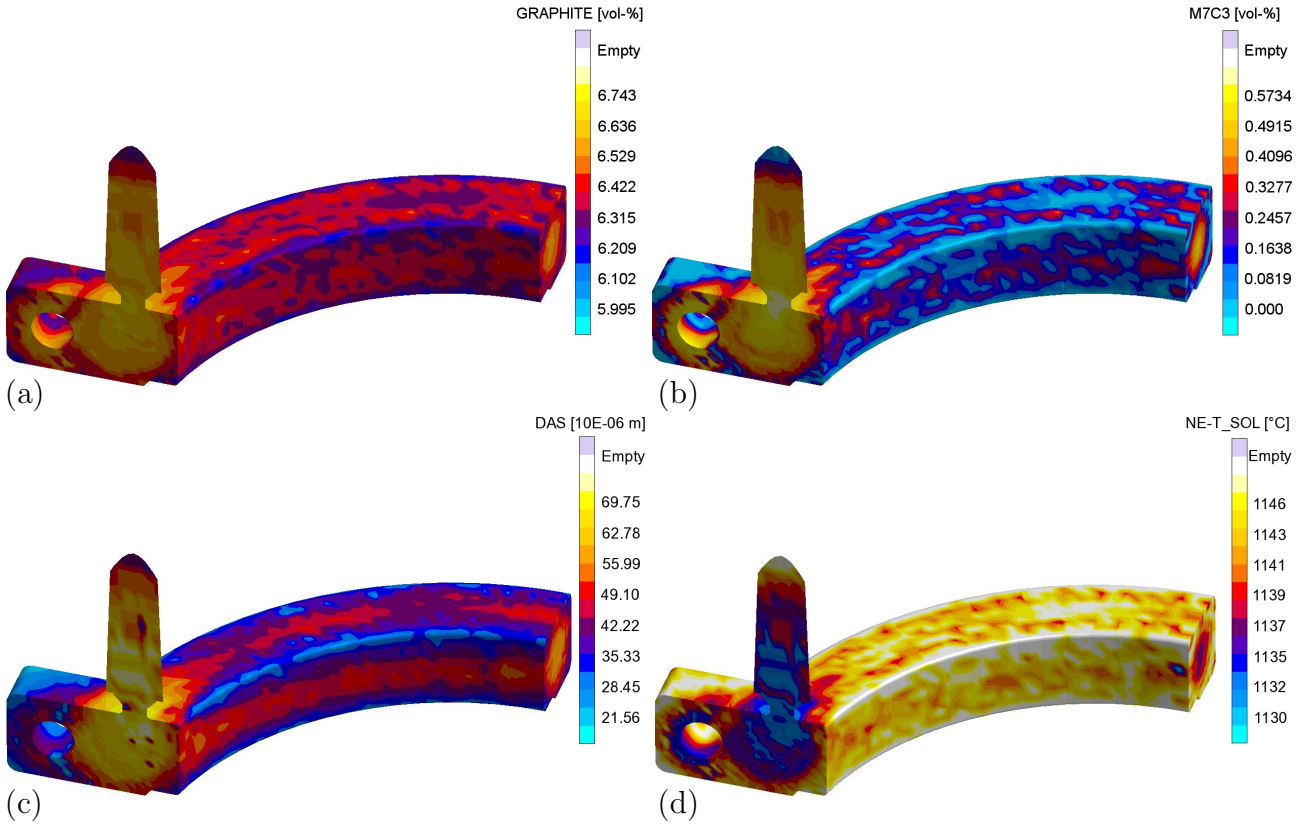


Fig. 11: Predicted distribution of (a) graphite, (b) M7C3 carbide, (c) dendrite arm spacing, and (d) solidification temperature.

VTC2 and VTC4 are predicted to be almost identical. This is similar to casting c_c , whereas in case of casting c_d there is more of resemblance between curves TC1 and TC4. This may be caused by slight displacement of thermocouples. In general, the predictions about cooling characteristics are very good, although, for the following reasons variations in absolute temperatures are apparent: Firstly, the nucleation of graphite may produce undercoolings up to 110°C until eutectic cementite forms according to a microsegregation simulation by suspension of graphite. However, under the experimental cooling conditions, no pronounced recalescence is visible. Secondly, there is uncertainty of composition when comparing the three analyses listed in Tab. 2. A concentration variation will tend to increase the liquidus temperature. Thirdly, there is insufficient experimental data for further database assessments and optimizations for relatively large carbon, silicon, and nickel compositions.

Since this temperature variation appears to be the only significant difference between the virtual and the experimental cooling curves, it is concluded that the innovative coupling procedure provides valid results.

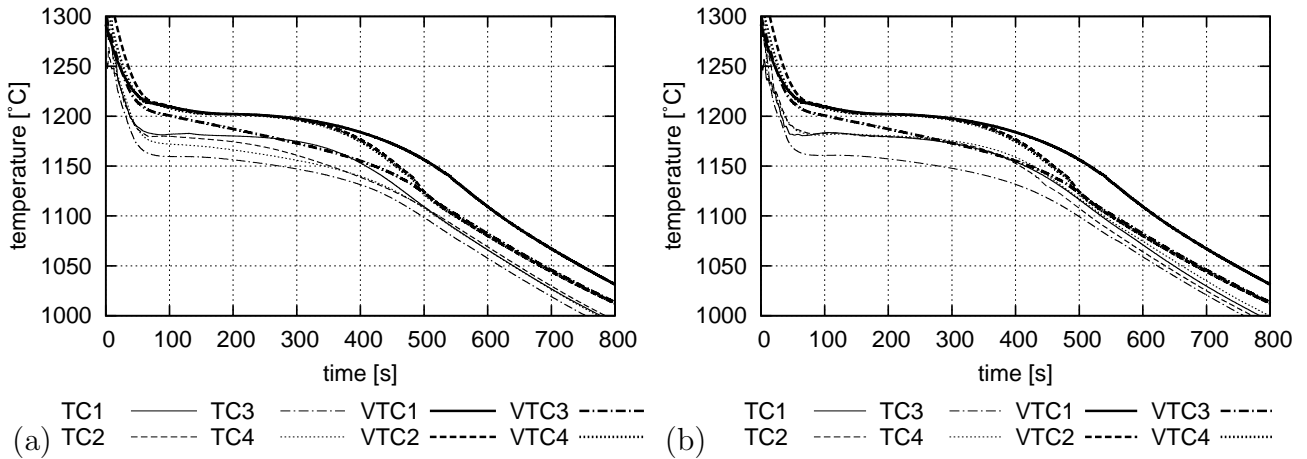


Fig. 12: Comparing experimental (TC) and virtual (VTC) cooling curves of (a) casting c_c and (b) casting c_d . The positions of the thermocouples are shown in Fig. 2 (a).

0.5.8 Validation of Porosity Predictions

Porosity prediction is based on local density and solid fraction data, which are forwarded from the material model to the process model during simulation. The porosity model itself is part of the commercial software and for this reason no further information can be provided. Fig. 13 (b) shows the porosity prediction. The efficiency of the feeder at the flange is predicted to be too low, meaning that the feeder provides less liquid material to the casting than necessary. This leads to a shrinkage pore below the feeder at the flange. The hot spot effect is assisted by a shift towards lower solidification temperatures over solidification time (cf. Fig. 11 (d)) which is an effect not predictable with uncoupled simulations. It can be said that the local development of microsegregations, dendrite arm coarsening, and cooling conditions are closely interacting and thus impacting porosity formation.

The porous area A correlates well with the experimental findings, especially in the case of casting c_c in Fig. 5 (a). The porous areas B and C are predicted to be in close proximity to the ingate that is very flat designed. This is due to the chill effect of the thin ingate. In castings c_c and c_d , that are shown in Fig. 5, this porosity is found somewhere along the center line of the ring and there is an accumulation in proximity to locations A, B, or C. In the case of clamp-ring c_d , the shrinkage cavity in the regions A, B, and C is continuous, whereas in the case of casting c_c , the porous areas B and C shift towards the flange. Thus, the location of porosity appears to be subject to statistical effects. This is explained by Jones et al. (JEG99) and called *non-classical pore nucleation theory* at entrained particles. To take account of this statistical effect, porosity detected in castings c_c , c_d , c_g , and c_h were superposed, as shown in Fig. 13 (a). From this superposition, agreement with the simulated results for porosity A, B, C, and D is confirmed. Apart from the low porosity E, the predictions correlate very well. A comparison with each individual casting shows that also the level of porosity is well predicted. The present

method, where local density and fraction solid data is provided for the porosity model, is verified by this application.

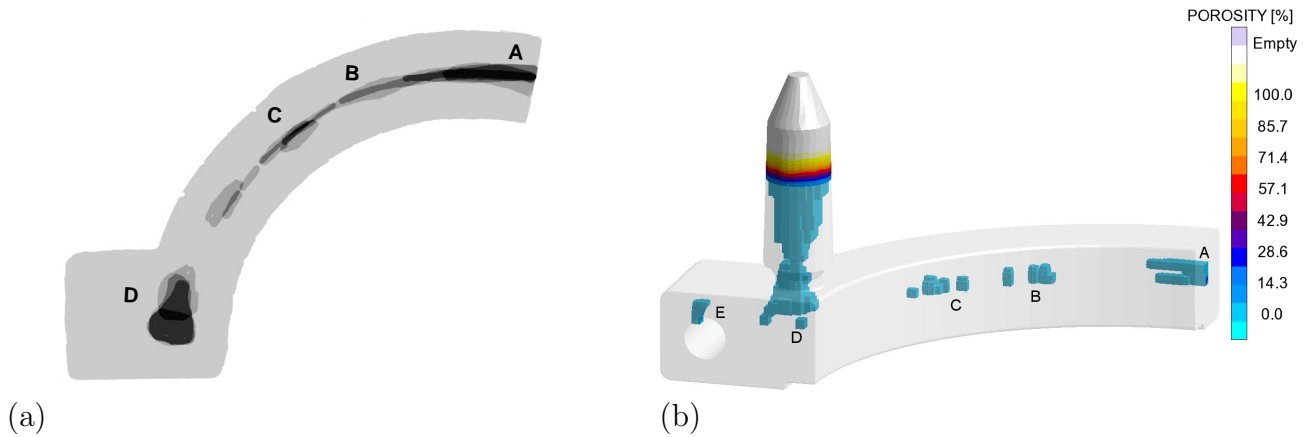


Fig. 13: (a) Experimental porosity superposition for the castings c_c , c_d , c_g , and c_h . (b) Porosity prediction applying a coupled simulation approach. The superposition (a) represents the frequency with which porosity is ascertained in experiments, *not* the level of porosity.

0.6 Summary and Conclusions

As distinct from empirical models, microsegregation models reflect time-dependent phase growth by simulation of diffusive transport and thermodynamic data, as pointed out in Section 0.2. Two- and three-dimensional models also take account of the microstructure evolution during solidification, but is, however, very time-consuming. Since the aim is direct coupling to a process simulation tool, microstructural variation in castings can be taken account of by modeling dendrite arm coarsening. This introduces an additional kinetic effect which corresponds to an expanding representative volume element during microsegregation simulations. To this end, a comprehensive microsegregation software has been generated. *The characteristics of the model presented were compared to decoupled and coupled state-of-the-art microsegregation models and four unique features were identified: (1) the coupling to porosity simulation, (2) the innovative macro coupling concept, (3) the multiphase concept, and (4) the mixed geometry concept.*

A series of GJSA-XNiCr20-2 clamp-rings was cast with variation of the inoculation state and the number of feeders. As an input quantity to the microsegregation model, the microstructure of the castings was characterized and a predominantly dendritic microstructure and chunky graphite were identified. With regard to this evidence, a mixed morphology in between dendritic and a cellular microstructure was assumed for the diffusion simulations and a purely dendritic microstructure for the dendrite arm coarsening simulation.

Determinations of transformation temperatures by evaluation of the cooling curves

recorded and DTA measurements proved to be consistent. DTA measurements enabled the deduction of a fraction solid curve, taken as a baseline for the predicted solidification kinetics. The database TCFE4, together with dendrite arm coarsening and the cross-diffusion model, most closely reflects the experimental solidification kinetics. According to the EPMA measurements in Section 0.4.4, M7C3 was analyzed. *TCFE4 in combination with the first analysis listed in Tab. 2 is the best selection for executing the material simulations with respect to prediction of transformation temperature, solidification kinetic, and M7C3 content.*

By consecutive executed variation of the heat extraction rate, it was possible to highlight that the chemical diffusion model does not mirror the experimental solidification kinetics over almost the entire range of technically relevant solidification times. *The chemical diffusion model therefore does not apply to this type of alloy.* Cross-diffusion leads to a strong up-hill flux of carbon which results in a pronounced microsegregation profile of carbon in austenite. *It was possible to demonstrate in this work that cross-diffusion is the chief cause of the graphite promoting effect of nickel, not merely the change of the carbon solubility over the nickel concentration, as stated by Spear (Spe93).*

Dendrite arm coarsening reduces the impact of heat extraction rate on phase fractions compared to the situation with cross-diffusion only. To analyze the effect of dendrite arm coarsening, three types of cooling characteristics were compared. *Dendrite arm coarsening causes the sensitivity of the model to cooling characteristics, while at the same time slightly reducing the sensitivity to variations in heat extraction rate.*

EDX analysis, which provide qualitative results, and EPM analysis, which provide quantitative microsegregation profiles, were executed. Through EPMA the following phases were identified: austenite, graphite, and a eutectic region consisting of M7C3 and a silicide. EDX and EPM line scans in eutectic cells provide concentration profiles for each element in austenite, whereby the gradient of nickel is negative. Silicon is homogeneously distributed and positive gradients were analyzed for the remaining alloying elements. *A comparison of an EPMA line scan with simulations shows good qualitative agreement for all alloying elements and good quantitative correlation for the important elements carbon and silicon.* The diffusion solver was validated by comparison to an analytical solution. *The diffusion solver without cross-diffusion was verified.*

Fully coupled simulations were performed by application of the innovative process coupling concept by varying the number of reference elements, as pointed out in Section 0.5.5. The results of coupled simulations depend on the number of reference elements. Computation time increases with the number of reference elements. Conversely, when a critical number is not reached, an inverse phase distribution is predicted. For the clamping casting, the number of reference elements identified as adequate for generating consistent results was 50. The distribution of microstructural quantities has been discussed

in Section 0.5.6 in relation to the cooling characteristics of the reference elements. The hot spot effect is aided by a shift towards lower solidification temperatures over solidification time. *The shift towards lower solidification temperatures is a consequence of the local cooling characteristics and cross-diffusion and can only be predicted by coupling directly material and process simulation.*

An analysis of cooling characteristics reveals that two types of reference elements are distinguishable: one predominantly impacted by latent heat and a second exposed to fast heat transport at the casting-mold interface. *The different cooling characteristics at reference elements result in very different phase fractions. This transition of cooling characteristics is accompanied by a transition from a globular-cellular to a chunky-dendritic microstructure, as observed in experiments (cf. Fig. 3).*

To validate the coupled approach, the cooling curves predicted were compared to experimental cooling curves from the clamp-ring casting in Section 0.5.7. The cooling characteristics predicted in the coupled simulation and the curves measured correlate very well, while the absolute temperatures show a discrepancy of approx. 20°C. Since this discrepancy is not caused by the coupling of the two models, the conclusion is that *the innovative coupling concept and its implementation generate valid results.* Porosity within the casting was analyzed by x-ray of consecutively cut samples. Porosity was detected along the center line of the ring and, especially, below the feeder at the flange. The inoculation state does not seem to impact the porosity formation for this kind of alloy. The porosity predictions from the process simulation tool based on the local development of phase fractions and density were compared to experimental findings, as discussed in Section 0.5.8. Porosity is predicted below the feeder at the flange and along the center line of the casting. *Concerning the statistical impact of non-classical pore nucleation, the porosity predictions and experiments correlate very well.*

The outcome of this work has been the creation of a complex and unique simulation tool. This model has undergone a detailed validation procedure, which is reviewed in Tab. 3 and confirms that the overall model has been verified. However, there is some doubt as

Tab. 3: Validation objectives and correlation level in categories given below the table.

Objective	Qualitative	Quantitative	Section
Solidification Algorithm	+++	+++	
Diffusion Solver	+++	+++	
Solidification Kinetics	++	++	0.5.4
Temperature Coupling	+++	+++	0.5.7
Porosity Coupling	++	++	0.5.8

+ fair ++ good +++ verified — no conclusive result

to the transformation temperatures. Variation analysis indicates that these reservations arise from limitations of the databases and graphite nucleation. It was possible to show,

that the chemical diffusion model cannot be applied to this kind of alloy because of high diffusive interactions. These cross-diffusion effects are also the chief reason for the graphite promoting effect of nickel in cast iron, as demonstrated in the present work. Because of the implementation of a dendrite arm coarsening model, the software is sensitive to cooling characteristics. This causes a shift towards lower solidification temperatures over solidification time, which supports the hot spot effect below the feeder and can only be predicted by a directly coupled simulation. The innovative coupling concept is valid and the porosity predictions correlate well with experimental findings both qualitatively and quantitatively. GJSA-XNiCr 20-2 is a challenging material. This work was able to throw some light on some of its mysteries. Because of the general formulation of the code, the model presented is not restricted to this particular alloy. This model was successfully applied to GJL-350 cast iron and other material groups, such as the aluminum wrought alloys AA2024 and AA3104.

1. Introduction and Motivation

Environmental and cost demands placed on technical products, such as castings, are constantly on the increase and this has been particularly apparent over the last two decades. These demands are achieved by lightweight designs and improvement in efficiency. This involves the development of new materials and processing concepts alongside gradual improvements to existing concepts. Austenitic cast iron, for instance, is a corrosion-resistant material suitable for higher temperatures. The reduction of defects in castings through alloy and process development achieves more homogeneously distributed properties and enables lightweight designs and applications demanding higher loads and temperatures. It is widely accepted that process simulations enable a deep understanding of complex phenomena and have contributed largely to the enormous technical progress of recent times. More and more companies are also discovering the benefits of material and thermodynamic simulations in material development.

The properties of cast iron and other alloys are a function of microstructure and defects on different length scales. The microstructure of industrial alloys consists in general of more than only one phase, each featuring different properties. A primary solidification structure and secondary substructures may be either (regular or irregular) cellular, dendritic, globular, or a mixture of these morphologies which determines solidification kinetics and the final properties of the product.

The solidification behavior of alloys is impacted by the quantitative contribution of various kinetic effects, such as constitutional, curvature, or kinetic undercooling. These effects are all associated with species diffusion, either in a bulk mixture phase, ahead of a curved solid-liquid interface, or across a curved interface. The conclusion is simple: solidification would be impossible without diffusion, even in pure alloys, since the rearrangement of atoms into an ordered crystal structure could not proceed. It is therefore desirable to find a general approach describing these kinetic effects, or at least the dominating ones, quantitatively. Some alloys tend to be very sensitive to diffusive effects, especially when fast and slow diffusing species are present, as in the case of austenitic cast iron which is the focus of the present work. According to Stefanescu (Ste02), "Cast iron is one of the most complex, if not the most complex, alloys used in industry, mostly because it can solidify with formation of either a stable (austenite-graphite) or a metastable

(austenite-cementite) eutectic. Furthermore, depending on composition and cooling rate, several graphite shapes can be obtained at the end of solidification”.

This work is aimed at modeling the solidification kinetics of austenitic cast iron on a thermodynamic physical basis, while keeping the approach simple enough to obtain time-efficient predictions enabling a direct coupling to process simulation. When a casting solidifies, heat is usually extracted through its surfaces. This leads to differences in local cooling conditions, microstructures, defects, and hence properties. On the other hand, microstructure evolution and the associated latent heat released by crystallization is a time-dependent process. This is especially characteristic for cast iron. It is therefore meaningful to couple heat transport simulation on the process scale and material simulation on the microscale to take account of local interaction effects between both scales.

An undesirable, but common casting defect is shrinkage porosity caused by volume reduction on crystallization. However, some phases, such as graphite in cast iron, increase in volume on precipitation and therefore help prevent shrinkage porosity. The accuracy of shrinkage prediction in the solid-liquid phase mixture is therefore a direct function of the accuracy of phase fraction and phase volume prediction.

Microsegregation models predict phase fractions and concentration profiles (microsegregations) in a representative part of the microstructure. Microsegregations build up in solid phases through redistribution of alloying elements ahead of the moving solid-liquid interface and are reduced by diffusion of species. Furthermore, averaged thermodynamic properties for the resulting phase mixture, such as heat capacity, density, and latent heat, can be obtained. These are necessary in order to determine the heat transport on the process scale when a coupling of both scales is desired. Other, more sophisticated approaches for simulating microstructures, such as the phase field method or the cellular automaton technique, are too time-consuming for a direct coupling. The author is aware of only one commercial microsegregation model that neither provides a programming interface for a direct coupling nor seems to be stable and fast enough for such an undertaking. For these reasons, the author was motivated to develop a model based on the work of predecessors, such as Greven (Gre00) and Fackeldey (FLS96).

Another motivation originates from cooperation in joint research projects, such as the SFB370 *Integral Materials Modeling*. Integral casting simulation was the first process step in a simulation chain involving heat treatment, hot rolling, cold rolling, and finally cup drawing with the aluminum alloy AA3104. This topic is discussed by Neumann et al. (NKH⁺07). Pustal et al. (PWB⁺07) further report about this project where casting simulation is focused. After SFB370, the transfer domain TFB63 *Modeling Tools Relevant for Practice* was established. The objective of sub-project five of TFB63, porosity prediction during solidification of austenitic cast iron, is the objective of the present work. Publications by Pustal et al. (PBS⁺07; PBS⁺09; PSS⁺09; PSH⁺10) touching this topic also originate from this cooperation. Moreover, a detailed description of a coupled precursor

version of the present model and its application to the wrought alloy AA2024 is given by Pustal et al. (PBL⁺03).

This book is organized as follows: Abstracts are included at the end of the book to outline the present work. Furthermore, an executive summary is included at the beginning. After to Chapter 1, Introduction and Motivation, some facts regarding microsegregations, thermodynamics, transport equations, their discretization, and, at last, cast iron are given in Chapter 2, Fundamentals. In Chapter 3, State-of-the-Art, microsegregation modeling and coupling in recent times and early ages are reviewed. Picking up graphite structures of cast iron, as already discussed in Chapter 2, the spares articles published over the last years regarding chunky graphite are reviewed. In Chapter 4, Model Description, first the features of the model presented are compared to those of the most comprehensive state-of-the-art models. Then, deep insight is given into the concept and realization of the model. The nomenclature is explained in the context and, moreover, in Appendix A. To improve the readability of this book, discretization of formulas, derivatives, and structure charts are located in Appendices B - D. For software validation extensive experimental work was executed by casting and analyzing GJSA-X NiCr 20-2 clamp-rings, as described in Chapter 5, Experiments and Evaluation. In Chapter 6, Model Sensitivity and Model Validation, answer is given to the question as to how sensitive the particular submodels are to variations in heat extraction rate, cooling characteristics, and chemical composition? Moreover, first the stand-alone version of the code is validated and then the coupled version with reference to the clamp-ring casting. Chapter 7, Summary and Conclusions, summarizes the chief results and conclusions of the present work and provides questions for further investigations.

2. Fundamentals

2.1 Objectives

In this chapter the reader is introduced to fundamental aspects of this work and where appropriate reference is given to further reading. The formation of microsegregations involving thermodynamics, diffusion, and dendrite arm coarsening is explained in Section 2.2 and thus provides a link to the following sections. Section 2.3.1 deals with fundamental laws of thermodynamics establishing the basis in understanding equilibrium conditions introduced in Section 2.3.2. These conditions are frequently used in the model presented to perform equilibrium calculations. The Gibbs-Thomson relation is introduced in Section 2.3.3 linking undercooling to curvature. This relation is applied to describe dendrite arm ripening. Transport equations and constitutive laws, provided in Section 2.4, are utilized in Section 4.3.2 to deduce a specific form of this equation. Subsequently, this equation is discretized by application of the finite volume method, as explained in Section 2.5. Since especially the graphite formation of cast iron is complex and chunky graphite, a defective graphite structure, was observed in the microstructure of the clamp-rings analyzed, graphite formation is focused in Section 2.6.

2.2 Microsegregations

Fig. 2.1 illustrates the formation of microsegregations in a solid phase S as the solid concentration x^S changes with temperature T during solidification. Positive microsegregations are formed when the solubility of an alloying element in the solid phase is smaller than the initial concentration in the liquid phase. Because of this redistribution process, the composition of the liquid phase L rises, leading to an increase in solubility in the solid phase as temperature decreases. This enrichment of the liquid phase causes other phases to nucleate, when a critical temperature and concentration is reached. These phases may be, for instance, deleterious metal carbides at grain boundaries reducing mechanical properties and machinability of iron castings. It is possible to correlate liquid concentration x^L , solid concentration x^S , and temperature T by thermodynamic descriptions, such as the linearized phase diagram shown in Fig. 2.1.

On the other hand, chemical diffusion reduces in general microsegregations by smoothing gradients of the chemical potential. The impact of diffusion on the characteristic microsegregation profile also defines the phase fraction precipitated at a particular temperature. This means that for a non-equilibrium system, hold at a constant temperature, the solid fraction increases as microsegregations degenerate until an equilibrium state is reached. This state is characterized by a homogeneous concentration x^S in both solid and liquid phase. Since diffusion is a time-dependent phenomenon, microsegregations constitute a kinetic effect on solidification. The coarsening microstructure introduces an additional kinetic effect. Dendrite arm coarsening causes large dendrite arms to grow at the cost of small dendrite arms through diffusive transport of solute in the liquid matrix phase. This process is driven by the energy consumed to hold up a curved interface. The energy difference between a curved and a planar interface is given by the Gibbs-Thomson relation.

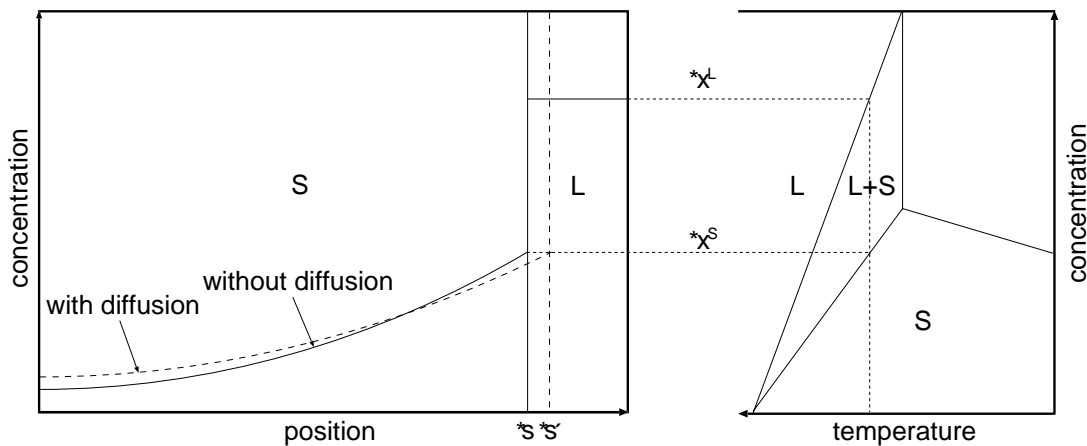


Fig. 2.1: Formation of microsegregations due to an increase in solid concentration x^S at the interface, and degeneration of microsegregations due to diffusion in solid. Diffusion causes the solid fraction to increase, and hence, the position of the interface changes from x^s to $x^{s'}$.

2.3 Thermodynamics

2.3.1 Fundamental Laws and Equations

Thermodynamics is based on three fundamental laws that may be formulated with reference to Lukas et al. (LFS07) as follows:

1. “The sum of the heat and work transferred to an otherwise closed system defines a function not depending on the way in which this transfer took place.”
2. “A function of state, called entropy and denoted S , can be defined, which can increase, but never decrease, in a closed system.”

3. “The change in entropy of a reversible reaction approaches 0 when the reaction temperature approaches 0K.”

A thermodynamic energy potential is a function consisting of intensive and extensive variables. This potential represents the thermodynamic state of a system. An intensive variable is a driving potential causing a change of an extensive variable or quantity. This means that variables defining a thermodynamic state cannot change independently from each other. Conjugated variables are combinations of a driving potential and the corresponding extensive quantity, such as PV , TS , and μN , where P denotes pressure, V volume, T temperature, S entropy, μ chemical potential, and N the number of moles in a system. The four fundamental thermodynamic equations may be deduced applying Legendre transformations to the energy potential equations listed in table 2.1.

Tab. 2.1: Table of energy potentials as functions of intensive and extensive variables showing also the natural variables of the corresponding energy potential according to Alberty (Alb01).

Name	Quantity	Natural Variables
1. Internal energy	$U = TS - PV + \sum_{i=1}^n \mu_i N_i$	S, V, N_i
2. Helmholtz free energy	$F = U - TS$	T, V, N_i
3. Enthalpy	$H = U + PV$	S, P, N_i
4. Gibbs free energy	$G = U + PV - TS$	T, P, N_i

Here, n is the number of alloying elements in a system. A more simple way to achieve the fundamental equations is provided by the Guggenheim scheme in Fig. 2.2 showing how to obtain energy potentials from the corresponding intensive and extensive variables. The natural variables, which need to be differentiated, are put next to the energy potential under consideration. Terms crossing from left to right get a positive sign and otherwise a negative sign, as indicated in Fig. 2.2.

$$\begin{array}{ccccc}
 & S & U & V & \\
 + & \mathbf{H} & & \mathbf{F} & - \\
 & P & \mathbf{G} & T &
 \end{array}$$

Fig. 2.2: Guggenheim scheme showing how to compose fundamental thermodynamic equations combining energy potentials (bold) with the corresponding intensive (normal) and extensive (italic) variables.

When applying this scheme, for example, to the Gibbs free energy potential, the corresponding fundamental thermodynamic equation is given by:

$$dG = V dP - S dT + \sum_{i=1}^n \mu_i dN_i . \quad (2.1)$$

From Tab. 2.1 follows by casting Eq. 1 into Eq. 4, that the chemical potential is another word for the partial molar Gibbs energy $G = \sum \mu_i N_i$ with the total derivative:

$$dG = \sum_{i=1}^n d\mu_i N_i + \sum_{i=1}^n \mu_i dN_i . \quad (2.2)$$

Equating this with Eq. (2.1) provides the important Gibbs-Duhem relation among the intensive variables μ_i , P , and T :

$$\sum_{i=1}^n d\mu_i N_i = V dP - S dT . \quad (2.3)$$

Due to the relation: $\sum N_i = N^0$, where N^0 is the total number of moles in a system, the degree of freedom \hat{f} in the Gibbs-Duhem relation (2.3) equals $n + 1$.

2.3.2 Equilibrium Conditions

The thermodynamic degree of freedom is given by Gibbs' phase rule where the number of phases m precipitated simultaneously equals the number of independent state variables:

$$\hat{f} = n - m + 2 - \hat{c} . \quad (2.4)$$

Here, \hat{c} is the number of constraints, for example, a pressure P or a temperature T . By keeping pressure and temperature constant and setting $N^0 = 1$ mol, the fundamental thermodynamic equation (2.1) for a change in Gibbs free energy with respect to concentrations reduces for one solid phase S and liquid phase L to:

$$d(\Delta G) = dG^S + dG^L = \sum_{i=1}^n \mu_i^S(T, x_i^S) \cdot dx_i^S + \mu_i^L(T, x_i^L) \cdot dx_i^L = 0 . \quad (2.5)$$

From this equation a thermodynamic equilibrium may be deduced which is characterized by a minimum in Gibbs free energy difference. For an ideal mixture phase the constraints $dx_i^S = -dx_i^L$ and $\sum dx_i^S = df^S$ may be applied leading to *Gibbs' equilibrium conditions*:

$$\frac{d(\Delta G)}{df^S} = \sum_{i=1}^n \mu_i^L(T, x_i^L) - \mu_i^S(T, x_i^S) = 0. \quad (2.6)$$

The constraints mentioned imply that this equation also holds for each individual species which means: $\mu_i^S(T, x_i^S) = \mu_i^L(T, x_i^L)$. In general, the chemical potential and also the Gibbs free energy are composed from the following terms:

$$\begin{aligned} \mu_i(T, x_i) &= \mu_i^0 + RT \ln x_i + \mu^{\text{exc}} \\ G(T, x_i) &= G^0 + G^{\text{phy}} - TS^{\text{cnf}} + G^{\text{exc}}. \end{aligned} \quad (2.7)$$

Here, μ_i^0 and $G^0 = \sum x_i \mu_i^0$ are values at reference state, G^{phy} is the Gibbs energy contribution due to physical models, $S^{\text{cnf}} = -R \sum x_i \ln x_i$ the configurational entropy of a phase, and G^{exc} the excess Gibbs free energy which is the difference between the real Gibbs free energy and the preceding terms in Eq. (2.7). The formulation used for Gibbs' equilibrium conditions is very useful as long as chemical potentials are given as functions of concentration. In today's thermodynamic codes however, equilibrium conditions are formulated with respect to site fractions y_i considering also the composition of sublattices and involving therefore internal degrees of freedom. These kind of thermodynamic equilibrium conditions are referred to as *Hillert's equilibrium conditions* consisting of five equations, as explained by Lukas et al. (LFS07).

2.3.3 Gibbs-Thomson Relation

When comparing a particle with a planar solid-liquid interface to a particle with a curved solid-liquid interface, it is found that the particle with the curved interface is at a higher level of Gibbs energy than the one with the planar interface. This is because of the energy consumed to build the curved interface. This implies that the total difference in volumetric Gibbs free energy ΔG^V between a liquid phase and a curved solid phase consists of a volume specific term $\Delta G^{\text{L,S}}$ due to phase change and a surface energy term γ associated with the surface area A :

$$\Delta G^V = V \Delta G^{\text{L,S}} + A \gamma. \quad (2.8)$$

Equilibrium requires minimization of difference in Gibbs free energy by setting the derivative of (2.8) with respect to the radius r equal zero. The volume specific change in Gibbs free energy due to curvature energy γC may be formulated as deviation of the Gibbs free energy from the value at equilibrium temperature T_e :

$$\Delta G^{\text{L,S}}(T) - \Delta G^{\text{L,S}}(T_e) + \gamma C = 0. \quad (2.9)$$

Combining Eq. 3. and Eq. 4. in Tab. 2.1 and successively applying a Legendre transformation yields the difference in Gibbs free energy contributed by a term taking account of enthalpy change and a second of entropy change:

$$\Delta G^{\text{L,S}} = \Delta H^{\text{L,S}} + T \Delta S^{\text{L,S}}. \quad (2.10)$$

Casting this into Eq. (2.9) and assuming that $\Delta G^{\text{L,S}}$ only changes with temperature, results in an undercooling ΔT_C of the curved interface with reference to the planar interface at equilibrium:

$$\Delta T_C = T_e - T = -\frac{\gamma C}{\Delta S^{\text{L,S}}} = -\frac{\gamma C T_e}{\Delta H^{\text{L,S}}}. \quad (2.11)$$

This equation is known as the Gibbs-Thomson relation, where $\Delta S^{\text{L,S}}$ and $\Delta H^{\text{L,S}}$ are volume specific quantities.

2.4 Transport Equations and Constitutive Laws

For closed systems, transport equations are a mathematical formalism of Lavoisier's principle of conservation: *nothing is lost, nothing is created, everything is transformed*. The transported (conserved) quantities can be either mass, energy (heat), species, or momentum. For the models described in the present work, only heat and species transport equations are relevant. For details about other transport equations, the reader is referred to Rappaz et al. (RBD03). In a Eulerian frame of reference, conservation equations, in general, consist of a transient, an advective, a diffusive, and a source terms for exchange with the ambient when open system are considered. Omitting mechanical contributions, such as compression and strain, the heat conservation equation may be written as:

$$\frac{\partial(\rho H)}{\partial t} + \text{div}(\rho H \mathbf{u}) + \text{div}(\mathbf{j}_H) = \dot{h}. \quad (2.12)$$

The first two terms on the left represent the change in enthalpy with time and due to advection, respectively. The other terms, however, need to be quantified by suitable constitutive laws. The diffusive heat flux \mathbf{j}_H is constituted by Fourier's law and the source term \dot{h} may be an external heat source, such as a heater. The change in enthalpy due to phase transition is taken account of by splitting up the transient term into two separated terms: one representing the change in average heat content $C_p \partial T$ and the second in latent heat of fusion L_f , which is related to phase change ∂f^{S} . Furthermore, the non-conservative

form of Eq. (2.12) approximates density and heat capacity to be constant during time change:

$$\rho C_p \frac{\partial T}{\partial t} + \rho L_f \frac{\partial f^S}{\partial t} + \text{div}(\rho H \mathbf{u}) + \text{div}(\mathbf{j}_H) = \dot{h} . \quad (2.13)$$

The transport of species i in a phase j is an analogous case to transport of heat:

$$\frac{\partial(\rho w_i^j)}{\partial t} + \text{div}(\rho w_i^j \mathbf{u}) + \text{div}(\mathbf{j}_i^j) = \dot{X}_i^j . \quad (2.14)$$

Both conservation equations, transport of heat and species are volume-specific since the weight-specific transport quantity is multiplied by the density ρ . Besides the volume-specific formulation of Eq. (2.14) associated with a weight-specific concentration w , also the molar formulation associated with the molar fraction x , ensures continuity of species as long as the volume is kept constant. In order to avoid the use of additional variables, the species flux \mathbf{j} and the source term \dot{X} in Eq. (2.14) or Eq. (2.15) are considered to have the same specific unit as the transported quantity w or x , respectively. This yields:

$$\frac{\partial x_i^j}{\partial t} + \text{div}(x_i^j \mathbf{u}) + \text{div}(\mathbf{j}_i^j) = \dot{X}_i^j . \quad (2.15)$$

The diffusive transport of species may be modeled by Fick's law constituting that the concentration gradient $\mathbf{grad}(x_i^j)$ is driving the species flux \mathbf{j}_i^j of the species i in phase j :

$$\mathbf{j}_i^j = -D_i^j \mathbf{grad}(x_i^j) . \quad (2.16)$$

Here, D is the chemical diffusion coefficient. Darken (Dar49) demonstrated in experiments with two connected steel bars, very different in silicon composition, but about equal in carbon composition, that most of the carbon diffused *uphill* into the bar with the lower silicon content when holding the bars at approx. 1050 °C for 13 days. The reason for this behavior is that silicon increases the chemical potential μ of carbon in austenite and the species flux is rather associated with the gradient in chemical potential than in concentration. From this insight, the thermodynamic version of Fick's law was deduced involving the mobility matrix \mathbf{M} and the gradient in chemical potential $\mathbf{grad}(\mu_b^j)$ of the species b inducing a flux of species i :

$$\mathbf{j}_i^j = -\sum_{b=1}^n \mathbf{M}_{ib}^j x_i^j \mathbf{grad}(\mu_b^j) . \quad (2.17)$$

The same behavior may be modeled by using a chemical diffusion matrix \mathbf{D} where the effective species flux is a function of the gradients of all n alloying elements:

$$\mathbf{j}_i^j = - \sum_{b=1}^n \mathbf{D}_{ib}^j \mathbf{grad}(x_b^j). \quad (2.18)$$

The diffusion matrix may be deduced from the mobility matrix including the impact of thermodynamics, as demonstrated by Campbell et al. (CBK02). The interdependence of diffusing alloying elements is often referred to as *cross-diffusion*.

2.5 Finite Volume Method

Because no general analytical solution is given for transient diffusion problems, a numerical method is applied to solve Eq. (2.15). This demands a discretization of the given problem in time and space. In the present work, the finite volume method (FVM) is applied which is a variant of the finite differences method, but with the property of self-conservation. To find a numerical solution for species transport, Eq. (2.15) is discretized in time and space in combination with the actual calculation domain. Therefore, the calculation domain, which is a representative volume element of the microstructure, is subdivided into finite volume elements. Each of these volume elements has boundaries located in the center between two neighboring volume elements. For this purpose, the specific form of the transport equation is integrated over the volume of each finite volume element and over the time of a finite time step. When there is only one neighboring volume element present, that is at the boundaries of the calculation domain, appropriate boundary conditions must be applied. More details about discretization methods can be found by Patankar (Pat80). This discretization results in a system of algebraic equations that is solved by application of a suitable solver, for example, the well-known Gauss algorithm.

2.6 Cast Iron and Graphite Shape

Ruxanda et al. (RBMS01) detected in a pore, shown in Fig. 2.3, that the solidification morphology of spheroidal graphite iron (SGI) can be dendritic during primary solidification of austenite, while on eutectic solidification, also grains with a globular structure are precipitated.

This effect is explained by Liu et al. (LLS85). According to Fig. 2.4 austenite and graphite nucleate separately in the liquid. While graphite grows spherically, primary austenite usually forms dendrites. The primary dendrites may degenerate by formation of an austenitic shell around the slower growing graphite which is called a eutectic cell. Graphite spheres nucleating separately are transported to dendrite arms by flotation or convection and then incorporated into these arms or eutectic cells.

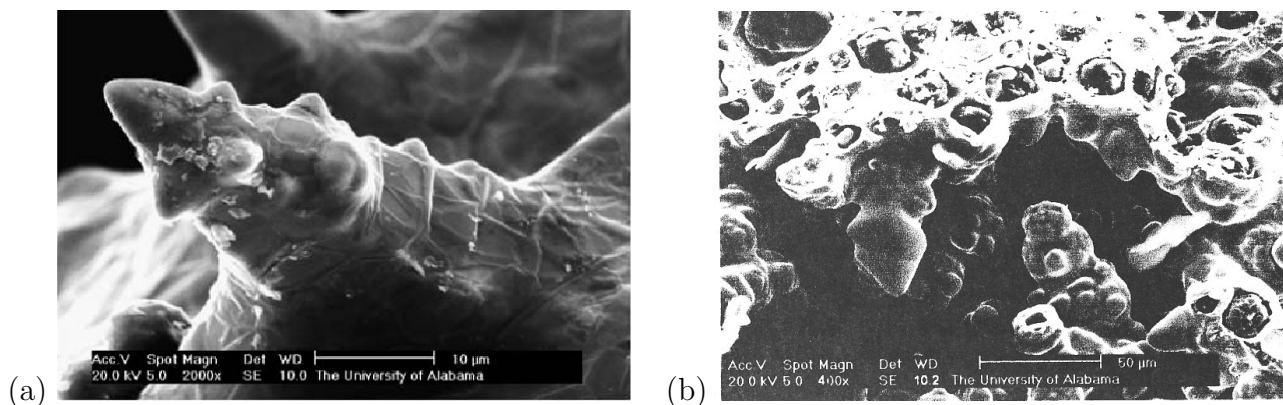


Fig. 2.3: (a) Primary dendrite and (b) eutectic grain found in the same micro-shrinkage cavity in an SGI plate, according to Ruxanda et al. (RBMS01).

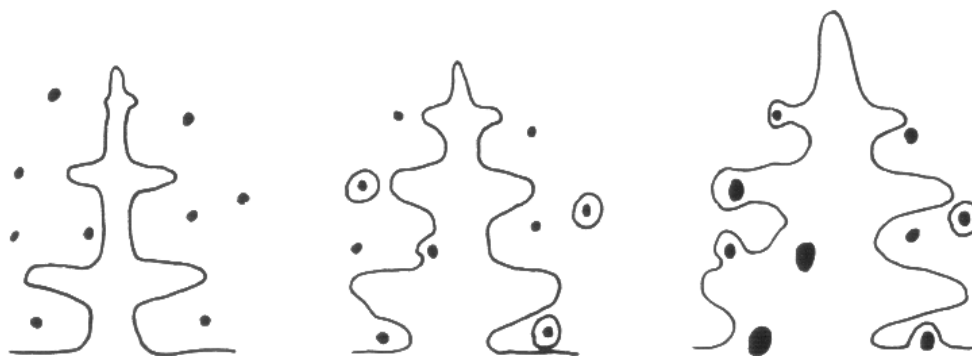


Fig. 2.4: Sketch about decoupled nucleation and growth of graphite and austenite in three steps, according to Liu et al. (LLS85).

On eutectic solidification carbon diffuses through the austenitic shell around graphite nodules constraining its growth. After to solidification various solid state transformations may take place, such as the formation of ferrite, pearlite, bainite, or even martensite.

In order to understand the mentioned phenomena that lead to various shapes and defect structures of graphite, such as chunky graphite, first, graphite structures and then growth theories of graphite are reviewed with reference to Stefanescu (Ste93). Fig. 2.5 indicates the hexagonal crystallographic structure of graphite that is characterized by Miller-Bravais indices $(hkil)$ for planes. Herforth (Her65) states that three shapes of graphite may form depending on the relation of growth velocities between the basal plane (0001) and the prism plane $(10\bar{1}0)$. The particular growth velocity of the faces on crystals is impacted by the presence of nodularizers, such as magnesium, cerium, and lanthanum or by surface active elements, such as sulfur and oxygen. Furthermore, spheroidal graphite is a polycrystal, whereas in a pure environment single crystals form in a specific shape called *coral graphite*.

This is supported by Double and Hellawell (DH74) who explained that the spherical

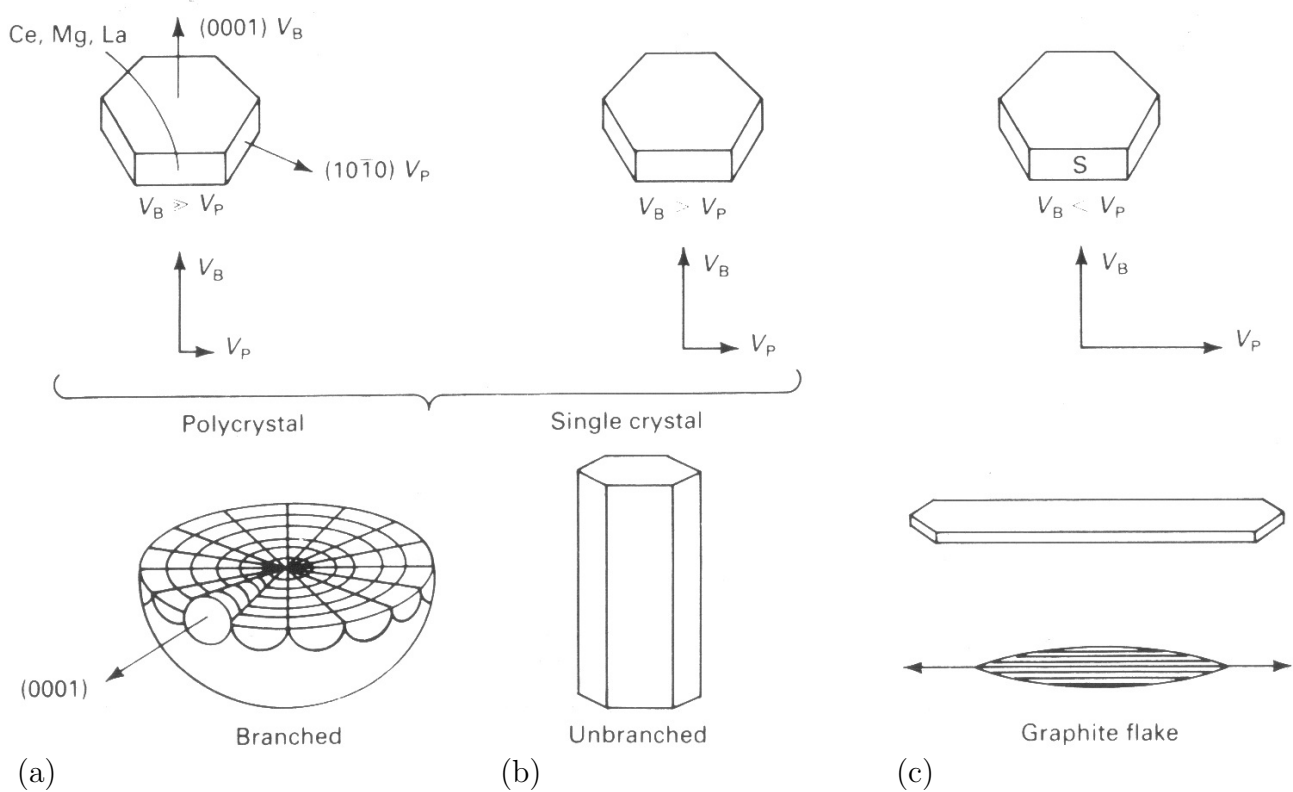


Fig. 2.5: Scheme representing the change in the growth velocity of graphite due to adsorption of foreign atoms: (a) nodularizer (Mg, Ce, La) added as reactive impurity; (b) pure environment; (c) environment contaminated with surface-active elements, such as sulfur and oxygen adsorbed on the prism faces Herfurth (Her65).

polycrystal consists of conical helices, as shown in Fig. 2.6. These helices grow in $[10\bar{1}0]$ direction and form tilt / twist boundaries in between the segments.

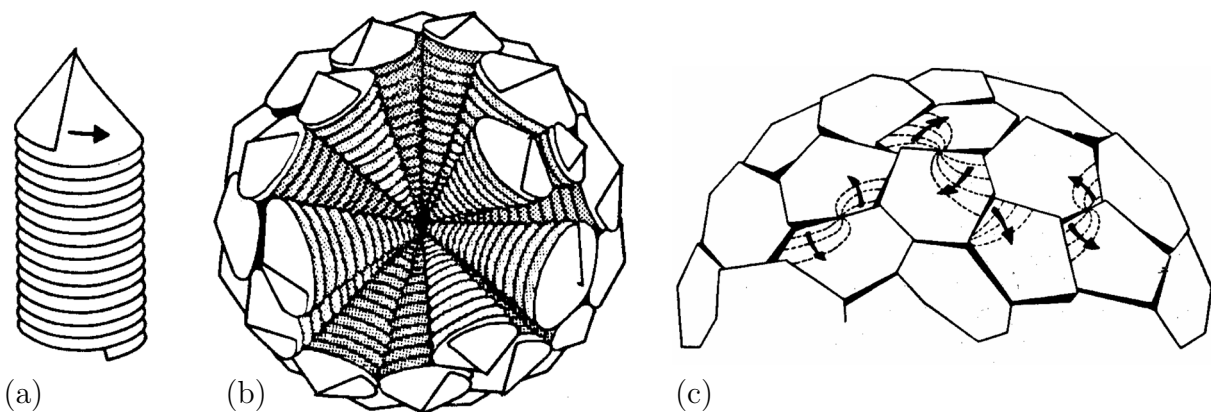


Fig. 2.6: Growth of graphite spheroids from conical helix crystals: (a) conical helix structure of graphite basal sheet; (b) nucleus of a spheroid composed of numerous close-packed, conical helices growing from one common center; (c) tilt / twist boundaries between individual crystal segments on the surface of a graphite spheroid, according to Double and Hellawell (DH74).

At the same time, Sadocha and Gruzleski (SG74) proposed a more simple model where the crystal grows in a-direction in a circumferential manner, and the c-face (0001) is exposed to the liquid phase, as shown in Fig. 2.7. The growing steps run into one another causing a cabbage-leaf effect on the surface of the crystal.

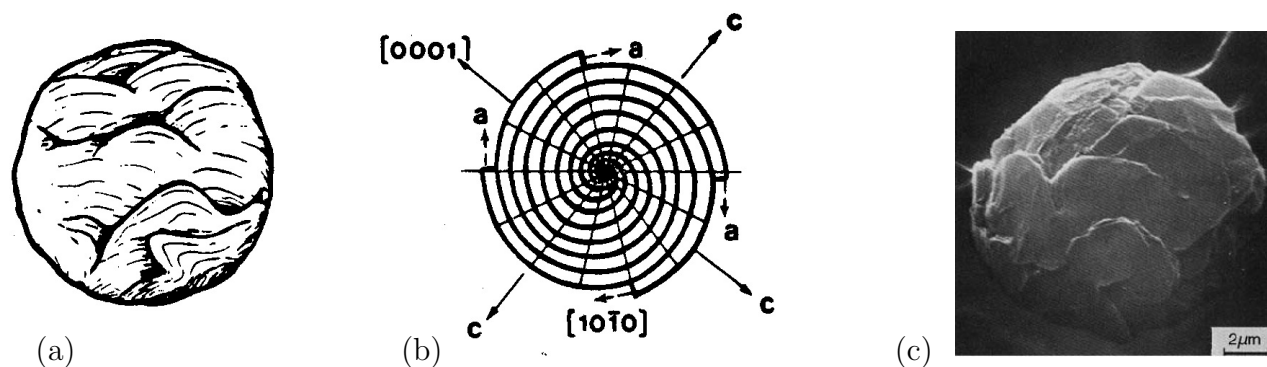


Fig. 2.7: Circumferential growth of graphite spheroids: (a) surface showing leaf effect; (b) diametrical section showing growth in the a-direction according to Sadocha and Gruzleski (SG74). (c) Experimental evidence of graphite growth along the a-axes provided by Lux et al. (LMMT74).

Over the years, very different theories were developed trying to find the reason for spherical growth of graphite when nodularizer is added to the melt. Among these theories are the *solid state growth theory*, the *growth of graphite through the austenitic shell theory*, the *growth on particular nuclei theory*, the *growth in gas bubbles theory*, and the *surface energy theory*. These theories are described by Stefanescu (Ste93) and substantial disagreement with other observations was found. Besides the *surface energy theory* also the *surface adsorption theory* and the *defect growth of graphite theory* are based on a variation in growth velocities of the basal (0001) and the prism ($10\bar{1}0$) face when surface active elements are removed or nodularizer is added to the melt. The *surface adsorption theory* was developed by Herfurth (Her65). Fig. 2.5 shows that in a pure environment the (0001) plane with the larger atom density has the largest growth rate leading to the formation of single crystal coral graphite. When sulfur and oxygen are present, these elements are adsorbed on the (0001) plane which achieves fewer satisfied bonds. This changes the relation of atom densities and surface energies between the (0001) and the ($10\bar{1}0$) plane. When the growth velocity of the basal plane is lower than that of the prism plane, lamellar graphite is formed. Nodularizing elements scavenge the melt of surface-active elements and block additionally the growth in [$10\bar{1}0$] direction leading to a polycrystalline spheroidal graphite shape. The *defect growth of graphite theory* by Minkoff and Lux (ML74) is based on three possible growth mechanisms of graphite: (a) by two dimensional nucleation or (b) at the step of a twisted boundary or at the ($10\bar{1}0$) plane, both with an exponential growth law, or (c) by screw dislocations at the (0001) plane with a parabolic growth law. Contaminating elements, such as sulfur and oxygen, change

the curvature energy of steps and promote, therefore, lamellar growth. The change in curvature is associated with a relative change in undercooling for each growth mechanism. Magnesium and other nodularizing elements react with the surface and prevent the growth at steps of twist boundaries. In a later theory of Minkoff (Min83), the graphite shapes are directly correlated with different undercoolings. Furthermore, Minkoff declares that pyramidal instabilities on $(10\bar{1}1)$ planes may form at undercoolings greater 29°C . These pyramidal crystals lead to imperfect shapes of graphite, such as chunky graphite. According to Liu et al. (LLWL83) chunky graphite forms due to extensive branching of spheroids as depicted in Fig. 2.8. Chunky graphite is interconnected and may be fractured by melt flow. It forms at low cooling rates and may be reduced by lowering the carbon equivalent.

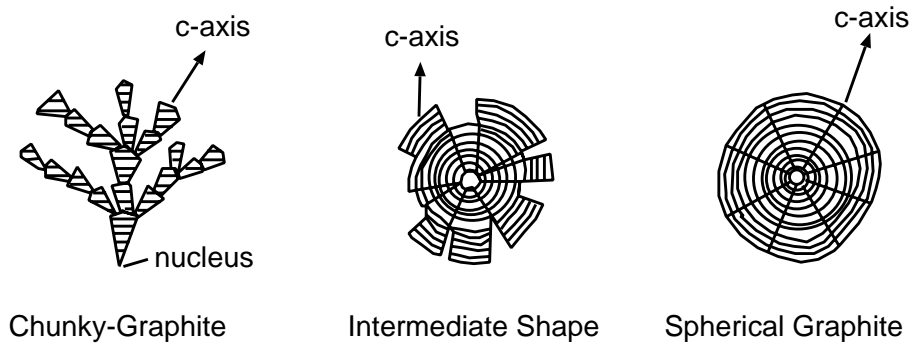


Fig. 2.8: Sketch on the the formation of chunky graphite and link to spheroidal graphite, according Liu et al. (LLWL83).

Later on Double and Hellawell (DH95) found in experiments with graphene sheets doped with oxygen and sulfur that graphene growth is blocked in direction of the basal plane, as shown in Fig. 2.9. Without impurities, which may be scavenged by magnesium or cerium, bending and wrapping of graphene layers is facilitated by the monolayer structure of the graphite sheets. The significant mismatch between the graphite layers must be accommodated by radial faults. This mechanism is reflected by the proposed circumferential growth model of Sadocha and Gruzleski (SG74) when graphite spherulites grow from the liquid phase. When an austenitic shell has developed around a spherulite, a polycrystal builds up by pyramidal growth. Insufficient nodularizer partially blocks the growth in c -direction which leads to tilt boundaries and causes degenerated spherulites and thus a transition to compact graphite. To this end, spheroidal graphite appears to be the natural graphite shape.

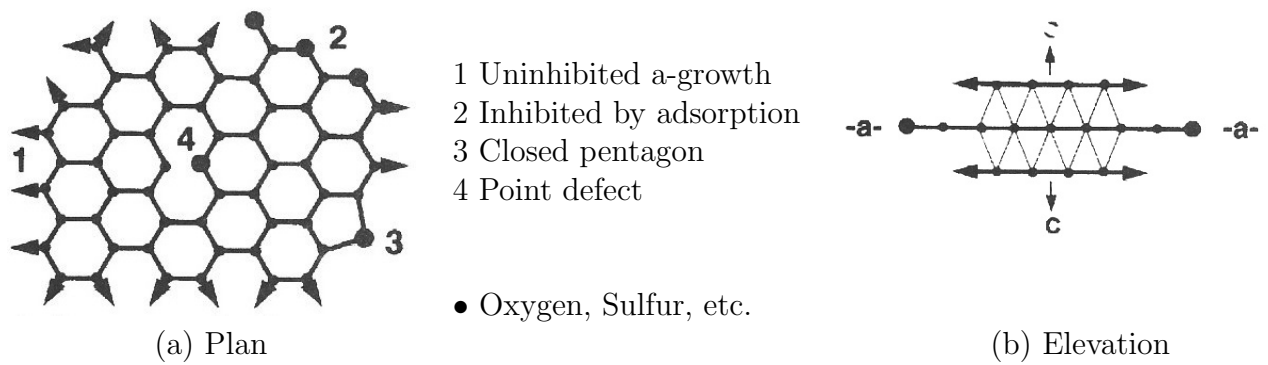


Fig. 2.9: (a) Plan of graphene sheets, doped with oxygen or sulfur to form heterocyclic rings, and (b) growth in c-direction becomes more probable if that in the a-direction is retarded by adsorption into saturated heterocyclic rings, according to Double and Hellawell (DH95).

3. State-of-the-Art

3.1 Objectives

Section 3.2 starts introducing kinetic effects arising during solidification with increasing interface velocity. Subsequently, a number of comprehensive stand-alone models for simulating microsegregation are discussed with focus on a commercial software product. This product is applied for a comparative simulation in Section 6.4.1. To identify the field of application for microsegregation models also more sophisticated two- and three-dimensional microstructure simulation codes are characterized. After discussing advantages and disadvantages of microsegregation models, macroscopically coupled software packages are presented. In order to reduce a disadvantage of microsegregation models, the kinetics of microstructure evolution is taken account of by dendrite arm coarsening, as discussed in the paragraph following that section. Microsegregation models dealing with cast iron are treated separately in Section 2.6 since cast iron is an exceptional alloy regarding kinetic effects. This also provides a link to the following Section 3.3 where the sparse information in relation to austenitic cast iron is gathered. Section 3.4 treats a recent work about the formation of chunky graphite, a defective graphite structure which was also observed in experiments of the present work.

3.2 Material Models for Solidification

As distinct from empirical models, solidification modeling on the microscale involves space-resolved physics-based calculations that model the time-dependent microstructure evolution. This time-dependency is caused by a number of kinetic effects. According to Boettinger and Coriell (BC85), some of these effects are classified in Tab. 3.1 relating to the solid-liquid interface velocity *u .

This classification is focused on the solid-liquid interface velocity and, as the velocity exceeds 1 nm/s, chemical diffusion in the bulk solid phases or the liquid phase is the dominating effect for departure from equilibrium. The very first numerical approach taking account of solid diffusion on solidification, dates back to 1966, when Brody and Flemings (BF66) developed a microsegregation model. In their simulation half of a dendrite

Tab. 3.1: Classification of non-equilibrium effects occurring with increasing solid-liquid interface velocity *u according to Boettinger and Coriell (BC85).

$^*u \approx 1 \text{ nm/s}$	Full Diffusional Equilibrium <ul style="list-style-type: none"> • no chemical potential gradients (composition of phases are uniform) • no temperature gradients • lever rule
$^*u \approx 1 \text{ }\mu\text{m/s}$	Local Interfacial Equilibrium <ul style="list-style-type: none"> • phase diagram gives the compositions and temperatures only at the solid-liquid interface • corrections made for interface curvature (Gibbs-Thomson Effect)
$^*u \approx 1 \text{ mm/s}$	Metastable Local Interfacial Equilibrium <ul style="list-style-type: none"> • stable phases can not nucleate or grow sufficiently fast • metastable phase diagram (a true thermodynamic phase diagram missing the stable phase or phases) gives the interface conditions
$^*u \approx 1 \text{ m/s}$	Interfacial Non-Equilibrium <ul style="list-style-type: none"> • phase diagram fails at interface • chemical potentials are not equal at interface • free energy functions of phases still lead to criteria for the impossible

arm spacing was selected as representative volume element (RVE) of the microstructure. The RVE was approximated by a plate-like geometry using Cartesian coordinates. Over the following four decades, similar models were developed and further kinetic effects were added. Kraft and Exner (KE96) and Kraft and Chang (KC97) reviewed numerous microsegregation models. These models encompass various morphological assumptions, solid state diffusion, dendrite arm coarsening, and undercooling effects. The authors concluded: microsegregation models, in relation to all of the effects discussed, are capable of predicting microsegregations very accurately. Kattner et al. (KBC96) coupled a microsegregation model to thermodynamic calculations to predict the solidification path of an eight-component superalloy. Xie et al. (XYD⁺03) studied the solidification of an AA7050 alloy. They compared three geometrical assumptions: plate-like, cylindrical, and spherical geometry to an experimental test case. They concluded that the cylindrical geometry shows the closest correlation.

Andersson et al. (AHJA90) and later Crusius et al. (CIK⁺92) started to develop a tool for diffusion-controlled transformation (DICTRA¹), that was commercialized in 1994. It is the most commonly used product today because it offers a wide range of applications and is the only commercial microsegregation software the present author is aware

¹DICTRA is a trademark of Thermo-Calc AB, Stockholm, Sweden

of. DICTRA solves the multicomponent diffusion and moving boundary problem which requires diffusion coefficients and thermodynamic equilibrium information at the moving interface. Furthermore, submodels were implemented for dispersed systems, particle coarsening, cooperative growth, and a cell model. DICTRA was applied to solidification problems, solid state phase transformations, interdiffusion in compounds, carburizing, nitriding, and so on. The simulated materials were steels, superalloys, aluminum alloys, cemented Carbides, etc. More information about Thermo-Calc² and DICTRA is given in a review article by Andersson et al. (AHH⁺02). DICTRA was verified for various applications: the classical experiments carried out by Darken (Dar49), solidification of an Fe Co13.4 Ni11.1 Cr3.1 Mo1.2 C0.23 wt.-% steel (LCB⁺98), transient liquid-phase bonding in the Ni-Al-B system (CB00), and for growth, dissolution, and coarsening of carbides in an Fe Cr10.5 Mo1.0 W1.0 C0.14 wt.-% steel (BH01).

Jacot and Rappaz (JR02) presented a two-dimensional microsegregation model to simulate the microstructure formation on solidification in multicomponent systems. This model is based on a pseudo-front tracking (PFT) technique to determine the evolution of the solid-liquid interface. This evolution is governed by solute diffusion and the Gibbs–Thomson effect. The diffusion equations are solved in the primary solid phase and in the liquid phase. The interface is reconstructed with the piecewise linear interface calculation (PLIC) technique. The concentrations at the solid-liquid interface are calculated using thermodynamic data provided by a phase diagram software.

It is also possible to simulate the microstructure evolution in two or even three dimensions applying the phase-field method (PFM). Based on a free energy functional, an equation of motion for the moving interface was derived which may be discretized by the finite differences method, for example. The phase-field method overcomes the problem of an explicit front-tracking technique introducing an order parameter, that is the phase-field parameter. The transition from liquid to solid is continuous which is in contrast to microsegregation models featuring a sharp interface. This continuous transition of concentration and phase field was proposed by Cahn and Hilliard (CH58). An introduction to the phase-field model is, for instance, given by Boettinger et al. (BWBK02).

Besides deterministic models also stochastic models, such as the Monte Carlo (MC) technique, where the evolutionary rules are stochastic or the cellular automaton technique (CA), where algorithms or probabilistic rules control the evolution, were developed. With help of these methods, it is possible to simulate grain structures and also dendritic structures, as demonstrated by Beltran-Sanches and Stefanescu (BS04). Further information about these methods is supplied by Stefanescu (Ste02).

The two- and three-dimensional material simulation methods mentioned not only provide solidification kinetics, but also information about microstructure, even for complex multicomponent and multiphase systems. However, this information is expensive in

²Thermo-Calc is a trademark of Thermo-Calc AB, Stockholm, Sweden

terms of computation time when morphological information is not required as a result, but can be provided as an input quantity. For purely predicting solidification kinetics, one-dimensional approaches generate similar results while needing considerably less computation time. One disadvantage of microsegregation models is the common restriction to only two solid phases simultaneously growing into the liquid phase from either side of the representative volume element. As distinct from empirical models, such as the Avrami (Avr40) model, microsegregation models reproduce precipitation kinetics on a physical and thermochemical basis. Thus, microsegregation models combined with thermodynamic and kinetic databases constitute a general approach. Empirical models are in principle restricted to the particular alloy under consideration. Dioszegi and Svensson (DS05) proposed an inverse kinetic analysis to determine the parameters for such models.

A coupling of microsegregation and process simulation is therefore advantageous to incorporate local precipitation kinetics, as proposed by Sasikumar and Exner (SE92). Kraft (Kra95) used a simplified approximation for this coupling. A first, but indirect, coupling was presented by Fakedey et al. (FLS96), in which the microsegregation simulations were performed after temperature simulation. Directly coupled results of a two-dimensional casting were first presented by Banerjee et al. (BSKB97). They used a simplified model according to Wang and Beckermann (WB96) for treating diffusion in the solid phase. Greven (Gre00) coupled a microsegregation model to a finite element temperature solver. He introduced directly coupled simulations for three-component aluminum alloys and a simple step casting discretized with an FEM mesh consisting of 400 nodes. This model was further developed by Pustal et al. (PBL⁺03) and applied to a more complex case where an AA2024 ingot casting including gating system was simulated with a mesh consisting of 3000 nodes, although the model was still restricted to three-component systems. Both, Greven and Pustal applied a direct coupling procedure where microsegregation simulations were performed for every particular finite element. This means that redundant and therefore time-consuming microsegregation simulations were performed, for example, at symmetrically placed nodes. Shawn et al. (SCK03) introduced, by then, an uncoupled Gulliver-Scheil approach while the authors focused on an open formulation of this model for a coupling to a macrosegregation code. Rady and Arquis (RA06) report on a two-component microsegregation model being directly coupled to a macrosegregation tool. In this study, the model is applied to a $\text{NH}_4\text{Cl-H}_2\text{O}$ -system. As before Banerjee, Tournet and Gandin (TG09) made use of the simplified microsegregation model from Wang and Beckermann. Tournet and Gandin extended this model for eutectic and peritectic transformations occurring on solidification of a Ni-Al alloy.

As mentioned before, microstructure information is an input quantity to microsegregation simulations. For uncoupled simulations with alloys solidifying with a dendritic structure, the dendrite arm spacing may be measured or approximated to define the size of the representative volume element and hence the associated diffusion distance. In a casting, however, the dendritic microstructure alternates with local cooling conditions. This

change in microstructure is taken account of by introduction of a dendrite arm coarsening model. Apart from alloy specific empirical models, as presented by Rontó and Roósz (RR01), dendrite arm coarsening models were developed based on solute transport between two unequally sized dendrite arms while the larger dendrite arm is ripening due to the Gibbs-Thomson effect (2.11) which is reported by Kattamis et al (KCF67) for binary alloys. Later, Beaverstock (Bea97) and Rappaz and Boettinger (RB99) made use of this concept for multicomponent systems.

Lacaze (Lac99) utilized a microsegregation model to study the solidification behavior of a spheroidal graphite iron consisting of the three fundamental components: iron, carbon, and silicon. Lacaze found that on solidification pronounced microsegregations build up, which are expected to impact the subsequent solid state transformations, as denoted by Dorazil (Dor91). Svensson and Dugic (SD99) demonstrated the possibility to calculate an average density of the phase mixture (liquid and solid phases) by using molar volumes of each phase and molar masses of each element to predict the shrinkage behavior in cast iron. Celentano et al. (CDGB08) coupled a macroscopic FEM temperature solver with a microsegregation model for ductile iron by taking into account nucleation and diffusion controlled growth, which is determined by the carbon and silicon profile. This model is using a quasi-stationary analytical solution proposed by Su et al. (SOYF84) with a polynomial description of liquidus and solidus line, but only on eutectic solidification.

In Section 4.2 the features of the most comprehensive coupled and decoupled microsegregation models, introduced here, are compared to the microsegregation model presented.

3.3 Austenitic Ductile Iron

The carbon flux in austenite is considerably impacted by gradients of other species, such as silicon or copper, which is called *cross-diffusion*, as explained in Section 2.4. The time-dependent phase fractions precipitated, especially of graphite, must be known to correctly predict the feeding in iron castings. In this respect, austenitic cast irons tend to be very sensitive since on eutectic solidification graphite is also precipitated directly from the liquid phase as chunky graphite. Also carbides may form due to chromium and manganese.

Spear (Spe93) stated, despite of the lower carbon content of approx. 3 wt.-% compared to 3.5-3.9 wt.-% in common SGI grades, the total amount of graphite, which is formed on solidification of austenitic SGI, is similar to that of common ductile iron. This is because nickel reduces the solid solubility of carbon on solidification. In a diagram of Schelleng (Sch61), Fig. 3.1, can be seen that nickel reduces the eutectic carbon concentration over the silicon content. Hasse (Has08) refers to a phase diagram originating from E. Morgan showing an isothermal cut through the ternary Fe-Ni-Si system at room temperature.

With increasing nickel concentration, first pearlite is stable, and then, in a two-phase region, martensite and austenite coexist up to approx. 17 wt.-% nickel. Above this value, austenite is the stable phase at room temperature. With increasing silicon concentration also silicides may be precipitated from the liquid phase on solidification. Spear further

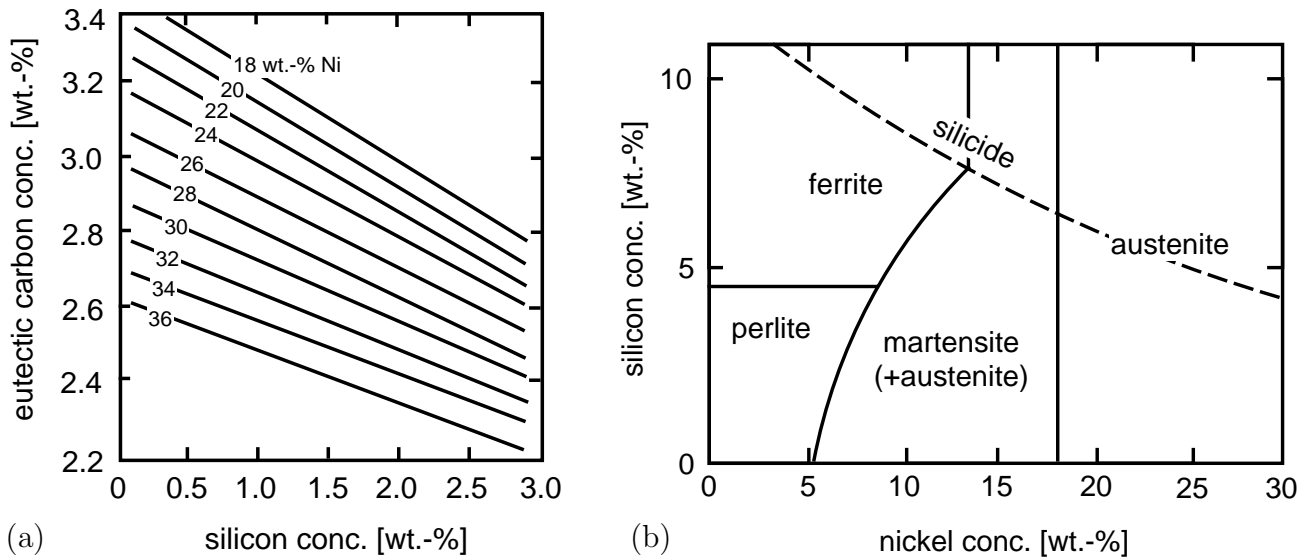


Fig. 3.1: (a) Impact of nickel and silicon on the eutectic carbon concentration in austenitic cast iron according to Schelleng (Sch61) and (b) stable phase regions, as provided by Hasse (Has08) with reference to E. Morgan.

stated, in chromium-containing grades, chromium reacts with carbon at late stages of solidification and thus initiates carbide formation at grain boundaries due to microsegregations. As a result, solidification shrinkage increases due to lack of graphite expansion for which reason chromium-enriched grades approximate the solidification shrinkage behavior of steel, whereas those without chromium show a shrinkage similar to that of ductile iron.

3.4 Formation of Chunky Graphite

The structure transition from spheroidal graphite to incomplete spheres and chunky graphite is described at the end of Section 2.6 and is shown in Fig. 2.8. Zhou et al. (ZSE87) is in the opinion, that chunky graphite develops by a coupled growth mechanism of graphite and austenite. This mechanism was similar to lamellar growth, but slightly looser. On the other hand, Liu et al. (LLWL83) states, chunky graphite-austenite eutectic growth is decoupled and thus more similar to spheroidal graphite. Yet, the growth is preferentially in c-direction, as illustrated in Fig. 3.2, whereas the growth of spheroidal graphite is in a-direction, which is shown in Fig. 2.7. However, the actual cause for this change in growth direction remains unknown. Since there is neither conclusive evidence

for the theory of Zhou nor for that of Liu, the present author adopted the opinion of Zhou by modeling coupled growth, as described in Section 6.2.

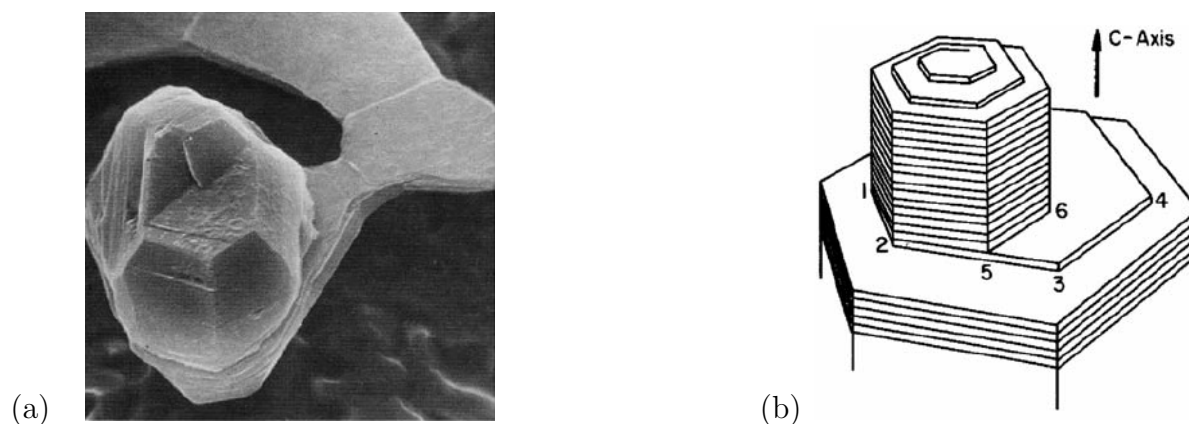


Fig. 3.2: (a) Experimental finding and (b) sketch of graphite growth along the c-axes, according to Lux et al. (LMMT74).

Furthermore, it is unclear whether the formation of chunky graphite is an effect caused by local cooling conditions, that are taken into account in the present work, or macrosegregations, that are neglected in this study. Larrañaga et al. (LAS⁺09) analyzed the impact of antimony on the formation of chunky graphite in thick-walled castings. In the center of a block casting, as shown in Fig. 3.3 (a), the area affected by chunky graphite is clearly distinguishable from the surrounding chill zone with spheroidal graphite. Because the chunky graphite zone is separated sharply and of symmetrical appearance, this effect is rather related to cooling than macrosegregation. Fig. 3.3 (b) shows a micrograph with spheroidal and chunky areas. In Fig. 3.4, SEM pictures of depth-etched samples are presented. As can be seen, chunky graphite crystallites build an interconnected network and sometimes transient shapes are observed consisting of incomplete spheres. Larrañaga et al. investigated the positive effect of micro-alloying antimony which helps preventing or reducing chunky graphite in cerium nodularized SGI. Spear (Spe93) stated, that cerium instead of magnesium helps to prevent the formation of chunky graphite in austenitic cast iron.

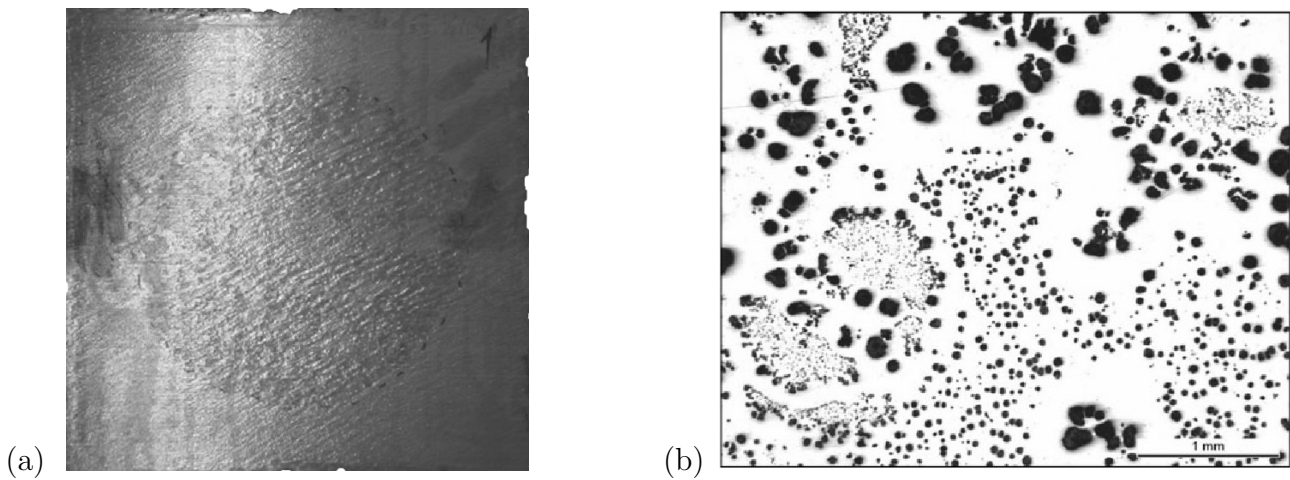


Fig. 3.3: (a) Section of a block casting showing the central zone being affected by chunky graphite. (b) Optical micrograph of a heavy section SGI casting showing dendrite-like ex-austenite with large nodules embedded in cells of chunky graphite and areas of usual spheroidal graphite, according to Larrañaga et al. (LAS⁺09).

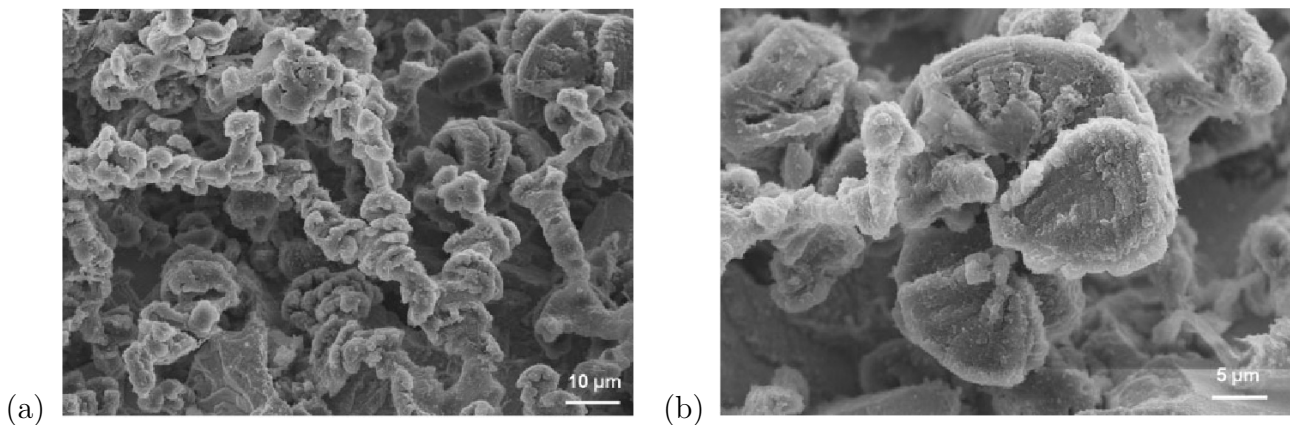


Fig. 3.4: (a) Interconnected strings of graphite crystallites observed by SEM in a depth-etched sample. (b) Termination of a graphite string with an incomplete graphite nodule, according to Larrañaga et al. (LAS⁺09).

4. Model Description

4.1 Objectives

This section is dedicated to the description of the microsegregation model, submodels, and algorithms. To improve the readability of this chapter, large equations and structure charts are located in Appendices B-E. Nomenclature and abbreviations are explained in the context and, moreover, listed in Appendix A.

Besides the coupled version of the code, also a stand-alone version was programmed enhancing the applicability and testability of the model. First the characteristics of the model are discussed within the scope of state-of-the-art microsegregation software in Section 4.2. This comparison outlines aspects and features of the model. As explained in Section 4.3.1, the representative volume element provides the fundamental concept for understanding the model. In this representative part of the microstructure, diffusion simulations are performed. Diffusion is a kinetic effect that impacts the velocity of the solid-liquid interface and hence, the fraction solid on solidification, as pointed out in Section 4.3.2 and 4.3.3. Averaged quantities, such as the concentration transported by diffusion, depend on the geometry of the RVE, as explained in Section 4.3.4. An additional kinetic effect is taken into account through adaptation of a dendrite arm coarsening model in Section 4.3.7. Following the description of essential elements of the model, peripheral elements are treated. Section 4.4 explains, how molar quantities are transformed into weight or volume-specific quantities. The usage of the thermodynamic query interface for obtaining equilibrium data is described in Section 4.5.1. The latent heat and thermodynamic properties for each phases according to Section 4.5.4, and thus also for the phase mixture, are the essential parameters for the coupling to the heat conservation equation. This procedure is pointed out in Section 4.6 alongside other possibilities of time-temperature correlation. Finally, the structure of the code is explained, which is divided classically into preprocessing (cf. Section 4.7), main processing (cf. Section 4.8), and postprocessing (cf. Section 4.10). The concept and structure of coupling to the process simulation is considered as a part of main processing and therefore also described within this scope.

4.2 Model Characteristics

In Tab. 4.1 the characteristics of the present approach are compared to the most comprehensive state-of-the-art models, such as the commercial software DICTRA described by Andersson et al. (AHH⁺02). Apart from the present work, DICTRA is the only model listed taking account of cross-diffusion and enables precipitation of multiple solid phases. However, DICTRA's multiphase concept is based on additional volumes called cells. These cells are not generated automatically when an additional phase becomes active. Cells and cell size need to be predefined by the user. On the other hand, DICTRA offers additional features which are not focus of the present work. Some of these features are described in Chapter 3. The model presented by Xie et al. (XYD⁺03) is coupled to the commercial thermodynamic software module PANENGINE¹ and takes account of dendrite arm coarsening by an approach of Beaverstock (Bea97) that was extended by Rappaz and Boettinger (RB99). Both, DICTRA and the model of Xie et al., enable multiple geometries of the representative volume element, that is plate-like geometry, cylindrical, and spherical geometry. This geometry concept was generalized in the present work in order to map mixed geometries on the representative volume element, as described in Section 4.3.4. Celentano et al. (CDGB08) present a coupled model for cast iron which is somewhat limited compared to the uncoupled models mentioned. The most comprehensive coupled software is based on the work of Greven (Gre00), a precursor version of the present work. Greven's model is restricted to some distinctive three-component aluminum alloys and coupled to the thermodynamic software interface ChemApp². Diffusion and dendrite arm coarsening were simulated only on primary solidification of a step casting with a mesh consisting of 400 nodes. Subsequently to Greven, Hofmeister (Hof02) reports of a similar version. Additional features of this version, such as the coupling to Thermo-Calc and diffusion during the complete solidification process, were added and described by Pustal et al. (PBL⁺03). Unique features of the present work, alongside changes, improvements, and enhancements made since Greven and Hofmeister published their work, are listed below.

Unique features of the present model with reference to Tab. 4.1 are:

1. direct coupling to porosity prediction, according to Section 4.9,
2. innovative concept of coupling to the process simulation, according to Section 4.9,
3. multiphase concept generalizing the local phase fraction approach, as described in Section 4.3.1 and
4. mixed geometry concept introducing a geometry factor, which is explained in Section 4.3.4.

¹PANENGINE is a trademark of CompuTherm LLC, Madison, USA

²ChemApp is a trademark of GTT GmbH, Herzogenrath, Germany

Tab. 4.1: Comparing features of the approach presented to the most comprehensive state-of-the-art microsegregation models.

Model Reference	Pustal Present Work	Greven (Gre00)	Celentano (CDGB08)	DICTRA (AHH ⁺ 02)	Kattner (KBC96)	Xie (XYD ⁺ 03)
Porosity-Coupling	3D	—	—	—	—	—
Macro-Coupling	3D	3D	2D	—	—	—
Components	n	3	3	n	n	n
Solid Phases	m	2	2	2 ⁺	2	2
Cross-Diffusion	yes	—	—	yes	—	—
Geometry	mixed	1	3	1, 2, 3	1	1, 2, 3
DAS coarsening	(RB99)	(RHE86)	—	—	—	(Bea97)
Thermodynamics	TC	CA	—	TC	OA	PE
Diffusion Solver	num.	num.	anal.	num.	num.	num.

TC: Thermo-Calc

CA: ChemApp

OA: Own Approach

PE: PANENGINE

Further new features compared to precursor versions of Greven (Gre00) and Hofmeister (Hof02) are:

- the cross-diffusion model, Eq. (2.18), and implementation in Section 4.3.6,
- the multicomponent concept implementing a Householder algorithm (Hou58) in Section 4.3.3,
- input concentrations for precipitation calculations modified by diffusion in Section 4.5.2 which improved significantly the stability and applicability to large solidification times,
- the stand-alone version of the code for decoupled simulations and for comprehensive testing and debugging introducing the time-temperature correlations described in Section 4.6.
- the multicomponent dendrite arm coarsening model adapting the approach provided by Rappaz and Boettinger (RB99) in Section 4.3.7,
- diffusion simulation during all stages of solidification,
- diffusion in the liquid phase introducing a Neumann boundary condition according to Eq. (4.10),
- the general formulation and applicability by coupling to Thermo-Calc in Section 4.5,
- the FVM discretization provided in Appendix C and the averaging concept in Section 4.3.4,

- the graphical frontend described in Section 4.7,
- the conversion of results into user specific quantities in Section 4.4 and
- the automated postprocessing through a coupling to Gnuplot in Section 4.10.

4.3 Microsegregation Model

4.3.1 Representative Volume Element

One example of a typical representative volume element (RVE) is shown in Fig. 4.1. The characteristic length of the RVE corresponds, for instance, to an average grain radius or half of an average dendrite arm spacing $\lambda/2$. In the RVE shown, two solid phases α and β are growing from the left side into the liquid phase L on the right. The concentration profiles x^α and x^L are plotted on the left ordinate as a function of the location s . The concentration profile for the β -phase is omitted for the sake of clarity in the diagram.

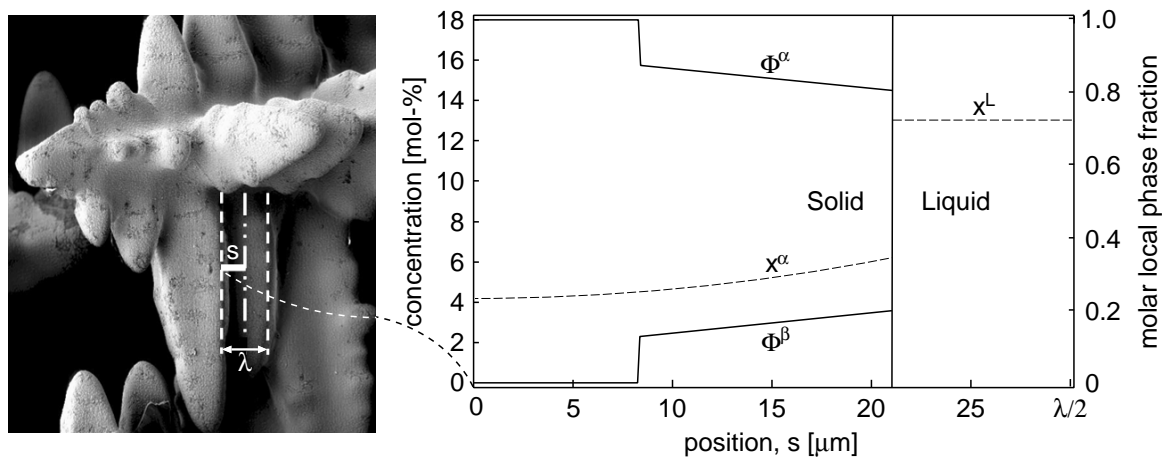


Fig. 4.1: Multiphase concept in the RVE of the microsegregation model (right). The characteristic length corresponds to half of an average dendrite arm spacing (left) or to an average grain radius for example.

A diffusion type needs to be selected for each phase, that is complete mixing, final diffusion, or no diffusion. The solid phases and the liquid phase are strictly separated from each other by the solid-liquid interface, and diffusion is modeled in each contemplated phase. Exchange of species between the phases is realized by boundary conditions which depend on the diffusion type selected for each phases. If, for example, no diffusion is assumed in the α -phase, the concentration profiles are only impacted by redistribution. In this case, the imposed interface concentration *x originating from a thermodynamic equilibrium calculation, is simply interpolated between *x and the interface concentration at the previous time step, as indicated in Fig. 4.2 (a). The index “ \star ” is used for quantities at the solid-liquid interface. When final diffusion is selected for the α -phase, a diffusion simulation is carried out based on this interpolated concentration profile. For this purpose,

a Dirichlet boundary condition corresponding to a fixed equilibrium concentration ${}^*x^\alpha$ is applied at the solid-liquid interface, as shown in Fig. 4.2 (b). In the case of complete mixing in the liquid phase, a uniform concentration according to Eq. (4.9) is assumed directly resulting from the flux balance equation. For the liquid phase also finite diffusion may be selected. However, the diffusion problem is treated different from diffusion in solid phases. This is because of species, that cannot be incorporated into solid phases by diffusion and, therefore, remaining in the liquid phase. In this case, a Neumann boundary condition is deduced from Eq. (4.10) corresponding to an imposed species flux.

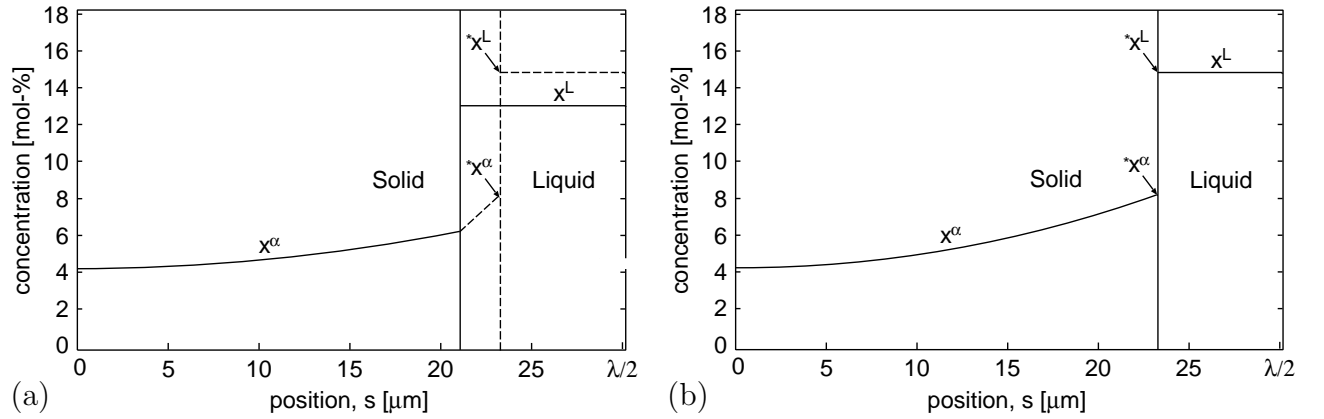


Fig. 4.2: (a) Interpolation of concentration ${}^*x^\alpha$ at the solid-liquid interface and new homogeneous concentration x^L in the liquid phase at a discrete time step. (b) The same situation after a diffusion simulation in the α -phase.

Following the approach of Chen and Chang (CC92) for eutectic growth of two solid diffusion phases, the local phase fraction ${}^*\phi^j$ is introduced for each solid phase j as shown in Fig. 4.3 (a). This local quantity depends on change in phase fraction Δf^j of the solid phase j and changes in phase fractions Δf^b of all m currently precipitated solid phases:

$${}^*\phi^j = \Delta f^j / \sum_{b=1}^m \Delta f^b . \quad (4.1)$$

This definition implies that ϕ^j is a complementary function at each location of the RVE. Because of discretization in time and space, the local phase fraction changes discontinuously over the position. However, the continuous species conservation equation (4.2) is multiplied by the local phase fraction and thus reducing each term by ϕ^j . Therefore, the local phase fraction needs to be transformed into a continuous function of position, as shown in Fig. 4.3 (b). This is achieved by an interpolation procedure guaranteeing conservation of phase fractions while at the same time the local phase fraction ${}^*\phi^j$, directly at the interface, is represented by Eq. (4.1) to avoid oscillations. This concept allows for the precipitation of multiple layers of solid diffusion phases in a eutectic manner. For degenerated eutectic growth, precipitation of one solid phase on the right side of the RVE is possible so as to enclose the liquid phase by two solid phases.

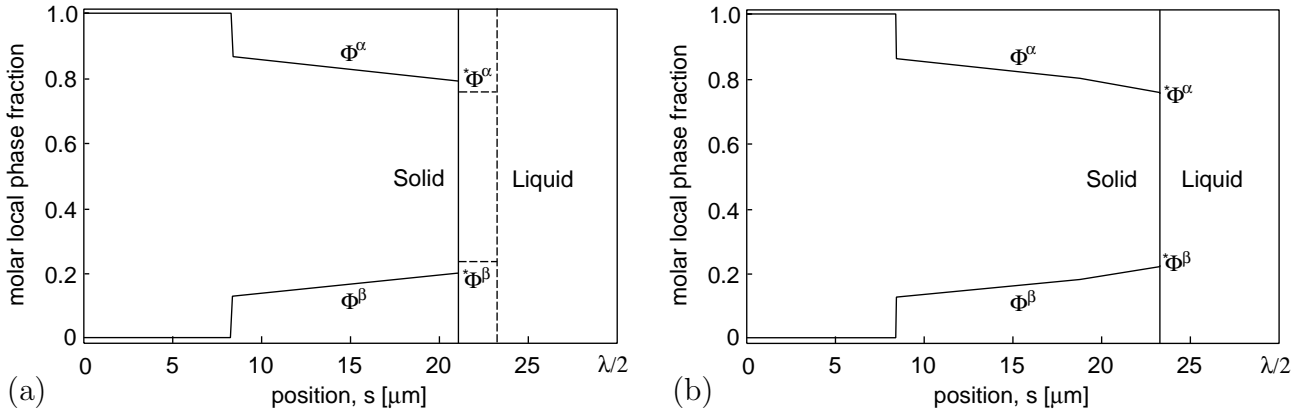


Fig. 4.3: (a) Local phase fraction at the solid-liquid interface at a discrete time step according to Eq. (4.1) and (b) profiles of the local phase fraction after conservative interpolation.

4.3.2 Species Conservation Equation

To calculate microsegregation patterns of each species i in each diffusion phase j , the species conservation equation (2.15) is adapted to the microsegregation model by multiplying with the local phase fraction ϕ^j :

$$\frac{\partial(\phi^j x_i^j)}{\partial t} + \text{div}(\phi^j \mathbf{j}_i^j) = \phi^j \dot{X}_i^j. \quad (4.2)$$

The first term of this equation takes account of a time-dependent change in concentration x^j . The diffusive fluxes \mathbf{j}_i^j may be either constituted in chemical form according to Eq. (2.16) or thermodynamic form according to Eq. (2.17). Alternatively, as in this work, Eq. (2.18) may be used involving both approaches. The term on the right-hand side is a species source term \dot{X} . For general applicability, the species conservation equation (4.2) is discretized in time and space. This is obtained by application of the finite volume method (FVM), as described in Chapter 2.5. Details about the discretization procedure are provided in Appendix C.1. Eq. (4.2) is integrated over time t and volume ΔV_k of each element which is directly related to the volume fraction $f_V^{\Delta V_k}$. Furthermore, an underrelaxation factor θ is introduced weighting the previous ${}_\omega x$ and current ${}_\nu x$ concentration solution, for which concentration gradients and source terms are evaluated. This means, any underrelaxation factor in the range $[0, 1]_{\mathbb{R}}$ may be selected in which 0 represents a purely explicit and 1 a purely implicit scheme. Since the introduction of the underrelaxation factor leads to long expressions, the abbreviated notation in Eq. (C.5) is applied throughout the present work. By application of the averaged quantities introduced in Section 4.3.4, a discrete change of the averaged product is obtained as follows:

$$\begin{aligned}
\langle \phi^j x_i^j \rangle_{\omega^t}^{\Delta V_k} f_V^{\Delta V_k} &= - \left[\sigma_e \phi_e^j \mathbf{j}_{i,e}^j \theta - \sigma_w \phi_w^j \mathbf{j}_{i,w}^j \theta \right]_{-\omega^t}^{\omega^t} \Delta t \\
&+ \langle \phi^j \rangle_{\omega^t}^{\Delta V_k} \langle x_i^j \rangle_{\omega^t}^{\Delta V_k} f_V^{\Delta V_k} + \langle \phi^j \rangle_{\omega^t}^{\Delta V_k} \left[\dot{X}_i^j \theta \right]_{-\omega^t}^{\omega^t} \Delta t f_V^{\Delta V_k}.
\end{aligned} \tag{4.3}$$

The first term on the right-hand side takes account of diffusive fluxes across the boundaries of a finite volume element. The second term on the right is extracted from the transient term at the left-hand side and prevents a change in concentration as the local phase fraction is interpolated at the solid-liquid interface. This is further explained in Appendix C.1. The third term is a source term to vary the concentration for an intended implementation of solid state transformations. Constituting the diffusion flux according to Eq. (2.18) and rearranging Eq. (4.3) for the unknown concentrations at grid points, as in Eq. (C.12), yields a system of equations with a tri-diagonal coefficient matrix. At the boundaries of each phase appropriate boundary conditions need to be introduced which is also pointed out in Appendix C.1. At moving interfaces usually Dirichlet boundary conditions are imposed for species, while at other phase boundaries homogeneous Neumann boundary conditions (i.e. no chemical flux) are applied. The discretization generates a system of algebraic equations with a tri-diagonal $k \times k$ coefficient matrix \mathbf{K} , a vector \mathbf{X} of unknown concentrations at grid points, and on the right, a vector \mathbf{Y} for each phase j and component i at each grid point k :

$$\sum_{b=k-1}^{k+1} \mathbf{K}_{ib}^j \mathbf{X}_{i,k}^j = \mathbf{Y}_{i,k}^j. \tag{4.4}$$

The assignment of this system of equations is represented by structure chart E.5, and its corresponding solution is obtained by the tri-diagonal matrix algorithm E.6.

4.3.3 Species Flux Balance

Equilibrium calculations applying Thermo-Calc involve systematical variations of phase fractions and concentrations until a minimum in Gibbs free energy difference is reached, as explained in Section 2.3.2. During this procedure, concentrations and phase fractions are coupled via a species flux balance. Vice versa, it is also possible to determine phase fractions by equilibrium concentrations. For the microsegregation model, flux balance equations are applied to determine new phase fractions by adding the contributions due to back-diffusion. An integral version of an enhanced flux balance is given by Eq. (4.5). It is similar to the well-known lever rule, while taking account of average concentrations $\langle x_i \rangle$ in the liquid phase L and in m solid phases j . These concentrations are weighted according to the particular phase fraction f . The sum of these products equals the average initial concentration $\langle x_i \rangle^0$, given as:

$$\langle x_i \rangle^L f^L + \sum_{j=1}^m \langle x_i \rangle^j f^j = \langle x_i \rangle^0 . \quad (4.5)$$

This integral flux balance is quite useful since it is self-conserving. However, when applying this balance equation to obtain phase fractions, potential programming or modeling errors may go unrecognized due to this conservative property. Moreover, numerical integration over the whole RVE is required to obtain average concentrations in each phase. Therefore, Eq. (4.5) is applied as a checksum defining the relative failure in concentration:

$$E_x = \frac{\langle x_i \rangle^L f^L + \sum_{j=1}^m \langle x_i \rangle^j f^j - \langle x_i \rangle^0}{\langle x_i \rangle^0} . \quad (4.6)$$

In order to determine phase fractions, local flux balance equations at the solid-liquid interfaces are applied instead of Eq. (4.5) which is reformulated in rate form and rearranged as follows:

$$\sum_{j=1}^m \left({}^*x_i^L - {}^*x_i^j \right) \partial f^j = \sum_{j=1}^m \partial \langle x_i \rangle^j f^j + \partial \langle x_i \rangle^L f^L . \quad (4.7)$$

Here, the condition $\sum \partial f^j = -\partial f^L$ is applied and quantities at the interface are denoted by “ \star ”. The chemical fluxes $\partial \langle x_i \rangle^j f^j$ into solid phases j are deduced from local concentration gradients $\mathbf{grad}({}^*x_i^j)$ at the interface according to Eq. (2.18). This gradient is very sensitive to the grid spacing at the interface. To avoid numerical instability and to increase the precision of the solution, gradients at the interfaces are evaluated by a second order concentration function (C.19) determined by a linear regression of grid point values. An alternative method to deduce a local flux balance is given in Appendix C.2 in order to discretize Eq. (4.7). This results in the following system of flux balance equations containing all n alloying elements and m phases, that are simultaneously precipitated:

$$\begin{bmatrix} ({}^*x_1^L - {}^*x_1^1) & \dots & ({}^*x_1^L - {}^*x_1^m) \\ \vdots & \ddots & \vdots \\ ({}^*x_n^L - {}^*x_n^1) & \dots & ({}^*x_n^L - {}^*x_n^m) \end{bmatrix} \begin{pmatrix} \Delta f^1 \\ \vdots \\ \Delta f^m \end{pmatrix} = \begin{pmatrix} \begin{matrix} {}^* \left[\sigma (\phi^L \mathbf{j}_{1,w}^L - \sum_{j=1}^m \phi^j \mathbf{j}_{1,e}^j) \theta \right]_{-\omega\theta}^{\nu\theta} \Delta t \\ \vdots \\ {}^* \left[\sigma (\phi^L \mathbf{j}_{n,w}^L - \sum_{j=1}^m \phi^j \mathbf{j}_{n,e}^j) \theta \right]_{-\omega\theta}^{\nu\theta} \Delta t \end{matrix} \\ \end{pmatrix} . \quad (4.8)$$

The solute fluxes \mathbf{j}_i^L and \mathbf{j}_i^j arising from this equation are evaluated according to Eq. (C.17). Comparing Eq. (4.7) to Eq. (4.8) reveals flux balance equations not only holding for each individual alloying element i , but for all n alloying elements contributing to a change in solid fraction. However, this condition is hard to fulfill since, in general, individual chemical fluxes are unequal. The system of equations (4.8) is overdetermined as long as the number of phases m precipitated is smaller than the number of alloying components n . This corresponds to the thermodynamic degree of freedom given by Gibbs' phase rule (2.4). As long as Eq. (4.8) is overdetermined, the solution is not unique and phase fractions are obtained by a least-square fit. An effective solution method for overdetermined systems of equations is provided by the Householder algorithm (Hou58) which is implemented in the model presented. It is indispensable by this procedure that the solution quality is unequal for each individual alloying element. When assuming complete mixing in the liquid phase, Eq. (4.8) may be rearranged for the liquid concentration of each individual species to compensate for the inequality of chemical fluxes:

$$\nu x_i^L = \frac{\omega x_i^L \omega f^L + \sum_{j=1}^m \left[(x_i^L - x_i^j) \Delta f^j + \sigma \phi^j \mathbf{j}_{i,e}^j \Delta t \theta \right]_{-\omega \theta}^{\nu \theta}}{\omega f^L}. \quad (4.9)$$

Otherwise, when the liquid phase is considered to be a diffusion phase, a Neumann boundary condition is applied at the western boundary of the liquid phase for diffusion calculation. This Neumann condition is deduced by rearrangement of Eq. (4.8) for each individual species to compensate for this inequality by a fixed species flux into the liquid phase:

$$\hat{\mathbf{J}}_{i,w}^L = \sum_{j=1}^m \left[(x_i^L - x_i^j) \Delta f^j / \Delta t + \sigma \phi^j \mathbf{j}_{i,e}^j \theta \right]_{-\omega \theta}^{\nu \theta}. \quad (4.10)$$

4.3.4 Morphology and Averaged Quantities

The solidification morphology of cast iron can be partially dendritic and partially globular, as pointed out in Section 2.6. The predominance of the particular morphology depends on nucleation and growth conditions of austenite and graphite. A one-dimensional RVE only enables the reproduction of simple geometries. To map mixed morphologies on the RVE, a geometry factor for diffusion g in the range $[1, 3]_{\mathbb{R}}$ is introduced, where 1 corresponds to a plate-like, 2 to a cylindrical, and 3 to a globular geometry. For dendritic solidification morphologies, a value between a plate-like and a cylindrical geometry of 1.5 may be selected, or for dendritic-globular solidification morphologies, as for ductile iron, a value of 2.7 may, for instance, be appropriate.

By the aid of finite volume elements ΔV_k , three types of continuous spatial functions are reproduced within the RVE. To model a transient change in concentration in a finite volume element, averaged quantities need to be generated considering interdependencies among the average values of these functions in the following order:

1. The volume fraction $f_V^{\Delta V_k}(s)$ of a finite volume element $\Delta V_k(s)$ and the relative surface area $\sigma(s)$ are functions of position s and interrelated to the geometry coefficient g .
2. The average local phase fraction $\langle \phi^j \rangle^{\Delta V_k}(\Delta V)$ of a phase j within a finite volume element is considered to be a function of volume difference ΔV .
3. The average concentration $\langle x_i^j \rangle^{\Delta V_k}(\Delta V, \phi^j)$ of a component i in a phase j within a finite volume element is a function of both, the development of volume difference and local phase fraction.

The method approximating concentration and local phase fraction as functions of volume differences, varying linearly between neighboring elements, is advantageous in terms of avoiding the use of different coordinate systems. The local surface area $A(s)$ is necessary in diffusion simulation to obtain an absolute species flux at each position s . This is, for instance, the case at boundaries of finite volume elements. When dividing the species conservation equation by the volume ΔV^R of the RVE, volume fractions instead of volume differences arise. The division by ΔV^R is necessary to deduce a relative surface area $\sigma(s)$ in Eq. (4.11). This enables a general geometrical concept, not depending on particular geometries. A spherical geometry with a geometry coefficient $g = 3$, for example, results in the particular relative surface area $\sigma(s) = A(s)/\Delta V^R = 4\pi s^2/(4/3\pi l^3) = 3s^2/l^3$. This may also be demonstrated for plate-like geometry, $g = 1$, and for cylindrical geometry $g = 2$. This procedure is generalized in the following way, as long as g is in the range $[1, 3]_{\mathbb{R}}$:

$$\sigma(s) \equiv \frac{A(s)}{\Delta V^R} = \frac{g s^{g-1}}{l^g}. \quad (4.11)$$

To compute a volume fraction limited by the eastern and western boundary with the indices e and w , respectively, the volume fraction $f_V^{\Delta V_{e,w}}(s)$ may be written analogous as a function of the local volume differences $\Delta V_{e,w}$ relating to the volume ΔV^R :

$$f_V^{\Delta V_{e,w}}(s) \equiv \frac{\Delta V_{e,w}}{\Delta V^R} = \frac{s_e^g - s_w^g}{l^g}. \quad (4.12)$$

The western and eastern boundaries correspond, for instance, to a section of a finite volume element. The average phase fraction $\langle f^j \rangle^{\Delta V_k}$ in the volume ΔV_k corresponds to product of the average local phase fraction $\langle \phi^j \rangle^{\Delta V_k}$ and the element volume fraction $f_V^{\Delta V_k}$:

$$\langle f^j \rangle^{\Delta V_k} = \langle \phi^j \rangle^{\Delta V_k} f_V^{\Delta V_k}. \quad (4.13)$$

As illustrated in Fig. 4.4, the local phase fraction ϕ^j is averaged by weighting the contributions from the partial volumes $\Delta V_{k,w}$ and $\Delta V_{e,k}$ over the total volume $\Delta V_k = \Delta V_{k,w} + \Delta V_{e,k}$ at each finite volume element. This averaging procedure also implies the

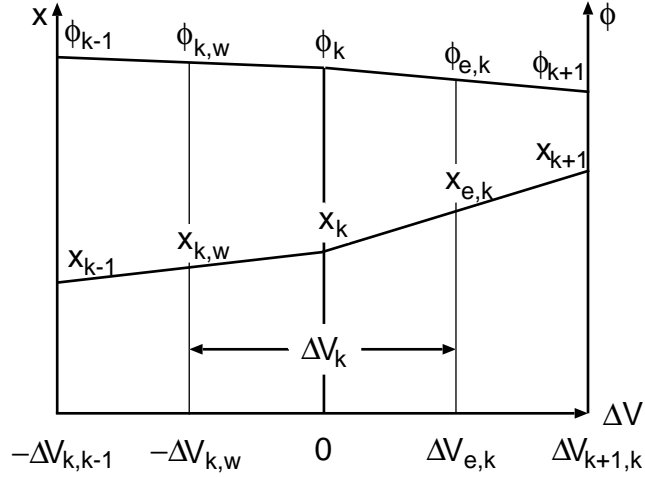


Fig. 4.4: Sketch illustrating volume differences in a finite volume element and between neighboring elements. Furthermore, concentration $x_k(\Delta V)$ and local phase fraction $\phi_k(\Delta V)$ are given as functions of volume difference ΔV relating to the center of gravity of the node k .

slope $(\phi^j)' = \Delta\phi^j / \Delta V$ over the volume differences between the neighboring volume elements $\Delta V_{k,k-1}$ and $\Delta V_{k+1,k}$. Thus, these volume differences also contribute to the weighting factors \mathcal{C}_{w2} and \mathcal{C}_{e2} given in Eq. (B.9) to obtain the average local phase fraction in volume element ΔV_k :

$$\langle \phi^j \rangle^{\Delta V_k} = \phi_k^j + (\phi_{k-1}^j - \phi_k^j) \mathcal{C}_{w2} + (\phi_{k+1}^j - \phi_k^j) \mathcal{C}_{e2}. \quad (4.14)$$

The average concentration in the partial volume $\Delta V_k^j = \Delta V_k \langle \phi^j \rangle^{\Delta V_k}$ of the volume element ΔV_k that is occupied by the phase j is given by:

$$\langle x_i^j \rangle^{\Delta V_k^j} = \frac{\langle \phi^j x_i^j \rangle^{\Delta V_k}}{\langle \phi^j \rangle^{\Delta V_k}}. \quad (4.15)$$

Therefore, first the averaged product $\langle \phi^j x_i^j \rangle^{\Delta V_k}$ of the local phase fraction $\phi^j(\Delta V)$ and concentration function $x_i^j(\Delta V)$ are determined. This product arises from the species conservation equation and needs to be provided as function of grid point values. To this end, averaging parameters at grid point k to the west \mathcal{C}_w^j , at the center \mathcal{C}_c^j , and to the east \mathcal{C}_e^j are given in Eq. (B.8) and defined as follows:

$$\langle \phi^j x_i^j \rangle^{\Delta V_k} = \mathcal{C}_w^j x_{i,k-1}^j + \mathcal{C}_c^j x_{i,k}^j + \mathcal{C}_e^j x_{i,k+1}^j. \quad (4.16)$$

4.3.5 Front-Tracking

Grid points are equidistantly distributed in each phase, except for the first and last grid point, as shown in Fig. 4.5. The position of each equidistant grid point is therefore linked to the grid point number and the grid point spacing: $s(k) = (k - 1)\Delta s$. The position of the first grid point in solid phases results from initialization. For the given example, the α -phase is initialized at grid point 1 and the β -phase at grid point 5. The current position *s of the solid-liquid interface, is stored explicitly for both, the last grid point in all currently precipitated solid phases and the first grid point in the liquid phase. This position is deduced from Eq. (4.12) as function of the geometry coefficient g and the change in liquid fraction Δf^L :

$${}^*s = ({}^*s^g - \Delta f^L {}^*l^g)^{1/g}. \quad (4.17)$$

Fig. 4.5 shows the current position of the solid-liquid interface at grid point 14 (dashed line). The interface position at the previous time step is located at grid point 12 (solid line). As can be seen, grid point 14 is very close to grid point 13. When this distance is below a critical value, grid point 13 is skipped during diffusion simulation and instead grid point 12 is the nearest western neighbor of grid point 14 to avoid numerical instability and division by zero. The size l of the RVE is represented by the same position as the last grid point z in the liquid phase. This size is deduced from Eq. (4.25) by the simple relation: ${}^*l = {}^*z/2$. When the position of the interface *s is known, a local phase fraction ϕ^j for each solid phase j is assigned to each grid point according to Eq. (4.1), as shown in Fig. 4.5 for the α -phase and β -phase. Subsequently, the local phase fraction at the interface ${}^*\phi^j$ is interpolated in a manner conserving the phase fraction to achieve a continuous function ϕ^j , as demonstrated in Fig. 4.3 (b).

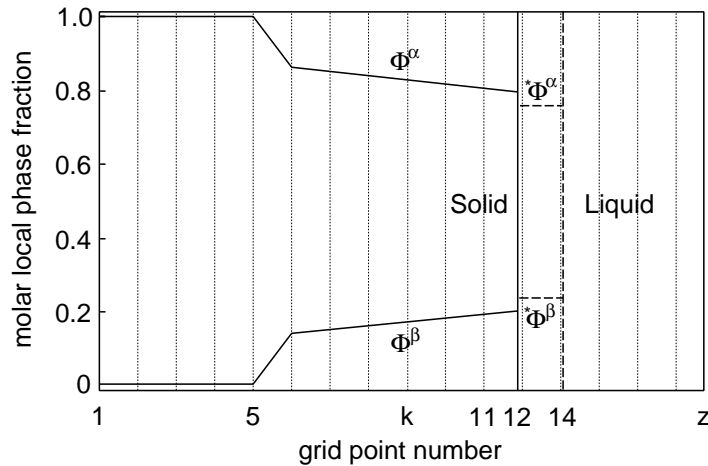


Fig. 4.5: Front-tracking and grid points within the RVE.

4.3.6 Implementation of Cross-Diffusion

Cross-diffusion effects, where the gradient of one species induces a chemical flux \mathbf{j}_i of another species i , are taken into account in both, species flux balance equation (4.8) and species conservation equation (4.4). Cross-diffusion is constituted according to Eq. (2.18). When specific fluxes are multiplied by σ and ϕ^j in the scope of the discretization procedure, absolute fluxes across the boundaries of finite volume elements or at phase boundaries are obtained. As mentioned in Appendix C.1, gradients in diagonal diffusion terms may be evaluated by selecting an underrelaxation factor in the range $[0, 1]_{\mathbb{R}}$. Cross-diffusion fluxes $\Delta \mathbf{J}_{ib}^j$ with $b \neq i$, which are the off-diagonal terms in Eq. (C.12), are considered to be purely explicit corresponding to an underrelaxation factor of 0. To avoid numerical instability, the time step width for the species conservation equation is reduced individually for each species in order to fulfill Fourier's stability criterion, as described by Rappaz et al. (RBD03). This stability criterion depends on the underrelaxation factor θ and the chemical Fourier number $Fo_i^j = D_i^j \Delta t / \Delta s^2$ as follows:

$$Fo_i^j (1 - 2\theta) \leq \frac{1}{2}. \quad (4.18)$$

4.3.7 Dendrite Arm Coarsening

For alloys with dendritic solidification morphology, the dendrite arm spacing defines the length of the RVE and hence the diffusion distances within the RVE. Additional kinetic effects are introduced by application of a dendrite arm coarsening model since diffusion distances evolve with time, and therefore, these are function of cooling conditions. The coarsening model implemented is limited to the effect of dendrite arm ripening on solidification. When considering two neighboring dendrite arms, one with a large radius R associated with the curvature C_R and a second with a small radius r associated with the curvature C_r , the undercooling ΔT_C between both arms is represented by the Gibbs-Thomson relation (2.11):

$$\Delta T_C = \frac{\gamma}{\Delta S_{L,S}} (C_R - C_r). \quad (4.19)$$

Kattamis et al. (KCF67) formulated the undercooling associated with a curved interface as concentration shift introducing the slope of the liquidus line m_i^L for a linearized two-component system. Beaverstock (Bea97) and Rappaz and Boettinger (RB99) applied this method to linearized multicomponent systems. This approach is adapted for use with the microsegregation model, but the phase diagram is linearized locally at each time step. Introducing the difference in concentration ${}_r x_i^L - {}_R x_i^L$ between two neighboring arms and the slope of the liquidus line yields:

$$\sum_{i=1}^n m_i^L ({}_r x_i^L - {}_R x_i^L) = \frac{\gamma}{\Delta S^{L,S}} (C_R - C_r). \quad (4.20)$$

From the balance equating the solute remelting flux of the smaller dendrite arm with the diffusive flux towards the larger dendrite arm over the distance λ and by approximating ${}_r x_i^L \approx x_i^L$ follows:

$$\frac{\partial r}{\partial t} \sum_{i=1}^n m_i^L (x_i^L - x_i^S) = \frac{1}{\lambda} \sum_{i=1}^n D_i^L m_i^L ({}_r x_i^L - {}_R x_i^L). \quad (4.21)$$

The curvature $C = (\tilde{g} - 1)/r$ depends on the geometry coefficient for coarsening \tilde{g} which equals in general the geometry coefficient g for diffusion. However, because of the mixed morphology model, the geometry coefficient for diffusion may be selected different from the purely dendritic geometry for coarsening. Comparing the term on the left in Eq. (4.20) with the sum on the right in the previous equation yields after rearrangement the shrinkage rate for the smaller dendrite arm:

$$\frac{\partial r}{\partial t} = \left(\frac{1}{R} - \frac{1}{r} \right) \frac{\gamma(\tilde{g} - 1)}{\lambda \Delta S^{L,S}} \sum_{i=1}^n \frac{D_i^L}{m_i^L (x_i^L - x_i^S)}. \quad (4.22)$$

Integrating this equation over the radius r of the smaller dendrite arm and applying the initial radius $r = r_0$ and final radius $r = 0$, the critical time t^{crit} is obtained at which the smaller dendrite arm is completely dissolved:

$$t^{crit} = \left[R^2 \ln \left(1 - \frac{r_0}{R} \right) + R r_0 \right] \frac{\lambda \Delta S^V}{\gamma(\tilde{g} - 1)} \sum_{i=1}^n \frac{m_i^L (x_i^L - x_i^S)}{D_i^L}. \quad (4.23)$$

When the correlation $R = (f^S)^{1/g} \lambda$ between the radius R of the larger dendrite arm, the fraction solid f^S , and the dendrite arm spacing λ is introduced follows:

$$t^{crit} = \left[\ln \left(1 - \frac{r_0}{R} \right) + \frac{r_0}{R} \right] \frac{\lambda^3 (f^S)^{2/g} \Delta S^V}{\gamma(\tilde{g} - 1)} \sum_{i=1}^n \frac{m_i^L (x_i^L - x_i^S)}{D_i^L}. \quad (4.24)$$

After rearranging this equation for λ^3 and the differentiation in time $\partial(\lambda^3)/\partial t$, the current dendrite arm spacing ${}_\nu \lambda$ is given in rate form as:

$$\begin{aligned} \nu\lambda &= \left(\omega\lambda^3 + \dot{\lambda}\partial t \right)^{\frac{1}{3}}, \text{ with} \\ \dot{\lambda} &= \frac{\gamma(\tilde{g} - 1)}{(f^S)^{2/g} \Delta S^{L,S} \left[\ln\left(1 - \frac{r_0}{R}\right) + \frac{r_0}{R} \right]} \sum_{i=1}^n \frac{D_i^L}{m_i^L (x_i^L - x_i^S)}. \end{aligned} \quad (4.25)$$

Because the smaller dendrite arm was integrated over the dissolution time, Eq. (4.25) consists only of quantities related to a physical meaning. Dendrite arm coarsening causes the liquid phase to grow in combination with the RVE by $\Delta l = \dot{\lambda}/2 \Delta t$. This is implemented applying an explicit formulation and has also impact on phase fractions:

$$\omega\tilde{f}^j = \omega f^j \frac{\omega l^g}{\nu l^g} \quad \text{and} \quad \omega\tilde{f}^L = \omega f^L \frac{\omega l^g}{\nu l^g} + \frac{\nu l^g - \omega l^g}{\nu l^g}. \quad (4.26)$$

Since also thermodynamic properties of the phase mixture are functions of phase fractions, these properties alternate accordingly. The energetic properties deduced from the phase fractions ωf without coarsening are transformed according to Eq. (4.37): $\omega S, \omega H, \omega C_p \rightarrow \omega\tilde{S}, \omega\tilde{H}, \omega\tilde{C}_p$ applying the modified phase fractions $\omega\tilde{f}$. When complete mixing in the liquid phase is assumed, the composition is additionally modified due to a change in liquid fraction by: $(\nu l^g - \omega l^g)/\nu l^g$. This involves the initial concentration x_i^0 in the alloy as follows:

$$\omega\tilde{x}_i^L = \frac{\omega x_i^L \omega f^L + x_i^0 \frac{\nu l^g - \omega l^g}{\nu l^g}}{\omega\tilde{f}_i^L}. \quad (4.27)$$

Otherwise, when final diffusion is selected for the liquid phase, the Neumann boundary condition $\hat{\mathbf{J}}_{i,w}^L$ according to Eq. (4.10) needs to be modified due to coarsening:

$$\tilde{\mathbf{J}}_{i,w}^L = \hat{\mathbf{J}}_{i,w}^L \frac{\nu l^g}{\omega l^g}. \quad (4.28)$$

4.4 Specific Quantities

All procedures in the microsegregation model use molar quantities. However, transformation into mass- or volume-specific quantities is necessary for user input and output, for example, when computing the length of an RVE due to shrinkage according to Eq. (4.32), or especially, when applying a specific heat extraction rate (cf. Chapter 4.6). For this purposes, the molar mass M_i of the component i , the molar volume v^j , or the density ρ^j of the phase j are required. It is possible to retrieve the molar mass from thermodynamic databases, while the retrieval of the molar volume is only possible, when volume data

were assessed to the database. Where required, instead of molar volumes, the density of phases may be specified by the user providing a density ρ^0 at reference temperature T^0 along with a volumetric expansion coefficient $\hat{\gamma}^j$ for each phase:

$$\rho = \rho^0 [1 - \hat{\gamma} (T - T^0)] . \quad (4.29)$$

The molar volume v^j and density ρ^j are interrelated since the product of both quantities is the average molar mass M^j of phase j . This molar mass is a function of the average molar concentration $\langle x_i \rangle^j$ and molar mass M_i of the associated elements:

$$M^j = v^j \rho^j = \sum_{i=1}^n \langle x_i \rangle^j M_i . \quad (4.30)$$

The weight-specific concentration w_i^j of component i in phase j is given by the weighted molar mass of i over the average molar mass of phase j :

$$w_i^j = x_i^j M_i / M^j . \quad (4.31)$$

Accordingly, the weight fraction f_W^j of phase j is given by the weighted molar mass of phase j over the total molar mass of the system, that is the weighted sum of all m solid phases and the liquid phase L . The conversion into volume fractions f_V^j is executed in a similar way by weighting over a the molar volume that changes with temperature and concentration. To deduce the volume fraction $f_{V^0}^j$ revealing solidification shrinkage due to phase, temperature, and concentration change, the referring molar volume v^0 is kept constant at a value referenced to the initial temperature T^0 :

$$f_W^j = \frac{f^j M^j}{\sum_{b=1}^{m+1} f^b M^b}, \quad f_V^j = \frac{f^j v^j}{\sum_{b=1}^{m+1} f^b v^b}, \quad f_{V^0}^j = \frac{f^j v^j}{v^0} . \quad (4.32)$$

Here, the upper bound includes all m solid phases and the liquid phase. The molar energetic quantities of phases are divided by the molar mass M^j or molar volume v^j to obtain weight-specific or volume-specific quantities, respectively:

$$\begin{aligned} S_W^j &= S^j / M^j, & H_W^j &= H^j / M^j, & C_{pW}^j &= C_p^j / M^j \\ S_V^j &= S^j / v^j, & H_V^j &= H^j / v^j, & C_{pV}^j &= C_p^j / v^j . \end{aligned} \quad (4.33)$$

4.5 Thermodynamic Calculations

4.5.1 TQ-Interface

To perform thermodynamic calculations during the runtime of the microsegregation software, Thermo-Calc is applied via the thermodynamic query interface (tq-interface) that is linked to the code as a shared library, as described by Sundman and Chen (SC). It is necessary to initialize the tq-interface by reading in a thermodynamic data file and performing an initial equilibrium calculation above liquidus temperature including all phases potentially precipitated. In this initial step, Thermo-Calc configures sublattices of phases and subsequently orders these phases due to Gibbs free energy.

4.5.2 Precipitation Simulation

For the species flux balance equation (4.8), equilibrium concentrations at the solid-liquid interface are required. These are obtained by precipitation simulations. For this step, a set of thermodynamic constraints is defined to reduce the number of degrees of freedom to zero according to Eq. (2.4). These equilibrium conditions are namely:

1. the constant pressure of $P = 1013.15$ hPa,
2. the total number of moles in the system $N^0 = 1$ mol,
3. the temperature T according to Section 4.6 and
4. the input composition \tilde{x}_i^L deduced from the concentration x_i^L of the liquid phase according to Eq. (4.34).

This input concentration equals the liquid concentration at the preceding time step ${}_{\omega}x_i^L$, but is further modified with respect to the absolute diffusive fluxes $\mathbf{J}_{i,e}^j$ into solid phases:

$$\tilde{x}_i^L = {}_{\omega}x_i^L + \sum_{j=1}^m \left[\mathbf{J}_{i,e}^j \theta \right]_{-\omega\theta}^{\omega\theta} \Delta t / {}_{\omega}f^L . \quad (4.34)$$

The interrelation between liquid input concentration and equilibrium concentration returned by Thermo-Calc is sketched in Fig. 4.6. On the left, the situation on solidification is illustrated for the diffusion phase α and the stoichiometric phase β , both phases grow simultaneously into the liquid phase L. As temperature decreases, the equilibrium concentrations at the $\alpha, \beta - L$ interface change. The diffusive flux \mathbf{J}_e^α into the α -phase impacts additionally the input composition \tilde{x}^L for Thermo-Calc (right). During equilibrium

calculations, the phase fractions for α , β , and L are systematically varied in combination with concentrations until a minimum in Gibbs free energy difference is reached. Based on these equilibrium concentrations, the current non-equilibrium phase fractions and local phase fractions are determined, as described in Section 4.3.3.

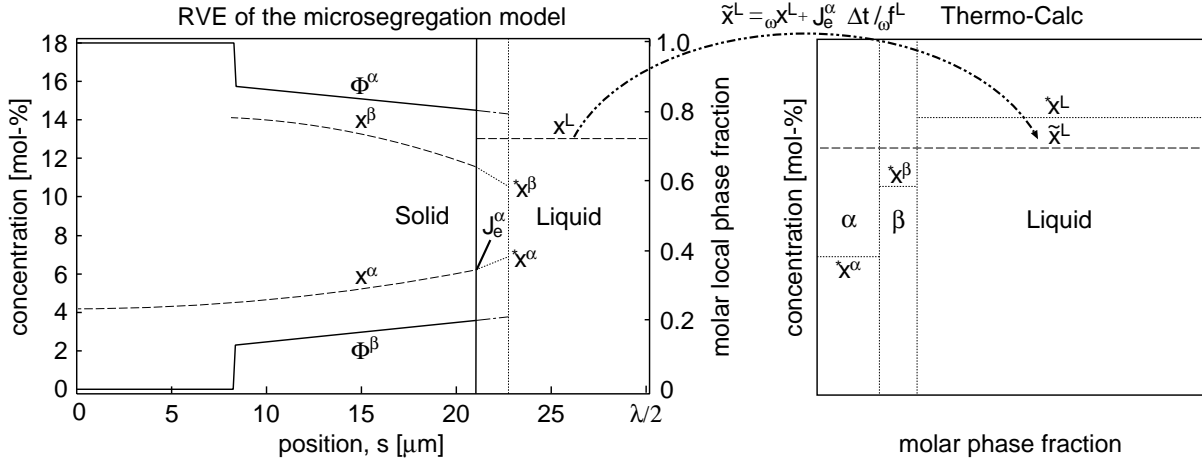


Fig. 4.6: Coupling of the microsegregation model to Thermo-Calc illustrating the interrelation between the input concentration \tilde{x}^L for Thermo-Calc and the equilibrium concentration *x returned for the microsegregation model.

Once the equilibrium concentrations are known, the concentration profiles are completed in the α - and β -phase by interpolating between the equilibrium concentration at the previous and current time step, as shown in Fig. 4.2 (a). In the case of the α -phase, a diffusion simulation is performed based on this profile. Diffusion defines the concentration gradient at the α -L interface and thus the diffusive flux into the α -phase according to Eq. (2.18). The new liquid concentration is in turn a function of the diffusive flux into the α -phase according to Eq. (4.9). Because of diffusion, the concentration in the liquid phase is usually different from the equilibrium concentration calculated.

In Section 4.8 a Gulliver-Scheil approximation is applied to estimate the change in phase fractions before the actual microsegregation simulation is performed. Behind this, is the interrelation between equilibrium phase fraction f_{EQ}^j and the change in phase fraction Δf_{GS}^j due to the Gulliver-Scheil approximation:

$$\Delta f_{GS}^j = f^L f_{EQ}^j \quad \text{and} \quad \Delta f_{GS}^L = - \sum_{j=1}^m \Delta f_{GS}^j. \quad (4.35)$$

Here, f^L refers to the current fraction liquid in the Gulliver-Scheil approximation or the microsegregation model, respectively.

4.5.3 Phase Activation

In precipitation simulations not all potential phases are included to save CPU time and to avoid distort equilibrium calculations due to inactive phases. Whether a phase is stable under the given constraints, or not, is evaluated determining the activation temperature for each potential phase. For this reason, the set of equilibrium conditions in Section 4.5.2 is modified by deleting the temperature condition 3 and by setting the number of moles to a small fixed number: $N^j = 1 \cdot 10^{-6}$ mol for each potential phase j . The result provides the activation temperature for each potential phase. When the activation temperature is smaller or equals the current temperature in the system, this phase is activated and included in the following precipitation simulations.

4.5.4 Thermodynamic Properties

After the iteration aiming for diffusion controlled phase fractions and phase concentrations (cf. Fig. E.1), thermodynamic properties are computed for the resulting phase mixture to solve the heat conservation equation. These properties are deduced for each individual phase by providing the average composition $\langle x_i \rangle^j$ of this phase and by successive small variations in temperature δT to gain numerical derivatives of the Gibbs free energy. The specific energetic quantities S^j , H^j , and C_p^j are given as direct or indirect functions of δG^j :

$$S^j = \frac{\delta G^j}{\delta T}, \quad H^j = G^j + T\delta S^j, \quad C_p^j = \frac{\delta H^j}{\delta T}. \quad (4.36)$$

It is also possible to retrieve these energetic quantities directly from the tq-interface, but the method introduced turned out to be more reliable. The integral energetic quantities are given applying the ideal mixture rule:

$$S = \sum_{j=1}^{m+1} S^j f^j, \quad H = \sum_{j=1}^{m+1} H^j f^j, \quad C_p = \sum_{j=1}^{m+1} C_p^j f^j. \quad (4.37)$$

Here, the index j includes all m solid phases and the liquid phase L. The latent heat of fusion L_f is given by the difference in enthalpy between the current ν and the preceding ω time step and by subtracting the contribution of heat capacity:

$$L_f = \nu H - \omega H - \nu C_p \Delta T. \quad (4.38)$$

When a potential phase becomes active or inactive, for example, when entering or leaving the mushy temperature range, the latent heat changes discontinuously and $\delta L_f / \delta T$

must be precalculated by estimating the subsequent iterated solution in order to avoid oscillations in temperature:

$$\frac{\delta L_f}{\delta T} = \sum_{j=1}^{m+1} H^j \frac{\delta f^j}{\delta T} - C_p^j \delta f^j . \quad (4.39)$$

The incremental change in phase fraction δf^j with temperature is estimated applying the Gulliver-Scheil approximation, as explained in Section 4.5.2. Otherwise, as long as no phase is activated nor deactivated, the function $\delta L_f/\delta T$ is considered to be continuous and approximated by an explicit formulation taking the values at the preceding time step.

4.6 Time-Temperature Correlation

To facilitate solidification from the liquid state, temperature needs to be reduced over time. Three different methods are implemented:

1. reading in a data file in which time and temperature are correlated in an arbitrary manner,
2. assuming a constant cooling rate and
3. assuming a constant specific heat extraction rate.

The first and second method are simple, whereas in the third method, temperature is deduced from the heat conservation equation (2.13). Heat capacity C_p and integral heat of fusion L_f are transformed into the same specific unit (cf. Section 4.4) as the user-defined specific heat rate \dot{h} . Therefore, the density ρ , appearing in the volume-specific heat conservation equation (2.13), is redundant. Heat diffusion and advection are not considered in this simple heat transport problem and thus the corresponding terms are omitted:

$$C_p \frac{\partial T}{\partial t} + L_f \frac{\partial f^S}{\partial t} = \dot{h} . \quad (4.40)$$

For process simulations the overall latent heat L_f , released over the complete mushy range, is in general reduced by the particular fraction solid Δf^S formed during a discrete time step Δt to obtain the latent heat being currently released. Since the overall latent heat is a priori unknown, in the present work the particular change in latent heat with temperature $\delta L_f/\delta T$ is used, according to Section 4.5.4. Because the heat conservation equation (4.40) is given in volume-specific, weight-specific, or a molar units, this equation only requires integration over time for discretization:

$$\left(C_p + \frac{\delta L_f}{\delta T} \right) \frac{\Delta T}{\Delta t} = \dot{h} . \quad (4.41)$$

After rearrangement of the discrete heat conservation equation, the new temperature ${}_{\nu}T$ is given by:

$${}_{\nu}T = {}_{\omega}T + \frac{\dot{h} \Delta t}{C_p + \frac{\delta L_f}{\delta T}} . \quad (4.42)$$

If, for example, a new phase is activated at the temperature T_{act} , that is in the range $\Delta T = {}_{\nu}T - {}_{\omega}T$, the change in latent heat $\delta L_f/\delta T$ is contributed by two terms: one above activation temperature ${}_{\omega}(\delta L_f/\delta T)$ and a second below activation temperature ${}_{\nu}(\delta L_f/\delta T)$:

$$\frac{\delta L_f}{\delta T} = \frac{{}_{\omega}\left(\frac{\delta L_f}{\delta T}\right) (T_{\text{act}} - {}_{\omega}T) + {}_{\nu}\left(\frac{\delta L_f}{\delta T}\right) ({}_{\nu}T - T_{\text{act}})}{{}_{\nu}T - {}_{\omega}T} . \quad (4.43)$$

Casting this equation into Eq. (4.41) yields after rearrangement for the new temperature:

$${}_{\nu}T = \frac{{}_{\omega}T \left[C_p + {}_{\omega}\left(\frac{\delta L_f}{\delta T}\right) \right] + T_{\text{act}} \left[{}_{\nu}\left(\frac{\delta L_f}{\delta T}\right) - {}_{\omega}\left(\frac{\delta L_f}{\delta T}\right) \right] + \dot{h} \Delta t}{C_p + {}_{\nu}\left(\frac{\delta L_f}{\delta T}\right)} . \quad (4.44)$$

When the condition: ${}_{\nu}(\delta L_f/\delta T) = {}_{\omega}(\delta L_f/\delta T)$ is fulfilled, Eq. (4.44) reduces to Eq. (4.42) since neither phase is activated nor deactivated.

4.7 Graphical Frontend

The graphical frontend is an interface between a user and the microsegregation software. The frontend is used on preprocessing to generate a file containing all necessary data for running a simulation. The structure of the frontend consists of five tabs:

1. initial conditions,
2. phase-specific data,
3. boundary and runtime conditions,
4. geometry and
5. output definitions.

Phase definitions and other specifications require an interaction between graphical frontend, which is implemented using the programming language QT4, and the tq-interface of Thermo-Calc, that is included via an F77 library. To enable communication between

the two software parts, a F90 / C⁺⁺ interface has been created. When the software is invoked without nominating a data file, the graphical frontend is started, as pointed out in the structure chart of the main routine Fig. E.1. Structure chart Fig. E.2 reveals the interaction between user and thermodynamic software. The user is requested to specify a thermodynamic data file to initialize the tq-interface. This file contains binary data and is generated by Thermo-Calc applying the Gibbs Energy System (GES) module along with a thermodynamic and mobility database. For simulation, thermodynamic data and mobility data are merged into one GES file. Further input in tab 1 is the base alloying element, initial composition, initial temperature, and termination temperature. This user information is forwarded to the microsegregation software via the F90 / C⁺⁺ interface to perform a one-dimensional phase mapping. This means, the temperature is consecutively decreased and active phases are selected to provide a reasonable preselection of potential phases for a subsequent microsegregation simulation. In tab 2, the user is prompted to nominate an initial matrix phase, for example, the liquid phase. Additional phases may be selected or preselected phases rejected. When a phase is selected, stoichiometries and molar masses are retrieved from the tq-interface. At the same time, the GES file is checked for volume and mobility data. If these are not included, the user is requested to provide density and diffusion data. In tab 3, boundary conditions for diffusion simulation along with time step width, type of time-temperature correlation, an underincrementation factor, and an underrelaxation factor are to be provided. Geometry, initial size of the RVE, and initial number of finite volume elements are specified in tab 4. If dendrite arm coarsening is requested, the initial size and the number of volume elements within the RVE may increase. In this case also an interface energy between coarsening and liquid phase is required. In tab 5, the user specifies output units, output frequency, and a number of options for results and presentation applying Gnuplot³. Gnuplot is implemented via a C-interface for creating graphical results on run-time and postprocessing.

4.8 Solution Algorithm

During main processing the various models and equations are processed in a certain sequence and under certain conditions so as to solve the so-called Stefan problem (Ste99). The solution of this problem requires solving the transient species transport problem in an expanding solid phase region where the position of the boundary is part of the solution.

The actual main processing starts according to Fig. E.1 after preprocessing by reading in a data file for simulation and initialization of global variables. In a loop over the time in discrete steps, time is correlated with temperature according to Section 4.6 or, alternatively, the temperature is forwarded to the microsegregation software from the process simulation in each reference element, as described in Section 4.9. A set of variables

³Copyright (C) 1986 - 1993, 1998, 2004, 2007 Thomas Williams, Colin Kelley

containing information about the previous time step is saved for subsequent use. The solidification state is classified as liquid, mushy, or solid and preselected by the current temperature and fraction liquid. Below liquidus temperature and above the a priori unknown solidification temperature, the solidification module is invoked, as described in the following paragraph. Afterwards, the average concentrations are determined by numerical integration in every phase and weighted by the corresponding phase fractions to deduce a checksum error according to Eq. (4.6). This error represents the quality of the overall solution. Average concentrations, phase fractions, and molar energetic quantities, resulting from Eqs. (4.36 - 4.38), are converted into a user-defined output unit by using Eq. (4.31), Eq. (4.32), and Eq. (4.33), respectively. These quantities are required to determine the enthalpy change with temperature (cf. Section 4.5.4) for the heat conservation equation (cf. Section 4.6). At the end of a time-loop, results are written to screen, files, diagrams, or passed to process simulation to simulate the temperature field at the subsequent time step.

On solidification liquid composition not only changes due to thermodynamics, but also due to diffusion. This is considered manipulating the input concentrations according to Eq. (4.34) for subsequent thermodynamic calculations (cf. Section 4.5.2), as shown in structure chart Fig. E.3. Applying these concentrations, potential phases are checked for their corresponding activation temperature and change in phase fraction, which is estimated applying the Gulliver-Scheil approximation (4.35). If phase change exceeds a certain limit, then the time and thus also the temperature interval is sub-divided, and an internal time-loop is initiated. When the activation temperature of a phase is in between that of the current and the preceding time step, this phase is activated. For an iteration, the corresponding variables are initialized and diffusion coefficients are retrieved from thermodynamic databases. When mobilities are not appended to the GES file, diffusion coefficients are computed according to the specifications made by the user on preprocessing. At each time step, an iteration is invoked to identify the current phase fraction which depends on the amount of solute diffusion into mixture phases. Multiphase equilibrium simulations are executed applying the tq-interface, as described in Section 4.5.2, to simulate the solid-liquid interface concentrations based on the ambient pressure, current temperature, and manipulated liquid composition. This composition and the current concentration gradients, evaluated at the solid-liquid interface according to Section C.2, are used to assign flux balance equations (4.8). This overdetermined system of flux balance equations is solved by application of a Householder algorithm (Hou58) according to Fig. E.4. This procedure yields the change in phase fractions and thus the position of the solid-liquid interface according to Eq. (4.17) and the local phase fractions according to Eq. (4.1). In the newly solidified volume, concentrations are interpolated using the equilibrium interface concentrations which also serve as Dirichlet boundary conditions to compute the species transport according to Fig. E.5. If complete mixing is assumed in the liquid phase, a uniform concentration is determined according to Eq.

(4.9) and assigned to finite volume elements in the liquid phase region. The iteration is exited when the liquid concentration x_i^L of the depending species i and the change in liquid fraction Δf^L converge according to the following termination criteria:

$$\epsilon_x \geq |x_i^L - x_{i,\text{iter}}^L| / |x_{i,\text{iter}}^L| \quad \text{and} \quad \epsilon_f \geq |\Delta f^L - \Delta f_{\text{iter}}^L| / |\Delta f_{\text{iter}}^L|. \quad (4.45)$$

Here, ϵ_x and ϵ_f are sufficiently small numbers and the index “iter” indicates values at the previous iteration. In the case of complete mixing in the liquid phase, dendrite arm coarsening is determined by solving Eq. (4.25), and phase fractions are modified according to Eq. (4.26) along with liquid concentrations according to Eq. (4.27) which are assigned to the corresponding volume elements. If, otherwise, final diffusion is to be simulated in the liquid phase, first a Neumann flux into the liquid phase is computed according to Eq. (4.10). This flux is modified according to Eq. (4.28) in the case of dendrite arm coarsening. Subsequently, diffusion in the liquid phase is simulated again, but applying the particular Neumann boundary condition (4.10) at the solid-liquid interface to correct the liquid concentrations for the inequality of chemical fluxes into mixture phases.

4.9 Coupling to Process Simulation

The microsegregation model is directly coupled to the temperature solver of the commercial process simulation tool MAGMASOFT⁴ (Stu04). Direct coupling means, both codes interact on runtime exchanging results. Moreover, these results are interdependent. For the given problem, the local properties of the solid-liquid phase mixture, the temperature field, as well as the time step width are exchanged. Local properties are density, heat capacity, latent heat of fusion, and fraction solid, which are derived from the mixture of individual phases with respect to the average composition, as explained in Section 4.5.4 and 4.4. Coupling to the temperature solver requires density, heat capacity, and latent heat of fusion, while this solver provides in return the temperature at each finite volume element. The local cooling characteristic defines the development of phase fractions and therefore also the properties of the phase mixture which is forwarded at each time step. Coupling to the algorithm for porosity prediction requires local density and fraction solid, as determined by the microsegregation model and provided via the same interface.

MAGMASOFT applies an FVM discretization which results in a large number of volume elements. It is almost impossible to simulate the precipitation kinetics of phases at each such volume element for industrial castings within a reasonable time. Therefore, a scheme has been developed consisting of *reference elements*, for which microsegregation simulations are actually carried out, while for the remaining elements, called

⁴MAGMASOFT is a registered trademark of Magma Gießereitechnologie GmbH, Aachen, Germany

interpolation elements, an interpolation of all necessary thermodynamic data over temperature or time is executed. The required steps of this concept are:

1. Definition of reference elements above liquidus temperature by a preferably homogeneous distribution in terms of temperature differences between reference elements. Below liquidus temperature the reference elements are fixed.
2. Saving the thermodynamic properties (f^j , H , C_p , ρ) of the phase mixture with temperature and solidification time at each reference element. *Solidification time* refers to the time elapsed once the liquidus temperature has been reached.
3. The incremental change in properties at interpolation elements is determined by interpolation between the nearest neighboring reference elements. When the slope of change with temperature becomes too steep, the properties of each reference element are assumed to change with time instead. The nearest neighbors are selected by similarity criteria relating to temperature, solidification time, and liquid fraction since the assignment of thermophysical data is not necessarily unique. Furthermore, a variable is defined reflecting the number of phases currently precipitated from the liquid phase by a prime factor. This is required for the interpolation over temperature since properties may change discontinuously when a phase is activated or deactivated.
4. An internal time-loop has been implemented to pass over reference elements or to add additional time steps if necessary.

The coupling procedure between process and microsegregation simulation is represented by Fig. E.7 and consists of four interfaces between the two software products. After invocation of process simulation, the first interface is used to initialize variables for coupling assuming a predefined number of potential reference elements. The thermodynamic properties of the liquid phase H , C_p , and ρ are precalculated for one reference element and afterwards assigned to all other reference elements as a function of temperature only. During a time-loop initiated by process simulation, the second interface is invoked. The properties $\delta L_f/\delta T$, C_p , ρ , and f at each macroscopic volume element are determined, and the time step width Δt for process simulation is manipulated with respect to the fastest cooling volume element. These properties result from the interpolation scheme described above by looping over both reference elements and interpolation elements. Furthermore, for the selection of appropriate reference elements, similarity criteria are applied regarding temperature T , fraction liquid f^L , and liquidus time t^L . This enables the temperature solver to predict the new temperature ${}_\nu T$ by solving a conservation equation of energy similar to Eq. (2.13). The new temperature is then forwarded to a third interface, where it is corrected according to Eq. (4.44) in the case the solidification state changes at a volume element. Simultaneously, volume elements are sorted by temperature. In a loop over this sorted list of volume elements, the number of fixed reference elements is determined. A

reference element is called *fixed* when its temperature is below liquidus temperature. The remaining number of reference elements is distributed in equidistant steps in the range above liquidus temperature. In a loop over a list of reference elements sorted by temperature, microsegregation simulations are executed at each reference element using a side entrance and exit, as remarked in the structure chart Fig. E.1. This loop is cycled when the absolute difference in temperature is too small, and, at the same time, the change in fraction liquid with temperature is too small. Otherwise, when the absolute change in temperature is above a critical value, the time step width and therefore also the change in temperature are sub-divided. To minimize the number of sub-divisions, the time step width is manipulated before the actual temperature solution in the second interface with respect to the fastest cooling volume element. The resulting properties are saved with temperature and time along with a state variable that represents the solidification state by a prime factor mirroring the number of active phases. The time-loop is terminated when the volume element with the highest temperature is below the termination temperature. Result files are written and closed in the fourth interface.

4.10 Postprocessing

As mentioned in Section 4.7, the graphical representation of concentration profiles, phase fractions, thermodynamic quantities, cooling curves, or supplementary data is realized applying Gnuplot macros that are generated and saved during the runtime of the microsegregation software. These macros and the resulting plots may be further modified and exported in various formats to match the requirements of the user. The microsegregation profiles and local phase fractions are saved at defined time moments, temperatures, or phase fractions for each phase precipitated. Phase fractions, density, enthalpy, entropy, and heat capacity are saved in a data file as functions of temperature and time in a user-defined output unit. At the end of this file, solidification time, latent heat of fusion, and dendrite arm spacing are listed. In addition, a tool has been programmed for decoupled simulations extracting thermophysical properties from this data file and processing these data in an automated manner to produce files formatted specifically for simple import into the process simulation tool.

In the case the microsegregation software is directly coupled to the process simulation, additional result files are generated for the postprocessor of the process simulation software. These result files comprise the distribution of quantities in a casting, such as dendrite arm spacing, phase fractions, local solidification time, and local solidification temperature. Furthermore, based on fraction solid and density data, as provided by the microsegregation software, porosity is predicted applying a feature of the process simulation tool.

5. Experiments and Evaluation

5.1 Objectives

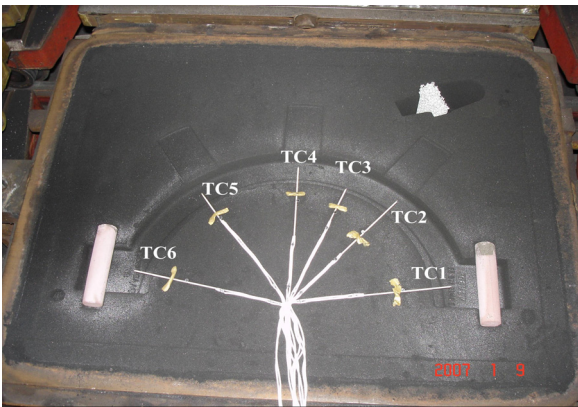
This Chapter reports about the production of a clamp-ring casting and subsequent analyses to obtain input and validation data for the microsegregation software presented. Section 5.2 describes the four variants of castings along with temperature measurement. To provide accurate chemical input data for the microsegregation model, chemical analyses were carried out applying three different methods, as described in Section 5.3. Moreover, in Section 5.4, the microstructure of the casting is characterized and needs to be provided as input for the microsegregation model. Since the eutectic temperature obtained from thermocouples and that resulting from thermodynamic calculations mismatch, DTA measurements were carried out, as explained in Section 5.5. Since phase characterization and microsegregation measurement applying EDX produced only qualitative results, as reported in Section 5.6, EPM analysis was additionally executed, as described in Section 5.7. To validate porosity predictions, the clamp-rings were successively cut and x-rayed, as shown in Section 5.8.

5.2 Production of Castings

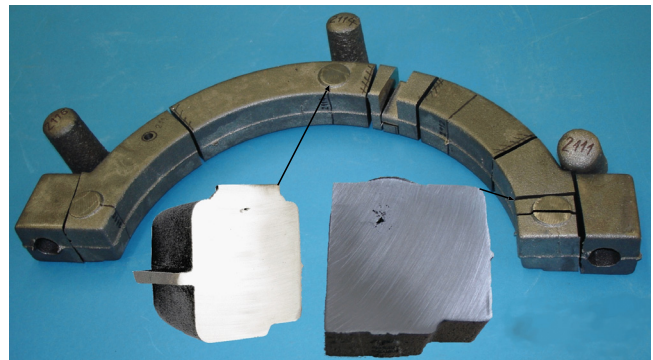
A series of eight clamp-rings made of GJSA-XNiCr20-2 was cast in a foundry under production conditions with variation of the inoculation state and the number of feeders, i.e. the central feeder was omitted for four castings. Fig. 5.1 (a) shows the drag of a green sand mold. Thermocouples of type S were used to record cooling curves at positions 1 through 6. The initial casting temperature in the case of the first, good inoculation treatment (castings c_a - c_d) was 1403°C , and in the case of the second, poor inoculation treatment (castings c_e - c_h) 1425°C . The castings c_a , c_b , c_e , and c_f were produced using all three feeders, whereas c_c , c_d , c_g , and c_h with only two feeders. In Fig. 5.1 (b) clamp-ring c_b is photographed together with a magnified cross-section at the right flange where porosity was detected. Porosity was also found at its counterpart to the left and, less pronounced, directly below the neck of the central feeder.

There is some doubt, whether the asymmetrically designed gating system impacts

the symmetry of cooling on solidification or not. Since symmetry is presumed for coupled simulations in Section 6.5, this topic is discussed in that section. Fig. 5.2 (a) shows cooling curves at the symmetrical positions TC1 and TC6 placed in the castings c_a through c_d below the feeder at the left or the right flange, respectively. The castings were consecutively cast using the same recording device and one time line. The decreasing casting temperature is correlated to a decreasing peak value measured at the flange. The thermocouples in castings c_b and c_d indicate a symmetrical solidification behavior, whereas the thermocouples in casting c_c don't. Thermocouple TC6 in casting c_a had a loose contact. Asymmetric cooling in the case of casting c_c is probably a consequence of displaced thermocouples. In Fig. 5.2 (b) the experiments c_f and c_g show symmetry of cooling, while in the case of casting c_e thermocouples seem to be inverted. With regard to casting c_g , molding material apparently broke off at both of the flanges, and, therefore, cooling is different. Thermocouple TC1 in clamp-ring c_h seems to be defective or encapsulated by a gas pocket. All in all, symmetry of cooling may be presumed. Furthermore, it is noted that none of the exothermic feeders ignited to provide external heat.



(a)



(b)

Fig. 5.1: (a) Drag of a green sand mold with thermocouples of type S numbered from 1-6 and (b) GJSA-XNiCr20-2 casting c_b with cut-off feeders and two magnified porous cross-sections, one below the central feeder and one below the feeder at the right flange.

The castings c_a through c_f were taken into account to evaluate the non-equilibrium eutectic temperature. For this purpose, eutectic temperatures were averaged over the cooling curves measured, as shown in Fig. 5.2. If the respective cooling curve indicates a clear breakpoint on nucleation, this temperature was considered and, else, the beginning of the meniscus at the eutectic breakpoint. Averaging the thus obtained eutectic temperatures yields approx. 1190°C .

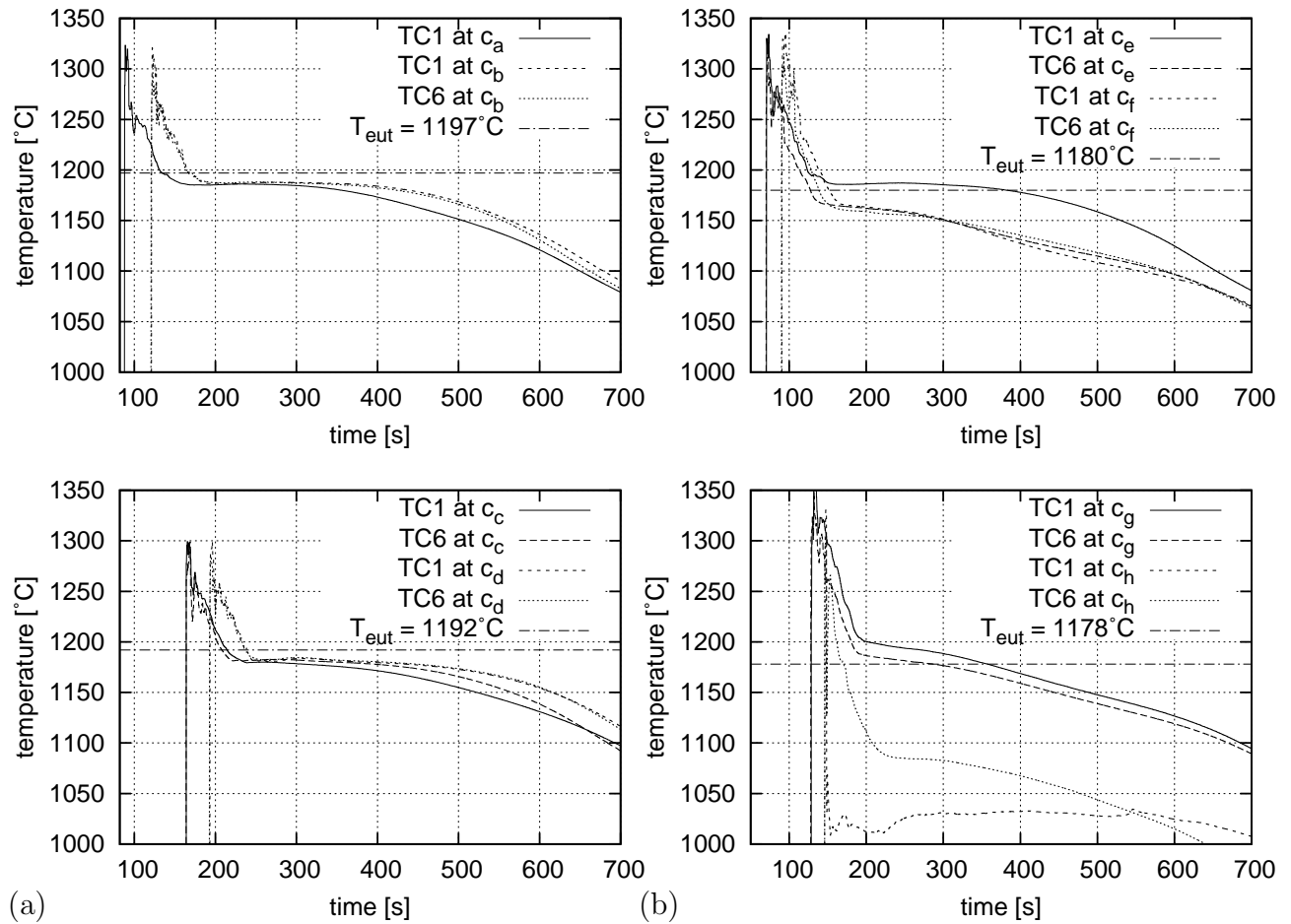


Fig. 5.2: Cooling curves in castings $c_a - c_h$ at TC1 and TC6 indicating, in general, symmetry of cooling.

5.3 Chemical Analysis

Composition analyses were executed using various methods summarized in Tab. 5.1. Coin samples were chilled for optical emission spectrometry (OES), while for inductively coupled plasma (ICP), infrared (IR), and gravimetric analysis samples or drilling chips from casting c_b were retained. Regarding the second method in Tab. 5.1, carbon and sulfur were measured applying IR; manganese, phosphorus, chromium, nickel, and magnesium using ICP; and silicon was analyzed gravimetrically. However, the analyses showed inconsistency, leading to an uncertainty about alloy composition, as quantified by the root mean square deviation (RMSD).

5.4 Microstructure Characterization

In Fig. 5.3 (a) a polished and etched sample is presented, cut from below the feeder at the left flange of clamp-ring c_b . The microstructure in this casting was analyzed along

Tab. 5.1: Comparison of various analyses of the same cast alloy. The values are given in wt.-%.

method	Ni	C	Si	Mn	Cr	P	S	Mg
1. OES	20.90	2.66	2.46	1.28	1.22	0.01	0.00	0.04
2. ICP, IR, grav.	20.10	2.80	2.76	1.20	1.00	0.01	0.01	0.05
3. grav.	20.60	2.90	2.53	1.14	1.08	<0.05	0.02	0.05
average value	20.53	2.78	2.58	1.21	1.10	0.01	0.01	0.05
RMSD	0.40	0.13	0.16	0.07	0.11	0.00	0.01	0.01

the horizontal and vertical line as indicated by taking the pictures 1 through 16 and 18 through 35, respectively. Three distinct zones A, B, and C were identifiable. In chill zone A, at the rim of the sample, a clearly globular eutectic morphology formed in an austenite matrix containing well-distributed small carbides and some chunky graphite, as shown in Fig. 5.3 (b). Zone B and C mainly consist of austenitic dendrites surrounded by chunky graphite and a small number of large areas of carbides. Sometimes, islands of eutectic grains appear in zone B and C, as can be seen in Fig. 5.3 (c). Zone C also includes shrinkage porosity.

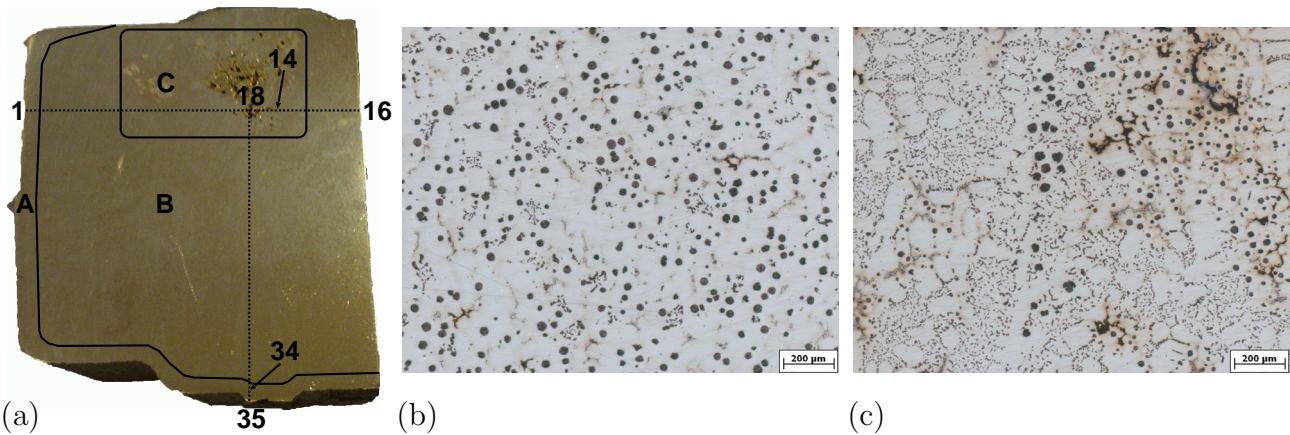


Fig. 5.3: (a) A polished and etched sample retained from clamp-ring c_b below the feeder at the left flange. (b) Microstructure in zone A (picture 34) and (c) in zone C (picture 14).

5.5 Differential Thermal Analysis

Drilling chips were retained from casting c_a for differential thermal analysis (DTA). Averaged transformation temperatures were evaluated from three DTA cycles for cooling at a rate of $10^\circ\text{C}/\text{min}$, as shown in Fig. 5.4. For the three cooling cycles, the non-equilibrium eutectic temperature is approx. 1202°C and solidification temperature approx. 1134°C . A fraction solid curve was estimated from the relative fraction of latent heat released on cooling averaging the three cycles. However, the eutectic temperature rises with every

cycle by approx. 5°C which means, the sample was losing carbon on processing, even though argon was used as an inert gas. With respect to this effect, a linear extrapolation of the non-equilibrium eutectic temperatures to the state on solidification of the clamping yields the actual non-equilibrium eutectic temperature in the range between 1185°C and 1195°C .

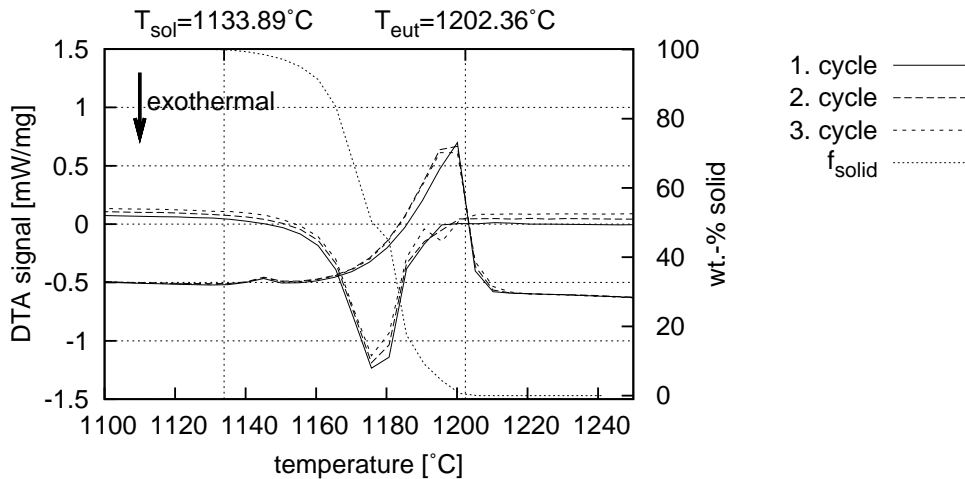


Fig. 5.4: DTA analysis of drilling chips retained from casting c_a . Three cycles of heating and cooling were run. The average values of the non-equilibrium liquidus and solidification temperature are indicated. The fraction solid curve was estimated from the relative fraction of latent heat released on solidification.

5.6 Electron Dispersive X-Ray Analysis

Fig. 5.5 (a) shows the micrograph of a eutectic cell containing different phases using scanning electron microscopy (SEM). The sample shown was retained from clamp-ring c_a in proximity of the right flange. To identify the phases precipitated on solidification and to carry out the line scan indicated, electron dispersive x-ray (EDX) was calibrated using a reference sample to improve quantitative analysis for carbon. However, it turned out, that this method is not quantitative for carbon analysis, and the compositions analyzed for the unknown phases UP1 and UP2 are not suitable for identifying possible stoichiometries. Nevertheless, contrast differences among the phases clearly indicate different compositions of the C-Ni-Si-Mg rich phase UP1 and the C-Fe-Ni-Mg rich phase UP2. According to Fig. 3.1 (b) also martensite may form on cooling of austenitic cast iron. In proximity of UP1 and UP2 a second mixture phase formed, that is most likely martensite because it contains more chromium and manganese than the austenite matrix. Assumed by contrast, the phase mixture at top of Fig. 5.5 consists of the same phases, but on a length scale being too small for EDX analysis.

Concentrations were measured in this eutectic cell along the line indicated in Fig. 5.5 (a). The step size for EDX analysis was $2\ \mu\text{m}$. The measurements start in graphite, pass

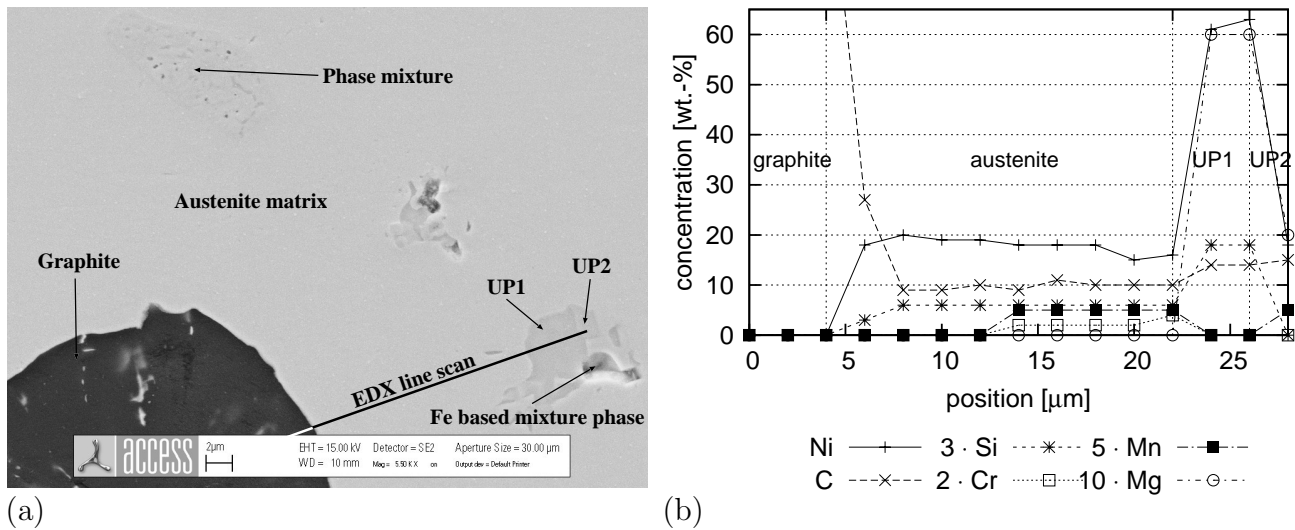


Fig. 5.5: (a) SEM micrograph with different phases and (b) EDX line scan. To improve the clarity of the diagram, some concentrations are multiplied by a fixed factor provided in the legend.

through austenite, the first unknown phase, and end in the second unknown phase. Fig. 5.5 (b) shows that nickel segregates inversely, while the other elements segregate forming a positive gradient, except for silicon, revealing a uniform concentration in austenite. In spite of EDX calibration, the carbon concentration in austenite even exceeds the initial concentration in the alloy given in Tab. 5.1. Therefore, EDX results are only usable for qualitative validation.

5.7 Electron Probe Micro Analysis

For quantitative carbon analysis and phase identification, the same sample as for EDX was analyzed using electron probe micro analysis (EPMA), that is based on wave length dispersive x-ray (WDX). An element distribution in the microstructure of a eutectic region was measured, as shown in Fig. 5.6. This finely structured eutectic area is a mixture of eutectic austenite, chunky graphite, a silicide and M_7C_3 where M can be iron, chromium, or manganese. The eutectic region is enclosed by the austenite matrix. A backscattering electron picture (Fig. 5.7) of the same area displays two line scans A and B. Linescan B in Fig. 5.8 (b) passes through austenite, the finely structured eutectic region, M_7C_3 , again a mixed region, and ends in silicide. Linescan B provides the composition of silicide and M_7C_3 . Both are given in Tab. 5.2 along with the average concentrations in austenite and graphite. Quantitative carbon analysis is only given for low carbon concentrations, at which EPMA was optimized. This optimization was carried out using reference samples of cementite for which reason the carbon concentration in graphite is way too low.

Tab. 5.2: Average composition [mol-%] of phases deduced from Linescan A and B, as shown in Fig. 5.8.

	Fe	Ni	C	Si	Mn	Cr	Mg
Austenite	71.36	14.33	3.36	5.48	2.41	2.94	0.12
Graphite	4.15	2.10	92.69	0.51	0.25	0.30	0.00
M7C3	58.47	2.98	27.07	0.72	3.31	6.74	0.72
Silicide	6.77	46.50	0.54	10.79	0.77	0.29	34.34

The microsegregation profile of nickel in austenite, represented by line scan A in Fig. 5.8 (a), shows a negative slope due to inverse segregation, while the slope of other alloying elements is positive, except for silicon, which appears to be homogeneously distributed in austenite. This has already been concluded evaluating the EDX results in Section 5.6.

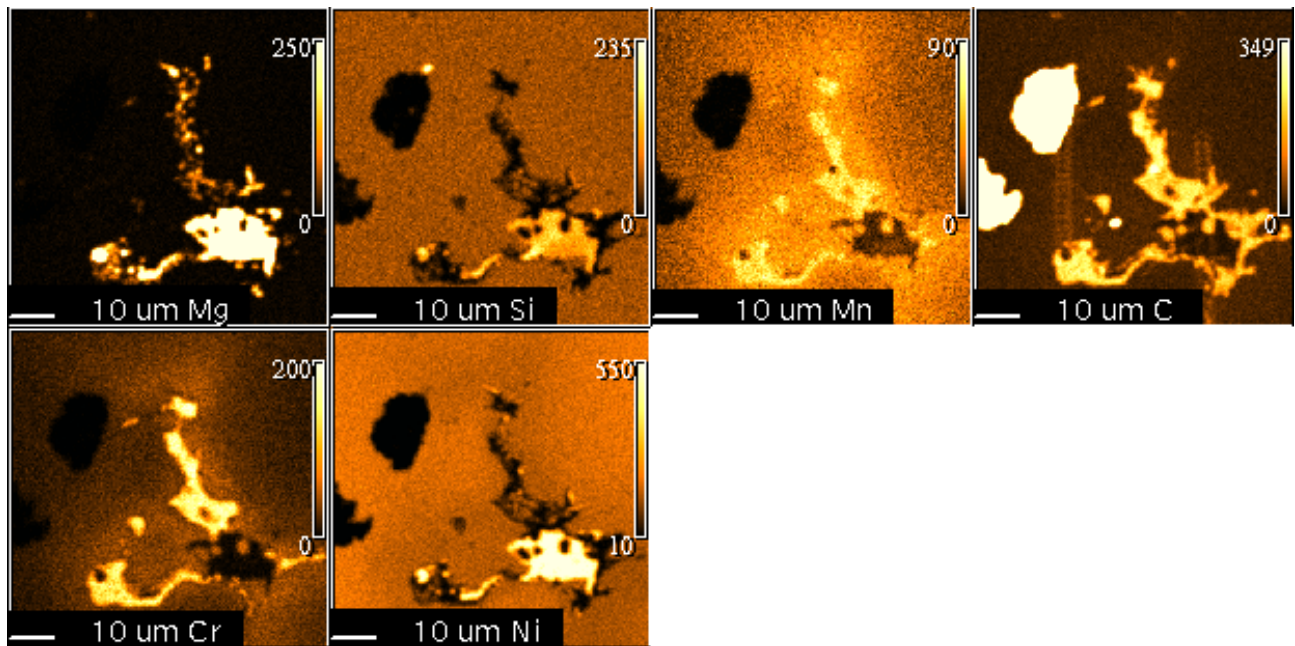


Fig. 5.6: Element distribution in a segregation-enriched zone. The charts represent the element intensity given in counts per second.

5.8 X-Ray Analysis

The castings c_a , c_c , c_d , c_f , c_g , and c_h were consecutively cut into slices using a water-jet cutter. Porosity found below the feeders of casting c_b is shown in Fig. 5.1 (b). To locate shrinkage porosity, the cut samples were x-rayed, and samples containing porosity are shown to point out the level of occurrence. Locations where porosity was detected are

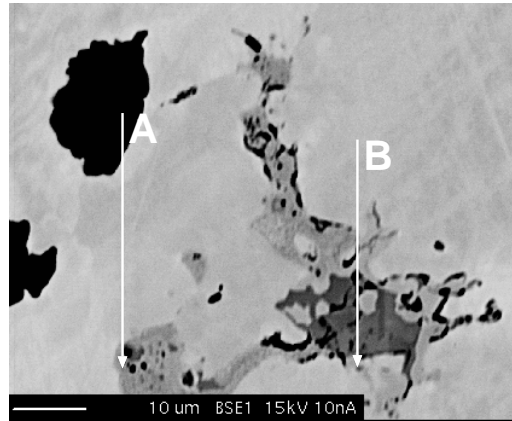


Fig. 5.7: SEM micrograph of a eutectic region indicating line scan A and B, as shown in Fig. 5.8 (a) and (b), respectively.

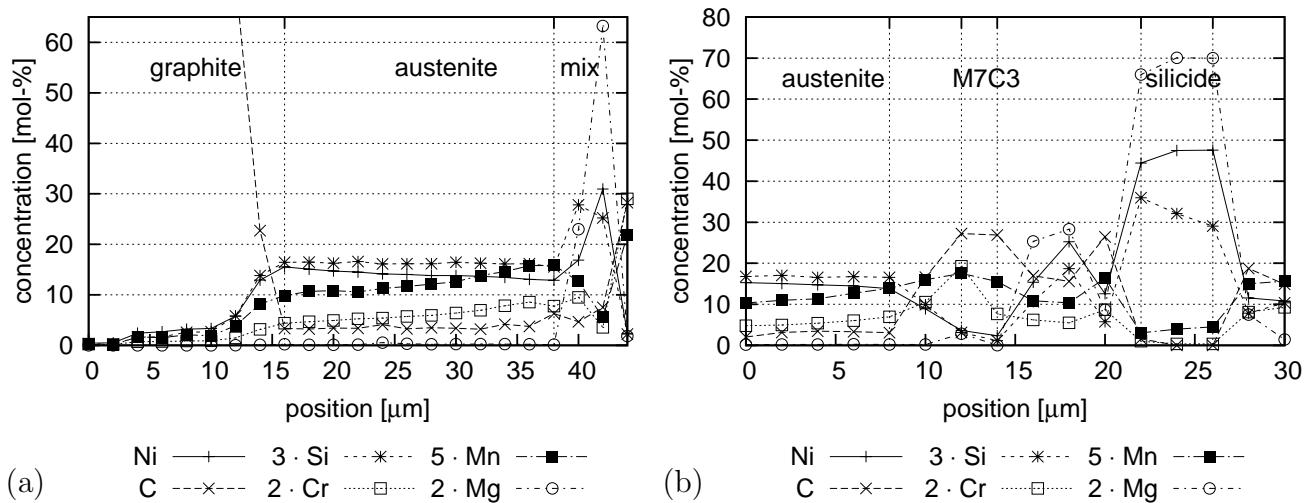


Fig. 5.8: (a) EPMA line scan A and (b) line scan B in a eutectic region, as indicated in Fig. 5.7. To improve the clarity of the diagram, some concentrations are multiplied by a fixed factor provided in the legend.

labeled A through D. When the porous area was not found in the particular casting, the corresponding label is omitted. Locations containing porosity are additionally marked black on each casting for better comparison with simulated results. In the case of casting c_a in Fig. 5.9 (a) porosity D was found directly below the feeder at the flange and porosity B, less pronounced, in proximity of the ingate. Unlike clamp-ring c_b in Fig. 5.1 (b), porosity A within the central feeder is not ranging into the casting c_a . Casting c_f in Fig. 5.9 (b), which was inoculated poorly, includes a small amount of porosity at position A and B, while both are continuous. Porosity C is also found in casting c_f along with a large cavity at location D, which is below the feeder at the flange.

Casting c_c was cast omitting the central feeder, as shown in Fig. 5.10 (a). A massive shrinkage cavity formed at location A, while the porous locations B and C shift towards the flange and D towards the ring. In the case of clamp-ring c_d in Fig. 5.10 (b), a severe

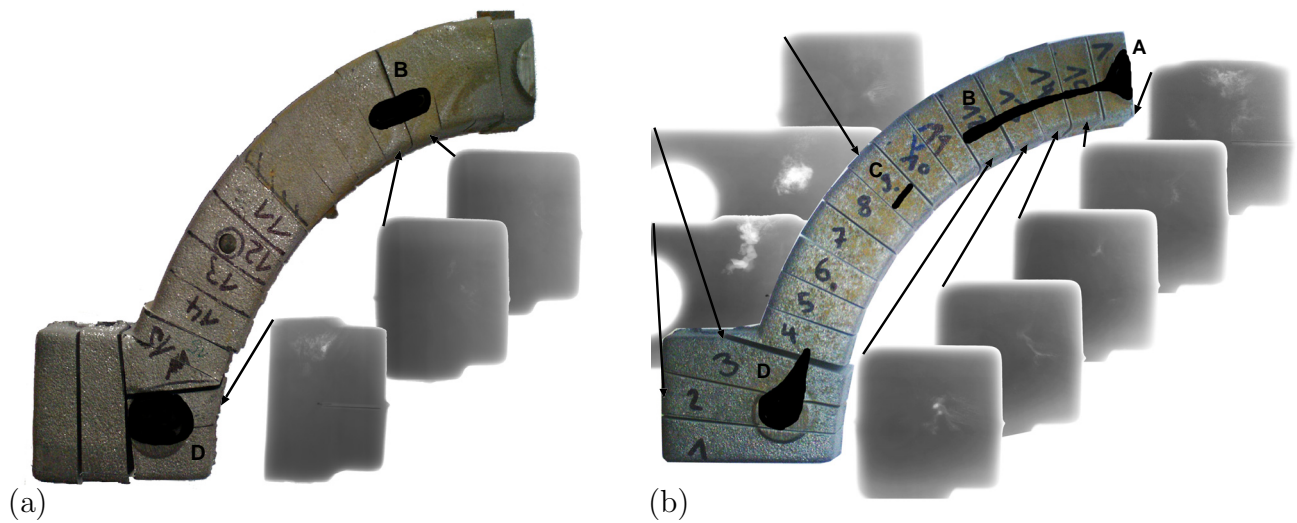


Fig. 5.9: (a) One half of casting c_a cut into 18 slices and (b) casting c_f cut into 16 slices, both with central feeder. The slices were x-rayed to locate porosity as shown. For better comparison with simulated results, porosity locations are marked black at the castings.

shrinkage cavity formed at location D. When compared to casting c_c , porosity A, B, and C appear less pronounced and distributed along the center line. The overall porosity in regions A, B, C, and D in clamp-ring c_g in Fig. 5.11 (a) extends in a similar way as in casting c_c , but the location of porosity is shifted. Casting c_g is falsified due to molding material break-off at the left flange, as can be seen at the right upper corner of the second sample. Curiously, this also happened at the right flange of this casting. The level of porosity occurring in casting c_h in Fig. 5.11 (b) is in between that of casting c_c and c_d .

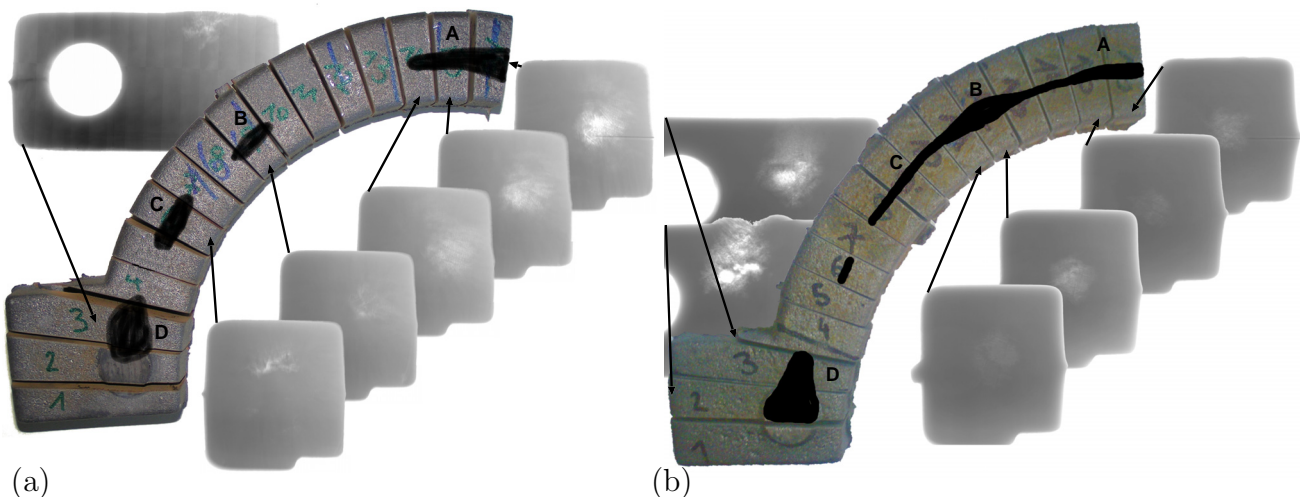


Fig. 5.10: (a) One half of casting c_c and (b) casting c_d . Both were cut into 16 slices and have no central feeder. The slices were x-rayed to locate porosity as shown. For better comparison with simulated results, locations containing porosity are marked black at the castings.

Summarizing this experiment, firstly, porosity at location D was detected in all cases. In the castings c_a , c_c , c_g and c_h this porosity is of medium extend, while the castings c_d

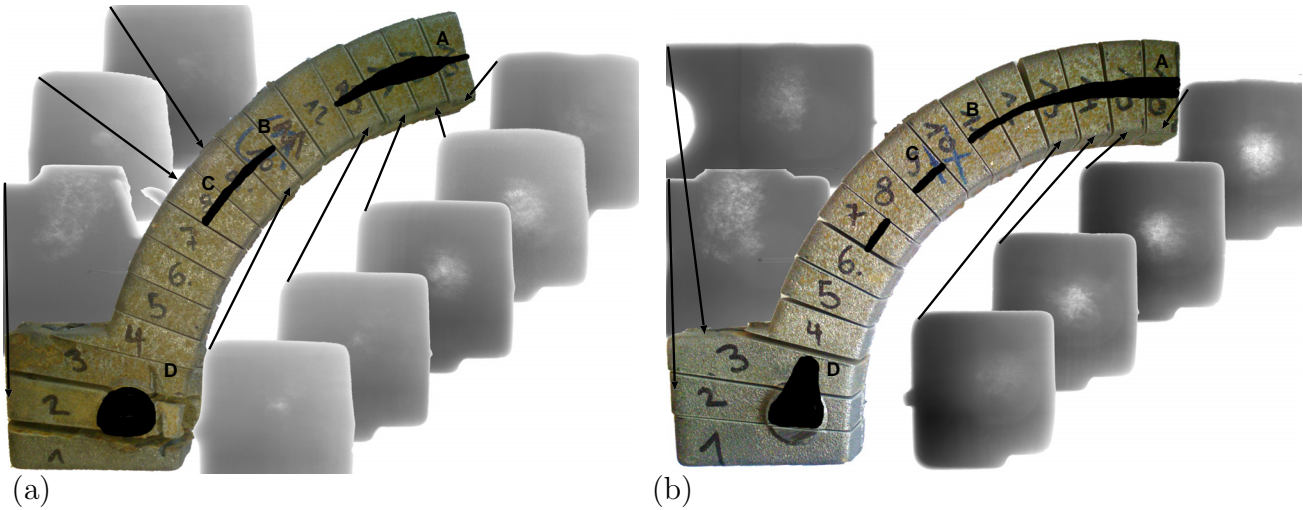


Fig. 5.11: (a) One half of casting c_g and (b) casting c_h both cut into 16 slices without central feeder. The slices were x-rayed to locate porosity as shown. For better comparison with simulated results, locations containing porosity are marked black at the castings.

and c_f show a massive shrinkage cavity. Secondly, porosity along the center line of the ring was detected in every case. The lowest level of porosity is found in the castings c_a and c_f with central feeder, which reduces definitively porosity along the center line. Thirdly, the inoculation treatment does not appear to impact porosity formation. When comparing castings c_a and c_f , indeed, casting c_f holds notably more porosity, but in the case of the clamp-rings c_d and c_g it is vice versa. When on the other hand, the considerable difference between the castings c_c and c_d is taken into account, both cast under similar conditions, the impact of inoculation treatment on porosity formation appears to be insignificant. The variance in location of porosity is due to statistical effects since porosity forms on entrained particles. To take account of this effect, the porosity of the castings c_a and c_b as well as c_c , c_d , c_g , and c_h were superimposed in Fig. 6.22.

6. Model Sensitivity and Model Validation

6.1 Objectives

In this chapter, first the stand-alone version of the microsegregation code is applied to point out its sensitivity with respect to submodels in Section 6.3.1, thermodynamic databases in Section 6.3.2, and alloy composition in Section 6.3.3. Significant results are discussed in line with experimental findings and statements of other authors to point out the relevance. The impact of the mold filling process on the symmetry of solidification and cooling is discussed in Section 6.3.4.

Subsequently, simulations are executed to investigate the validity of the microsegregation model. In Section 6.4.1 results of commercial software are examined to validate the cross-diffusion model and the solution of the solidification problem. Moreover, validation is carried out comparing microsegregation profiles to results obtained by EPMA in Section 6.4.2 and to an analytical solution of the diffusion problem in Section 6.4.3. In Section 6.4.4 the simulated solidification kinetics and characteristic temperatures are compared to a fraction solid curve deduced from DTA experiments.

Finally, the coupled approach is applied to the clamp-ring casting to validate the overall model. Initial conditions and the impact of the number of reference elements on the resulting phase distribution is introductorily explained in Section 6.5.1. To understand the variation in results when changing the number of reference elements, and the patched appearance in Section 6.5.3, cooling characteristics of selected reference elements are discussed in Section 6.5.2 with regard to phase fractions and solidification temperatures. To show proof of validity of the innovative coupling procedure, simulated cooling curves are compared to experiments in Section 6.5.4. For porosity prediction, local density and local phase fraction are passed from the microsegregation model to the process simulation tool. Based on this local information, porosity simulation is carried out applying a feature of the process simulation tool, as described in Section 6.5.5.

6.2 Introduction

For the material simulations presented in this chapter, initial, boundary, and runtime conditions were applied as listed in Tab. 6.1. Within the scope of the sensitivity analysis, described in Section 6.3, a number of these condition were consecutively varied as specified in the context. The first alloy composition given in Tab. 5.1 neglecting sulfur, phosphorus, and manganese was selected since it correlates most closely to the transformation temperatures determined by experiments. Furthermore, when applying this composition, the largest content of the diagnosed metal carbide M7C3 is achieved, as pointed out in section 6.3.3. It was impossible to include silicides in simulations due to the lack of thermodynamic data. As shown in Fig. 5.3, the microstructure predominant in GJSA-XNiCr20-2 is dendritic containing chunky graphite. Fig. 4.1 shows a typical shape of a dendrite arm corresponding most closely to an ellipsoid. This shape is approximated by the geometry coefficient $\tilde{g} = 1.7$ for dendrite arm coarsening, while the geometry coefficient $g = 2.3$ is selected for diffusion corresponding to a mixed geometry of imperfect spheres (2.9) and dendrite arms (1.7). The radius ratio $r/R = 0.5$ between the shrinking and growing dendrite arm is assumed to be constant. For decoupled simulations, a heat extraction rate of 1000 W/kg is assumed being equivalent to approx. 5 min solidification time which meets the cooling conditions on solidification of the clamp-ring. In agreement with Zhou et al. (ZSE87), the austenite - chunky graphite precipitation is assumed to be a loosely coupled eutectic growth.

Tab. 6.1: Initial, boundary, and runtime conditions for material simulations if not specified otherwise in the context.

databases	TCFE4 (TCF06)		MOB2 (MOB07)		
alloying elements	C	Cr	Mn	Ni	Si
composition [wt.-%]	2.66	1.22	1.28	20.90	2.46
phase	liquid	austenite	graphite	M7C3	cementite
diffusion type	compl. mixing	cross-diff.	—	—	—
diffusion geometry	2.3	2.3	—	—	—
temperature by	$T_{\text{ini}} = 1405\text{ }^{\circ}\text{C}$	$T_{\text{end}} = 1000\text{ }^{\circ}\text{C}$	$\dot{h} = -1000\text{ W/kg}$		
DAS coarsening with	$\lambda_{\text{ini}} = 20\text{ }\mu\text{m}$	$\tilde{g} = 1.7$	$\gamma = 0.2\text{ J/m}^2$	$r/R = 0.5$	

6.3 Model Sensitivity

6.3.1 Comparison of Submodels

In Fig. 6.1 (a) the development of fraction liquid with temperature is plotted for equilibrium and a Gulliver-Scheil solution, i.e. no diffusion in austenite and complete mixing in liquid. These two approximations are compared to microsegregation simulations at a heat extraction rate of 1000 W/kg. When the model without cross-diffusion is applied, this results in a solidification time of 4.6 min, with cross-diffusion 5.6 min, and with cross-diffusion in combination with dendrite arm coarsening 5.5 min. It is notable for this kind of alloy that solidification behavior in the case of chemical diffusion is very different from the case with cross-diffusion effect. Without this effect, solidification ends in a eutectic-like manner at approx. 1154 °C. This seems to be unnatural compared to DTA measurements in Fig. 5.4, for example. As the heat extraction rate is reduced to 100 and 10 W/kg, solidification time increases and at 1 W/kg the solutions of all approaches reflect the equilibrium solution.

The abrupt end of solidification in the case of chemical diffusion can be explained by looking at the development of liquid concentrations on solidification in Fig. 6.1 (b). In contrast to the case with cross-diffusion, the liquid phase depletes of nickel and silicon while the concentrations of chromium and manganese increase in the same manner as the fraction liquid decreases with temperature. Conversely, the slope of the carbon concentration appears to be constant. In this way, a critical concentration is reached at which the two solid phases, austenite and graphite, can grow without chemical restrictions. The formation of this critical composition is given for a wide range of heat extraction rates. In Fig. 6.1 (a) the critical composition is reached at a heat extraction rate of 1000 and 50, but not at 10 W/kg corresponding to 4.6 min, 1.6 h, and 8.1 h solidification time, respectively. The range of heat extraction rates, for which this behavior is observed, can be metered in Fig. 6.3. It ranges from approx. 50 W/kg to 10 kW/kg corresponding to 28 s solidification time. From these results is concluded that the chemical diffusion model is not applicable for austenitic cast iron since the solidification kinetics observed in experiments are not reproduced in nearly the entire range of technically relevant solidification times.

In Fig. 6.2 the impact of cross-diffusion is pointed out by comparing carbon profiles resulting from simulations taking / not taking account of cross-diffusion. At the end of solidification, the carbon profile is distributed nearly homogeneously in austenite at a level of approx. 7.0 mol-% in a simulation applying the chemical diffusion model. To demonstrate the impact of cross-diffusion, the gradient of nickel in austenite is plotted on the right ordinate. This impacts the diffusion of carbon, which is quantified by the chemical diffusion matrix provided in Tab. 6.2. Nickel promotes significantly the up-hill

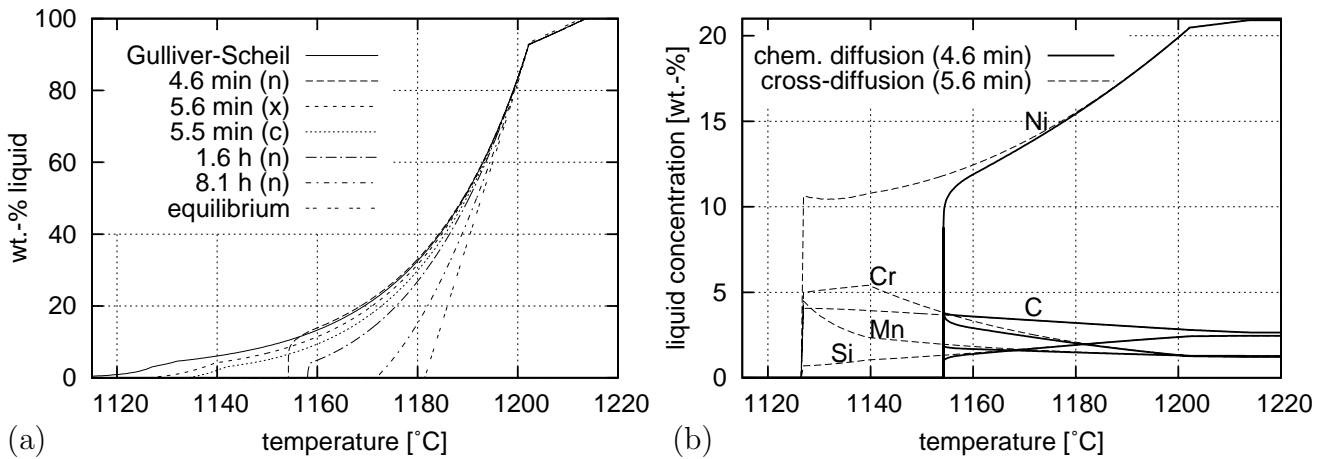


Fig. 6.1: (a) Impact of submodels on liquid fraction where (n) labels chemical diffusion, (x) cross-diffusion, and (c) cross-diffusion in combination with dendrite arm coarsening. In the chemical diffusion model, the heat extraction rate was varied: $50 \text{ W/kg} \hat{=} 1.6 \text{ h}$ and $10 \text{ W/kg} \hat{=} 8.1 \text{ h}$. (b) The liquid concentrations during solidification gives an indication of the abrupt decrease in liquid fraction on application of the chemical diffusion model.

diffusion of carbon in combination with other alloying elements. The simulation results imply negative gradients of nickel and silicon, while the diffusion interaction coefficients are positive. Conversely, the gradients of chromium and manganese are positive, while the diffusion interaction coefficients are negative. Summation of the individual diffusive fluxes of carbon according to Eq. (2.18) leads to strong up-hill diffusion, resulting in a pronounced microsegregation profile of carbon. This effect explains the promotion of graphite formation with increasing nickel content. This topic is the focus of Section 6.3.3.

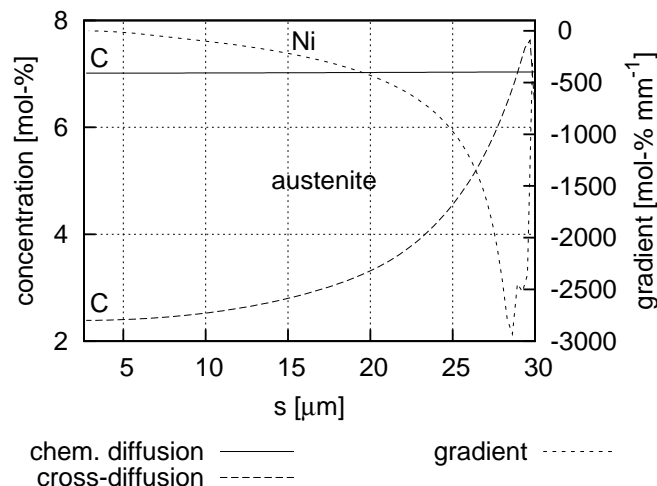


Fig. 6.2: Comparing the microsegregation patterns of carbon in austenite at the end of solidification taking / not taking account of cross-diffusion effects. One example for diffusive interaction of species is the pronounced gradient of nickel plotted on the right ordinate. According to Tab. 6.2, the interaction coefficient is positive explaining the strong up-hill diffusion of carbon.

In Fig. 6.3 and Fig. 6.4 the impact of submodels is highlighted comparing the variation

Tab. 6.2: Chemical diffusion matrix at the beginning of solidification at about 1213 °C for the conditions given in Tab. 6.1.

	C	Cr	Mn	Ni	Si
C	2.7813E-10	-4.2551E-11	-1.1087E-11	3.5762E-11	9.1116E-11
Cr	-1.3571E-15	2.4276E-14	5.3286E-16	7.5408E-17	-5.0050E-16
Mn	-3.6571E-16	1.3547E-16	1.0932E-14	-2.7984E-16	-6.1111E-16
Ni	7.4223E-15	-2.6010E-15	-4.7960E-15	9.2163E-15	-8.9675E-15
Si	1.0820E-14	-6.0898E-16	-5.9079E-16	4.9827E-16	5.3963E-14

in phase fractions and solidification temperature with the logarithm of the heat extraction rate. When applying the chemical diffusion model, as shown in Fig. 6.3, the solidification temperature decreases considerably at first which degrades in between 50 and 10 kW/kg at which the solidification temperature remains nearly constant. This effect is caused by the abrupt end of solidification illustrated in Fig. 6.1. When the heat extraction rate further increases, again the solidification temperature declines steeper by consecutive precipitation of M7C3, cementite, and then both carbides at late stages of solidification. The graphite fraction shows a minimum over the logarithmic heat extraction rate located at approx. 5 kW/kg.

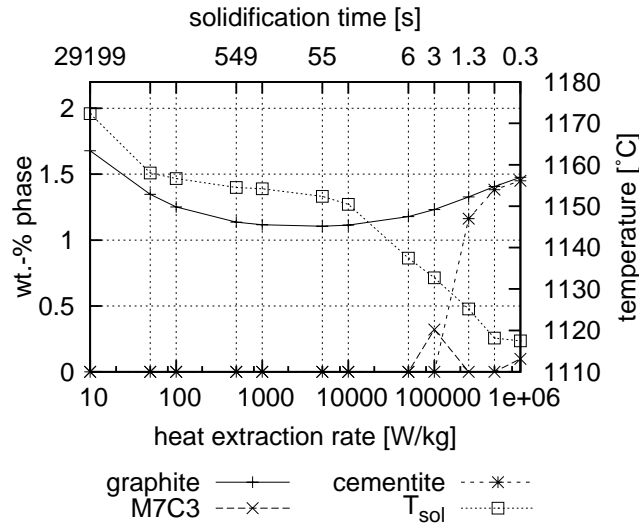


Fig. 6.3: Impact of the heat extraction rate on phase fractions and solidification temperature applying the chemical diffusion model.

When the heat extraction rate is varied by application of the cross-diffusion model, as shown in Fig. 6.4 (a), the solidification temperature is continuously decreasing and the graphite fraction shows a maximum over the logarithm of the heat extraction rate, whereas in the case of the chemical diffusion model, the graphite fraction shows an opposite trend. M7C3 starts forming as the heat extraction rate exceeds 50 W/kg and

decreases in accordance with the graphite fraction above 100 kW/kg because cementite is precipitated. When dendrite arm coarsening additionally impacts the precipitation kinetics of phases, as shown in Fig. 6.4 (b), solidification temperature decreases in a linear manner with the logarithm of the heat extraction rate. This is due to a decreasing dendrite arm spacing associated with a decreasing diffusion distance. Furthermore, dendrite arm coarsening reduces the impact of heat extraction rate on phase fractions compared to the situation with cross-diffusion only.

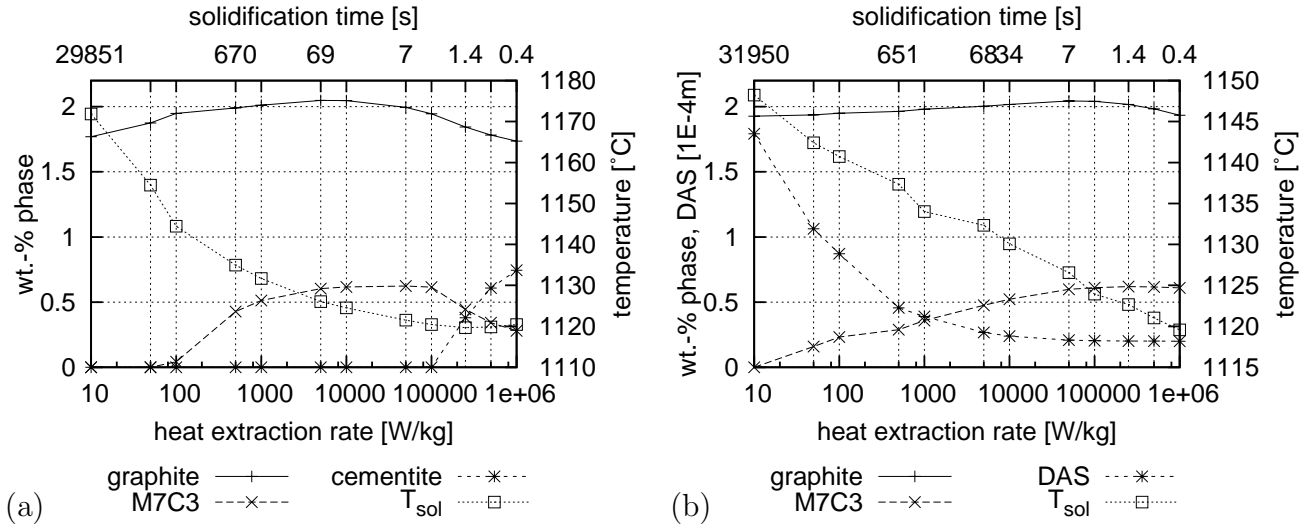


Fig. 6.4: Impact of the heat extraction rate on phase fractions and solidification temperature applying (a) the cross-diffusion model and (b) additionally the dendrite arm coarsening model.

Phase fractions and solidification temperatures are not only sensitive to the heat extraction rate, but also to cooling characteristics. This is demonstrated by comparing phase fractions as functions of temperature in Fig. 6.5 (a) applying a constant cooling rate, a constant heat extraction rate, and a cooling curve resulting from a coupled simulation at a position of the clamp-ring exposed to fast cooling. All three time-temperature correlations are selected in a way that the solidification time is approx. 135 s. The resulting phase fractions and solidification temperatures are very similar for the constant cooling rate and constant heat extraction rate model, where approx. 0.4 and 0.43 wt.-% M7C3 is formed, respectively. When, in contrast, the displayed cooling curve is applied, significantly less graphite is formed and no M7C3. The reason for this behavior is that the early stage of solidification, where usually most of the dendrite arm coarsening takes place, is passed very fast. This leads to a dendrite arm spacing of only 22.51 μm , which is very close to the initial value of 20.00 μm . Due to this small DAS, the solidification behavior is closer to equilibrium compared to the case at a constant heat extraction rate resulting in a DAS of 31.10 μm . Applying a constant cooling rate leads to slower cooling during primary formation of austenite, and, consequently, a DAS of 36.25 μm results. This is because the coarsening rate is high at the beginning of solidification when the dendrite arm radius is small, as shown in Fig. 8 (b). Thus, dendrite arm coarsening is behind the

sensitivity of the model to cooling characteristics, but slightly reduces sensitivity when only the heat extraction rate is varied, as illustrated in Fig. 6.4.

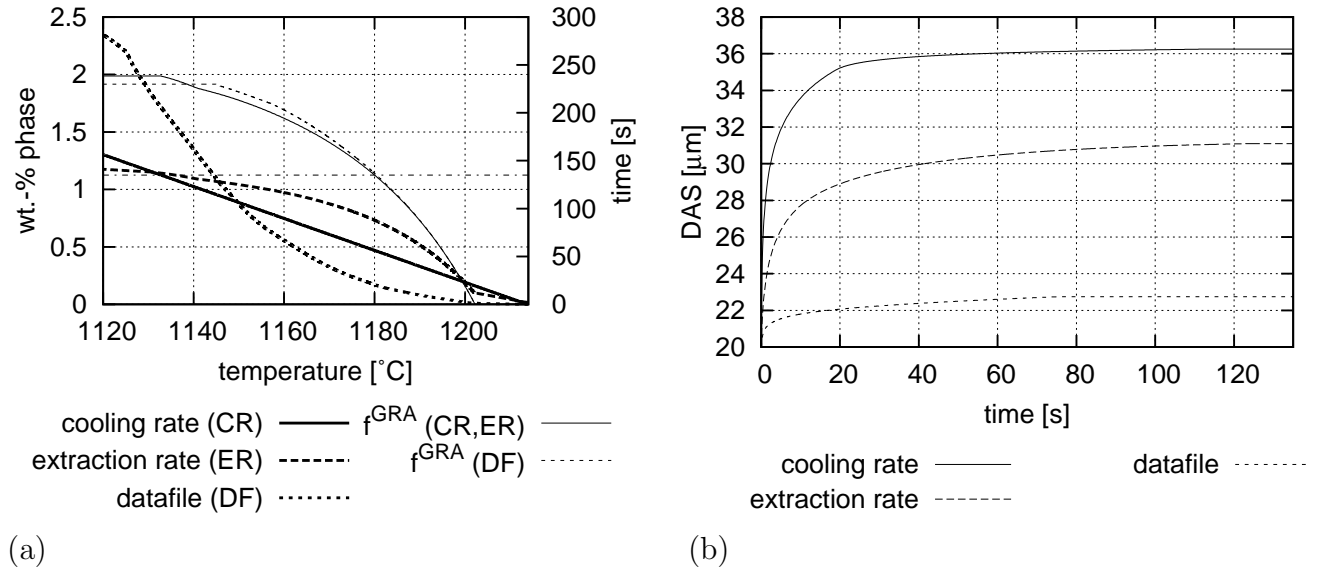


Fig. 6.5: (a) Three different cooling characteristics (CR: cooling rate, ER: heat extraction rate, DF: cooling curve from a data file) and its impact on the resulting graphite fraction, when solidification time is kept constant at approx. 135 s (dash-dot line); (b) the corresponding dendrite arm coarsening.

6.3.2 Comparison of Databases

The three thermodynamic databases IRON-01c (IRO09), TCFE4 (TCF06), and TCFE5 (TCF07) are compared in Fig. 6.6 (a) with regard to the phases precipitated, phase fractions, and transformation temperatures resulting from microsegregation simulations applying the conditions listed in Tab. 6.1. It should be noted that the overall fraction of carbon-rich phases, graphite, M7C3, and cementite, is increasing as follows: TCFE4, TCFE5, IRON-01c, where IRON-01c predicts a large fraction of cementite and no M7C3. In contrast, TCFE4 and TCFE5 predict under the given conditions no cementite at all. Liquidus, eutectic temperature and solidification range are increasing in the same order of databases. Compared to the non-equilibrium eutectic temperatures determined by experiments ranging from 1185 °C to 1195 °C, as deduced from DTA in Section 5.5 or cooling curves in Fig. 6.20, all equilibrium eutectic temperatures are predicted to be too high by approx. 21 to 43 °C. Details about solidification kinetics by comparing the three databases are provided in Section 6.4.4, where the development of solid fraction is compared to experimental results from DTA.

One reason for the discrepancy between experimental and predicted eutectic temperatures is nucleation of graphite which may lead to undercoolings up to 110 °C until eutectic cementite forms according to a microsegregation simulation suspending graphite.

However, under the experimental cooling conditions in Fig. 5.2 no pronounced recalescence is noted. A second reason could be uncertainty of composition, as shown in Fig. 6.6 (b) comparing the three analyses listed in Tab. 5.1. As discussed in Section 6.3.3, a concentration variation will tend to increase the liquidus temperature. A third reason contributing to this problem is insufficient experimental data for further database assessments and optimizations for relatively large carbon, silicon, and nickel compositions.

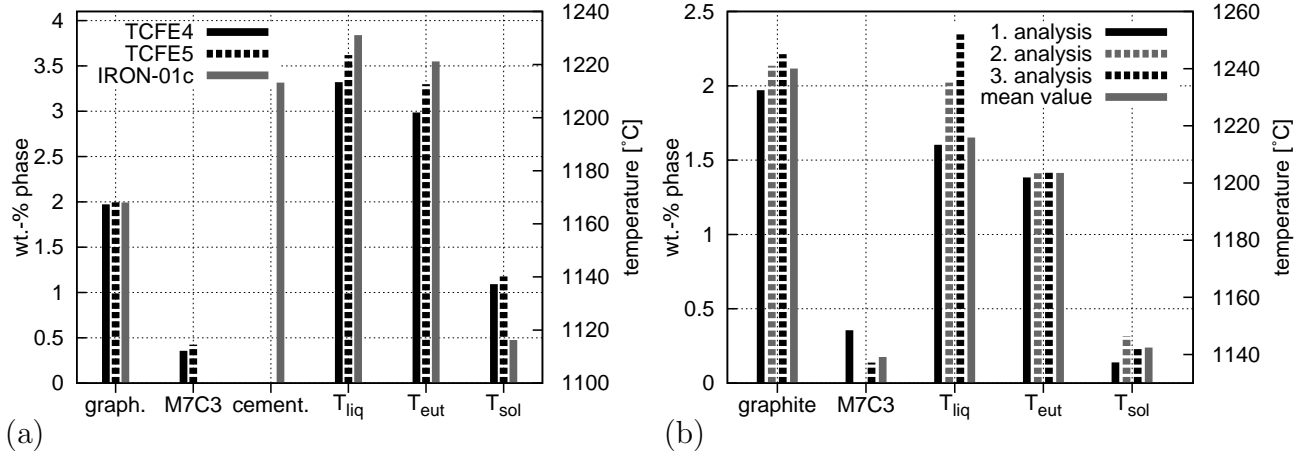


Fig. 6.6: (a) Impact of databases assuming the first composition listed in Tab. 5.1 and (b) of alloy analysis according to Tab. 5.1 on phase fractions and transformation temperatures.

6.3.3 Variation of Chemical Composition

As discussed in Section 5.3, the alloy composition was analyzed applying various methods leading to an inconsistent alloy composition. Fig. 6.6 (b) correlates the alloy analyses with a variation in phase fractions and transformation temperatures. The first analysis contains the least amount of carbon and silicon, but the most amount of manganese and chromium leading to the fact that less graphite and more M7C3 is formed on solidification compared to the other analyses. The third analysis yields the highest carbon equivalent and therefore the most graphite is formed, but less carbides compared to the first analysis since the content of manganese and chromium is lower. The second and third analysis are both hypereutectic with reference to TCFE4. Therefore, the liquidus temperatures are increasing with the analysis number, while the eutectic temperature only changes by approx. 2 °C. Also, the solidification temperatures of the first and second analysis are higher than that of the first analysis. When simulations are performed with the average value of the three analyses, the results are similar to that of the first analysis, but more graphite and less M7C3 is precipitated. Because M7C3 was analyzed by EPMA in Section 5.7, TCFE4 or TCFE5 in combination with the first analysis appear to be the best selection for executing the material simulations.

To study the impact of each individual element, microsegregation simulations were

executed varying the concentration based on the conditions provided in Tab. 6.1. Fig. 6.7 (a) shows a constant increase in fraction of graphite with carbon content, while M7C3 increases up to 2.5 wt.-% carbon and remains nearly constant above this concentration since the amount of chromium and manganese is constant. Both elements promote the formation of M7C3. The liquidus temperature falls sharply from 1403°C showing a narrow-ranged eutectic and increases again sharply until the liquidus temperature for graphite is reached. The temperature of the graphite-austenite eutectic increases as graphite starts forming at approx. 1 wt.-% carbon and remains constant above 3 wt.-%. Conversely, the solidification temperature decreases over the carbon composition with a minimum at about 2.5 wt.-% carbon and increases slightly above this value. Fig. 6.7 (b) reveals an increase in graphite fraction, while the M7C3 content decreases over the silicon content. This is because silicon raises the solubility of chromium and manganese in austenite. When alloying 1 wt.-% silicon, for instance, the chromium concentration in austenite is approx. 2.5 wt.-% at the end of solidification. Whereas, when alloying 4 wt.-% silicon, the chromium content is approx. 3.7 wt.-%. Furthermore, silicon promotes eutectic solidification. The liquidus temperature shows a minimum in between 2.5 and 2.7 wt.-% which corresponds to the silicon concentration measured, while the eutectic temperature has a maximum at approx. 4.5 wt.-%. The solidification temperature increases slightly at low concentrations of silicon and is at maximum at about 4.3 wt.-%. Above this value, silicon is not dissolved any more in austenite, and the solidification temperature is decreasing dramatically, at least as long as no silicon-rich phase forms, such as silicides. This is shown in Fig. 3.1 representing an isothermal cut of the Fe-Si-Ni system at room temperature.

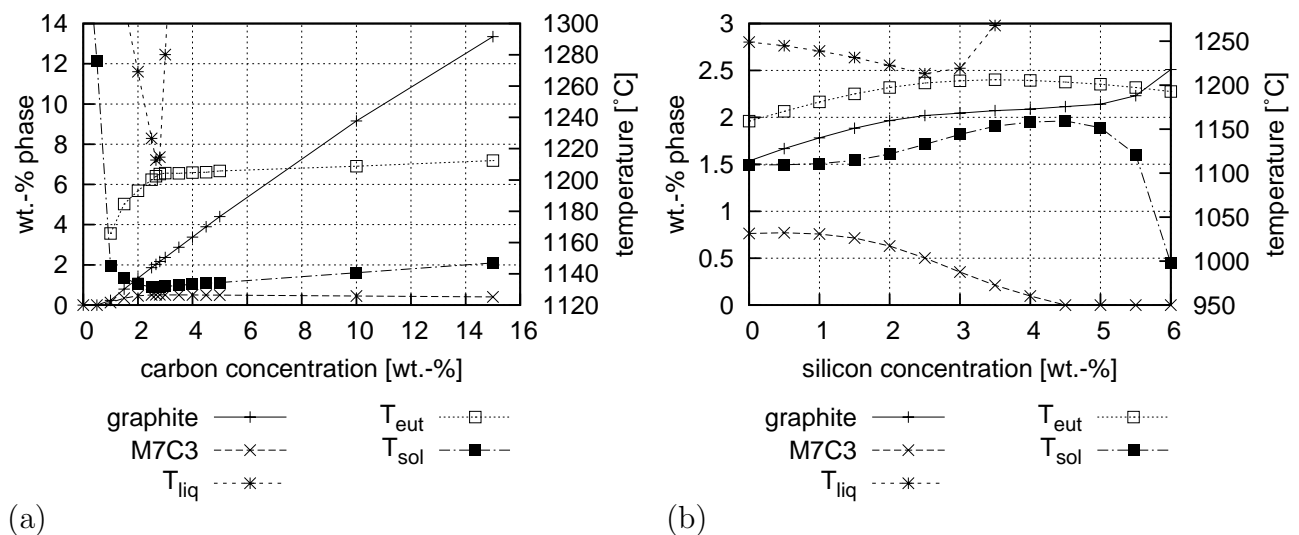


Fig. 6.7: (a) Impact of carbon and (b) silicon on phase fractions and transformation temperatures applying the cross-diffusion model.

Spear (Spe93) states that the promotion of graphite formation with increasing nickel content is because nickel reduces the solubility of carbon in austenite. However, this

appears to be only half the truth. As clarified in Fig. 6.8 (a), graphite correlates linearly over the nickel content and no carbides are formed as long as cross-diffusion effects are neglected. Conversely, when cross-diffusion effects are taken into account, up to 10 wt.-% nickel a considerable amount of cementite and above this value M7C3 is precipitated in addition to graphite. Furthermore, significantly more graphite is formed than in the case without cross-diffusion since the slope of increase is sharper. Thus, it is concluded that the graphite promoting effect of nickel is mostly due to cross-diffusion leading to strong uphill diffusion of carbon in austenite and enriching the carbon concentration in the liquid phase, as discussed in Section 6.3.1. Fig. 6.8 (b) shows a minimum in liquidus temperature at about 20 wt.-% nickel. With further additions of nickel, the liquidus temperature rises again up to 1396 °C at 35 wt.-%. The eutectic temperature shows a linear increase with nickel concentration. It should be noted that the solidification range spreads more steeply when cross-diffusion is taken into account.

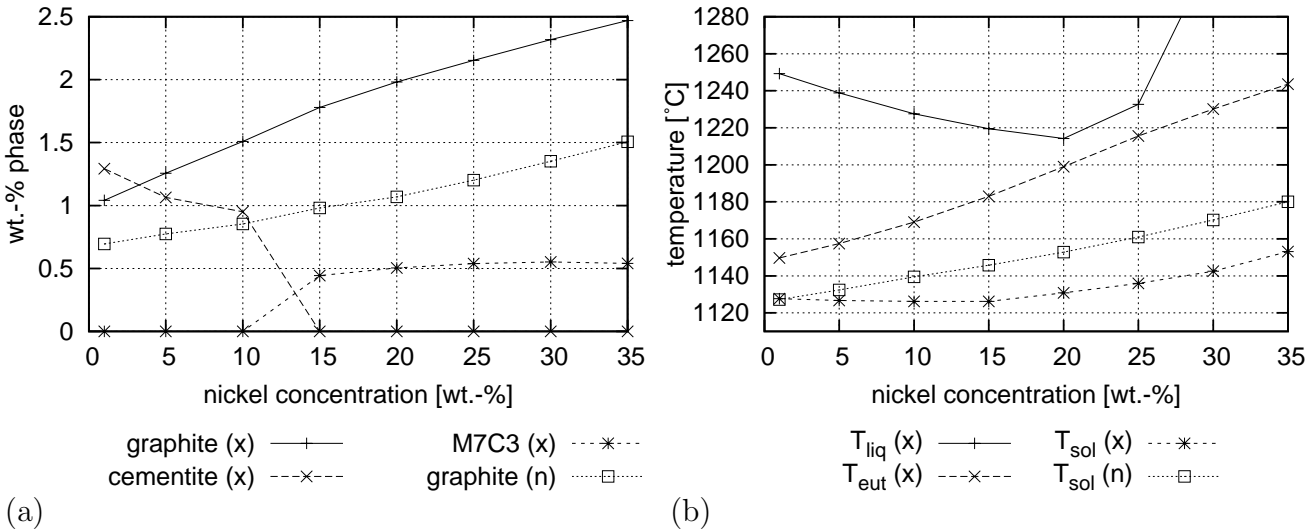


Fig. 6.8: (a) Impact of nickel on phase fractions and (b) transformation temperatures when applying the chemical (n) and the cross-diffusion (x) model, respectively.

Fig. 6.9 (a) illustrates the reduction and ending of graphite precipitation at approx. 15 wt.-%, while M7C3 increases sharply with the chromium concentration. At approx. 9 wt.-% even primary M7C3 forms, as indicated by the sudden increase in liquidus temperature. The solidification temperature has a minimum at approx. 2 wt.-% chromium, and the eutectic temperature decreases up to the end of graphite precipitation. Manganese assists the formation of M7C3, as Fig. 6.9 (b) shows. Above 10 wt.-%, cementite is additionally precipitated and the graphite fraction is at maximum. Liquidus, eutectic, and solidification temperature decrease with increasing manganese concentration.

This variation analysis leads to the conclusion that the alloy under consideration is well designed since carbon and silicon only provide a small concentration range for eutectic solidification. It was shown that the alloy is very close to the eutectic composi-

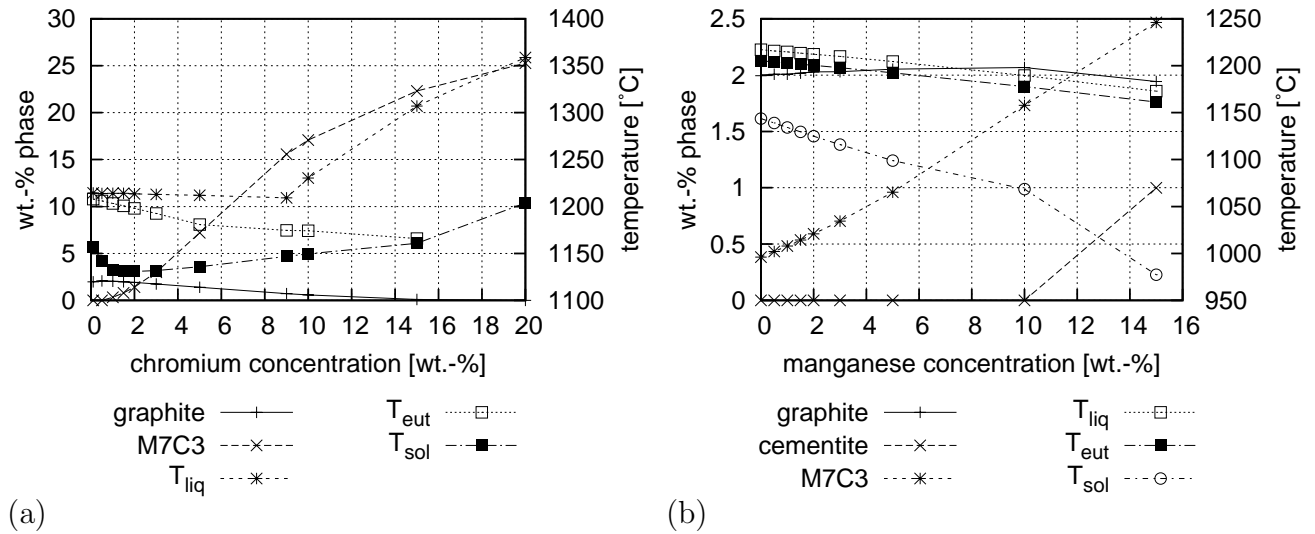


Fig. 6.9: (a) Impact of chromium and (b) manganese on phase fractions and transformation temperatures applying the cross-diffusion model.

tion regarding the elements carbon, silicon, and nickel. Further reduction of nickel up to 20 wt.-% impacts the liquidus temperature by -2.3°C . Manganese and chromium show nearly no impact on transformation temperatures when varying the composition in the range of ± 1 wt.-%. A cumulative variation of concentrations decreases the liquidus temperature at most by -5°C . Moreover, silicon increases the solubility of chromium and manganese compensating for the deleterious impact of these components both promoting M7C3 and cementite formation. Cross-diffusion leads to strong up-hill diffusion in austenite. The slope of graphite content over the nickel concentration is sharper when compared to the chemical diffusion model. Thus, cross-diffusion is the dominant effect promoting the graphite precipitation with increasing nickel content.

6.3.4 Impact of Mold Filling

The mold filling process is preceding the solidification process and may have impact on solidification in a number of aspects of which two are important for the present work. Firstly, when melt is in contact with air, dross forms, and due to turbulent mold filling also other particles, such as dross, slag or molding material may be entrained into the mold cavity. On the rough surface of these particles or in between oxide films are enclosed gas pockets, where nucleation of shrinkage or gas porosity is unnecessary. Entrained particles promote therefore the formation of porosity. This is explained by Jones et al. (JEG99) and called *non-classical pore nucleation theory*. The risk of turbulence and mold erosion is obviously a function of melt velocity within the gating system and casting.

To analyze velocities and temperatures on mold filling, coupled simulations of mold filling and solidification were carried out in an explicit manner, applying an initial tem-

perature of 1405°C at the inlet and 20°C for the mold. The Newtonian viscosity of the liquid phase increases from $0.942\text{ mm}^2/\text{s}$ at 1400°C up to $1.6\text{ mm}^2/\text{s}$ at 1211°C . The heat transfer coefficient decreases linearly over the temperature within the mushy zone. Above the liquidus temperature at 1211°C and below the solidification temperature at 1138°C the coefficient is kept at a constant value of $3.5\text{ kW}/\text{m}^2\text{K}$ and $150\text{ W}/\text{m}^2\text{K}$, respectively. To determine thermophysical data for the present cast alloy, a microsegregation simulation was conducted applying the conditions listed in Tab. 6.1. The resulting data, such as latent heat $L_f = 282.2\text{ kJ}/\text{kg}$, density, isobar heat capacity, and fraction of solid are shown in Fig. 6.10. Due to lack of better data, the heat conductivity was assumed constant at $20\text{ W}/\text{mK}$.

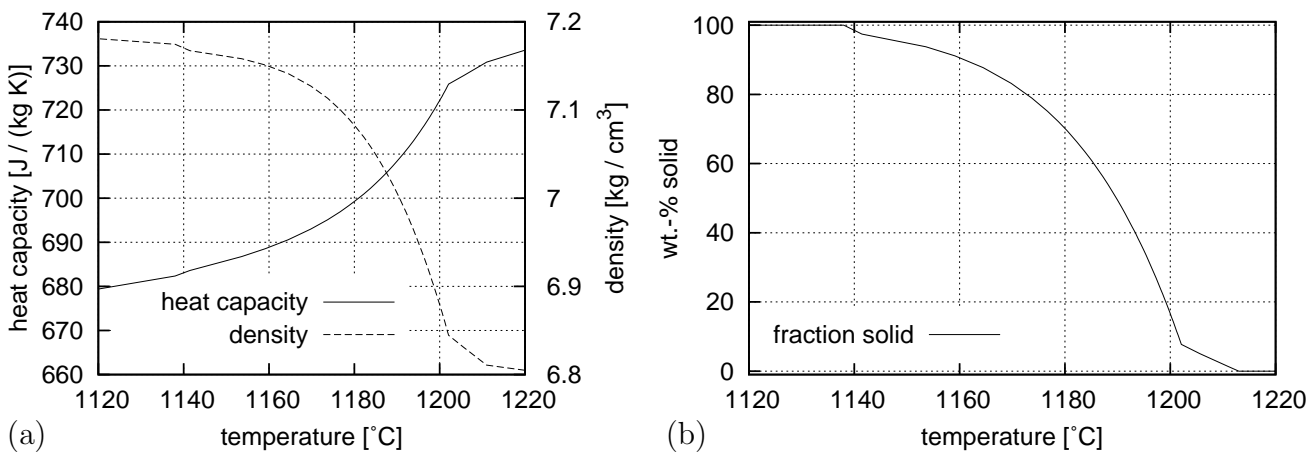


Fig. 6.10: (a) Heat capacity, density, and (b) fraction of solid over temperature serving as input data for process simulation. These data were generated by application of the microsegregation model taking into account cross-diffusion and dendrite arm coarsening.

Fig. 6.11 (a) shows the velocity field during mold filling as melt enters the casting. Moreover, the elements of the gating system are labeled for the following discussion. Fig. 6.11 (b) shows the same situation one second later. It is typical for an unpressurized gating system that the highest velocity at approx. $1.8\text{ m}/\text{s}$ is located inside the downsprue. Because a filter was used to hold back slag and other particles, the melt is slowed down at the junction between downsprue and runner connection. The highest velocity inside the gating system, approx. $1\text{ m}/\text{s}$, is found at the junction of runner connection and runner as well as at the left and central ingate which is due to the asymmetrically placed downsprue. The runner is not completely filled up for several seconds since melt enters preferentially the left side of the runner. However, no turbulence is expected in this region because the velocity is low at approx. $15\text{ cm}/\text{s}$. From this point of view, the gating system is well designed, and the risk of dross formation and erosion of molding material is low. Secondly, when hot melt flows on cold molding material, the liquid metal cools down, while the mold is heating up. In this way, temperature gradients within the casting may be set up by positioning ingates accordingly. This is analyzed by evaluation of the simulated temperature field shown in Fig. 6.12 (a). After 3.7 s , melt starts entering the right flange.

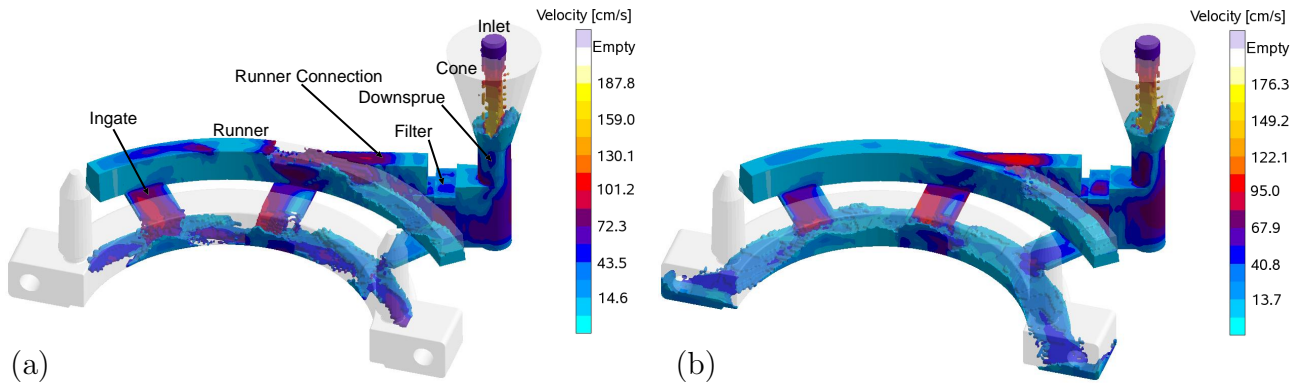


Fig. 6.11: Simulated velocity field during mold filling (a) after 2.7 s and (b) after 3.7 s assuming a total filling time of 8 s.

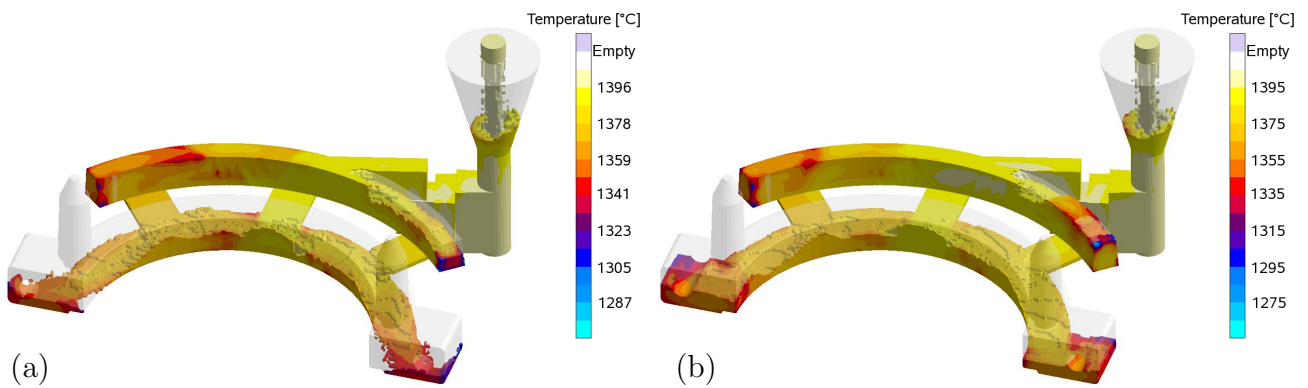


Fig. 6.12: Simulated temperature field during mold filling (a) after 3.7 s and (b) after 4.3 s assuming a total filling time of 8 s.

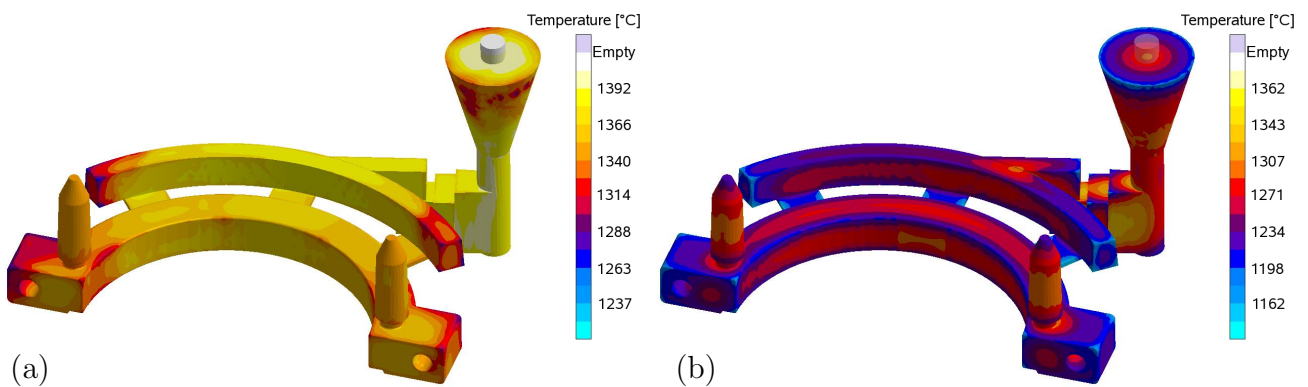


Fig. 6.13: Simulated temperature field (a) after mold filling is completed at 8.0 s and (b) at 38.4 s when solidification initiates.

The temperature difference between the right and left flange is approx. 20°C . Because of the heavy-sectioned casting, this temperature difference reduces considerably within 0.5 s as more melt enters the right flange shown in Fig. 6.12 (b). Fig. 6.13 (a) shows the temperature field at the end of mold filling being still slightly asymmetrical. However, as solidification initiates, no significant asymmetry is noted within the casting, as shown in

Fig. 6.13 (b). It is concluded that mold filling has no significant impact on solidification of the clamp-ring in terms of symmetry of the temperature field.

6.4 Model Validation

6.4.1 Cross-Diffusion and Solidification Model

To validate the present solidification model along with the cross-diffusion solver, microsegregations and phase fractions are compared to verified commercial software (AHH⁺02). Fig. 6.14 (a) shows results for a test case assuming a plate-like geometry with $g = 1$ and initially $60 \mu\text{m}$ length after 4.6 min solidification at 1162°C . To produce results suitable for a comparison, the RVE was modified. Austenite grows from the left hand side into the liquid phase, while graphite is assumed to expand on solidification and located at the right hand side of the RVE. In the commercial approach, graphite is assumed to increase in volume since carbon is modeled assuming a molar volume of $0 \text{ cm}^3/\text{mol}$ in austenite and liquid, but $10 \text{ cm}^3/\text{mol}$ in graphite. In contrast, all substitutional alloying elements are modeled assuming $10 \text{ cm}^3/\text{mol}$ in austenite and liquid. From this assumption, pseudo volume fractions $f_{V_o}^j$ are deduced for each phase j according to Eq. (4.32). The particular pseudo volume fraction corresponds to a certain distance in the RVE that is larger than the distance deduced from molar fractions, as shown in Fig. 6.14. The actual microsegregation patterns are therefore elongated accordingly. The approach of pseudo volume fractions is only applied for this comparative calculation. For all other simulations in the present work, diffusion distances are approximated according to molar fractions.

This comparative calculation was executed taking into account cross-diffusion and applying the thermodynamic database TCFE4 (TCF06) along with the mobility database MOB2 (MOB07). Moreover, a constant cooling rate of $0.5^\circ\text{C}/\text{s}$ was assumed, and composition number three was selected, as listed in Tab. 5.1, but neglecting minor additions of sulfur, phosphorus, and magnesium. As explained in Section 6.3.1, the diffusion flux of carbon is up-hill and directed towards the solid-liquid interface. This increases the carbon content in the liquid phase with solidification time promoting formation of graphite. This topic is discussed in detail in Section 6.3.1 and 6.3.3. When looking at the carbon profile in Fig. 6.14 (a), one distinct difference between the predictions is noted, that is in carbon diffusion which appears to be much faster in the present approach. This difference was quantified by trial. It corresponds to a reduction of diffusive fluxes in austenite by the particular molar interface concentration. Fig. 6.14 (b) shows a simulation in which the diffusion coefficients in austenite were multiplied by the corresponding interface concentrations in austenite. In this case, no significant difference is noted, neither in microsegregation profiles nor in phase fractions. However, the diffusion coefficients deduced from MOB2, that are listed in Tab. 6.2, appear to be correct.

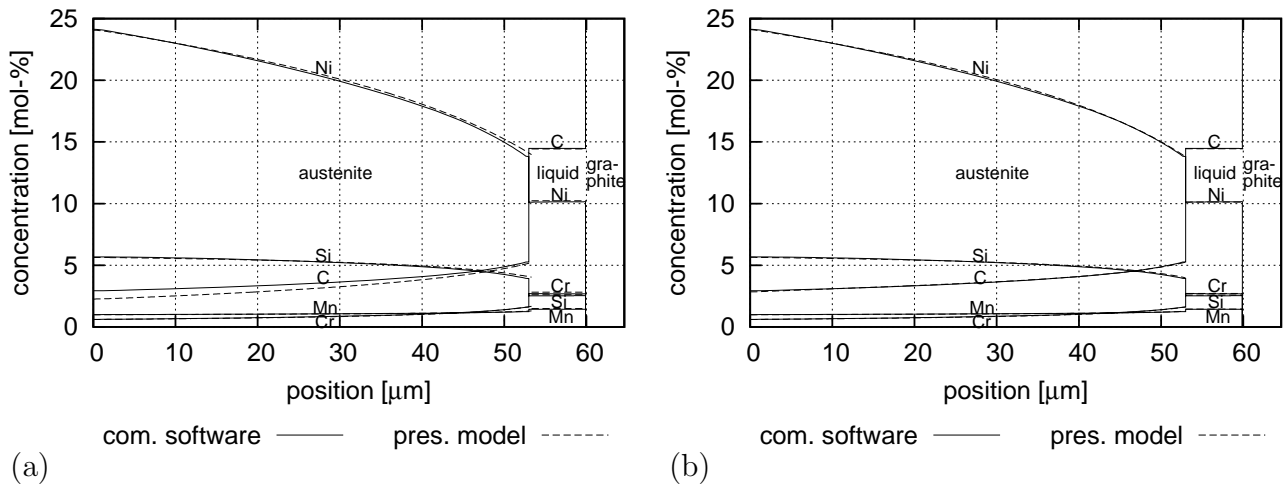


Fig. 6.14: (a) Comparing microsegregation patterns and phase fractions from the commercial software (AHH⁺02) to results from the present model. (b) The same situation applying modified diffusive fluxes.

Since the present approach is proved valid for chemical diffusion (cf. Section 6.4.3), and cross-diffusion fluxes arise explicitly in the discretized conservation equation (C.12), the cause of this discrepancy is unclear. In conclusion, it was impossible to verify the cross-diffusion solver by this test case. However, a simulation applying modified fluxes produced identical results. This means, both flux balance equations yield the same result. Thus, the fundamental solidification problem is solved correctly. Furthermore, as discussed in Section 6.4.4, solidification kinetics was compared to a fraction solid curve deduced from DTA experiments. Fig. 6.17 clarifies that solidification kinetics tend to degrade when applying the modified diffusion coefficients that correlate with the solution of the commercial software.

6.4.2 Comparison with Microsegregations from EPMA

A microsegregation simulation was executed to compare the resulting microsegregation profiles to EPMA line scan A shown in Fig. 5.8. For this simulation, a geometry coefficient of 3 and a length of 42 μm was assumed for the representative volume element. In addition, the conditions given in Tab. 6.1 were applied. These results are compared to the line scan in the austenitic region, as shown in Fig. 6.15. The concentration profiles of carbon and manganese are approximated astonishingly well since the values simulated represent the state at solidification temperature. Subsequent to solidification, additional graphite is usually precipitated which has impact on the carbon concentration in austenite. This effect appears not to be of great extend for this kind of alloy. The trend of the nickel profile is in agreement with experiments, however, the quantity predicted is approx. 5 to 8 mol-% larger. This is similar in the case of chromium in Fig. 6.15 (b), for which the concentrations are approximately twice the value predicted. Conversely, the silicon

concentration coincides precisely at the beginning, but at the end of the RVE, the experimental silicon concentration remains constant, whereas the profile predicted shows clearly inverse segregation. The trend of the microsegregation patterns in the EPMA line scan in Fig. 5.8 (b) as well as the EDX line scan in Fig. 5.5 are consistent. Conclusively, this comparison verifies the present model at least qualitatively. It is remarkable that the microsegregations of the important elements carbon and silicon are reproduced very well. In spite of this consistency, this method appears to be inappropriate for validation of the cross-diffusion solver because neither the solidification morphology of the sample depicted in Fig. 5.7 is known nor its average concentration. Therefore, the diffusion solver is compared to an analytical solution in Section 6.4.3.

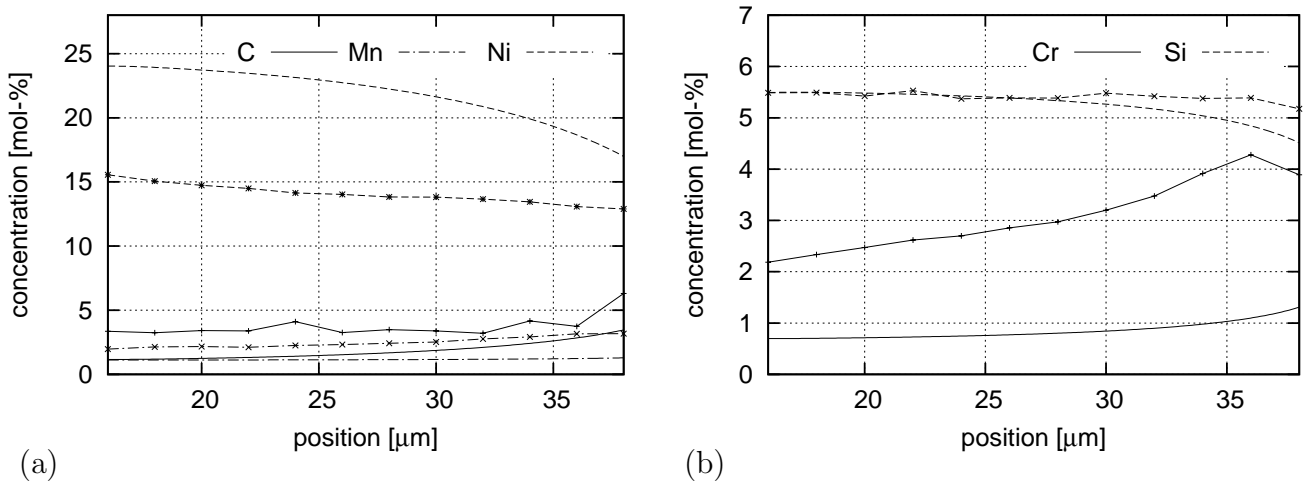


Fig. 6.15: Comparison of virtual concentration profiles and EPMA (cf. Fig. 5.8) for (a) carbon, manganese, and nickel and (b) chromium and silicon. Experimental values are plot using the corresponding line-point style.

6.4.3 Diffusion Solver

The accuracy of the diffusion solver is of great importance since diffusion defines the shape of the microsegregation pattern. Furthermore, from this shape, the species gradient and therefore the diffusive flux at the solid-liquid interface is determined which in turn has impact on the solid fraction according to Eq. (4.8). Therefore, the diffusion solver is tested by application to a simple diffusion problem for which an analytical solution exists. The derivation of this equation is given in Appendix D. At the left boundary, a Dirichlet condition $x(0, t) = \hat{x}$, $\forall t > 0$ is applied and the initial concentration $x(s, 0) = x^0$ is selected which yields the following equation:

$$x(s, t) = (x^0 - \hat{x}) \operatorname{erf}\left(\frac{s}{\sqrt{4Dt}}\right) + \hat{x}, \quad \forall t > 0. \quad (6.1)$$

The result from the microsegregation code is compared to this function in Fig. 6.16

assuming a plate-like RVE, $g = 1$, the length, $l = 6$ mm, and the diffusion coefficient, $D = 8 \cdot 10^{-10}$ m²/s. Moreover, the concentrations $\hat{x} = 0$ mol-% and $x^0 = 19.66$ mol-% are applied. The diffusion profiles predicted and the analytical solutions are identical. In other words, the diffusion solver is verified.

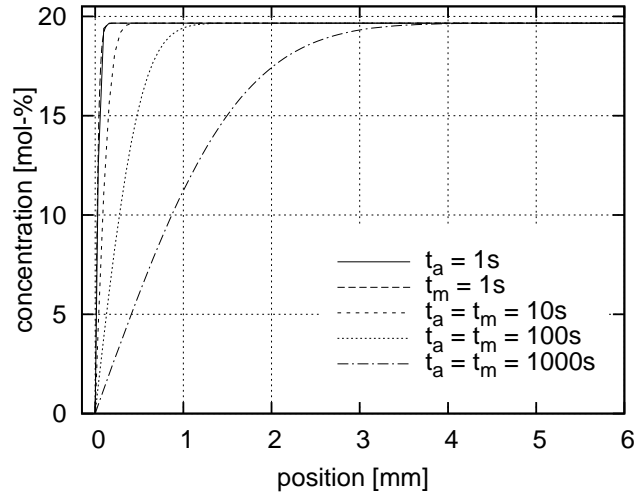


Fig. 6.16: Comparing analytical solutions according to Eq. (6.1) and denoted t_a to predictions from the microsegregation model for various time moments denoted t_m .

6.4.4 Comparison with Solidification Kinetics from DTA

The fraction solid curve deduced by averaging three DTA cycles (cf. Section 5.5) is compared to microsegregation simulations in Fig. 6.17. These simulations were executed taking into account cross-diffusion and dendrite arm coarsening. All three databases were applied along with the first composition listed in Tab. 5.1. With reference to the DTA processing conditions, constant cooling at 10°C/min was applied as runtime condition for the simulations. As already mentioned in Section 6.3.3, all databases yield eutectic temperatures that are too high. It should be noted at this point that the non-equilibrium eutectic temperature on solidification of the clamp-ring is approx. 15°C lower than the averaged value for reasons given in Section 5.5. Thus, the solidification range is even smaller changing the solidification kinetics accordingly. However, the solidification temperatures show good correlation when applying TCFE4 (TCF06) and TCFE5 (TCF07). Regarding IRON-01c (IRO09), the solidification range is predicted to be too large. The slope of the experimental fraction solid curve indicates a hypoeutectic composition since the slope increases as graphite starts precipitating. The best approximation of this behaviour is given when the microsegregation code is applied in combination with TCFE4. However, at the end of solidification, the slope of the curve determined experimentally is steeper compared to predictions applying TCFE4 or TCFE5. Additionally, a special test case was set up referring to Section 6.4.1 for which the diffusion coefficients were multiplied by the corresponding interface concentration in austenite. As can be seen, this

rather degrades solidification kinetics above 60 wt.-% solid fraction compared to results applying unmodified diffusion coefficients. Moreover, all other concentrations listed in Tab. 5.1 were tested as well as the cross-diffusion model assuming a constant DAS of approx. $50\ \mu\text{m}$. On the whole, simulations applying the database TCFE4 along with the cross-diffusion and dendrite arm coarsening model provide the closest approximation to experimental solidification kinetics.

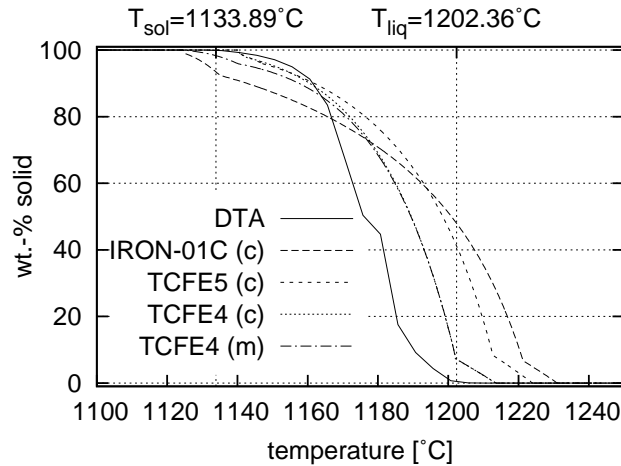


Fig. 6.17: Comparing the fraction solid curve deduced from DTA to various databases taking into account cross-diffusion and dendrite arm coarsening, which is denoted by (c). Moreover, (m) refers to a test case for which the diffusive fluxes were modified.

6.5 Coupled Simulations: Model Application and Validation

6.5.1 Simulation Setup

Fully coupled material and process simulations were performed for a casting with and without a central feeder. Since the experiments shown in Fig. 5.2 and the simulated temperature field in Fig. 6.13 indicate a symmetrical solidification behavior at the beginning of solidification, simulations were executed for one half of the clamp-ring at an initial temperature of 1405°C in a green sand mold at initially 20°C . The heat transfer coefficient and the heat conductivity were assumed as provided in Section 6.3.4. The experiments also indicate that none of the exothermic feeders ignited, as can be seen from Fig. 5.2. Therefore, the feeders were modeled as isolating feeders. Furthermore, initial and boundary conditions were used for the microsegregation simulations according to Tab. 6.1. A grid consisting of 959616 volume elements was generated with 47985 metal cells, and during simulation 306 reference elements were selected. Simulations ran for approx. 60 h on a current standard PC using an open source operating system. The same problem has also been solved using only 50 reference elements in approx. 10 h with similar

results, using 28 reference elements in approx. 9 h with slight differences regarding the phase distribution, and using 10 reference elements in 5.5 h, which generated an inverse distribution of phases. This study reveals that in order to generate consistent results, a number of 50 reference elements is sufficient for the clamp-ring casting.

6.5.2 Cooling Characteristics of Reference Elements

As already shown in Fig. 6.5, cooling characteristics have significant impact on the resulting phase fractions which is predominantly due to dendrite arm coarsening. Fig. 6.18 (b) shows cooling curves of selected reference elements with unequal cooling characteristics and labeled solidification times. For instance, the curves corresponding to 230.2 s and 273.0 s solidification time, show an inverse curvature and thus very different solidification temperatures. This is a consequence of dendrite arm coarsening at the beginning of solidification. Above 1200 °C, the cooling rate of the latter mentioned reference element is significantly higher than that of the former mentioned reference element, which is directly linked to DAS, solidification temperature, and phase fractions, as illustrated in Fig. 6.18 (a). The curves solidifying in 230.2 s, 496.6 s, 611.2 s, and 624.2 s are more impacted by the latent heat released, while the curves solidifying at 9.5 s, 118.7 s, and 273.0 s are mainly impacted by heat diffusion. The reference element solidifying at 568.6 s shows intermediate cooling characteristic.

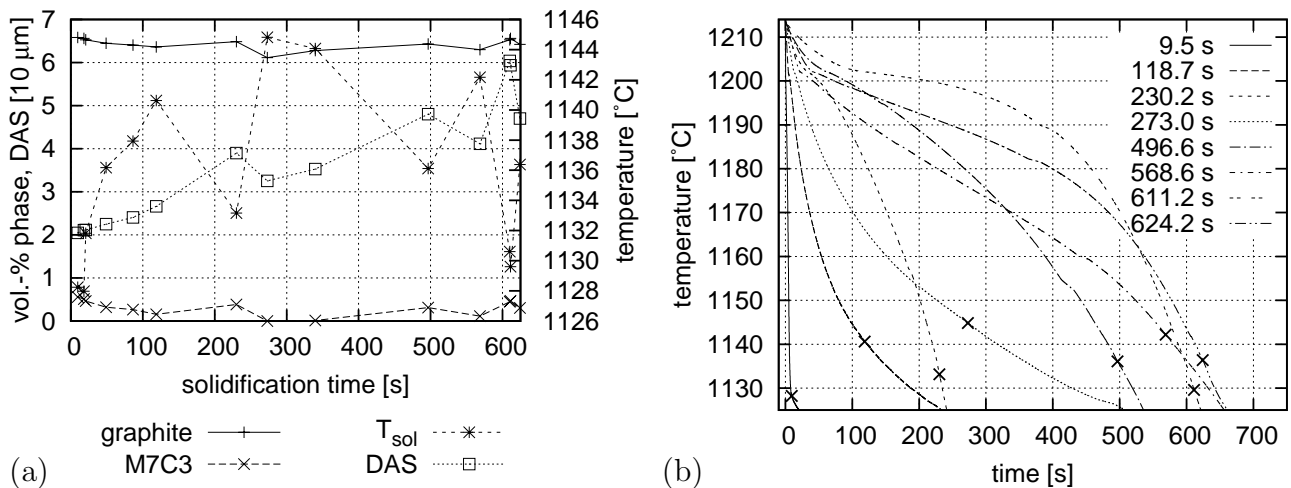


Fig. 6.18: (a) Phase fractions, dendrite arm spacing, and solidification temperature at various reference elements. (b) Cooling curves with labeled solidification times at selected reference elements. Solidification temperatures are marked by “x”.

As can be seen from the distribution of dendrite arm spacing in Fig. 6.19 e, f, reference elements impacted by heat diffusion are located at the rim of the casting, while reference elements impacted by latent heat are located at the center of the clamp-ring. It should be noted that this transition of cooling characteristics is accompanied by a change

in microstructure from globular-eutectic grains in the chill zone to a primary dendritic structure with chunky graphite in the remaining casting, as pointed out in Fig. 5.3.

6.5.3 Distributions of Microstructural Quantities

During the solidification simulation, austenite, graphite, and the metal carbide M_7C_3 were precipitated from the liquid phase. The patchy impression of the results is due to the interpolation procedure, introduced in Section 4.9. This procedure is not based on geometric data, but on similarity criteria in relation to the cooling conditions. In this spirit, two reference elements meeting the similarity criteria for the particular interpolation element are generally selected. Obviously, these reference elements are not necessarily in the immediate neighborhood of the corresponding interpolation element. Slight differences in cooling characteristics lead to variation in phase fraction, as already discussed in 6.5.2. For this reason, the fluctuations in the results are insignificant. However, the trend of the results is significant.

Fig. 6.19 a, b, c, and d indicate the formation of more graphite and metal carbides in areas of low cooling rate. It would appear to make sense that in regions of low cooling more austenite is formed, since solidification is closer to equilibrium than in regions exposed to fast cooling. In these regions, however, also the DAS increases accompanied by increasing diffusion distances and thus resulting in a departure from equilibrium. The dendrite arm coarsening at the hot spot below and inside the feeder is shown in Fig. 6.19 e, f. Moreover, this effect is significantly supported by cross-diffusion since the carbon flux progresses in direction of the carbon gradient, that is towards the liquid phase, as can be seen from Fig. 6.2. Thus, this excessive carbon promotes graphite and metal carbide formation. These effects are accompanied by a decreasing solidification temperature, departing from equilibrium, as shown in Fig. 6.19 g, h. This material behavior increases the hot spot effect in the area below the feeder. Hence, the major microstructural differences between both castings are predominantly in proximity to the central feeder.

6.5.4 Comparison of Cooling Curves

Fig. 6.20 a, b compares cooling curves in casting c_a and c_b to the corresponding virtual cooling curves resulting from a coupled simulation. The cooling characteristics were predicted very well, while discrepancies in absolute temperatures are noted for the reasons given in Section 6.3.2. The fourth thermocouple in casting c_a broke completely on casting and thermocouple three after approx. 480s solidification time. The third thermocouple in the case of clamp-ring c_a shifts significantly towards lower temperatures. The plateau is approx. 35°C lower than in the case of casting c_b . Possible reasons for this shift are displacement, inaccuracy due to a bad contact, or, for some reason, larger undercooling

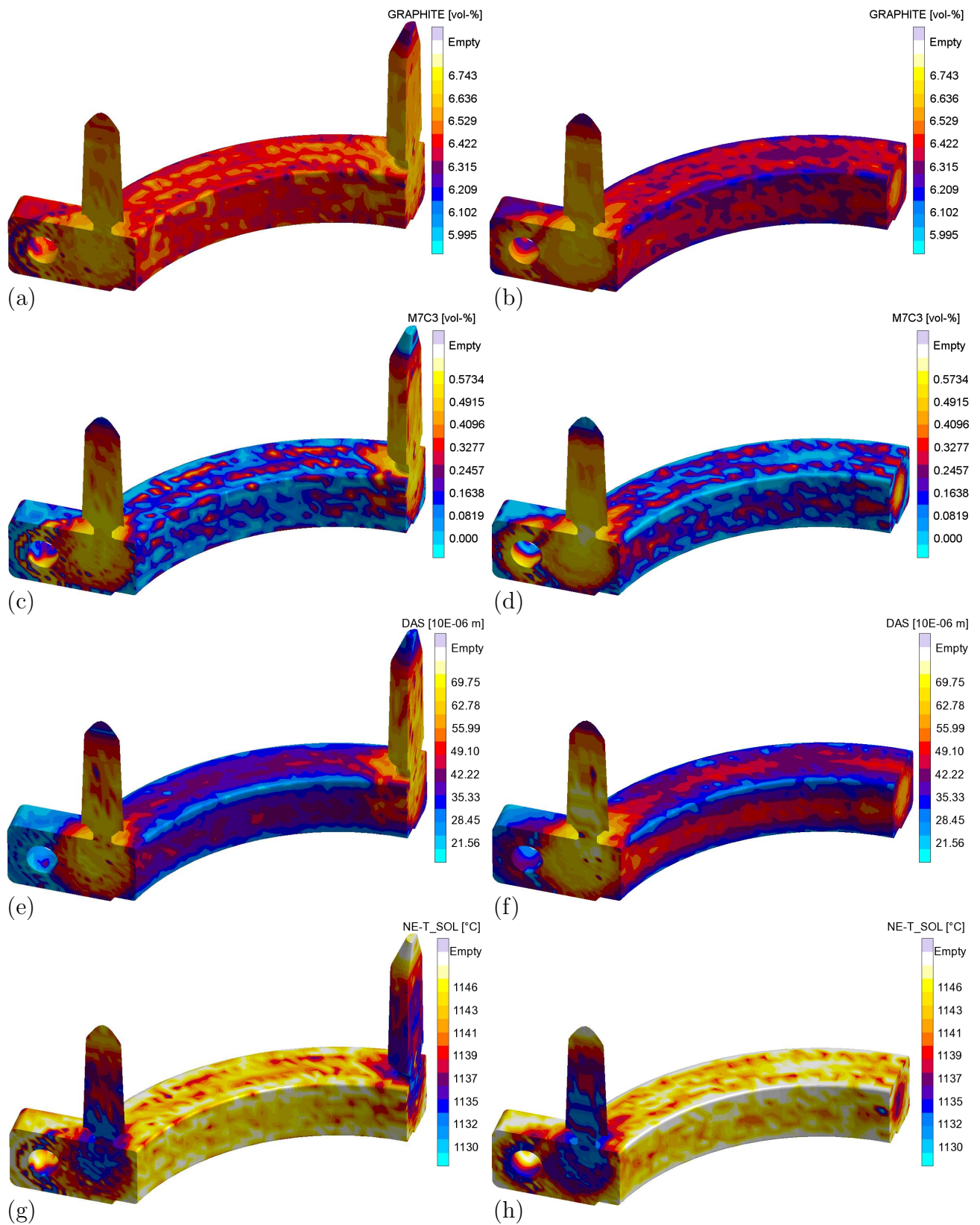


Fig. 6.19: Predicted distribution of the graphite (a, b), metal carbide (c, d), dendrite arm spacing (e, f), and solidification temperature (g, h) in a casting with and without central feeder, respectively.

than in the remaining casting. Casting c_b shows the best correlation between experiment and simulation, in which thermocouple four had a loose contact at the beginning and started recording again after approx. 350s. All thermocouples worked in castings c_c and c_d , as shown in Fig. 6.20 c, d. The virtual cooling curves VTC2 and VTC4 are predicted to be almost identical. This is similar in experiments regarding the casting c_c , whereas in the case of casting c_d rather the curves TC1 and TC4 are alike.

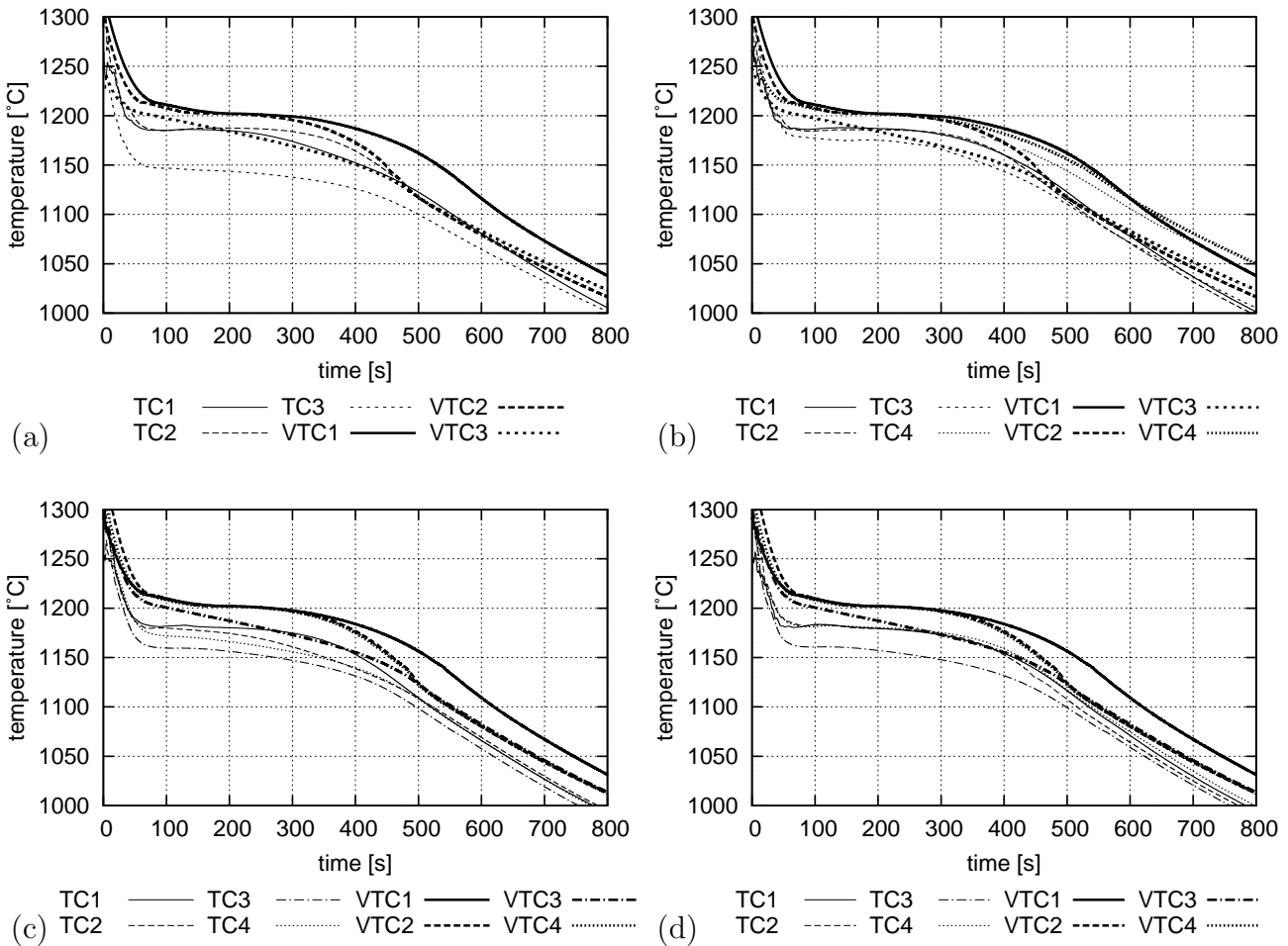


Fig. 6.20: Comparing virtual cooling curves (VTC) to measurements in castings (TC): (a) casting c_a , (b) casting c_b , and (c) casting c_c , (d) casting c_d with / without central feeder, respectively. The positions of thermocouples are shown in Fig. 5.1 (a).

In conclusion, this innovative procedure of coupling is valid because the discrepancy in temperature appears to be the only significant difference between virtual and experimental cooling curves.

6.5.5 Validation of Porosity Prediction

Porosity prediction is based on local density and solid fraction data, which are forwarded from the material model to the process model during simulation. The porosity model

itself is part of the commercial software, and for this reason no further information can be provided. Fig. 6.21 shows the porosity prediction for a casting with and without a central feeder. Porous area A is predicted to be located within the neck of the central feeder, whereas in the case of the casting without central feeder a shrinkage cavity along the center line of the casting is predicted. The efficiency of the feeder at the flange is predicted to be too low, meaning the feeder provides less liquid material to the casting than necessary. This leads to a shrinkage pore below the feeder at the flange. The hot spot effect is assisted by a shift towards lower solidification temperatures over solidification time, as shown in Fig. 6.19 (h). This effect is not predictable with uncoupled simulations. It can be said that the local development of microsegregations, dendrite arm coarsening, and cooling conditions are closely interacting and thus impacting porosity formation.

By comparing Fig. 6.21 (a) to casting c_a in Fig. 5.9 (a), it is noted that porosity at location A was not detected within the casting. This is in contrast to casting c_b in Fig. 5.1 (b) which shows porosity penetrating into the casting and was cast under very similar conditions. Casting c_f in Fig. 5.9 (b) with a poor inoculation state shows shrinkage porosity located below the feeder which is interconnected with porous area B. The porosity in the regions B and C were both predicted and detected in casting c_f , while porosity in casting c_a could be only found in section B. Porosity in area D, that is located below the feeder at the flange, was discovered in every casting, as predicted by simulation. Conversely, porous area E, predicted adjacent to the core hole, was never found in any of the castings analyzed.

Regarding the castings without central feeder, porous area A correlates well with experimental findings, especially, in the case of casting c_c in Fig. 5.10 (a). Porous areas B and C are predicted in proximity to the very flat designed ingate which is due to the chill effect of the thin ingate. In castings c_c , c_d , and c_g in Fig. 5.10 and Fig. 5.11, this porosity is found along the center line of the ring and is accumulated in the proximity of locations A, B, and C. In the case of clamp-ring c_d the shrinkage cavity in regions A, B, and C is continuous, while in casting c_c porous areas B and C shift towards the flange. Thus, the location of porosity appears to be subject to statistical effects. This is explained by Jones et al. (JEG99) and called *non-classical pore nucleation theory* at entrained particles.

To take account of this statistical effect, porosity detected in castings c_a and c_f were superposed, as shown in Fig. 6.22 (a). From this superposition, agreement with the simulated results for porosity A, B, C, and D is confirmed. The location of porosity A is predicted within the neck of the central feeder. Due to statistical impacts, it is also found below the feeder. The same procedure was carried out in Fig. 6.22 (b), but the four results regarding casting c_c , c_d , c_g , and c_h were superposed to compare with Fig. 6.21 (b). Apart from the small porosity E, the predictions correlate very well. A comparison with each individual casting with the predictions shows that also the level of porosity is well

predicted. The present method, where local density and fraction solid data is provided for the porosity model, is verified by this application.

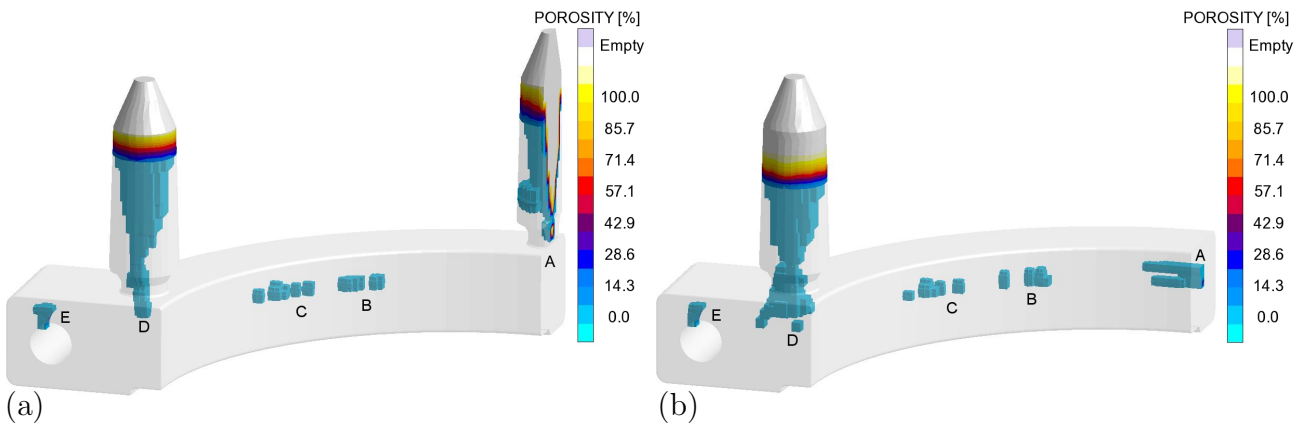


Fig. 6.21: Porosity prediction applying a coupled simulation approach for a casting (a) with and (b) without central feeder.

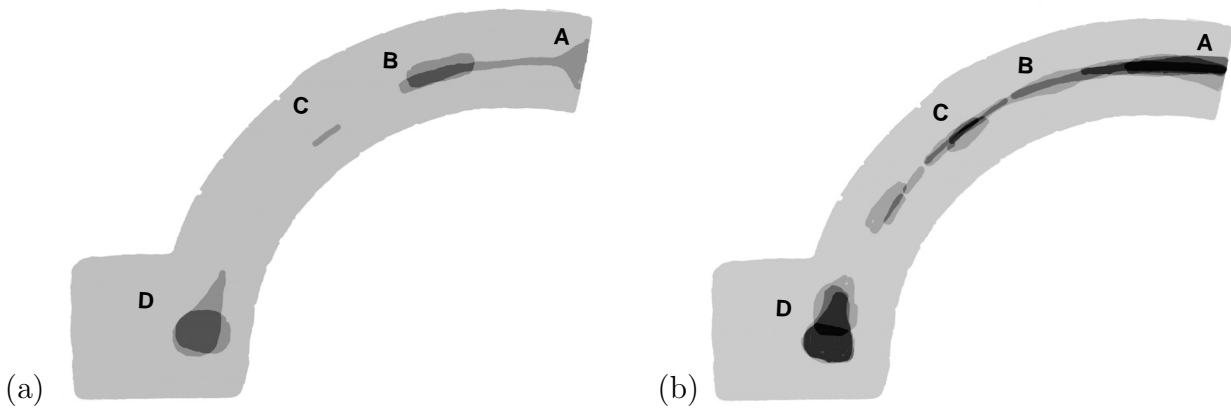


Fig. 6.22: Superposition of porosity detected in castings (a) with (cf. Fig. 5.9) and (b) without central feeder (cf. Fig. 5.10 and 5.11). The superposition (a) represents the frequency with which porosity is ascertained in experiments, *not* the level of porosity.

7. Summary and Conclusions

Because solid concentrations change with temperature, microsegregations build up in solid phases during solidification. Diffusion usually reduces these microsegregations introducing a kinetic effect on solidification. As distinct from empirical models, microsegregation models reflect time-dependent phase growth by simulation of diffusive transport and thermodynamic data, as pointed out in Section 3.2. Two- and three-dimensional models also take account of the microstructure evolution during solidification, but is, however, very time-consuming. Since the aim is direct coupling to process simulation, microstructural variation in castings are taken account of by modeling dendrite arm coarsening. This introduces an additional kinetic effect which corresponds to an expanding representative volume element during microsegregation simulations. To this end, a comprehensive microsegregation software has been generated that is characterized by

1. graphical preprocessing (cf. Section 4.7),
2. robust main processing (cf. Section 4.8),
3. easy manageable postprocessing (cf. Section 4.10),
4. general applicability due to the
 - (a) multicomponent concept (cf. Section 4.3.3),
 - (b) multiphase concept (cf. Section 4.3.1),
 - (c) thermodynamic coupling (cf. Section 4.5),
 - (d) cross-diffusion model (cf. Section 4.3.6),
 - (e) mixed geometry model (cf. Section 4.3.4),
 - (f) multicomponent dendrite arm coarsening model (cf. Section 4.3.7),
5. time-efficient predictions (cf. Section 6.5),
6. innovative macro coupling procedure and
7. innovative porosity coupling (cf. Section 4.9).

The characteristics of the model presented have been compared to decoupled and coupled state-of-the-art microsegregation models, and four unique features have been identified: (1) the coupling to porosity simulation, (2) the innovative macro coupling concept, (3) the multiphase concept, and (4) the mixed geometry concept.

The complex effects interacting on solidification and cooling of cast iron were demonstrated in Section 2.6. The transformation kinetics, for instance, is impacted by various graphite shapes which may also be present simultaneously in castings, i.e. austenitic dendrites with incorporated graphite nodules, eutectic cells, and defective graphite structures. Chunky graphite is a degenerated graphite shape forming by extensive branching of pyramidal crystals. The actual cause of this structure transition is unclear. However, the transition appears to be a function of solidification time and micro-alloying elements, such as magnesium, cerium, and antimony.

A series of GJSA-X NiCr 20-2 clamp-rings was cast with variation of inoculation state and number of feeders. As an input quantity to the microsegregation model, the microstructure of the castings was characterized and a predominantly dendritic microstructure and chunky graphite were identified. With regard to this evidence, a mixed morphology between a dendritic and a cellular microstructure was assumed for the diffusion simulations and a purely dendritic microstructure for the dendrite arm coarsening simulation.

The composition of the cast alloy was analyzed using various methods which, however, show inconsistency. Nevertheless, the composition is a sensitive input parameter to the microsegregation simulation, and the transformation temperatures are predicted to be too high compared to measurements. Thus, each alloying element was varied in a technically relevant range to study the impact on transformation temperatures and phase fractions, as discussed in Section 6.3.3. It was found that the alloy is very close to the eutectic composition. A cumulative change in concentrations decreases the liquidus temperature at most by -5°C . *Concentration variations of approximately twice the largest root mean square deviation, as shown in Tab. 2, do not significantly lower transformation temperatures.* Silicon increases the solubility of chromium and manganese which partially compensates for the deleterious impact of these components, that is the promotion of carbide formation.

Transformation temperatures were determined consistently evaluating recorded cooling curves and DTA measurements. DTA measurements enabled deducing a fraction solid curve which was taken as a baseline for predicted solidification kinetics. The database TCFE4, along with dendrite arm coarsening and the unmodified cross-diffusion model most closely reflect the experimental solidification kinetics. The impact of various thermodynamic databases was investigated in Section 6.3.2 by comparing phase fractions and transformation temperatures. Experimental non-equilibrium eutectic temperatures are 21 to 43°C lower than database predictions. Possible reasons for this discrepancy are nucleation undercooling of graphite, uncertainty about alloy composition, or imprecise thermodynamic data. No pronounced recalescence is visible, while the undercooling is large in relation to the temperatures predicted. A composition variation tends to increase the liquidus temperature. Therefore, the most probable reason is lack of experimental

data for relatively large carbon, silicon, and nickel compositions to assess and extend the validity of the databases. TCFE4 (TCF06) predicts the lowest liquidus and eutectic temperature of all databases. Three different analyses, listed in Tab. 5.1, were tested regarding these criteria. The first analysis yields the lowest transformation temperature and the largest M7C3 content. According to the EPMA measurements in Section 5.7, M7C3 was analyzed. *TCFE4 in combination with the first analysis listed in Tab. 5.1 is the best selection to execute material simulations with respect to prediction of transformation temperature, solidification kinetics, and M7C3 content.*

By consecutive executed variation of the heat extraction rate, it was possible to highlight the impact of the three submodels in Section 6.3.1. The chemical diffusion model does not mirror the experimental solidification kinetics over almost the entire range of technically relevant solidification times. *The chemical diffusion model therefore does not apply to this type of alloy.* Cross-diffusion produces a strong up-hill flux of carbon resulting in a pronounced microsegregation profile of carbon in austenite. *It was possible to demonstrate that cross-diffusion is the chief cause for graphite promotion of nickel, not only the change of the carbon solubility with nickel concentration, as stated by Spear (Spe93).*

To analyze the effect of dendrite arm coarsening, three types of cooling characteristics were compared. Dendrite arm coarsening reduces the impact of heat extraction rate on phase fractions compared to the situation with only cross-diffusion, as shown in Section 6.3.1. Moreover, phase fractions and solidification temperatures are sensitive to cooling characteristics. *Dendrite arm coarsening causes the sensitivity of the model to cooling characteristics, while at the same time slightly reducing the sensitivity to variations in heat extraction rate.*

EDX analysis, providing qualitative results, and EPM analysis, providing quantitative microsegregation profiles, were executed. Through EPMA the following phases were identified: austenite, graphite, and a eutectic region consisting of M7C3 and a silicide. EDX and EPM line scans in eutectic cells provide concentration profiles for each element in austenite, while the gradient of nickel is negative. Silicon is homogeneously distributed, and positive gradients were analyzed for the remaining alloying elements. *A comparison of an EPMA line scan with simulations in Section 6.4.2 shows good qualitative correlation for all alloying elements and good quantitative correlation for the important elements carbon and silicon.*

Mold filling simulations were executed in Section 6.3.4 to constitute the symmetry assumption in coupled simulations. The validity of this assumption was clearly demonstrated and fortified by comparing experimental cooling curves below the right and left feeder in Section 5.2.

During mold filling the largest velocity in the runner and ingates is approx. 1 m/s. The filling process is slightly asymmetrical. This asymmetry vanishes as solidification starts.

The gating system is well designed and therefore the risk of erosion of molding material and dross generation, both promoting the porosity formation, is low. In conclusion, *mold filling shows no impact on solidification regarding the symmetry of the temperature field.*

In Section 6.4.1 results of the present model were compared to a numerical solution from verified commercial software, which takes account of cross-diffusion. The solutions of both codes are identical, when the diffusive fluxes are reduced by multiplication with concentrations in austenite at the interface. Because the phase fractions predicted coincide in this case, the solidification problem is solved correctly. Furthermore, the diffusion solver was validated by comparing numerical results to analytical diffusion solutions in Section 6.4.3. *Thus, the solution of the solidification problem is identical to that of verified commercial software, when the diffusive fluxes are reduced. The diffusion solver without cross-diffusion was verified.*

Fully coupled simulations were performed applying the innovative concept of process coupling with variation of the number of reference elements, as pointed out in Section 6.5.1. The results of coupled simulations depend on the number of reference elements. Computation time increases with the number of reference elements. Conversely, when a critical number is not reached, an inverse phase distribution is predicted. For the clamp-ring casting the critical number of reference elements identified as adequate for generating consistent results was 50.

The distribution of microstructural quantities was discussed in Section 6.5.3 in relation to cooling characteristics of reference elements. The hot spot effect is aided by a shift towards lower solidification temperatures over solidification time. Accordingly, the major differences in microstructure between the two variants of castings are located predominantly around the central feeder. *The shift towards lower solidification temperatures is a consequence of local cooling characteristics and cross-diffusion and can only be predicted by coupling directly material and process simulation.*

The impact of cooling characteristics at reference elements on phase formation and transformation temperatures was investigated in Section 6.5.2. This analysis reveals that two types of reference elements are distinguishable: one predominantly impacted by latent heat and a second exposed to fast heat transport at the casting-mold interface. *The different cooling characteristics at reference elements result in very different phase fractions. This transition of cooling characteristics is accompanied by a transition from a globular-cellular to a chunky-dendritic microstructure, as observed in experiments (cf. Fig. 5.3).*

To validate the coupled approach, the cooling curves predicted were compared to experimental cooling curves from the clamp-ring casting in Section 6.5.4. The cooling characteristics predicted in the coupled simulation and the curves measured correlate very well, while the absolute temperatures show a discrepancy by approx. 20 °C. Since this discrepancy is not caused by the coupling the two models, the conclusion is that

the innovative coupling concept and its implementation generate valid results. Porosity within the casting was analyzed by x-ray of consecutively cut samples. Porosity was found along the center line of the ring and, especially, below the feeder at the flange. In two of three cases porosity was also found below the central feeder. The porosity predictions from the process simulation tool based on the local development of phase fractions and density were compared to experimental findings, as discussed in Section 6.5.5. Porosity is predicted below the feeder at the flange, at the center line of the casting in close proximity to the ingates, and within the neck of the central feeder. When the central feeder is omitted, pronounced porosity is formed in this area. *Concerning the statistical impact of non-classical pore nucleation, the porosity predictions and experiments correlate very well.*

The outcome of this work has been the creation of a complex and unique simulation tool. This model has undergone a detailed validation procedure, which is reviewed in Tab. 7.1 and confirms the validity of the overall model.

Tab. 7.1: Validation objectives and correlation level in categories given below the table.

Objective	Qualitative	Quantitative	Section
Solidification Algorithm	+++	+++	6.4.1
Cross-Diffusion Test 1	—	—	6.4.1
Cross-Diffusion Test 2	++	+	6.4.2
Diffusion Solver Test 3	+++	+++	6.4.3
Solidification Kinetics	++	++	6.4.4
Temperature Coupling	+++	+++	6.5.4
Porosity Coupling	++	++	6.5.5

+ fair ++ good +++ verified — no conclusive result

However, there is some doubt as to the transformation temperatures. The variation analysis indicates that these reservations arise from limitations of databases and graphite nucleation. Thus, the present work paves the way for future research:

1. How good is the agreement with experiments when the validity of thermodynamic databases is extended to large contents of carbon, silicon, and nickel?
2. Under what conditions is chunky graphite precipitated? Is cross-diffusion involved in this process, or is this structural transition only correlated to the cooling velocity and disabled nodularizing elements?
3. Are macrosegregations involved in chunky graphite formation, or is the change in cooling characteristics accompanied by a change in diffusion distances which appears to be the most probable reason, as the present work indicates?

4. Is it possible to approach to the experimental globular-cellular / chunky-dendritic transition in microstructure by additional models for cellular-eutectic growth and nucleation of graphite and austenite?
5. Is the cross-diffusion solver conclusively validated?
6. How important is solid-state graphite precipitation for feeding? Will microsegregation profiles be in better agreement with EPMA measurements when this effect is included in simulations?

All in all, it was shown that the chemical diffusion model is not applicable for this kind of alloy, because of high diffusive interactions. These cross-diffusion effects are also the chief cause for graphite promotion of nickel in cast iron, as demonstrated in the present work. Because of the implementation of a dendrite arm coarsening model, the software is sensitive to cooling characteristics. This causes a shift towards lower solidification temperatures with solidification time, which supports the hot spot effect below the feeder and is only predictable by coupling directly material and process simulations. The innovative coupling concept is valid, and the porosity predictions correlate well with experimental findings both qualitatively and quantitatively. GJSA-XNiCr 20-2 is a challenging material. This work was able to throw light on some of its mysteries. Because of the general formulation of the code, the model presented is not restricted to this particular alloy. It was successfully applied to GJL-350 cast iron and other material groups, such as the aluminum wrought alloys AA2024 and AA3104 mentioned at the beginning in Chapter 1.

8. Bibliography

- [AHH⁺02] ANDERSSON, J.O. ; HELANDER, T ; HÖGLUND, L. ; SHI, P.F. ; SUNDMAN, B.: Thermo-Calc and DICTRA, Computational Tool for Material Science. In: *CALPHAD* 26 (2002), pp. 273–312
- [AHJA90] ANDERSSON, J.O. ; HÖGLUND, L. ; JÖNSSON, B. ; AGREN, J.: Computer Simulation of Multicomponent Diffusional Transformations in Steel. In: PURDY, G.R. (editor): *Fundamentals and Applications of Ternary Diffusion*. 1990, pp. 153–163
- [Alb01] ALBERTY, R. A.: Use of Legendre Transforms in Chemical Thermodynamics. In: *Pure Appl. Chem.* 73 (2001), pp. 1349–1380
- [Avr40] AVRAMI, M.: Kinetics of Phase Change. In: *Journal of Chemical Physics* 8 (1940), pp. 212–224
- [BC85] BOETTINGER, W.J. ; CORIELL, S.R.: Microstructure Formation in Rapidly Solidified Alloys. In: *Proc. NATO Advanced Res. Workshop on Rapid Solidification Technologies: Science and Technology of the Undercooled Melt*. Theuern, Germany, 1985, pp. 81–109
- [Bea97] BEAVERSTOCK, R.C.: Secondary Dendrite Arm Coarsening and Microsegregation in Multicomponent Alloys. In: *Proc. 4th Decennial Intern. Conf. on Solidification Processing, Sheffield, UK* (1997), pp. 321–324
- [BF66] BRODY, H.D ; FLEMMINGS, M.C.: Solute Redistribution in Dendritic Solidification. In: *Trans. Met. Soc. AIME* 236 (1966), pp. 615
- [BH01] BJÄRBO, A. ; HÄTTESTRAND, M.: Complex carbide growth, dissolution, and coarsening in a modified 12 pct chromium steel - an experimental and theoretical study. In: *Met. Mat. Trans. A* (2001)
- [BS04] BELTRAN-SANCHEZ, L. ; STEFANESCU, D.M: A Quantitative Dendrite Growth Model and Analysis of Stability Concepts. In: *Met. Mat. Trans. A* 35A (2004), pp. 2004–2471
- [BSKB97] BANERJEE, D.K. ; SAMONDS, M.T. ; KATTNER, U.R. ; BOETTINGER, W.J.: Coupling of Phase Diagram Calculations for Multicomponent Alloys with Solidification Micromodels in Casting Simulation Software. In: *Proc. 4th Decennial Intern. Conf. on Solidification Processing, Sheffield, UK* (1997), pp. 354–357

- [BWBK02] BOETTINGER, W.J. ; WARREN, J.A. ; BECKERMANN, C. ; KARMAN, A.: Phase-field simulation of solidification. In: *Annual Review of Materials Research* 32 (2002), pp. 163–194
- [CB00] CAMPBELL, C.E. ; BOETTINGER, W.J.: Transient liquid-phase bonding in the Ni-Al-B system. In: *Met. Mat. Trans. A* 31A (2000), pp. 2835–2847
- [CBK02] CAMPBELL, C.E. ; BOETTINGER, W.J. ; KATTNER, U.R.: Development of a Diffusion mobility Database for Ni-Base Superalloys. In: *Acta Mater.* 50 (2002), pp. 775–792
- [CC92] CHEN, S.W. ; CHANG, Y.A.: Microsegregation in Solidification for Ternary Alloys. In: *Met. Mat. Trans. A* 23A (1992), pp. 1038–1043
- [CDGB08] CELENTANO, D.J. ; DARDATI, P.M. ; GODOY, L.A. ; BOERI, R.E.: Computational Simulation of Microstructure Evolution During Solidification of Ductile Iron. In: *Int. J. Cast Metals Res.* 21 (2008), pp. 416–426
- [CH58] CAHN, J.W. ; HILLIARD, J.E.: Free Energy of a Nonuniform System.1. Interfacial Free Energy. In: *Journal of Chemical Physics* 28 (1958), pp. 258–267
- [CIK⁺92] CRUSIUS, S. ; INDEN, G. ; KNOOP, U. ; HÖGLUND, L. ; AGREN, J.: On the Numerical Treatment of Moving Boundary Problems. In: *Zeitschrift für Metallkunde* 83 (1992), pp. 673–678
- [Dar49] DARKEN, L.S.: Diffusion of Carbon in Austenite with a Discontinuity in Composition. In: *Trans. AIMME* 180 (1949), pp. 430–438
- [DH74] DOUBLE, D.D. ; HELLAWELL, A.: Growth Structure of Various Forms of Graphite. In: LUX, B. (editor) ; MINKOFF, I. (editor) ; MOLLARD, F. (editor): *The Metallurgy of Cast Iron*, Georgi Publishing, Switzerland, 1974, pp. 509–525
- [DH95] DOUBLE, D.D. ; HELLAWELL, A.: The Nucleation and Growth of Graphite – The Modification of Cast Iron. In: *Acta Met. Mat.* 43 (1995), pp. 2435–2442
- [Dor91] DORAZIL, E.: *High Strength Austempered Ductile Iron*. Ellis Horwood Ltd., 1991
- [DS05] DIOSZEGI, A. ; SVENSSON, I.L.: Inverse Kinetic Analysis Method to Study Eutectic Growth. In: *Int. Journal of Cast Metals Res.* 18 (2005), pp. 41–45
- [Eva98] EVANS, L.C.: *Partial Differential Equations*. AMS Press, 1998
- [FLS96] FACKELDEY, M. ; LUDWIG, A. ; SAHM, P.R.: Coupled modelling of the solidification process predicting temperatures, stresses and microstructures. In: *Comp. Mat. Sci.* 12 (1996), pp. 194–199
- [Gre00] GREVEN, K.: *Makro- und Mikroskopisch gekoppelte numerische Simulation der diffusionskontrollierten Gefügeentwicklung bei der Erstarrung metallischer Legierungen*, Gießerei-Institut der RWTH Aachen, Germany, Diss., 2000

- [Has08] HASSE, S.: *Gefüge der Gusseisenlegierungen*. Schiele & Schön, 2008
- [Her65] HERFURTH, K.: Investigations Into the Influence of Various Additions on the Surface Tension of Liquid Cast Iron With the Aim of Finding Relationships Between the Surface Tension and the Occurrence of Various Forms of Graphite. In: *Freiberger Forschungshefte* 105 (1965), pp. 267
- [Hof02] HOFMEISTER, T.: *Numerische Simulation des Erstarrungsgefüges multikomponentiger Aluminiumlegierungen*, Gießerei-Institut der RWTH Aachen, Germany, Diss., 2002
- [Hou58] HOUSEHOLDER, A.S.: Unitary Triangularization of a Nonsymmetric Matrix. In: *J ACM* 5 (1958), Nr. 4, pp. 339–342
- [IRO09] IRON-01C BY BENGT HALLSTEDT: *Thermodynamic database for iron based alloys*. Material Chemistry at RWTH Aachen University, Germany, 2009
- [JEG99] JONES, S.F. ; EVANS, G.M. ; GALVIN, K.P.: The cycle of bubble production from a gas cavity in a supersaturated solution. In: *Advances in Colloid and Interface Science* 80 (1999), pp. 51–84
- [JR02] JACOT, A. ; RAPPAZ, M.: A pseudo-front tracking technique for the modelling of solidification microstructures in multi-component alloys. In: *Acta Materialia* 50 (2002), pp. 1909–1926
- [KBC96] KATTNER, U.R. ; BOETTINGER, W.J. ; CORIELL, S.R.: Application of Lukas' Phase Diagram Programs to Solidification Calculations of Multicomponent Alloys. In: *Zeitschrift für Metallkunde* 97 (1996), pp. 522–528
- [KC97] KRAFT, T. ; CHANG, Y.A.: Predicting Microstructure and Microsegregation in Multicomponent Alloys. In: *JOM* 49 (1997), pp. 20–28
- [KCF67] KATTAMIS, T.Z. ; COUGHLIN, J.C. ; FLEMINGS, M.C.: Influence of Coarsening on Dendrite Arm Spacing of Aluminum-Copper Alloys. In: *Trans. AIME* 239 (1967), pp. 1504–1511
- [KE96] KRAFT, T. ; EXNER, H.E.: Numerical simulation of solidification. Part 1 : Microsegregation in binary alloys. In: *Zeitschrift für Metallkunde* 87 (1996), pp. 598–611
- [Kra95] KRAFT, T.: *Numerische Simulation der Erstarrung in mehrkomponentigen Legierungen*, TH Darmstadt, Darmstadt, Germany, Diss., 1995
- [Lac99] LACAZE, J.: Solidification of spheroidal graphite cast irons: III. Microsegregation related effects. In: *Acta Materialia* 47 (1999), pp. 3779–3792
- [LAS⁺09] LARRAÑGA, P. ; ASENJO, I. ; SERTUCHA, J. ; SUÁREZ, R. ; FERRER, I. ; LACAZE, J.: Effect of Antimony on the eutectic Reaction of Heavy Section spheroidal Graphite Castings. In: *Int. Journal of Cast Metals Research* 22 (2009), pp. 192–195

- [LCB⁺98] LIPPARD, H.L. ; CAMPBELL, C.E. ; BJÖRKLIND, T. ; BORGGREN, U. ; KELLGREN, P. ; DRAVID, V.P. ; OLSON, G.B.: Microsegregation behavior during solidification and homogenization of AerMet100 steel. In: *Met. Mat. Trans. B* 29B (1998)
- [LFS07] LUKAS, H.L. ; FRIES, S.G. ; SUNDMANN, B.: *Computational Thermodynamics*. Cambridge University Press NY, 2007
- [LLS85] LIU, P.C ; LOPER, C.R. ; SHIRVANT, S.: Inoculation of Gray Cast Irons With Carbonaceous Materials. In: *AFS Transactions* 93 (1985), pp. 501
- [LLWL83] LIU, P.C ; LI, C.L. ; WU, D.H. ; LOPER, C.R.: SEM Study of Chunky Graphite in Heavy-Section Ductile Iron. In: *AFS Transactions* 91 (1983), pp. 119–126
- [LMMT74] LUX, B. ; MINKOFF, I. ; MOLLARD, F. ; THURY, E.: In: LUX, B. (editor) ; MINKOFF, I. (editor) ; MOLLARD, F. (editor): *The Metallurgy of Cast Iron*, Georgi Publishing, Switzerland, 1974, pp. 495–508
- [Min83] MINKOFF, I.: *The Physical Metallurgy of Cast Iron*. John Wiley & Sons, 1983
- [ML74] MINKOFF, I. ; LUX, B.: Graphite Growth from Metallic Solution. In: LUX, B. (editor) ; MINKOFF, I. (editor) ; MOLLARD, F. (editor): *The Metallurgy of Cast Iron*, Georgi Publishing, Switzerland, 1974, pp. 473–491
- [MOB07] MOB2: *Mobility database for iron based alloys*. Thermo-Calc AB, Stockholm, Sweden, 2007
- [NKH⁺07] NEUMANN, L. ; KOPP, R. ; HIRT, G. ; JANNOT, E. ; GOTTSTEIN, G. ; HALLSTEDT, B. ; SCHNEIDER, J.M. ; PUSTAL, B. ; BÜHRIG-POLACZEK, A.: Aluminum Through-Process Modeling: From Casting to Cup Drawing (TP C6). In: GOTTSTEIN, G. (editor): *Integral Materials Modeling: Towards Physics-Based Through-Process Models*. Wiley, 2007
- [Pat80] PATANKAR, S.V.: *Numerical Heat Transfer and Fluid Flow*. Hemisphere Publications, NY, 1980
- [PBL⁺03] PUSTAL, B ; BÖTTGER, B ; LUDWIG, A ; SAHM, P.R ; BÜHRIG-POLACZEK, A.: Simulation of Macroscopic Solidification with an Incorporated One-Dimensional Microsegregation Model Coupled to Thermodynamic Software. In: *Metallurgical and Materials Transactions B* 34B (2003), pp. 411–419
- [PBS⁺07] PUSTAL, B. ; BERGER, R. ; SUBASIC, E. ; LASCHET, G. ; SCHÄFER, W. ; BARTELS, C. ; BÜHRIG-POLACZEK, A.: Multi-Phase Microsegregation Modelling During Solidification of Ductile Iron. In: *Solidification Processing 2007*. Sheffield, UK, July 2007, pp. 89–93
- [PBS⁺09] PUSTAL, B. ; BERGER, R. ; SUBASIC, E. ; LASCHET, G. ; SCHÄFER, W. ; BÜHRIG-POLACZEK, A.: A Multi-Phase Micro-Segregation Model. In: *Int. Journal of Cast Metals Research* 22 (2009), pp. 252–255

- [PSH⁺10] PUSTAL, B. ; SUBASIC, E. ; HALLSTEDT, B. ; SCHÄFER, W. ; BARTELS, C. ; SIEBERT, H. ; SCHNEIDER, J.M. ; BÜHRIG-POLACZEK, A.: Modeling Porosity Formation in Alloyed SGI Castings Using a Physics Based Material Model. In: *Advanced Engineering Materials* 12 (2010), pp. 158–169
- [PSS⁺09] PUSTAL, B. ; SIEBERT, H. ; SUBASIC, E. ; HALLSTEDT, B. ; SCHNEIDER, J.M. ; BÜHRIG-POLACZEK, A.: Simulation of Alloyed Cast Iron on Process and Material Scale: A Physics and CALPHAD based Approach. In: COCKCROFT, S. L. (editor) ; MAIJER, D.M. (editor): *Int. Conf. on Modeling of Casting, Welding and Advanced Solidification Processes XII*. Vancouver, Canada : TMS, 7.-14. June 2009, pp. 261–268
- [PWB⁺07] PUSTAL, B. ; WARNKEN, N. ; BUSSMANN, M. ; RENNER, B. ; HOLLANDS, A.-P. ; WALTER, C. ; HALLSTEDT, B. ; SCHNEIDER, J.M. ; SENK, D. ; MICHAELI, W. ; STEINBACH, I. ; BÜHRIG-POLACZEK, A.: Microstructure Modeling during Solidification of Castings. In: GOTTSTEIN, G. (editor): *Integral Materials Modeling: Towards Physics-Based Through-Process Models*. Wiley, 2007
- [RA06] RADY, M.A. ; ARQUIS, E.: A Micro-macro Model for Numerical Simulation of Dendritic Alloy Solidification. In: *Int. Conf. on Modeling of Casting, Welding and Advanced Solidification Processes XI*. Opio, France, 2006, pp. 259–266
- [RB99] RAPPAZ, M. ; BOETTINGER, W.J.: On Dendritic Solidification of Multicomponent Alloys with Unequal Liquid Diffusion Coefficients. In: *Acta Materialia* 47 (1999), pp. 2305–2319
- [RBD03] RAPPAZ, M. ; BELLET, M. ; DEVILLE, M.: *Numerical Modeling in Material Science and Engineering*. Springer Verlag, Berlin Heidelberg, 2003
- [RBMS01] RUXANDA, R. ; BELTRAN-SANCHEZ, L. ; MASSONE, J. ; STEFANESCU, D.M.: On the Eutectic Solidification of Spheroidal Graphite Iron: An Experimental and Mathematical Modeling Approach. In: *Proceedings of Cast Iron Division, AFS 105th Casting Congress* Bd. 109. Dallas, USA : American Foundry Soc., Des Plaines (IL), April, May 2001, pp. 1037–1048
- [RHE86] ROÓSZ, A. ; HALDER, E. ; EXNER, H.E.: Numerical-Calculation of Microsegregation in Coarsened Dendritic Microstructures. In: *Mat. Sci. Tech. Ser. 2* (1986), pp. 1149–1155
- [RR01] RONTÓ, V. ; ROÓSZ, A.: The Effect of Cooling Rate and Composition on the Secondary Dendrite Arm Spacing During Solidification. In: *Int. J. Cast Metals Res.* 13 (2001), pp. 337–342
- [SC] SUNDMAN, BO ; CHEN, QUING ; THERMO-CALC SOFTWARE AB (editor): *tq-interface, Programmers Guide and Examples*. Version 5. Stockholm Technology Park, Björnäsvägen 21, SE-11347 Stockholm, Sweden: Thermo-Calc Software AB. – www.thermo-calc.se

- [Sch61] SCHELLENG, R.D.: Nickel Alloyed Austenitic Ductile Iron Graphite Structures. In: *AFS Transactions* 69 (1961), pp. 725–730
- [SCK03] SHAWN, A ; CEFALU, S.A. ; KRANE, M.J.M.: Microsegregation in Open and Closed Multicomponent Systems. In: *Mat. Sci. Eng. A* 359 (2003), pp. 91–99
- [SD99] SVENSSON, I. ; DUGIC, I.: Modelling of volumes in cast iron solidification to predict shrinkage. In: *IJCMR* 11 (1999), pp. 489–494
- [SE92] SASIKUMAR, R. ; EXNER, H.E.: Coupling of Microsegregation Models to Heat Flow simulations in Castings. In: *Modelling and Simulation in Materials Science and Engineering* 1 (1992), pp. 19–27
- [SG74] SADOCHA, J.P. ; GRUZLESKI, J.E.: The Mechanism of Graphite Spheroid Formation in Pure Fe-C-Si Alloys. In: LUX, B. (editor) ; MINKOFF, I. (editor) ; MOLLARD, F. (editor): *The Metallurgy of Cast Iron*, Georgi Publishing, Switzerland, 1974, pp. 509–525
- [SOYF84] SU, K. ; OHNAKA, I. ; YAMAUCHI, I. ; FUKUSAKO, T: Computer Simulation of Solidification of Nodular Cast Iron. In: *Proc. of the 3rd International Symposium on the Metallurgy of Cast Iron*. Stockholm, Sweden : Elsevier, New York, 1984, pp. 181–189
- [Spe93] SPEAR, W.M. ; HENNING, W.A. (editor) ; MERCER, J. (editor): *Ductile Iron Handbook*. American Foundrymen's Society, Inc., 1993. – pp. 52–65
- [Ste99] STEFAN, J.: In: *Sitzungsberichte der Mathematisch-Naturwissenschaftlichen Classe der Kaiserlichen Akademie der Wissenschaften* 98 (1899), pp. 473
- [Ste93] STEFANESCU, D.M. ; HENNING, W.A. (editor) ; MERCER, J. (editor): *Ductile Iron Handbook*. American Foundrymen's Society, Inc., 1993. – pp. 1–19
- [Ste02] STEFANESCU, D.M: *Science and Engineering of Casting Solidification*. Kluwer Academic / Plenum Publishers, 2002. – pp. 293
- [Stu04] STURM, J.C.: Stand der Simulation für Gusseisen. In: *Giesserei* 91 (2004), pp. 4
- [TCF06] TCFE4: *Thermodynamic database for iron based alloys*. Thermo-Calc AB, Stockholm, Sweden, 2006
- [TCF07] TCFE5: *Thermodynamic database for iron based alloys*. Thermo-Calc AB, Stockholm, Sweden, 2007
- [TG09] TOURET, D. ; GANDIN, CH.-A.: A Generalized Segregation Model for Concurrent Dendritic, Peritectic and Eutectic Solidification. In: *Acta Mater* 57 (2009), pp. 2066–2079

-
- [WB96] WANG, C.Y. ; BECKERMANN, C.: Equiaxed Dendritic Solidification with Convection: Part I. Multiscale/Multiphase Modeling. In: *Metallurgical and Materials Transactions* 27A (1996), pp. 2754–2764
- [XYD⁺03] XIE, F.Y. ; YAN, X,Y. ; DING, L. ; ZHANG, F. ; CHEN, S. ; CHU, M.G. ; CHANG, Y.A.: A Study of Microstructure an Microsegregation of Aluminum 7050 Alloy. In: *Mat. Sci. Eng. A-Struct.* 355 (2003), pp. 144–153
- [ZSE87] ZHOU, J. ; SCHMITZ, W. ; ENGLER, S.: Untersuchung der Gefügebildung von Gußeisen mit Kugelgraphit bei langsamer Erstarrung. In: *Giessereiforschung* 39 (1987), pp. 55–70

A. Nomenclature and Abbreviations

Tab. A.1: Thermodynamic Variables

Variable	Description
a	Activity of a species
C_p	Specific heat capacity of a system
C_p^j	Specific heat capacity of a phase in a system
L_f	Latent heat of fusion
\hat{c}	Number of constraints in Gibbs' phase rule
F	Specific free energy of a system
\hat{f}	Number of thermodynamic degrees of freedom
G	Specific free energy of a system
G^j	Specific free energy of a phase in a system
$\tilde{\gamma}$	Activity coefficient of a species
H	Specific enthalpy of a system
H^j	Specific enthalpy of a phase in a system
μ	Chemical potential of a species in a phase
N	substance quantity
P	Pressure of a system
S	Entropy of a system
S^j	Entropy of a phase in a system
T	Temperature
U	Specific internal energy of a system
V	Volume of a system
v	Molar volume of a species or a phase
w	Weight specific concentration
x	Molar concentration
y	Constituent fraction of a sublattice site

Tab. A.2: Model Specific Variables

Variable	Description
A	Surface of a volume element
C	Curvature
D	Chemical diffusion coefficient
\mathbf{D}	Matrix of chemical diffusion coefficients
Δt	time step width
E_x	Relative failure in concentration
f	Molar phase fraction
f_V	Volume specific phase fraction
f_W	Weight specific phase fraction
ϕ	Local phase fraction
\mathbf{j}	Specific species flux
\mathbf{J}	Absolute species flux
$\hat{\mathbf{J}}$	Fixed species flux
\mathbf{K}	Coefficient matrix in the system of flux balance equations
l	Size of the RVE
λ	Dendrite arm spacing
$\dot{\lambda}$	Dendrite arm coarsening rate
m	Slope of the liquidus line
\mathbf{M}	Mobility matrix
\dot{h}	Specific heat rate = – specific heat extraction rate
r	Dendrite arm radius
R	Dendrite arm radius being larger than r
ρ	Density of a system or a phase
s	Position within the RVE
σ	Relative surface at the boundary of a volume element
t	Time
\dot{T}	Temperature rate = – cooling rate

Continuing next page ...

... *Continuing Model Specific Variables*

T_{act}	Activation temperature of a phase
T_{ini}	Initial temperature of a simulation
T_{end}	Final temperature of a simulation
T_{liq}	Liquidus temperature of an alloy (equilibrium)
\mathbf{u}	Velocity of the phase solid-liquid interface
ΔV^{R}	Volume of the RVE
\mathbf{X}	Vector of unknown concentrations in the system of flux balance equations
\hat{x}	Fixed Concentration (Dirichlet Boundary)
\tilde{x}	Input concentration for thermodynamic precipitation simulations
*x	Interface concentration
\dot{X}	Specific species source term in the conservation equation
\mathbf{Y}	Solution vector in the system of flux balance equations

Tab. A.3: Constants, Parameters and Factors

Variable	Description
\mathcal{C}	Definable constant
ε	Epsilon environment (small number)
ϵ_f	Convergence criterion for fraction liquid
ϵ_x	Convergence criterion for the depending species in the liquid phase
θ	Underrelaxation factor weighting the previous (0) and the current (1) solution
g	Geometry coefficient for diffusion
\tilde{g}	Geometry coefficient for dendrite arm coarsening
γ	Interface energy between matrix and precipitated phase
$\hat{\gamma}$	Volume expansion coefficient

Continuing next page ...

... *Continuing Constants, Parameters and Factors*

M	Molar mass of a component or a phase
p	General parameter for a polynomial
R	General gas constant

Tab. A.4: Indices and Bounds

Variable	Description
*	Quantity at the solid-liquid interface
b	Index defined in the context
c	Quantity at the center (of a finite volume element)
e	Quantity at the eastern boundary (of a finite volume element)
i	Index for species
j	Index for phases
k	Index for finite volume elements
L	Index for liquid phase
m	Number of solid phases
n	Number of alloying elements
ν	Quantity referring to the current time step
ω	Quantity referring to the previous time step
S	Solid phase index representing one or all solid phases, respectively
w	Quantity at the western boundary (of a finite volume element)
z	Number of volume elements

Tab. A.5: Abbreviations and Definitions

Variable	Description
$\langle \rangle$	Averaged value of a quantity
DAS	Dendrite Arm Spacing
DTA	Differential thermal analysis
DBC	Dirichlet boundary condition, i.e. an imposed concentration
Divergence Theorem	Transforms a volume integral into a surface integral and vice versa by : $\int_{V^0} \text{div}(\mathbf{v}) dV = \int_{A^0} \mathbf{v} \cdot \mathbf{n} dA$
EDX	Electron dispersive X-ray
EPMA	Electron probe micro analysis
FDM	Finite differences method
FEM	Finite element method
FVM	Finite volume method
GES	Postfix for files containing thermodynamic data in binary format retrieved by Thermo-Calc
HNBC	Homogeneous Neumann boundary condition, i.e. no species flux
\mathbf{n}	normal vector at the boundary of each phase
NBC	Generalized Neumann boundary condition, i.e. a fixed species flux
RVE	Representative volume element, the control volume for microsegregation simulation
SGI	Spheroidal graphite iron
SEM	Scanning electron microscopy
TDMA	Tri-diagonal matrix algorithm
\mathbf{v}	General vector symbol
WDX	Wavelength dispersive X-ray

B. Deduction of Averaged Quantities

In order to solve the discretized species transport equation (C.6), the derivative of concentration in time and hence an average value for each species needs to be deduced at each finite volume element ΔV_k . As pointed out in Section 4.3.4, the average concentration of each species in each finite volume element depends on the geometry of the RVE and the variation of the local phase fraction $\phi^j(s)$ and concentration $x_1^j(s)$ which are both functions of the position s . For the discretization carried out in Appendix C, local phase fraction and composition of phases are required as functions of grid point values. Therefore, appropriate weighting and averaging parameters are deduced in this appendix. To simplify the following integration procedure, local phase fraction $\phi^j(\Delta V)$ and concentrations $x_1^j(\Delta V)$ are approximated as functions of volume differences ΔV , that are referenced to the center of these elements, as shown in Fig. 4.4. Depending on the selected geometry, the volume may vary in a non-linear manner. However, it is assumed that all variables vary piecewise linear between grid points. The average value of the local phase fraction $\langle \phi^j \rangle^{\Delta V_{e,w}}$ in the arbitrary volume $\Delta V_{e,w}$, which is constrained by the western w and eastern e boundary, is the given by:

$$\langle \phi^j \rangle^{\Delta V_{e,w}} = \int_0^{\Delta V_{e,w}} \frac{\phi_w^j + (\phi^j)' \Delta V}{\Delta V_{e,w}} d(\Delta V) = \phi_w^j + (\phi^j)' \frac{1}{2} \Delta V_{e,w}. \quad (\text{B.1})$$

Here, $(\phi^j)'$ is the first derivative of the local phase fraction with regard to the volume difference ΔV . This derivative is formulated applying values at the grid points $k-1$, k , and $k+1$. Here, and throughout this work, volume differences are used, as shown in Fig. 4.4. In general, the slope of ϕ^j to the west of the volume element is different from that to the east. Therefore, the average value of the local phase fraction $\langle \phi^j \rangle^{\Delta V_k}$ in a volume element is determined by weighting the average value of the local phase fraction to the west and east, respectively. This procedure is based on splitting up finite volume elements at the center of gravity into the partial volumes: $\Delta V_k = \Delta V_{k,w} + \Delta V_{e,k}$. This yields:

$$\begin{aligned} \langle \phi^j \rangle^{\Delta V_k} &= \frac{\langle \phi^j \rangle^{\Delta V_{k,w}} \Delta V_{k,w} + \langle \phi^j \rangle^{\Delta V_{e,k}} \Delta V_{e,k}}{\Delta V_k} \\ &= \phi_k^j + (\phi_{k-1}^j - \phi_k^j) \mathcal{C}_{w2} + (\phi_{k+1}^j - \phi_k^j) \mathcal{C}_{e2}. \end{aligned} \quad (\text{B.2})$$

The weighting parameters \mathcal{C}_{w2} and \mathcal{C}_{e2} defined through this equation, are given in Eq. (B.9). Fig. 4.4 shows that these weighting parameters involve the volume ΔV_k , which is

limited by the boundaries of each volume element, the partial volumes from the center to the west $\Delta V_{k,w}$ and east $\Delta V_{e,k}$, and the volumes $\Delta V_{k,k-1}$ and $\Delta V_{k+1,k}$ which correspond to distances to the center of neighboring volume elements. Through the introduction of the volume element fraction $f_V^{\Delta V_k} = \Delta V_k / \Delta V^R$ and the volume ΔV^R of the RVE, the average phase fraction $\langle f_V^j \rangle^{\Delta V_k}$ of phase j in volume element ΔV_k may be written as:

$$\langle f_V^j \rangle^{\Delta V_k} = \langle \phi^j \rangle^{\Delta V_k} f_V^{\Delta V_k}. \quad (\text{B.3})$$

The average value $\langle x_i^j \rangle^{\Delta V_{e,w}^j}$ of the concentration x_i^j depends on the development of $\phi^j(\Delta V)$ and the concentration function $x_i^j(\Delta V)$. Thus, the averaged concentration in the volume $\Delta V_{e,w}^j = \Delta V_{e,w} \langle \phi^j \rangle^{\Delta V_{e,w}}$ that is occupied by phase j is given by:

$$\langle x_i^j \rangle^{\Delta V_{e,w}^j} = \frac{\langle \phi^j x_i^j \rangle^{\Delta V_{e,w}}}{\langle \phi^j \rangle^{\Delta V_{e,w}}}. \quad (\text{B.4})$$

To solve this equation, first the averaged product $\langle \phi^j x_i^j \rangle^{\Delta V_{e,w}}$ needs to be determined. This is achieved by integration over the local phase fraction function $\phi^j(\Delta V)$ and concentration function $x_i^j(\Delta V)$:

$$\begin{aligned} \langle \phi^j x_i^j \rangle^{\Delta V_{e,w}} &= \int_0^{\Delta V_{e,w}} \frac{[\phi_w^j + (\phi^j)' \Delta V] [x_{i,w}^j + (x_i^j)' \Delta V]}{\Delta V_{e,w}} d(\Delta V) \\ &= \phi_w^j x_{i,w}^j + \left[\phi^j (x_i^j)' + (\phi^j)' x_i^j \right] \frac{1}{2} \Delta V_{e,w} + (\phi^j)' (x_i^j)' \frac{1}{3} \Delta V_{e,w}^2. \end{aligned} \quad (\text{B.5})$$

The average value of the product of local phase fraction and concentration in a finite volume element is obtained by weighting the average values to the west and east of the element:

$$\begin{aligned} \langle \phi^j x_i^j \rangle^{\Delta V_k} &= \frac{\langle \phi^j x_i^j \rangle^{\Delta V_{k,w}} \Delta V_{k,w} + \langle \phi^j x_i^j \rangle^{\Delta V_{e,k}} \Delta V_{e,k}}{\Delta V_k} \\ &= \phi_k^j x_{i,k}^j \frac{\Delta V_{k,w}}{\Delta V_k} - \left[\phi_k^j (x_{i,w}^j)' + (\phi_w^j)' x_{i,k}^j \right] \frac{\Delta V_{k,w}^2}{2\Delta V_k} + (\phi_w^j)' (x_{i,w}^j)' \frac{\Delta V_{k,w}^3}{3\Delta V_k} \\ &+ \phi_k^j x_{i,k}^j \frac{\Delta V_{e,k}}{\Delta V_k} + \left[\phi_k^j (x_{i,e}^j)' + (\phi_e^j)' x_{i,k}^j \right] \frac{\Delta V_{e,k}^2}{2\Delta V_k} + (\phi_e^j)' (x_{i,e}^j)' \frac{\Delta V_{e,k}^3}{3\Delta V_k}. \end{aligned} \quad (\text{B.6})$$

To allow this product to be used in the discretized species transport equation (C.6), grid point values need to be introduced. Thus, the concentration x_i^j at the grid points $k-1$, k , and $k+1$ are multiplied by the corresponding averaging parameters \mathcal{C}_w^j , \mathcal{C}_c^j , and \mathcal{C}_e^j :

$$\langle \phi^j x_i^j \rangle^{\Delta V_k} = \mathcal{C}_w^j x_{i,k-1}^j + \mathcal{C}_c^j x_{i,k}^j + \mathcal{C}_e^j x_{i,k+1}^j . \quad (\text{B.7})$$

The averaging parameters introduced through Eq. (B.7) are obtained from rearranging Eq. (B.6) as follows:

$$\begin{aligned} \mathcal{C}_w^j &= \phi_k^j \mathcal{C}_{w2} + (\phi_{k-1}^j - \phi_k^j) \mathcal{C}_{w3} \\ \mathcal{C}_c^j &= \phi_k^j + (\phi_{k-1}^j - 2\phi_k^j) \mathcal{C}_{w2} + (\phi_k^j - \phi_{k-1}^j) \mathcal{C}_{w3} \\ &\quad + (\phi_{k+1}^j - 2\phi_k^j) \mathcal{C}_{e2} + (\phi_k^j - \phi_{k+1}^j) \mathcal{C}_{e3} \\ \mathcal{C}_e^j &= \phi_k^j \mathcal{C}_{e2} + (\phi_{k+1}^j - \phi_k^j) \mathcal{C}_{e3} . \end{aligned} \quad (\text{B.8})$$

Here and in Eq. (B.2), the phase-independent weighting parameters referring to the west \mathcal{C}_{w2} , \mathcal{C}_{w3} and east \mathcal{C}_{e2} , \mathcal{C}_{e3} with respect to the center of each finite volume element are applied as follows:

$$\begin{aligned} \mathcal{C}_{w2} &= \frac{\Delta V_{k,w}^2}{2\Delta V_{k,k-1}\Delta V_k} , & \mathcal{C}_{w3} &= \frac{\Delta V_{k,w}^3}{3\Delta V_{k,k-1}^2\Delta V_k} , \\ \mathcal{C}_{e2} &= \frac{\Delta V_{e,k}^2}{2\Delta V_{k+1,k}\Delta V_k} , & \mathcal{C}_{e3} &= \frac{\Delta V_{e,k}^3}{3\Delta V_{k+1,k}^2\Delta V_k} . \end{aligned} \quad (\text{B.9})$$

C. Discretization of Governing Equations

C.1 Species Conservation Equation

The species conservation equation (4.2) is discretized applying the finite volume method (FVM) explained in Section 2.5. For spatial discretization, this equation is integrated over the element volume ΔV_k using the averaged quantities according to Eq. (B.5). For discretization in time an integration over the time step width Δt is carried out in a first instance:

$$\int_{\Delta t} \int_{\Delta V_k} \frac{\partial \langle \phi x_i \rangle^{\Delta V_k}}{\partial t} dV dt = - \int_{\Delta t} \int_{\Delta V_k} \text{div}(\phi \mathbf{j}_i) dV dt + \int_{\Delta t} \int_{\Delta V_k} \langle \phi \rangle^{\Delta V_k} \dot{X}_i dV dt. \quad (\text{C.1})$$

With reference to Tab. A.5, a volume integral may be transformed into a corresponding surface integral applying the divergence theorem. Because of the geometry concept, the surface σ is introduced relating to the volume of the RVE according to Eq. (4.11). This implicates that the volume terms need to be related to the RVE volume, too:

$$\int_{\Delta t} \int_{\Delta V_k} \frac{\partial \langle \phi x_i \rangle^{\Delta V_k}}{\partial t} \frac{dV}{\Delta V^R} dt = - \int_{\Delta t} \int_{\sigma_k} \phi \mathbf{j}_i d\sigma dt + \int_{\Delta t} \int_{\Delta V_k} \langle \phi \rangle^{\Delta V_k} \dot{X}_i \frac{dV}{\Delta V^R} dt. \quad (\text{C.2})$$

By introducing the volume fraction $f_V^{\Delta V_k} = \Delta V_k / \Delta V^R$ of a finite volume element and after integration over volume and time follows:

$$\langle \phi^j x_i^j \rangle^{\Delta V_k} \Big|_{\omega t}^{\nu t} f_V^{\Delta V_k} = - \left[\sigma_e \phi_e^j \mathbf{j}_{i,e}^j \Delta t - \sigma_w \phi_w^j \mathbf{j}_{i,w}^j \Delta t \right] + \langle \phi^j \rangle^{\Delta V_k} \dot{X}_i^j \Delta t f_V^{\Delta V_k}. \quad (\text{C.3})$$

The underrelaxation factor θ is introduced to allow for arbitrary mixtures of implicit and explicit solution schemes in time. This factor weights concentration solutions ${}_{\omega}x$ and ${}_{\nu}x$ from the previous and current time step for which concentration gradients and source terms are evaluated, respectively. This means that any underrelaxation factor within the range $[0, 1]_{\mathbb{R}}$ may be selected where 0 represents a purely explicit and 1 a purely implicit scheme. The actual underrelaxation factor θ is attributed ν to indicate the reference to

the current time step. Be ${}_{\nu}\theta$ defined as a fraction of the time step width $\Delta t = {}_{\nu}t - {}_{\omega}t$ in positive direction of the time axes and its complementary function ${}_{\omega}\theta$ in negative direction with reference to the time moment t :

$${}_{\nu}\theta = \frac{t - {}_{\omega}t}{\Delta t} \quad \text{and} \quad {}_{\omega}\theta = \frac{{}_{\nu}t - t}{\Delta t}. \quad (\text{C.4})$$

Furthermore, for convenience of notation, the following abbreviation is introduced:

$${}_{\nu}\theta + {}_{\omega}\theta = \left[\theta \right]_{-{}_{\omega}\theta}^{{}_{\nu}\theta}. \quad (\text{C.5})$$

Since ${}_{\nu}\theta$ and ${}_{\omega}\theta$ are complementary functions, it is feasible to multiply only terms containing the time step width Δt by $({}_{\nu}\theta + {}_{\omega}\theta)$ which yields:

$$\langle \phi^j x_i^j \rangle^{\Delta V_k} \Big|_{\omega t}^{{}_{\nu}t} f_V^{\Delta V_k} = - \left[\sigma_e \phi_e^j {}_{\nu, \omega} \mathbf{j}_{i, e}^j \theta - \sigma_w \phi_w^j {}_{\nu, \omega} \mathbf{j}_{i, w}^j \theta \right]_{-{}_{\omega}\theta}^{{}_{\nu}\theta} \Delta t + \langle \phi^j \rangle^{\Delta V_k} \left[{}_{\nu, \omega} \dot{X}_i^j \theta \right]_{-{}_{\omega}\theta}^{{}_{\nu}\theta} \Delta t f_V^{\Delta V_k}. \quad (\text{C.6})$$

Here, the chemical flux ${}_{\nu, \omega} \mathbf{j}$ and species source term ${}_{\nu, \omega} \dot{X}$ are optionally attributed by the subscripts ν and ω . This indicates that the particular quantity refers to the current ${}_{\nu}t$ or previous time ${}_{\omega}t$ when it is multiplied by ${}_{\nu}\theta$ or ${}_{\omega}\theta$, respectively. For convenience of notation, these subscripts are omitted throughout the present work.

Eq. B.4 shows the dependency of the average concentration $\langle x_i^j \rangle^{\Delta V_k}$ in phase j within volume element ΔV_k from the local phase fraction. However, the average values of local phase fraction in volume elements close to the solid-liquid interface vary from time step to time step which is due to the interpolation procedure pointed out in Fig. 4.3. For this purpose, the impact of these variations on the transient change in average concentration is eliminated applying the product rule:

$$\frac{\partial \langle \phi^j x_i^j \rangle^{\Delta V_k}}{\partial t} = \frac{\partial (\langle x_i^j \rangle^{\Delta V_k} \langle \phi^j \rangle^{\Delta V_k})}{\partial t} = \frac{\partial \langle \phi^j \rangle^{\Delta V_k}}{\partial t} \langle x_i^j \rangle^{\Delta V_k} + \langle x_i^j \rangle^{\Delta V_k} \frac{\partial \langle \phi^j \rangle^{\Delta V_k}}{\partial t}. \quad (\text{C.7})$$

Since only the average product of concentration and phase fraction is significant for Eq. (C.6), it is unreasonable to divide the averaged product $\langle \phi^j x_i^j \rangle^{\Delta V_k}$ by the average local phase fraction $\langle \phi^j \rangle^{\Delta V_k}$ to obtain the change in average concentration free from variations of the local phase fraction at the interface. Instead, Eq. (C.7) is rearranged after discretization as follows:

$$\langle x_i^j \rangle^{\Delta V_k} \Big|_{\omega t}^{{}_{\nu}t} \langle \phi^j \rangle^{\Delta V_k} = \langle \phi^j x_i^j \rangle^{\Delta V_k} \Big|_{\omega t}^{{}_{\nu}t} - \langle \phi^j \rangle^{\Delta V_k} \Big|_{\omega t}^{{}_{\nu}t} \langle x_i^j \rangle^{\Delta V_k}. \quad (\text{C.8})$$

Thus, it is only necessary to add the term taking account of changes in local phase fraction on the right hand side of Eq. (C.6) as follows:

$$\begin{aligned}
\langle \phi^j x_i^j \rangle_{\omega t}^{\Delta V_k} \Big|_{\omega t}^{\nu t} f_V^{\Delta V_k} &= - \left[\sigma_e \phi_e^j \mathbf{j}_{i,e}^j \theta - \sigma_w \phi_w^j \mathbf{j}_{i,w}^j \theta \right]_{-\omega t}^{\nu t} \Delta t \\
&+ \langle \phi^j \rangle_{\omega t}^{\Delta V_k} \Big|_{\omega t}^{\nu t} \langle x_i^j \rangle_{\omega t}^{\Delta V_k} f_V^{\Delta V_k} + \langle \phi^j \rangle_{\omega t}^{\Delta V_k} \left[\dot{X}_i^j \theta \right]_{-\omega t}^{\nu t} \Delta t f_V^{\Delta V_k}.
\end{aligned} \tag{C.9}$$

The specific diffusive flux \mathbf{j}_i^j in Eq. (C.6) is constituted according to Eq. (2.18), but separating for diagonal and off-diagonal terms arising from the cross-diffusion model. Gradients for diagonal terms may be evaluated selecting underrelaxation factors ν in the range $[0, 1]_{\mathbb{R}}$, while off-diagonal diffusive fluxes $\Delta \mathbf{J}_{ib}^j$ with $b \neq i$ are modeled applying a purely explicit scheme with $\nu = 0$. Introducing this yields:

$$\begin{aligned}
\langle \phi^j x_i^j \rangle_{\omega t}^{\Delta V_k} \Big|_{\omega t}^{\nu t} f_V^{\Delta V_k} &= \left[\sigma_e \phi_e^j D_{i,e}^j \mathbf{grad}(x_{i,e}^j) \theta - \sigma_w \phi_w^j D_{i,w}^j \mathbf{grad}(x_{i,w}^j) \theta \right]_{-\omega t}^{\nu t} \Delta t \\
&- \sum_{b=1, b \neq i}^n \Delta \mathbf{J}_{ib}^j \Delta t + \langle \phi^j \rangle_{\omega t}^{\Delta V_k} \Big|_{\omega t}^{\nu t} \langle x_i^j \rangle_{\omega t}^{\Delta V_k} f_V^{\Delta V_k} + \langle \phi^j \rangle_{\omega t}^{\Delta V_k} \left[\dot{X}_i^j \theta \right]_{-\omega t}^{\nu t} \Delta t f_V^{\Delta V_k}.
\end{aligned} \tag{C.10}$$

The divergence of the absolute cross-diffusion flux is given by the difference between the flux at the eastern and western boundary of each finite volume element:

$$\begin{aligned}
\sum_{b=1, b \neq i}^n \Delta \mathbf{J}_{ib}^j &= \sum_{b=1, b \neq i}^n \mathbf{J}_{ib,e}^j - \mathbf{J}_{ib,w}^j \\
&= \sigma_w \phi_w^j \sum_{b=1, b \neq i}^n \mathbf{D}_{ib,w}^j \mathbf{grad}(x_{b,w}^j) - \sigma_e \phi_e^j \sum_{b=1, b \neq i}^n \mathbf{D}_{ib,e}^j \mathbf{grad}(x_{b,e}^j).
\end{aligned} \tag{C.11}$$

Casting Eq. (4.16) into Eq. (C.10) to substitute the average product $\langle \phi^j x_i^j \rangle_{\omega t}^{\Delta V_k}$ by introducing the concentrations at grid points and relating these to the current ν and previous ω time step yields, after rearrangement for the unknown concentrations νx_i^j , the line entries of the system of equations to be solved:

$$\begin{aligned}
& \left[\nu \mathcal{C}_w^j f_V^{\Delta V_k} - \sigma_w \phi_w^j D_{i,w}^j \frac{\nu \theta \Delta t}{\Delta s_{k-1}} \right] \nu x_{i,k-1}^j \\
& + \left[\nu \mathcal{C}_c^j f_V^{\Delta V_k} + \sigma_e \phi_e^j D_{i,e}^j \frac{\nu \theta \Delta t}{\Delta s_{k+1}} + \sigma_w \phi_w^j D_{i,w}^j \frac{\nu \theta \Delta t}{\Delta s_{k-1}} \right] \nu x_{i,k}^j \\
& + \left[\nu \mathcal{C}_e^j f_V^{\Delta V_k} - \sigma_e \phi_e^j D_{i,e}^j \frac{\nu \theta \Delta t}{\Delta s_{k+1}} \right] \nu x_{i,k+1}^j = \\
& \left[\omega \mathcal{C}_w^j \omega x_{i,k-1}^j + \omega \mathcal{C}_c^j \omega x_{i,k}^j + \omega \mathcal{C}_e^j \omega x_{i,k+1}^j \right] f_V^{\Delta V_k} \\
& + \left[\sigma_e \phi_e^j D_{i,e}^j \mathbf{grad}(x_{i,e}^j) - \sigma_w \phi_w^j D_{i,w}^j \mathbf{grad}(x_{i,w}^j) \right] \omega \theta \Delta t \\
& - \sum_{b=1, b \neq i}^n \Delta \mathbf{J}_{ib}^j \Delta t + \langle \phi^j \rangle^{\Delta V_k} \Big|_{\omega^t} \langle x_i^j \rangle^{\Delta V_k} f_V^{\Delta V_k} + \langle \phi^j \rangle^{\Delta V_k} \left[\dot{X}_i^j \theta \right]_{-\omega^t}^{\nu \theta} f_V^{\Delta V_k} \Delta t.
\end{aligned} \tag{C.12}$$

In each phase, for both, the first grid point at the western boundary and the last grid point at the eastern boundary only one neighboring grid point is present. For these grid points appropriate boundary conditions need to be derived to solve the diffusion problem. Here, two types of boundary conditions are applied: Dirichlet boundary conditions where fixed concentrations are imposed and Neumann boundary conditions where fixed species fluxes across the boundary are assumed. In the case of Dirichlet boundary conditions, the predefined concentrations are not part of the solution. Therefore, all terms in Eq. (C.12) containing fixed concentrations are put on the right side of the corresponding line entry. In the following example, a Dirichlet condition at the western boundary is applied:

$$\begin{aligned}
& \left[\nu \mathcal{C}_c^j f_V^{\Delta V_k} + \sigma_e \phi_e^j D_{i,e}^j \frac{\nu \theta \Delta t}{\Delta s_{k+1}} + \sigma_w \phi_w^j D_{i,w}^j \frac{\nu \theta \Delta t}{\Delta s_{k-1}} \right] \nu x_{i,k}^j \\
& + \left[\nu \mathcal{C}_e^j f_V^{\Delta V_k} - \sigma_e \phi_e^j D_{i,e}^j \frac{\nu \theta \Delta t}{\Delta s_{k+1}} \right] \nu x_{i,k+1}^j = \\
& - \left[\nu \mathcal{C}_w^j f_V^{\Delta V_k} - \sigma_w \phi_w^j D_{i,w}^j \frac{\nu \theta \Delta t}{\Delta s_{k-1}} \right] \nu \hat{x}_{i,k-1}^j \\
& + \left[\omega \mathcal{C}_w^j \omega x_{i,k-1}^j + \omega \mathcal{C}_c^j \omega x_{i,k}^j + \omega \mathcal{C}_e^j \omega x_{i,k+1}^j \right] f_V^{\Delta V_k} \\
& + \left[\sigma_e \phi_e^j D_{i,e}^j \mathbf{grad}(x_{i,e}^j) - \sigma_w \phi_w^j D_{i,w}^j \mathbf{grad}(x_{i,w}^j) \right] \omega \theta \Delta t \\
& - \sum_{b=1, b \neq i}^n \Delta \mathbf{J}_{ib}^j \Delta t + \langle \phi^j \rangle^{\Delta V_k} \Big|_{\omega^t} \langle x_i^j \rangle^{\Delta V_k} f_V^{\Delta V_k} + \langle \phi^j \rangle^{\Delta V_k} \left[\dot{X}_i^j \theta \right]_{-\omega^t}^{\nu \theta} f_V^{\Delta V_k} \Delta t.
\end{aligned} \tag{C.13}$$

In the case of Neumann boundary conditions, fixed fluxes are defined at the first

or last grid point, respectively. When, for example, a volume element at the eastern boundary of a phase is selected, all eastern terms in Eq. (C.12) are replaced by a fixed flux on the right hand side as follows:

$$\begin{aligned}
& \left[\nu \mathcal{C}_w^j f_V^{\Delta V_k} - \sigma_w \phi_w^j D_{i,w}^j \frac{\nu \theta \Delta t}{\Delta s_{k-1}} \right] \nu x_{i,k-1}^j \\
& + \left[\nu \hat{\mathcal{C}}_c^j f_V^{\Delta V_k} + \sigma_w \phi_w^j D_{i,w}^j \frac{\nu \theta \Delta t}{\Delta s_{k-1}} \right] \nu x_{i,k}^j = \\
& \quad + \left[\omega \mathcal{C}_w^j x_{i,k-1}^j + \omega \hat{\mathcal{C}}_c^j \omega x_{i,k}^j \right] f_V^{\Delta V_k} \\
& - \left[\sigma_w \phi_w^j D_{i,w}^j \mathbf{grad}(x_{i,w}^j)_{\omega \theta} + \left[\hat{\mathbf{J}}_{i,e}^j \right]_{-\omega \theta}^{\nu \theta} - \sum_{b=1, b \neq i}^n \mathbf{J}_{ib,w}^j \right] \Delta t \\
& \quad + \langle \phi^j \rangle^{\Delta V_k} \Big|_{\omega t}^{\nu t} \langle x_i^j \rangle^{\Delta V_k} f_V^{\Delta V_k} + \langle \phi^j \rangle^{\Delta V_k} \left[\dot{X}_i^j \right]_{-\omega \theta}^{\nu \theta} f_V^{\Delta V_k} \Delta t.
\end{aligned} \tag{C.14}$$

It is remarkable that for this type of boundary condition, cross-diffusion is only modeled with the western neighbor since at the eastern boundary no gradient, but a fixed flux is given and thus no species interaction. The averaging parameter for the central grid point k at the eastern boundary $\hat{\mathcal{C}}_c^j$ is similar to \mathcal{C}_c^j , while omitting all eastern terms. From Eq. (C.12) and adequate boundary conditions, a system of equations is assembled consisting of a squared coefficient matrix \mathbf{K} , a vector \mathbf{X} containing the unknown concentrations, and a vector \mathbf{Y} on the right hand side for each phase j and component i at each grid point k :

$$\sum_{b=k-1}^{k+1} \mathbf{K}_{ib}^j \mathbf{X}_{i,k}^j = \mathbf{Y}_{i,k}^j. \tag{C.15}$$

C.2 Species Flux Balance

To discretize the species flux balance equation (4.7) in a formal manner, the species conservation equation (2.15) is multiplied with the local phase fraction ϕ^j and the divergence theorem (A.5) is applied. When considering a volume element at the solid-liquid interface with the thickness ε tending towards zero also the corresponding volume $V(\varepsilon)$ approaches zero. Thus, for integration over time, only surface terms $\star \sigma$ at the interface remain, that are namely the advective and diffusive term. The advective term characterizes the solidification flux due to the movement of the solid-liquid interface with the velocity $\star \mathbf{u}$. The interface grows with a difference in the product of local phase fraction and concentration as follows:

$${}^* \left[\sigma (\phi^L x_i^L - \sum_{j=1}^m \phi^j x_i^j) \mathbf{u} \theta \right]_{-\omega\theta}^{\nu\theta} \Delta t = {}^* \left[\sigma (\phi^L \mathbf{j}_{i,w}^L - \sum_{j=1}^m \phi^j \mathbf{j}_{i,e}^j) \theta \right]_{-\omega\theta}^{\nu\theta} \Delta t. \quad (\text{C.16})$$

Here, θ is the underrelaxation factor defined in Eq. (C.4). At the solid-liquid interface, the liquid phase is in general in equilibrium with multiple solid phases. Therefore, the sum over m solid phases is used. The diffusive fluxes arising in Eq. (C.16) are evaluated depending on the assumption for diffusion in each phase as follows:

$${}^* [\sigma \phi \mathbf{j}_i \Delta t] = \begin{cases} \Delta \langle x_i \rangle f & , \text{ complete mixing} \\ {}^* [\sigma \phi \mathbf{j}_i \Delta t] & , \text{ final diffusion, with } \mathbf{j}_i \text{ by Eq. (2.18)} \\ 0 & , \text{ no diffusion.} \end{cases} \quad (\text{C.17})$$

The change in phase fraction $\Delta f^j = {}^* [\sigma \phi^j \mathbf{u}] \Delta t$ replaces the interface velocity arising from Eq. (C.16). This results in a system of flux balance equations for multicomponent systems corresponding to the discretized version of Eq. (4.7):

$$\begin{bmatrix} ({}^*x_1^L - {}^*x_1^1) & \dots & ({}^*x_1^L - {}^*x_1^m) \\ \vdots & \ddots & \vdots \\ ({}^*x_n^L - {}^*x_n^1) & \dots & ({}^*x_n^L - {}^*x_n^m) \end{bmatrix} \begin{pmatrix} \Delta f^1 \\ \vdots \\ \Delta f^m \end{pmatrix} = \begin{pmatrix} {}^* \left[\sigma (\phi^L \mathbf{j}_1^L - \sum_{j=1}^m \phi^j \mathbf{j}_1^j) \theta \right]_{-\omega\theta}^{\nu\theta} \Delta t \\ \vdots \\ {}^* \left[\sigma (\phi^L \mathbf{j}_n^L - \sum_{j=1}^m \phi^j \mathbf{j}_n^j) \theta \right]_{-\omega\theta}^{\nu\theta} \Delta t \end{pmatrix}. \quad (\text{C.18})$$

The gradient at the solid-liquid interface is taken from the concentration solution applying the species conservation equation (C.15). According to Eq. (C.18), the change in phase fraction is sensitive to the species flux into diffusion phases which are in turn functions of the species gradient at the solid-liquid interface. To increase the stability of the solution, gradients are not determined by using the two grid points adjacent to the interface, but by a local regression function based on a fixed number of grid points in proximity to the interface. A linear regression function $x(s)$ of second order was selected to determine a concentration function $x(s)$ and thus also the gradient $x'(s)$ at the interface:

$$x(s) = p_1 + p_2 s + p_3 s^2, \quad x'(s) = p_2 + 2p_3 s. \quad (\text{C.19})$$

The three parameters p_1 , p_2 , and p_3 are determined in a way that the error square between regression function $x(s)$ and grid point values x_k is in minimum by introducing the error square function:

$$P(p_1, p_2, p_3) = \sum_{k=\hat{z}_1}^{\hat{z}_2} [x(s) - x_k]^2 \stackrel{!}{=} \min. \quad (\text{C.20})$$

The regression is usually realized by selecting 10 nodes at the interface: $\hat{z}_2 - \hat{z}_1 = 10$. The partial derivatives of the error square function with respect to each parameter p_1 , p_2 , and p_3 are given by:

$$\begin{aligned} \frac{\partial P}{\partial p_1} &= \sum_{k=\hat{z}_1}^{\hat{z}_2} [p_1 + p_2 s_k + p_3 s_k^2 - x_k] = 0 \\ \frac{\partial P}{\partial p_2} &= \sum_{k=\hat{z}_1}^{\hat{z}_2} s_k [p_1 + p_2 s_k + p_3 s_k^2 - x_k] = 0 \\ \frac{\partial P}{\partial p_3} &= \sum_{k=\hat{z}_1}^{\hat{z}_2} s_k^2 [p_1 + p_2 s_k + p_3 s_k^2 - x_k] = 0. \end{aligned} \quad (\text{C.21})$$

The three parameters are determined from these equations by consecutive substitution and rearrangement which gives:

$$\begin{aligned} p_3 &= \frac{\sum x_k s_k^2 - p_1 \sum s_k^2 - p_2 \sum s_k^3}{\sum s_k^4} \\ p_2 &= \left[\left(\frac{\sum x_k s_k}{\sum s_k^3} + \frac{\sum x_k s_k^2}{\sum s_k^4} \right) - p_1 \left(\frac{\sum s_k}{\sum s_k^3} - \frac{\sum s_k^2}{\sum s_k^4} \right) \right] / \left(\frac{\sum s_k^2}{\sum s_k^3} - \frac{\sum s_k^3}{\sum s_k^4} \right) \\ p_1 &= \frac{\left(\frac{\sum x_k}{\sum s_k^2} - \frac{\sum x_k s_k^2}{\sum s_k^4} \right) \left(\frac{\sum s_k^2}{\sum s_k^3} - \frac{\sum s_k^3}{\sum s_k^4} \right) - \left(\frac{\sum x_k s_k}{\sum s_k^3} - \frac{\sum x_k s_k^2}{\sum s_k^4} \right) \left(\frac{\sum s_k}{\sum s_k^2} - \frac{\sum s_k^3}{\sum s_k^4} \right)}{\left(\frac{\sum s_k}{\sum s_k^2} - \frac{\sum s_k^2}{\sum s_k^4} \right) \left(\frac{\sum s_k^2}{\sum s_k^3} - \frac{\sum s_k^3}{\sum s_k^4} \right) - \left(\frac{\sum s_k}{\sum s_k^3} - \frac{\sum s_k^2}{\sum s_k^4} \right) \left(\frac{\sum s_k^2}{\sum s_k^2} - \frac{\sum s_k^3}{\sum s_k^4} \right)}. \end{aligned} \quad (\text{C.22})$$

Here, the individual sums over node indices k are given within the bounds \hat{z}_1 and \hat{z}_2 .

D. Analytical Diffusion Solution

According to Evans (Eva98), the fundamental solution for a one-dimensional partial differential equation with a transient term and a term with a second derivative in space, such as the transport of species, is given by a concentration distribution function within the spatial $-\infty < s < \infty$ and the temporal limits $0 < t < \infty$ where $s, t \in \mathbb{R}$.

$$\frac{\partial x(s, t)}{\partial s} = \frac{1}{\sqrt{4\pi Dt}} e^{-\frac{s^2}{4Dt}} \quad (\text{D.1})$$

This concentration distribution function is integrated in space applying the error function which is given by:

$$\text{erf}(s) = \frac{2}{\sqrt{\pi}} \int_1^{s/\sqrt{4Dt}} e^{-y^2} dy, \quad (\text{D.2})$$

to obtain a concentration function of time and space. With constants of scaling and integration follows:

$$x(s, t) = \mathcal{C}_1 \text{erf}\left(\frac{s}{\sqrt{4Dt}}\right) + \mathcal{C}_2. \quad (\text{D.3})$$

When introducing a Dirichlet boundary at $x(0, t) = \hat{x}$ and an initial condition $x(s, 0) = x^0$ this function yields:

$$x(s, t) = (x^0 - \hat{x}) \text{erf}\left(\frac{s}{\sqrt{4Dt}}\right) + \hat{x}. \quad (\text{D.4})$$

E. Structure Charts

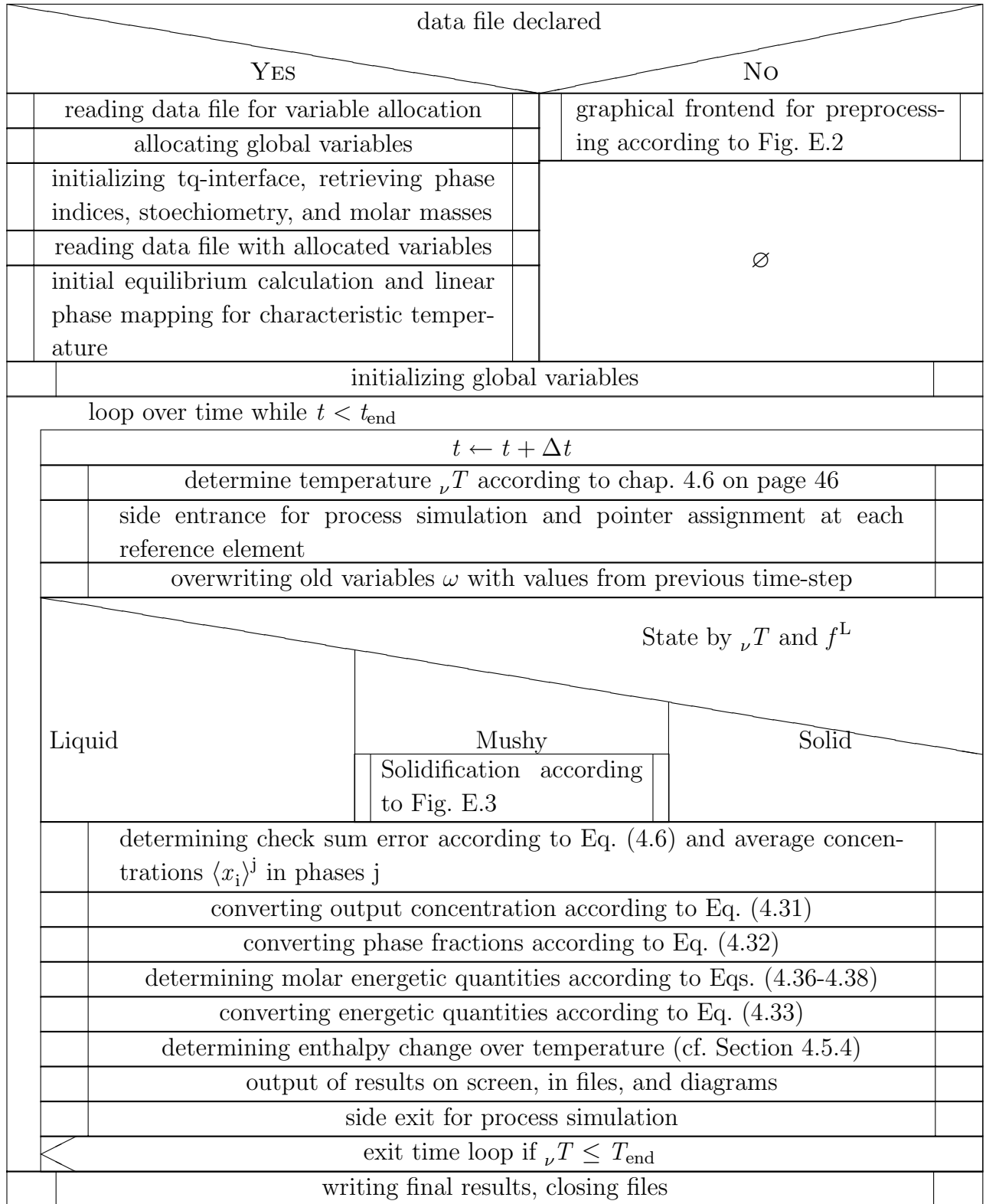


Fig. E.1: Structure chart of the microsegregation model

initial conditions: specification of a thermodynamic data (GES) file	
initializing tq-interface	
initial conditions: specification of initial concentration, temperature and termination temperature	
performing a one-dimensional phase mapping for a meaningful preselection of phases	
phases specific data: specifying a matrix phase, e.g. liquid, and phase selection	
retrieving stoichiometry, and molar masses during phase selection	
diffusion / volume data included in GES file	
YES	NO
retrieving diffusion / volume information from GES file	phases specific data: user input of diffusion and density data
phases specific data: selecting a phase type, i.e. complete mixing, cross-diffusion, diffusion, or no diffusion	
boundary and runtime conditions: user input of diffusion boundary conditions, time-step width, type of time-temperature correlation, underincrementation, and underrelaxation factor	
geometry: user input of a geometry coefficient, initial size of the RVE, and initial number of volume elements within the RVE	
coarsening	
YES	NO
geometry: user specification of coarsening phase, input of interface energy between liquid and coarsening phase, and a geometry coefficient for coarsening	\emptyset
output definitions: user specification of units of output quantities, Gnuplot output options, and output interval	
save input in a data file for simulation	

Fig. E.2: Substructure chart of the graphical frontend for data input, referring to Fig. E.1

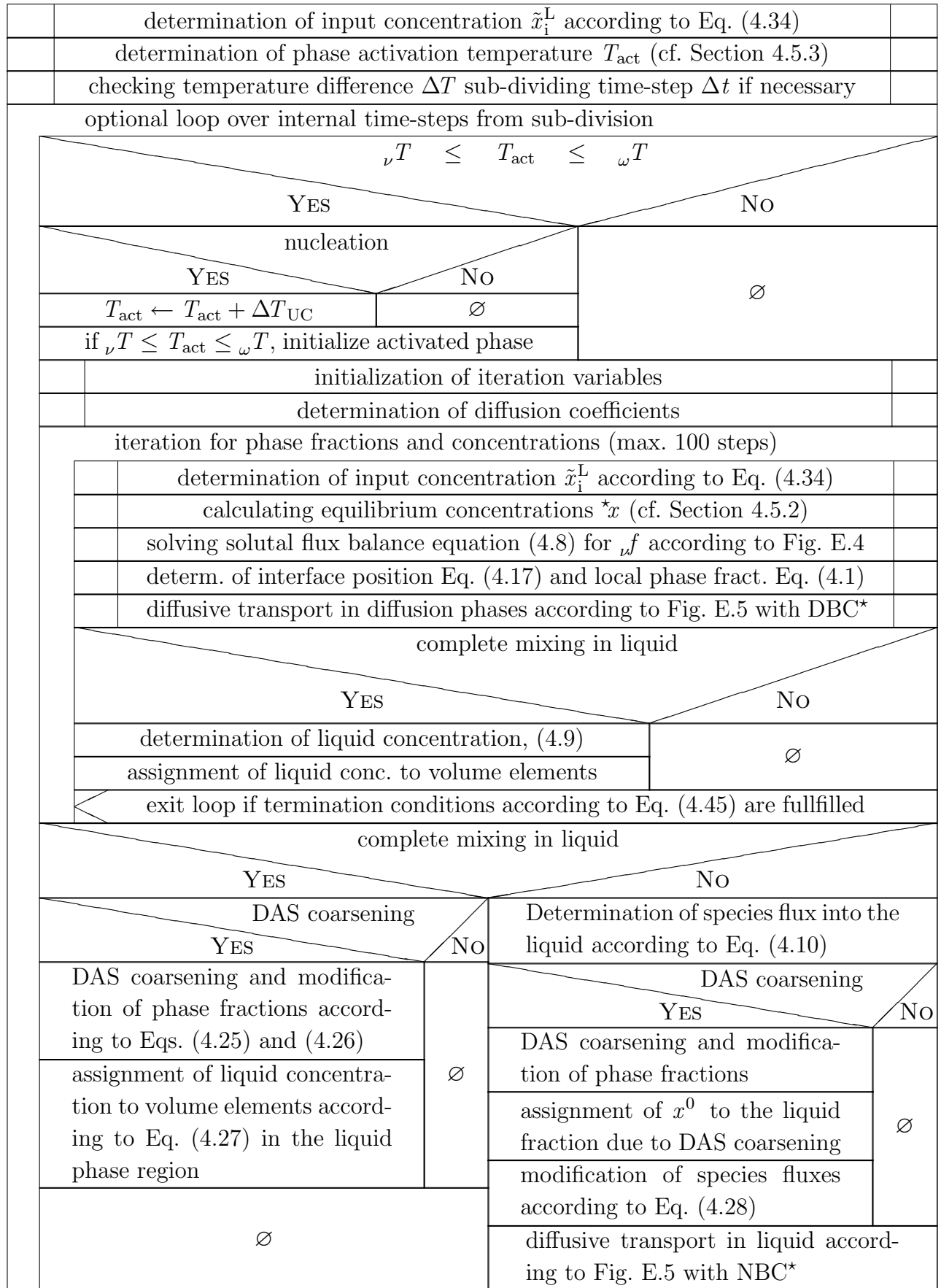


Fig. E.3: Substructure chart of a microsegregation loop during solidification, referring to Fig. E.1

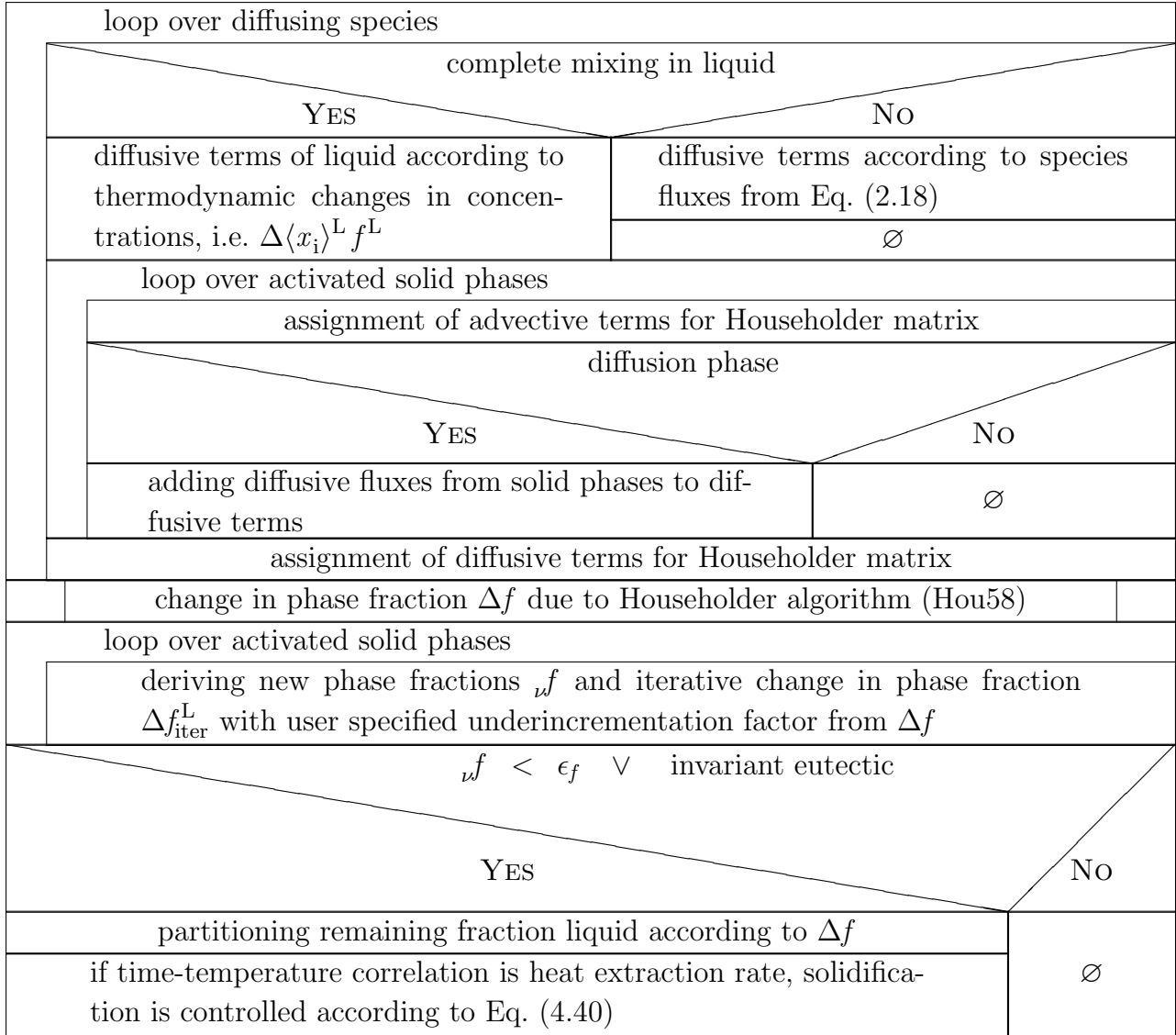


Fig. E.4: Substructure chart for assignment and solution of the solutal flux balance equation (C.18) applying a Householder (Hou58) algorithm, referring to Fig. E.3

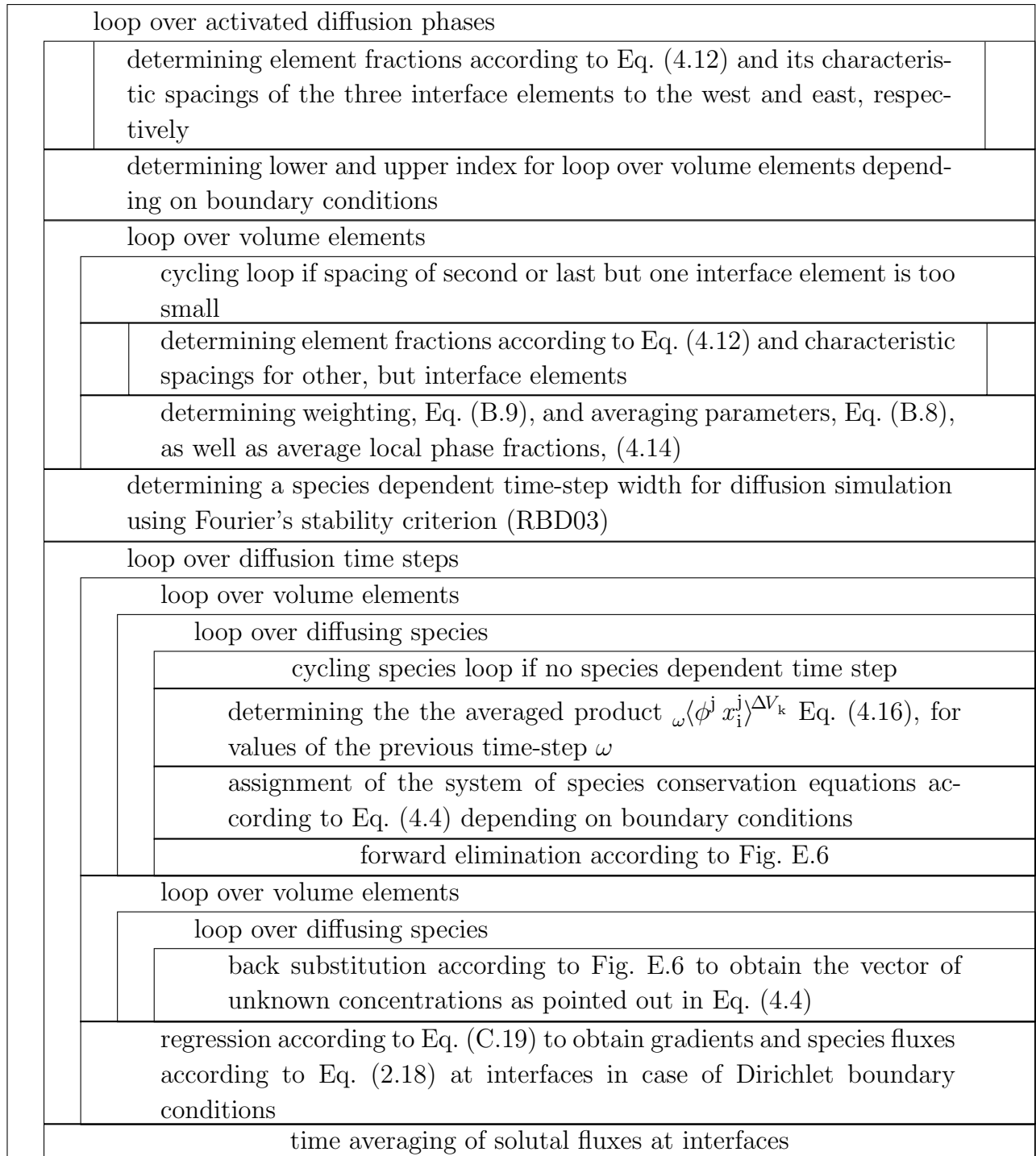


Fig. E.5: Substructure chart for assignment and solution of the solutal conservation equation (4.4), referring to Fig. E.3

variable declaration (further variables are declared in appendix A)	
U	{matrix, K , with eliminated lower diagonal}
R	{right side, Y , after elimination of lower diagonal}
$\mathbf{U}_{1,1} \leftarrow \mathbf{K}_{1,1}$	
$\mathbf{R}_1 \leftarrow \mathbf{Y}_1$	
loop over volume elements k ranging from 2 through z for forward elimination	
$\mathbf{U}_{k,k} \leftarrow \mathbf{K}_{k,k} - \frac{\mathbf{K}_{k,k-1}\mathbf{K}_{k-1,k}}{\mathbf{U}_{k-1,k-1}}$	
$\mathbf{R}_k \leftarrow \mathbf{Y}_k - \frac{\mathbf{K}_{k,k-1}\mathbf{R}_{k-1}}{\mathbf{U}_{k-1,k-1}}$	
$\mathbf{X}_z \leftarrow \frac{\mathbf{R}_z}{\mathbf{U}_{z,z}}$	
loop over the volume elements k ranging from z - 1 through 1 for back substitution	
$\mathbf{X}_k \leftarrow \frac{\mathbf{R}_k - \mathbf{K}_{k,k+1}\mathbf{X}_{k+1}}{\mathbf{U}_{k,k}}$	

Fig. E.6: Substructure chart for solution of tri-diagonal matrices, representing a TDM algorithm according to (RBD03), referring to Fig. E.5

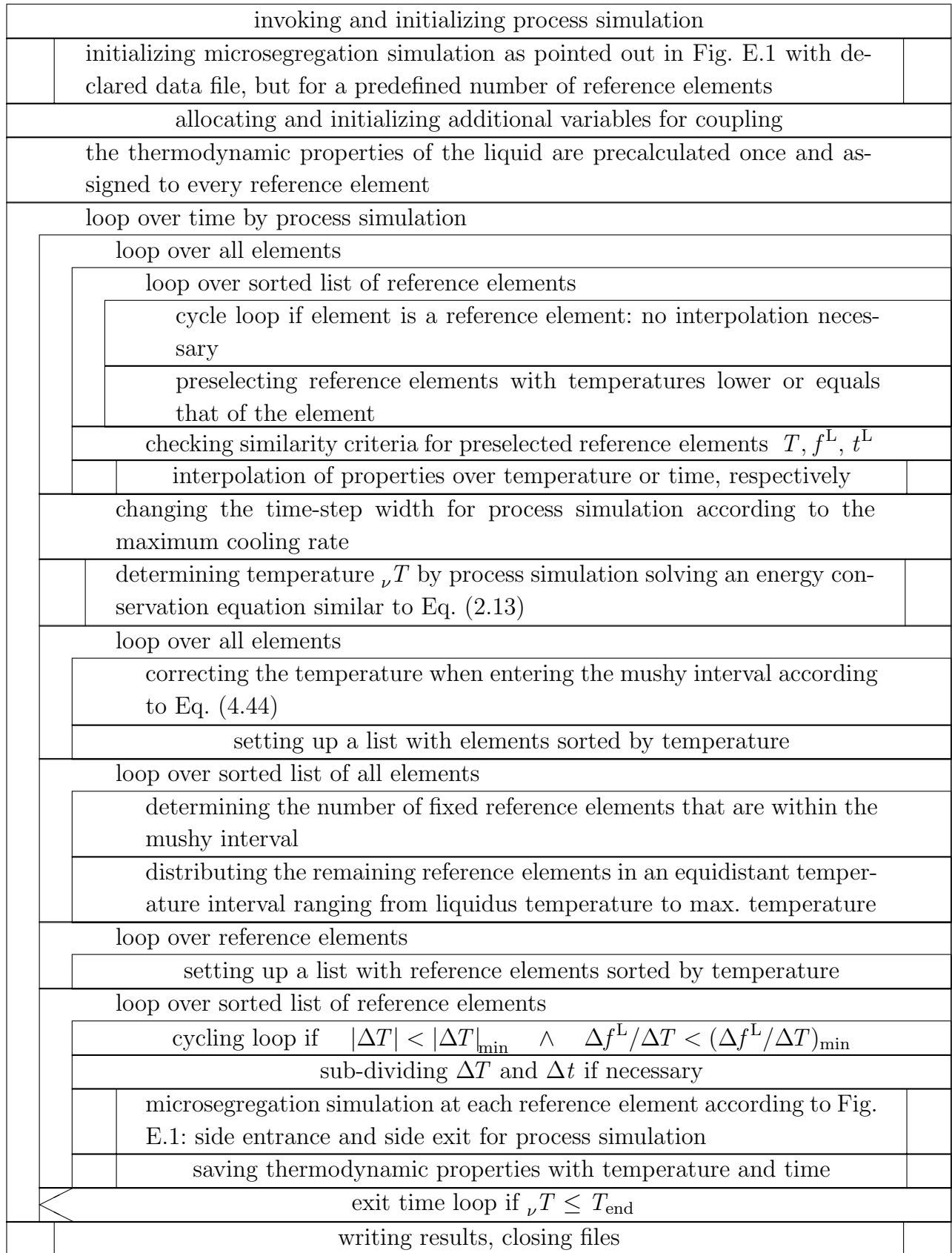


Fig. E.7: Structure chart for coupling to process simulation

F. Table of Figures

1	Representative volume element and multiphase concept	VI
2	Green sand mold with thermocouples and casting	XII
3	Etched sample and pictures of the microstructure	XIV
4	SEM backscatter electron picture of a eutectic region	XIV
5	X-rayed Casting c_c and c_d without central feeder	XV
6	Impact of submodels on the liquid fraction and liquid concentrations . . .	XVII
7	Impact of cross-diffusion on microsegregation of carbon	XVII
8	Impact of cooling characteristics on graphite fraction and coarsening . . .	XVIII
9	Impact of nickel on phase fractions	XIX
10	Comparison of the fraction solid deduced from DTA with different databasesXX	
11	Predicted distribution of microstructural quantities	XXII
12	Comparing experimental and virtual cooling curves of casting c_c and c_d .	XXIII
13	Experimental porosity superposition and predicted porosity	XXIV
2.1	Sketch about the formation and degeneration of microsegregations	6
2.2	Guggenheim scheme	7
2.3	Primary dendrite and eutectic grain in the same micro-shrinkage cavity .	13
2.4	Sketch about the decoupled growth of graphite and austenite	13
2.5	Scheme representing the change in growth velocity of graphite	14
2.6	Growth of graphite spheroids from conical helix crystals	14
2.7	Circumferential growth of graphite spheroids	15
2.8	Sketch about the formation of chunky graphite	16
2.9	Plan of graphene sheets and growth in c-direction	17
3.1	Impact of nickel and silicon on the eutectic carbon concentration	24
3.2	Experimental finding and sketch of graphite growth along the c-axes . . .	25
3.3	Central section of a block casting and a micrograph with chunky graphite	26

3.4	Interconnected strings of graphite crystallites	26
4.1	Representative volume element and multiphase concept	30
4.2	Interpolation of concentration and diffusion simulation	31
4.3	Change of local phase fraction in the RVE	32
4.4	Volumes, concentration, and local phase fraction in a finite volume element	37
4.5	Front-tracking and grid points within the RVE	38
4.6	Coupling of the microsegregation model to Thermo-Calc	44
5.1	Green sand mold with thermocouples and casting	54
5.2	Cooling curves in castings	55
5.3	Etched sample and pictures of the microstructure	56
5.4	DTA analysis of drilling chips retained from a casting	57
5.5	SEM micrograph with different phases and EDX line scan	58
5.6	Element distribution in a segregation-enriched zone	59
5.7	SEM micrograph of a eutectic region	60
5.8	EPMA line scan in a eutectic cell	60
5.9	X-rayed Casting c_a and c_f with central feeder	61
5.10	X-rayed Casting c_c and c_d without central feeder	61
5.11	X-rayed Casting c_g and c_h without central feeder	62
6.1	Impact of the submodels on liquid fraction and liquid composition	66
6.2	Impact of cross-diffusion on microsegregation of carbon	66
6.3	Varying the heat extraction rate applying the chemical diffusion model .	67
6.4	Application of the cross-diffusion and DAS coarsening model	68
6.5	Impact of cooling characteristics on graphite fraction and coarsening . . .	69
6.6	Impact of databases and alloy composition on phase fractions	70
6.7	Impact of carbon and silicon on phase fractions	71
6.8	Impact of nickel on phase fractions	72
6.9	Impact of chromium and manganese on phase fractions	73
6.10	Thermophysical data for simulations coupled explicitly	74
6.11	Simulated velocity field during mold filling	75

6.12	Simulated temperature field during mold filling	75
6.13	Simulated temperature field after mold filling	75
6.14	Comparison between commercial software and the present approach	77
6.15	Comparison of virtual and EPMA concentration profiles	78
6.16	Comparison of an analytical solution with predictions of the present model	79
6.17	Comparison of fraction solid from DTA with different databases	80
6.18	Phase fractions of various reference elements.	81
6.19	Predicted distribution of microstructural quantities	83
6.20	Comparing virtual cooling curves with those in castings	84
6.21	Porosity prediction applying a coupled simulation approach	86
6.22	Superposition of porosity detected in castings	86
E.1	Structure chart of the microsegregation model	121
E.2	Substructure chart of the graphical frontend	122
E.3	Substructure chart of a microsegregation loop	123
E.4	Substructure chart for solving the solutal flux balance equation	124
E.5	Substructure chart for solutal conservation equation	125
E.6	Substructure chart for solution of a tri-diagonal matrix	126
E.7	Structure chart for coupling to process simulation	127

G. Table of Tables

1	Comparison with state-of-the-art microsegregation models	V
2	Comparison of various analyses for the same cast alloy	XIII
3	Validation objectives and correlation level	XXVI
2.1	Energy potentials	7
3.1	Classification of non-equilibrium effects	20
4.1	Comparison to state-of-the-art microsegregation models	29
5.1	Comparison of various analyses of the same cast alloy	56
5.2	Composition of phases analyzed using EPMA	59
6.1	Initial, boundary, and runtime conditions for material simulations	64
6.2	Chemical diffusion matrix for GJSA-XNiCr20-2	67
7.1	Validation objectives and correlation level	91
A.1	Thermodynamic Variables	101
A.2	Model Specific Variables	102
A.3	Constants, Parameters and Factors	103
A.4	Indices and Bounds	104
A.5	Abbreviations and Definitions	105

“Solidification Modeling of Austenitic Cast Iron: A Holistic Approach“

Björn Pustal

Abstract

During solidification microsegregations build up in solid phases due to solid concentration variations with temperature. Diffusion, which is a kinetic process, usually reduces microsegregations. The present work aims at modeling such kinetic effects on solidification of austenitic cast iron applying a holistic approach. To this end, a microsegregation model was developed and validated. Moreover, this model was coupled directly to a commercial process simulation tool and thermodynamic software.

A series of GJSA-XNiCr 20-2 clamp-rings was cast varying inoculation state and number of feeders. The composition of this cast alloy was analyzed and the microstructure characterized to provide input data for the microsegregation model. To validate the software, cooling curves were recorded, and differential thermal analysis, electron dispersive x-ray analysis, and electron probe micro analysis were carried out. Furthermore, porosity within the casting was analyzed by x-ray.

Since significant discrepancies between the transformation temperatures measured and the values predicted by thermodynamic calculations became apparent, a numerical concentration variation analysis was performed. Moreover, two commercial and one open thermodynamic database, as well as three different chemical analyses of the cast alloy were compared. In this way, it was possible to determine the most appropriate combination of database and chemical analysis in relation to the predicted metal carbides, transformation temperatures, and solidification kinetics. Notwithstanding this effort, large temperature differences remain. The most probable reason for these discrepancies is nucleation and inaccuracy of the thermodynamic databases applied for this kind of alloy.

Various submodels for chemical diffusion, cross-diffusion, as well as cross-diffusion in combination with dendrite arm coarsening were compared as to identify their particular impact. This analysis shows that the chemical diffusion model does not reflect the solidification kinetics determined by experiments and is therefore not applicable to this type of alloy. In the present work, cross-diffusion was identified as the chief reason for the graphite promoting effect of nickel. Dendrite arm coarsening induces the sensitivity of the model to cooling characteristics, while at the same time reducing slightly the sensitivity to variations in heat extraction rate.

Validation of the model was attempted by comparing results to a solution from a commercial software product taking account of cross-diffusion. The results match when the diffusive fluxes are modified. Since in this case, the phase fractions correlate very well, the solution of the solidification problem is considered to be correct. To further validate the diffusion solver, it was compared to an analytical solution and could be verified by this test.

It could be shown through performing coupled simulations, that due to dendrite arm coarsening the different cooling characteristics within the casting lead to distinct differences in phase fractions and solidification temperatures. This transition of cooling characteristics is accompanied by a transition from a globular-eutectic to a chunky-dendritic microstructure in experiments. The hot spot effect below the feeders is aided by a shift towards lower solidification temperatures over solidification time. This shift is a result of local cooling characteristics which can only be predicted, if process simulation is directly coupled with material simulation. The porosity predictions and analyses show good agreement. A comparison between experimental and virtual cooling curves leads to the conclusion that the innovative coupling concept and its implementation are valid.

To achieve an effective coupling procedure between process and material simulation, a complex and unique microsegregation software has been generated. This model is notable for its time-efficient predictions and general applicability thanks to a multicomponent concept, thermodynamic coupling, cross-diffusion model, and multicomponent dendrite arm coarsening model. Furthermore, the characteristics of the present model were compared to decoupled and coupled state-of-the-art microsegregation models and four unique features were identified: (1) the innovative coupling concept to porosity prediction and (2) process simulation, (3) the multiphase concept, and (4) the concept for reproducing mixed geometries.

I. Curriculum Vitae

Björn Pustal

DOB 29th May, 1972 in Heidelberg

School Career

Aug. '91–Jun. '94 Staatl. Speyer-Kolleg, allg. Hochschulreife

Aug. '90–Jun. '91 Berufsbildende Schulen Speyer, Sekundarstufe I

Aug. '78–Jun. '87 GHS Altlußheim, Hauptschulabschluss

National Service

Jul. '95–Sep. '96 National service at Haus Kurpfalz: Wohnheim für ältere Menschen (home for senior citizens)

Apprenticeship

Aug. '87– Feb. '90 Foundry engeneer (Gießereimechaniker) at Mercedes Benz AG Mannheim, Certificate of apprenticeship

Higher Education

Sept. '04–Feb. '10 Doctoral study at the Foundry Institute at RWTH Aachen University

Okt. '96–Dez. '01 Course of study *Metallurgy and Materials Technique* Major Processes with focus on *Foundry Science* and *Metal Forming*, Diploma

Work Record

From Mar. '10 Senior teaching and research post (Akademischer Rat) at Foundry Institute at RWTH Aachen University

Sept. '04–Feb. '10 Scientific assistant at Foundry Institute at RWTH Aachen University

Jan. '03–Jan. '07 Head of the research group *Numerical Simulation and Fundamentals of Solidification* at Foundry Institute at RWTH Aachen University

Feb. '02–Sept. '04 Scientific researcher at Foundry Institute at RWTH Aachen University

Jul. '94–Jun. '95 Computer technician at GLOMAS Deutschland GmbH Speyer

Feb. '90–Aug. '90 Foundry engineer (Gießereimechaniker) at Mercedes Benz AG Mannheim

3rd December, 2010

“Erstarrungsmodellierung von austenitischem Gusseisen mit einem ganzheitlichen Ansatz”

Björn Pustal

Zusammenfassung

Bei der Erstarrung bilden sich in den Festkörperphasen Mikroseigerungen aus, da sich die Festphasenkonzentrationen mit der Temperatur ändern. Diffusion ist ein kinetischer Prozess und verringert Mikroseigerungen normalerweise. Die Modellierung solcher kinetischer Effekte während der Erstarrung von austenitischem Gusseisen in einem ganzheitlichen Ansatz ist Ziel dieser Arbeit. Zu diesem Zweck wurde ein Mikroseigerungsmodell entwickelt und validiert. Darüber hinaus wurde dieses Modell direkt an ein kommerzielles Prozesssimulationsprogramm und thermodynamische Software angebunden.

Es wurde eine Serie von Klemmringsen aus GJSA-X NiCr 20-2 abgegossen, wobei Impfzustand und die Anzahl der Speiser verändert wurden. Die Zusammensetzung dieser Gusseisenlegierung wurde analysiert und das Gefüge charakterisiert, um Eingabedaten für das Mikroseigerungsmodell zur Verfügung zu stellen. Zwecks Softwarevalidierung wurden Abkühlkurven aufgenommen, eine differenzielle thermische Analyse, eine elektronendispersive Röntgenanalyse und eine Elektronensonden-Mikroanalyse durchgeführt. Darüber hinaus wurde Porosität im Gussbauteil durch Röntgen analysiert.

Da erhebliche Abweichungen zwischen gemessenen und thermodynamisch vorherbestimmten Umwandlungstemperaturen zu beobachten waren, wurde eine numerische Konzentrationsvariationsanalyse durchgeführt. Des Weiteren wurden zwei kommerzielle und eine offene thermodynamische Datenbank ebenso wie drei unterschiedliche chemische Analysen der Gusseisenlegierung miteinander verglichen. Auf diese Weise konnte die beste Kombination von Datenbank und chemischer Analyse bezüglich der vorhergesagten Karbidbildung, der Umwandlungstemperaturen und der Erstarrungskinetik bestimmt werden. Trotz dieses Aufwands verbleiben große Temperaturunterschiede. Der wahrscheinlichste Grund für diese Abweichungen sind Keimbildung und die Ungenauigkeit der verwendeten thermodynamischen Datenbanken bei dieser Art Legierung.

Verschiedene Untermodelle für chemische Diffusion, Kreuzdiffusion sowie Kreuzdiffusion in Kombination mit Dendritenarmvergrößerung wurden verglichen, um deren jeweilige Auswirkung aufzuzeigen. Diese Analyse ergab, dass das chemische Diffusionsmodell die experimentell bestimmte Erstarrungskinetik nicht widerspiegelt und es für diese Art Legierung daher nicht anwendbar ist. In dieser Arbeit wurde erkannt, dass Kreuzdiffusion der Hauptgrund für den graphitfördernden Einfluss von Nickel ist. Dendritenarmvergrößerung führt einerseits die Empfindlichkeit des Modells bezüglich der Abkühlcharak-

teristik herbei und verringert andererseits leicht die Empfindlichkeit gegenüber Änderungen der Wärmeentzugsrate.

Zur Validierung wurde dieses Modell mit einer numerischen Lösung eines verifizierten kommerziellen Softwareprodukts verglichen, das Kreuzdiffusionseffekte während der Erstarrung berücksichtigt. Die resultierenden Lösung stimmen nur dann miteinander überein, wenn die diffusiven Flüsse modifiziert werden. Da in diesem Falle auch die Phasenanteile sehr gut übereinander liegen, wird die Lösung des Erstsarrungsproblems als richtig angesehen. Um den Diffusionslöser weiter zu validieren, wurde dieser anhand einer analytischen Lösung verifiziert.

Bei gekoppelten Simulationen führen die unterschiedlichen Abkühlcharakteristika zu ausgeprägten Unterschieden der Phasenanteile und der Erstarrungstemperaturen, was eine Folge der Dendritenarmvergrößerung ist. Dieser Wechsel der Abkühlcharakteristika wird bei den Experimenten von einem globulitisch-eutektischen zu einem knotenförmig-dendritischen Gefügeübergang begleitet. Die Ausbildung eines Wärmezentrums unterhalb der Speiser wird durch eine Verschiebung zu tieferen Erstarrungstemperaturen mit steigender Erstarrungszeit unterstützt. Diese Verschiebung ist ein Ergebnis der örtlichen Abkühlcharakteristika und kann nur dann vorhergesagt werden, wenn die Prozesssimulation unmittelbar an die Werkstoffsimulation angebunden ist. Die Porositätsvorhersage und die Porositätsanalyse weisen eine gute Übereinstimmung auf. Ein Vergleich zwischen experimentellen und virtuellen Abkühlkurven schließt mit dem Ergebnis, dass das neuartige Anbindungskonzept und seine Umsetzung gültig sind.

Im Sinne eines effektiven Anbindungsverfahrens zwischen Prozess- und Werkstoffsimulation wurde ein komplexes und einzigartiges Mikroseigerungsprogramm geschaffen. Dieses Modell zeichnet sich durch zeiteffiziente Vorhersagen und seine allgemeine Anwendbarkeit aus, was auf das Mehrkomponentenkonzept, die thermodynamische Kopplung, das Kreuzdiffusionsmodell und das mehrkomponenten Dendritenarmvergrößerungsmodell zurückzuführen ist. Darüber hinaus wurde das dargestellte Modell mit ungekoppelten und gekoppelten Mikroseigerungsmodellen, die dem Stand der Forschung entsprechen, verglichen. Es wurden vier Alleinstellungsmerkmale ermittelt: (1) die neuartige Anbindung an die Porositätsvorhersage und (2) die Prozesssimulation, (3) das Mehrphasenkonzept und (4) das Konzept zur Abbildung gemischter Geometrien.

K. Lebenslauf

Björn Pustal

Geburtsdatum: 29.05.1972

Geburtsort: Heidelberg

Schulbildung

08.1991–06.1994 Staatl. Speyer-Kolleg, allg. Hochschulreife

08.1990–06.1991 Berufsbildende Schulen Speyer, Sekundarstufe I

08.1978–06.1987 GHS Altlußheim, Hauptschulabschluss

Zivildienst

07.1995–09.1996 Zivildienst bei Haus Kurpfalz: Wohnheim für ältere Menschen

Berufliche Ausbildung

08.1987–02.1990 Ausbildung zum Gießereimechaniker bei der Mercedes Benz AG Mannheim, Berufsausbildungszeugnis

Studium / Promotion

09.2004–02.2010 Promotion am Gießerei-Institut der RWTH Aachen

10.1996–12.2001 Studiengang *Metallurgie und Werkstofftechnik* mit Vertiefungsrichtung Prozesse: Gießereikunde und Umformtechnik an der RWTH Aachen, Diplom

Beruflicher Werdegang

seit 03.2010 Akademischer Rat am Gießerei-Institut der RWTH Aachen

09.2004–02.2010 Wiss. Assistent am Gießerei-Institut der RWTH Aachen

01.2003–01.2007 Leiter der Forschergruppe *Numerische Simulation und Grundlagen der Erstarrung* am Gießerei-Institut der RWTH Aachen

02.2002–09.2004 Wiss. Angestellter am Gießerei-Institut der RWTH Aachen

07.1994–06.1995 Tätigkeit als Computertechniker bei der GLOMAS Deutschland GmbH Speyer

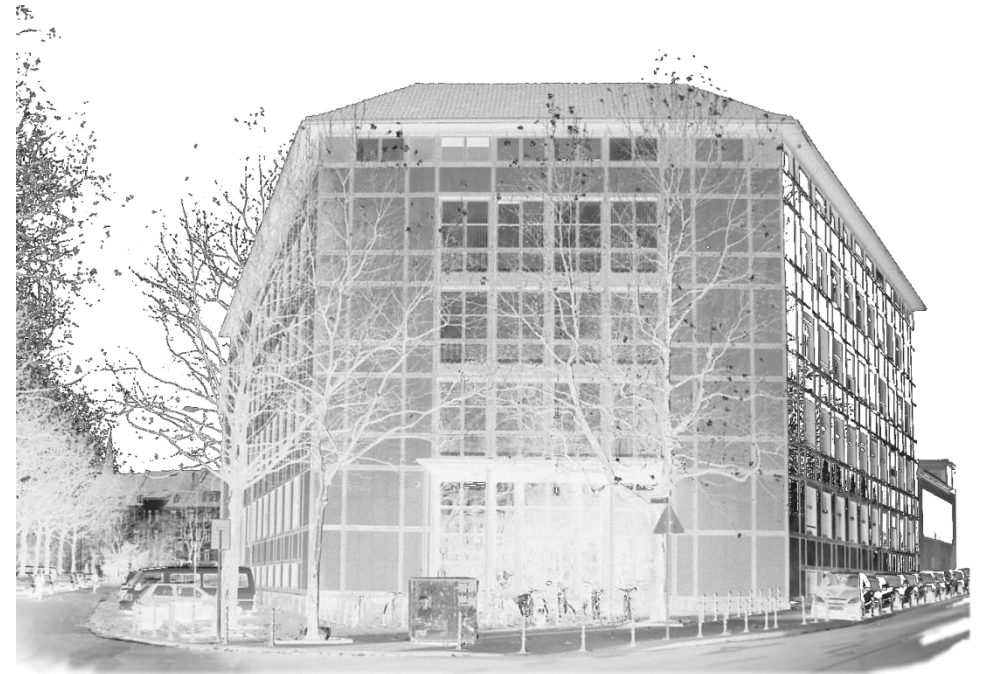
02.1990–08.1990 Tätigkeit als Gießereimechaniker bei der Mercedes Benz AG Mannheim

03.12.2010

Solidification Modeling of Austenitic Cast Iron: A Holistic Approach

Solidification Modeling of Austenitic Cast Iron: A Holistic Approach

Björn Pustal



Björn Pustal

ISBN 978-3-9813872-0-9 (eBook)

Band 1



Ergebnisse aus Forschung und Entwicklung

Herausgeber: Prof. Dr.-Ing. A. Bührig-Polaczek

RWTHAACHEN
UNIVERSITY